The Mechanisms of Deep Earthquakes

Andrew A. Hughes B.Sc. (Dunelm)

A thesis submitted in fulfillment of the requirements
for the degree of Doctor of Philosophy
to the
University of Edinburgh
1999

Abstract

In most tectonic settings, no earthquakes occur below about 30 km depth. This is because increasing pressure inhibits frictional sliding, whilst increasing temperature promotes ductile deformation. However, in subduction zones, earthquakes are observed to depths approaching 700 km, equivalent to pressures of around 25 GPa. Under such conditions, and according to the most basic principles of rock deformation, brittle failure should be impossible. Yet deep earthquakes are dominated by simple shear and appear similar to shallow earthquakes. Thus, some process must allow unstable sliding at great depth, either by reducing the effective coefficient of friction along the the fault, or by reducing the effective confining pressure. These mechanisms are often linked in the literature to the occurrence of mineral reactions.

In this thesis, two dimensional thermal models are calculated for many subduction zones, providing estimates of the temperature distribution in the subducting slab and the surrounding mantle. The slab geotherms are superimposed onto phase diagrams showing the equilibrium pressure–temperature stability fields of hydrous minerals thought to exist in the subduction zone environment, allowing comparison between the predicted positions of dehydration reactions and the observed patterns of seismicity. It is shown that deep seismicity is not directly related to the occurrence of dehydration reactions within the subducting crust. Furthermore, the observed double seismic zone beneath the Eastern Aleutian Islands also cannot be explained as resulting from dehydration reactions. However, the maximum depth of seismicity in all the subduction zones examined is consistent with a constant homologous temperature of approximately 0.4 $\times$ the dry peridotite solidus. The locus of this homologous temperature does coincide

with the Aleutian double seismic zone. These observations imply a thermally–activated control on seismicity which is relatively pressure–insensitive.

Although it is known that deep and shallow earthquakes are similar, knowledge of the detailed kinetics of deep sources is insufficient to determine whether or not they are the same as shallow tectonic sources. The polarities and relative amplitudes of P and its surface reflections at teleseismic distances are used to determine the amount of constraint which can be placed on eight deep earthquake sources, by inverting for a full range of possible point sources, including volume change and components of pure shear. All the earthquakes examined are compatible with a double couple source (constant volume, simple shear). The most well constrained solution, for an event in the Tonga subduction zone, shows that any reduction in volume accounts for less than 2% of the total seismic moment.

Variations in the duration of P and pP are modelled as directivity effects and are used to invert for the source geometry and velocity of rupture. The rupture velocities vary widely, with a minimum range of $1.2 \leq V_r \leq 4.5\,\mathrm{km\,s^{-1}}$, and are independent of pressure, temperature and fault plane orientation. The inversions show that all the compatible rupture surfaces are approximately circular.

Observed correlations between increases in seismic event rate and points where the Izu–Bonin slab is deflected by the mantle transition zone suggest that the global depth distribution of deep earthquakes correlates directly to variations in strain rate, and does not require different earthquake source processes at different depths, as in the standard model which requires dehydration induced embrittlement at intermediate depths and transformational faulting at great depths. All the results described are instead in agreement with the hypothesis that instability develops as a result of dynamic grain size reduction and / or heating through viscous dissipation in a predominantly plastic deformation regime. The effective coefficient of friction is lowered dramatically by the presence of ultrafine grain sizes or partial melt, allowing unstable frictional sliding. This mechanism is consistent with published field observations of pseudotachylytes in otherwise ductile shear zones from the deep crust and shallow lithospheric mantle.

Declaration

I declare that this thesis has been composed solely by myself and that it has not been submitted, either in whole or in part, in any previous application for a degree. Except where otherwise acknowledged, the work presented is entirely my own.

Andrew A. Hughes
December 1999

Acknowledgements

This project would not have been possible without help and support from many people. First, a thank you to my supervisors in Edinburgh, Ian Main and Bob Pearce, who devised the project. Their sound judgement and patience with my naive questions are much appreciated. Ian commented on the whole manuscript and provided many useful suggestions and frequent injections of enthusiasm.

The project was in collaboration with the Earth Sciences Department at ETH Zurich, where I spent 15 very productive weeks. Special thanks go to Alan Thompson, who supervised me during my time there and organised a superb, but exhausting, deep earthquake workshop, and also to Domenico Giardini and Edi Kissling, for many stimulating and enlightening lunchtime discussions. Peter Ulmer and Stefan Poli generously gave advice and phase diagrams prior to publication, and Yuri Podlatchikov pointed out many hidden possibilities. I thank all the staff and students at ETH for their help and hospitality, and Guy, Katja and Bruce for great friendship, food and grappa.

I am grateful to George Helffrich, who provided a copy of the thermal modelling code, and to Mike Kendall, who provided guidance about ray tracing techniques. I was indoctrinated into seismology and the GSPL software by Sarah Buchanan, who is a shining star. During spring (arctic winter?) '99, I spent a week at the Atomic Weapons Establishment, Blacknest, where I benefited immensely from the seismological expertise of Alan Douglas, David Bowers and all who work there. Thanks guys. Back in Edinburgh, Shane, Chis and Justin helped with lots of computing problems and even managed to fix the UNIX system after I broke it!

On a personal note, thanks to Mum and Dad for their unconditional and unfaltering faith in me, and for continued financial support above and beyond the call of duty. Numerous posties have been great friends and walking buddies, and Ellen made my final year immeasurably happier than it had any right to be. Extra special thanks go to Mike and Fi, without whom this thesis wouldn't exist and, also without whom, I would have sampled a lot less fine wine and whisky.

The project was funded by the Natural Environment Research Council, studentship GT4/96/85/E, for which I am grateful.

Contents

List of Figures

List of Tables

Notation, Definitions and Conventions

Symbols

σ Strike of a fault plane, measured clockwise from north. $0 \leq \sigma \leq 360°$.

δ Dip of a fault plane, measured clockwise from the strike. $0 \leq \delta \leq 180°$.

ψ Angle of slip of the footwall, measured in the fault plane with respect to the strike. $0 \leq \psi \leq 180°$.

k The fractional volumetric component of an earthquake source type.

T Measure of the constant volume component of an earthquake source type.

Q Quality factor. Q is inversely proportional to the amount of attenuation.

t* Measure of attenuation along a specific path, given by travel time over average Q.

Abbreviations

DPS Dry Peridotite Solidus

CMT Centroid Moment Tensor.

EHB The Engdahl, Hilst and Buland catalogue of earthquake hypocentres, in which depths are determined by the automated picking of surface reflections.

IASP91 Earth velocity model of Kennett & Engdahl (1991).

ISC International Seismological Centre (UK).

JMA Japanese Meteorological Agency.

Ma Million years.

NEIC National Earthquake Information Center (USA).

NUVEL1 Plate motion reconstruction of Demets *et al.* (1990).

PT Pressure–Temperature.

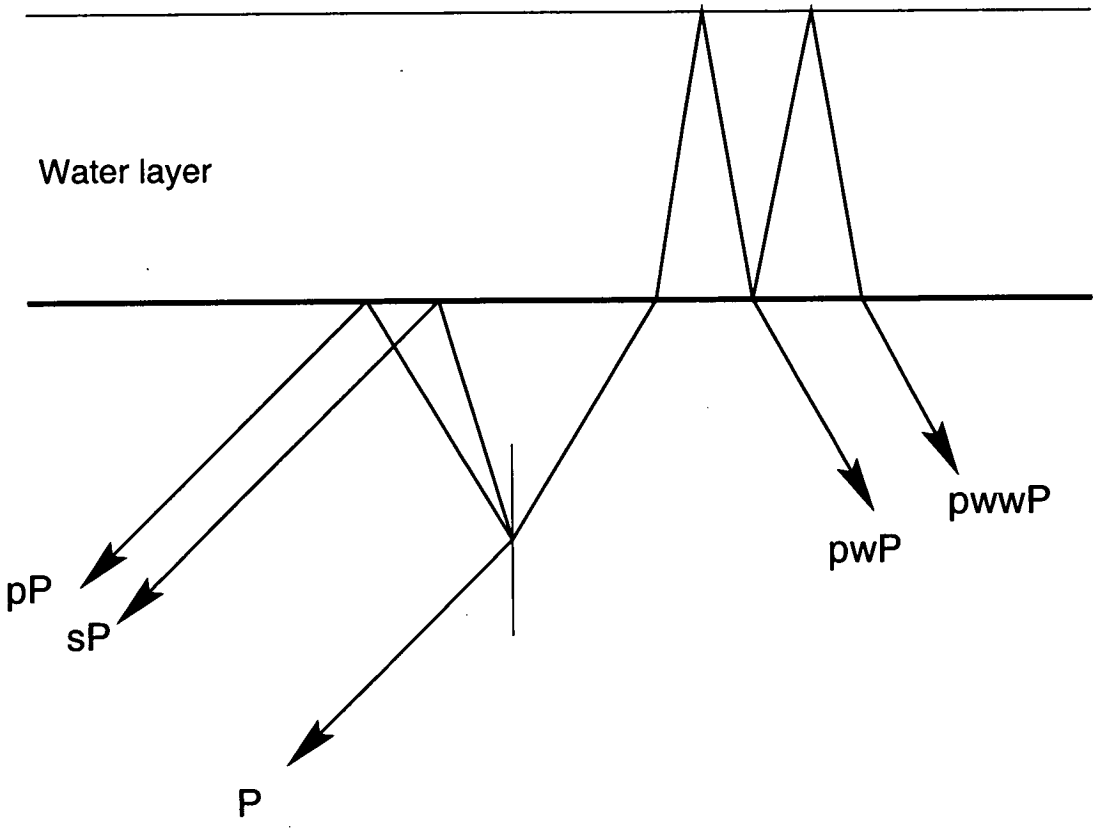

Figure 0.1.
The direct P–wave and various types of surface reflection. A source in the crust beneath a water layer is shown, with simplified ray paths for the key seismic phases used in this study. pP and sP are shown as reflections from the crust–water interface, but this terminology is used equally to describe reflections at the crust–air interface for continental paths. pwP and pwwP are reflections from the sea surface.

Mineral Compositions

Typical compositions of the minerals important in this study are given below.

Mineral name	**Composition**
Nominally anydrous minerals	
Olivine	$(Mg_{0.9},Fe_{0.1})_2SiO_4$
Perovskite	$MgSiO_3$
Magnesiowustite	(Mg,Fe)O
Periclase	MgO
Enstatite	$MgSiO_3$
Stishovite	SiO_2
Hydrous minerals and phases	
Lawsonite	$CaAl_2[Si_2O_7](OH)_2 \bullet H_2O$
Serpentine	$(Mg_{0.95},Fe_{0.05})_3[Si_2O_5](OH_4)$
Chlorite	$Mg_5Al_2Si_3O_{10}(OH)_8$
Brucite	$Mg(OH)_2$
Phase A	$Mg_7[SiO_4]_2(OH)_6$
10Å–phase	$Mg_3Si_4O_{10}(OH)_2 \bullet 2H_2O$
Super–hydrous phase B	$Mg_{10}Si_3H_4O_{18}$
Phase D	$Mg_2Si_3H_4O_{10}$
Phase E	$Mg_{2.3}Si_{1.25}H_{2.4}O_6$

Chapter 1

Introduction

Earthquakes release stresses which build up at or near the earth's surface. There are two simple requirements for their occurrence. Firstly, the forces acting on a fault between two rock masses must increase sufficiently to overcome the static frictional strength of the fault. Secondly, the dynamic frictional resistance must be lower than the original frictional strength. If these criteria are met, then unstable sliding will result, generating an earthquake. Sliding stops once sufficient stress has been released that the forces acting on the rock masses are no longer large enough to overcome the residual friction between the fault surfaces.

In a series of laboratory experiments, Byerlee (1968) showed that the coefficient of surface friction for nearly all geological materials was 0.6–0.7. This work led to the quantification for rock of Amontons' law of friction, which stated that the shear stress required for frictional sliding along a surface was equal to the coefficient of friction multiplied by the effective normal stress. Since the coefficient of friction for rock is a little less than 1, then the shear stress must be at least of the same order of magnitude as the confining pressure (equal to the effective normal stress in an isotropic stress field) if frictional sliding is to occur. This law has been shown to hold in the laboratory up to pressures approaching 2 GPa, equivalent to a depth of 70 km. A full review of the theory of friction can be found in Scholz (1990), and an up–to–date description of the rate– and state–variable friction laws, which govern whether or not frictional sliding will be unstable, is given by Scholz (1998).

The maximum shear stress that a rock can support is equal to its strength. Now, the resistance of rock to fracture and sliding increases with increasing pressure, whilst its resistance to flow decreases with increasing temperature. Thus, the strength of a rock, which is defined as the lowest stress at which it yields, varies with depth. Near the surface of the earth, temperatures are sufficiently low that rock yields in a brittle manner, that is, it fractures and slides and its strength increases with depth. However, below a certain depth, the resistance to flow by thermally activated processes becomes less than that of sliding, and the rock yields plastically. This point of transition between the two mechanisms is known as the brittle–ductile transition, and its depth varies according to the local geotherm and the time scale over which it is measured. Rock strength falls rapidly at depths below this point, because temperature continues to increase. As a result, earthquakes occur only in the field of brittle deformation, because it is only here that the shear stress can approach or exceed the confining pressure. This simple description of seismogenesis, or the processes which give rise to earthquakes, predicts the depth extent of seismicity to coincide with the onset of crystal plasticity. In quartz, this occurs at about 300 °C, corresponding to the typical maximum earthquake depth in continental crust of about 15 km (Scholz 1990, p129). Earthquakes in basaltic oceanic crust are typically bounded by the 450 °C isotherm, marking the onset of ductility in feldspar, the most ductile mineral in basalt (Scholz 1998). This isotherm usually lies between 20 and 30 km depth. It is, therefore, surprising that in some places, earthquakes occur all the way down to 700 km depth.

These deep earthquakes occur in subduction zones, linear features where the cold, outer shell of the earth, the lithosphere, sinks back into the deep interior, driven by negative buoyancy forces. Earthquakes are observed up to pressures of about 25 GPa, many times greater than estimates of the largest shear stresses that could occur in the earth. Thus, it should be impossible for frictional sliding to occur, since the rock should flow plastically. However, deep earthquakes appear to have simple sliding mechanisms, just like shallow earthquakes. Indeed, there are few observed differences at all between the two. So, the occurrence of deep earthquakes has offered a fundamental challenge to our understanding of rock deformation ever since they were first identified early in the twentieth century (Wadati 1928).

Many possible mechanisms have been proposed to account for the phenomenon of deep seismicity. Several of the most promising hypotheses invoke mineral reactions to provide a mechanism of embrittlement (Green & Houston 1995), which raises the possibility that the source mechanism may include a reduction in volume, a common feature of reactions which occur under high pressures. No such volume change has yet been detected [e.g. Kawakatsu (1991)], but the error bars associated with inversions for the source characteristics of deep earthquakes are generally larger than any predicted volume change.

In this thesis I use two methods of investigation to try and gain some understanding of the source processes which allow deep earthquakes. In chapters 3 and 4, I calculate two dimensional thermal models of subduction zones to determine the temperatures at which the earthquakes occur. Pressure is easily calculated from the depth of the earthquake, so it is possible to examine the relative importance of pressure and temperature in controlling seismicity. I show that the spatial distribution of deep seismicity is strongly controlled by temperature, just as in the case of earthquakes in the continental or oceanic crust, but is independent of pressure, suggesting that the local mechanism for seismogenesis is unrelated to the occurrence of mineral reactions, which are dependent on both pressure and temperature. However, mineral reactions do play a rôle in providing the driving force for deformation, in conjunction with the negative thermal buoyancy of the descending lithosphere, as will be described in section 2.2.

Although deep earthquakes appear similar to shallow earthquakes, they may have small differences in source mechanism which have not yet been recognised. In chapter 5, I describe methods which allow for high resolution determination of many of the physical characteristics of an earthquake. The eight deep earthquakes shown in figure 1.1 are analysed using these methods and the results are presented in chapter 6. They show that all eight earthquakes are compatible with a constant volume sliding source. The implications of both my results and the latest results from other workers are synthesised in chapter 7, leading to a hypothesis for the occurrence of deep earthquakes and providing a simple view on how seismicity can be generically classified according to the manner in which frictional sliding is enabled, either by the magnitude of the shear stress, a reduction in the effective coefficient of friction or by a reduction in the effective normal stress.

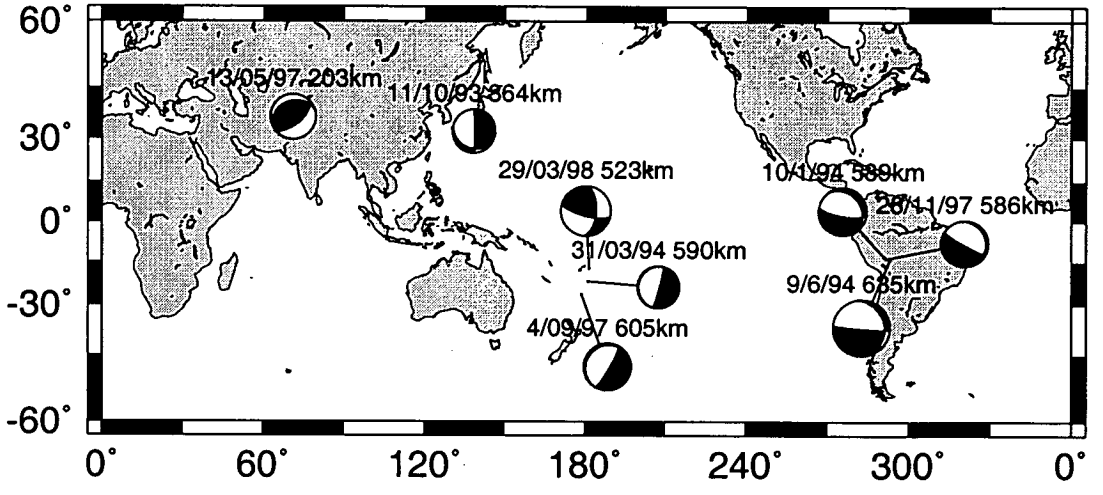

Figure 1.1.

The eight deep earthquakes investigated in this study. The focal mechanisms determined in chapter 6 are shown as lower focal hemispheres and indicate the epicentres of the earthquakes. All the earthquakes have a body wave magnitude greater than 6.0 and the radius of the focal mechanism is proportional to this magnitude. The event in continental Asia occurred beneath the Hindu Kush mountains, whilst all the other events are associated with subducting oceanic lithosphere.

Traditionally, earthquakes have been classified according to the depth at which they occur. Gutenberg & Richter (1954) defined earthquakes as shallow if they occurred between 0 and 70 km depth, intermediate between 70 and 300 km depth, and deep if they occurred at depths greater than 300 km. Throughout this thesis, I shall use the term "deep" to refer to any seismicity that occurs beneath 70 km depth, unless it is used in conjunction with "intermediate", when the precise definitions of Gutenberg & Richter (1954) are implied.

Recent work by Engdahl, van der Hilst & Buland (1998) has improved our knowledge of the depths at which earthquakes occur. Routine earthquake location is performed by the International Seismological Centre (ISC), using P–wave arrival times. The depth estimates so produced are often rather inaccurate and have large error bars. To improve depth estimates, Engdahl *et al.* (1998) developed a computer algorithm which identifies the surface reflections, pP and sP (defined in figure 0.1), and uses their arrival times to calculate the depth of the earthquake. This method provides depth estimates of much greater accuracy than using first arrival times alone and has been applied to all the large events in the ISC catalogue, which dates back to 1964, generating a global catalogue of seismicity with high quality depth estimates. It is referred to as the EHB catalogue and is used extensively in this thesis to plot local patterns of seismicity.

In many sections of this thesis, the frequency content of the seismic radiation emitted by deep earthquakes is an important parameter. I illustrate its characteristics here, in figure 1.2, rather than have multiple explanations of it throughout. Attenuation (described further in section 2.2) leads to the preferential loss of high frequency energy, but examination of many seismic spectra at similar epicentral distances confirmed that different earthquakes showed characteristically different source spectra. Figure 1.2 shows the amplitude spectra of two P–waves from different deep earthquakes, one of which has excited relatively high frequencies for a deep event, and the other of which emitted most of its energy at very low frequencies. However, in both cases, virtually all the energy is carried by frequencies of less than 0.5 Hz and it is clear from the examination of many such spectra that this a consistent feature amongst the eight events investigated. In several cases, some high frequency energy was present at frequencies of up to 4 Hz, but its amplitude was small. At frequencies greater than this, any energy from the

earthquake was of similar or lesser amplitude than the background noise and was, therefore, unidentifiable.

To appreciate the issues and complexities involved in the study of deep earthquakes, a wide range of petrological, seismological and rheological background knowledge is required. The key aspects of this background are presented in the following chapter, which also provides a review of the mechanisms proposed to explain deep seismicity.

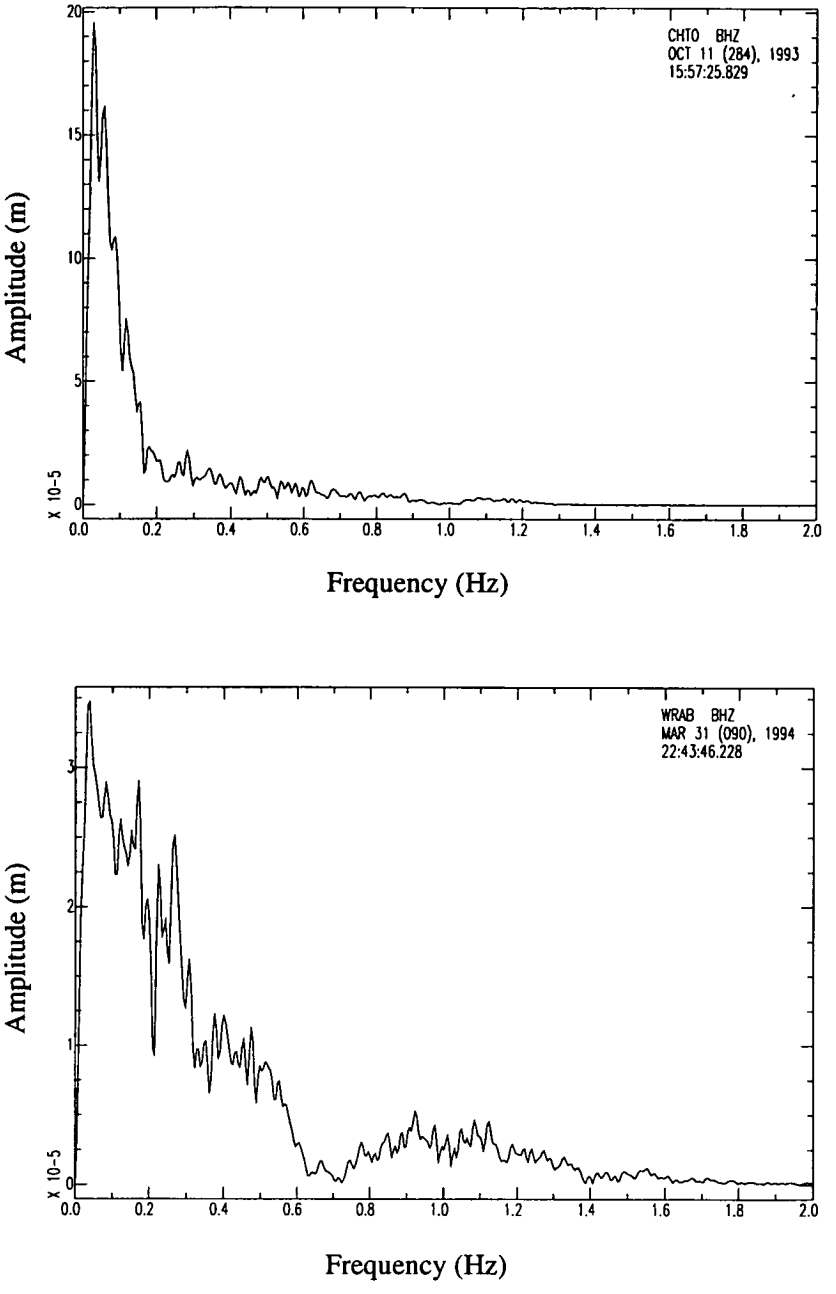

Figure 1.2.

P–wave amplitude spectra from two deep earthquakes. The graphs show the variation of amplitude with frequency of the direct P–wave. The spectra were obtained from the Fourier transform of part of the broadband seismogram and show that almost all the energy is carried at frequencies of less than 0.5 Hz. The maximum noise amplitude is less than 1×10^{-5} m and large amplitude noise occurs only below 0.3 Hz, where it causes some of the high–frequency fluctuations in the spectra.

Chapter 2

Subduction Zones and Earthquakes

2.1 Introduction

Deep earthquakes occur uniquely in subduction zones, sites where old, cold and normally, but not necessarily, oceanic lithosphere descends into the mantle. Moreover, they seem to occur only in the subducting lithosphere and not in the adjacent mantle, although this has yet to be proven beyond all doubt. Thus, it is essential to study the generic characteristics of subduction zones and subducting lithosphere in the search for the factors which govern the occurrence of deep earthquakes. However, any hypothesis explaining deep seismogenesis must be consistent with observations from individual subduction zones, rather than only with the globally averaged characteristics. To accommodate both approaches, many subduction zones are investigated in this thesis, but a few are examined in greater detail. The locations of all the oceanic subduction zones studied are shown in figure 2.1, a shaded topographic image of the Pacific Ocean and surrounding area, and the generic structure of subduction zones is described in section 2.2.

Most hypotheses regarding the source mechanisms of deep earthquakes have been based upon observations of the subduction zone environment, earthquake statistics and laboratory experiments. These lines of evidence are summarised and the

Figure 2.1.

Location map showing the oceanic subduction zones studied. Shaded topographic and bathymetric map of the Pacific Ocean and surrounding area. Ocean trenches are visible as fine white lines adjacent to thicker dark lines, representing the large contrast in elevation between the the trench and the associated volcanic arc. Subduction zones studied in this thesis are labelled by name, and the direction of each plate motion is shown by an arrow. Names are consistent with those given by Jarrard (1986).

proposed earthquake source processes explained in sections 2.4 to 2.7. However, any such hypothesis must also be consistent with the constraints that we can place on the physical source mechanism. Thus, prior to the discussion of specific processes, the theory of earthquake source types and source representation is presented in section 2.3.

2.2 Subduction Zone Structure

Subduction zones have a simple "first–order" structure. The subducting lithosphere, or slab, remains colder than the ambient mantle to great depths, and also has a higher seismic velocity. Long–period seismic waves travelling through the slab will lose less energy than if they travelled through normal mantle, that is, they suffer less *attenuation.* Attenuation describes all forms of energy loss, and three types are usually distinguished. *Geometrical spreading* is the loss of amplitude due to the expanding area covered by a spherical wavefront as it propagates away from a point. At any boundary or inhomogeneity, some of the energy will be reflected, converted to another type of radiation, refracted or diffracted. Such energy dispersal is known as *scattering.* The third form of attenuation results from the anelasticity of the material through which the wave is travelling. The ratio of the amount of stored energy to the rate of energy dissipation is called Q and is an inverse measure of the amount of *anelastic attenuation.* Thus, regions with high Q cause little attenuation, and vice versa.

The typically observed large scale characteristics of a subduction zone are illustrated in figure 2.2. The subducting slab has a high seismic velocity and high Q, characteristics caused by its lower temperature than typical mantle and resulting high viscosity. In contrast, the mantle overlying the slab has unusually low seismic velocity and low Q compared to average mantle (Barazangi & Isacks 1971). These latter characteristics are produced by two different processes. Firstly, some subduction zones migrate laterally in the direction of the ocean, a process known as "roll–back" and caused by the dense oceanic lithosphere sinking sub–vertically into the mantle. The resulting extension is accommodated by small scale spreading behind the volcanic arc, upwelling mantle resulting in an advective transfer of heat and decompression melting. The resulting presence of partial melt, and the

lower viscosity of the solid rocks due to high temperatures, dramatically increases the amount of anelastic attenuation and reduces seismic velocities, particularly S–wave velocities since S–waves cannot propagate through fluids. The second effect is the influence of volatile fluids liberated from the slab through dehydration reactions. These lower the melting point of the mantle, encouraging partial melting above the slab. The resulting melt rises buoyantly to the surface, where it fractionates and is ejected through the volcanoes of the volcanic arc. Both the melt and the volatile fluids reduce the seismic velocity and Q of the mantle.

The regions identified in figure 2.2 correlate well with the predicted distribution of temperature in a subduction zone. Figure 2.3 shows the thermal model of Schubert, Yuen & Turcotte (1975), one of the most referenced models of subduction zone thermal structure. The subducting lithosphere is anomalously cold, whilst the back–arc region is characterised by raised temperatures and high heat flow, consistent with the regions identified by velocity and attenuation measurements in figure 2.2.

Thus, the first order features of subduction zones are relatively simple. However, detailed observations reveal that smaller, second–order complexity also exists. Some of this is due to the continuous variation of temperature across the slab (Iidaka, Mizoue & Suyehiro 1992), whilst the rest is largely related to the exact structure and composition of the oceanic lithosphere prior to subduction (Helffrich 1996). A typical cross section through oceanic lithosphere is shown in figure 2.4, and demonstrates the extent to which the composition varies with depth. The crust, of basaltic composition, contains large amounts of water introduced by hydrothermal circulation in areas of high heat flow. Below the crust lies the mantle, which was depleted by the formation of the crust and which may have been completely dehydrated at the same time (Hirth & Kohlstedt 1996). At greater depth, the mantle is less depleted and contains some water bound in the crystal lattices of its constituent minerals. These minerals hold less than 1 wt% water and are termed *nominally anhydrous* minerals.

As the lithosphere subducts, it experiences progressively greater pressures and temperatures. Many of its constituent minerals undergo phase changes to a denser crystal structure. The hydrated basaltic crust is metamorphosed to a low temperature, high pressure blueschist assemblage, before changing to eclogite at

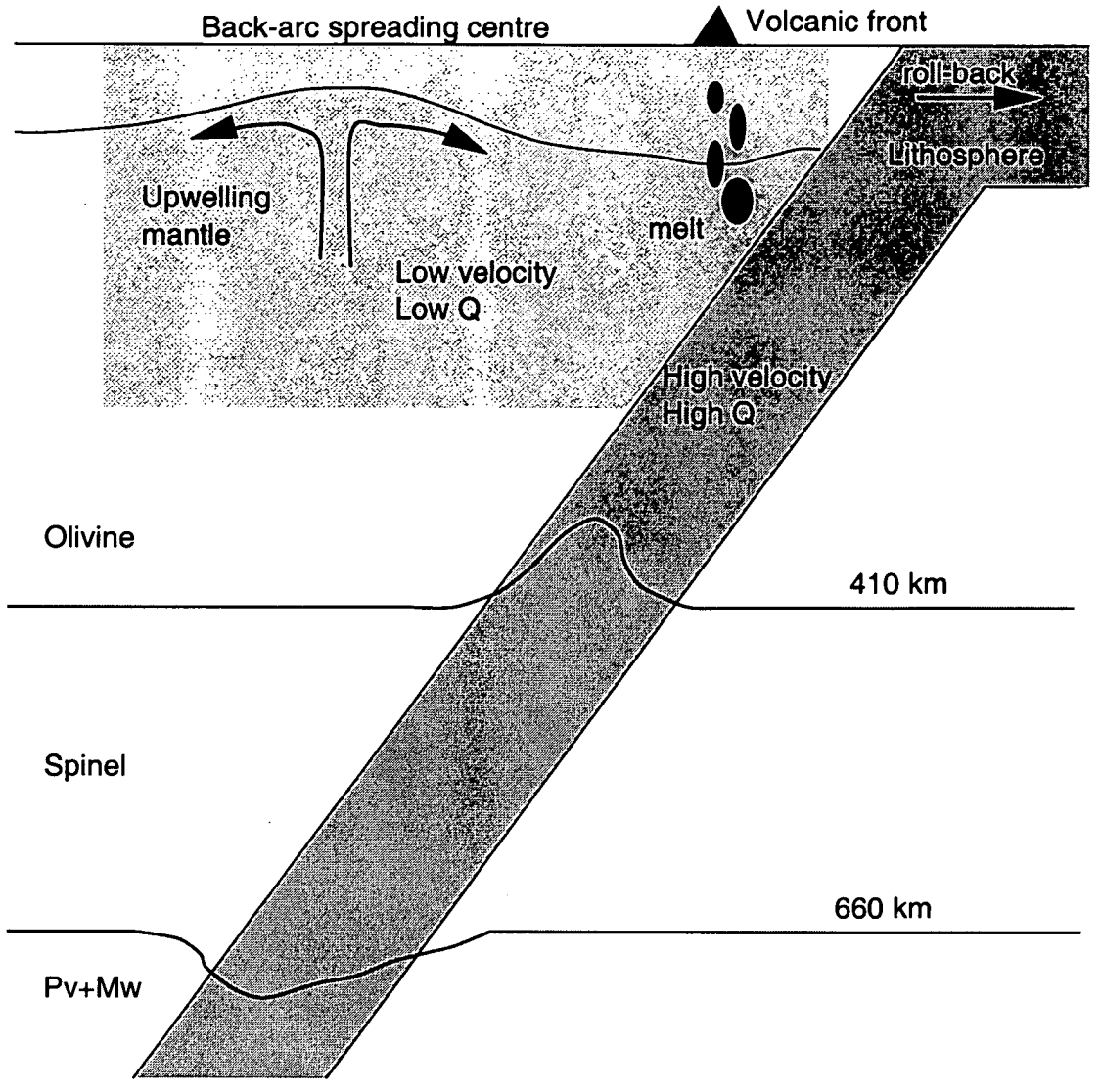

Figure 2.2.

Large scale structure of a typical subduction zone. The darker shaded region of high velocity and high Q is the subducting slab. The lighter shaded region of low velocity and low Q results from the flux of volatile fluids (mainly water and carbon dioxide) from the slab and from the high temperatures due to mantle flow (curved black arrows) induced by roll-back. The addition of fluids to the mantle lowers its melting point, allowing partial melting to occur. Black ellipses represent pockets of melt, which rise buoyantly to the surface and form the magma supply for a chain of volcanoes (black triangle), the oceanward limit of which is referred to as the volcanic front. At greater depth, the line at 410 km represents the equilibrium transformation between olivine, the most abundant shallow mantle mineral, and its denser form, with a spinel type structure. At 660 km, the spinel structure disassociates to form perovskite and magnesiowüstite (Pv+Mw). Both these reactions are displaced by the cold temperatures in the slab.

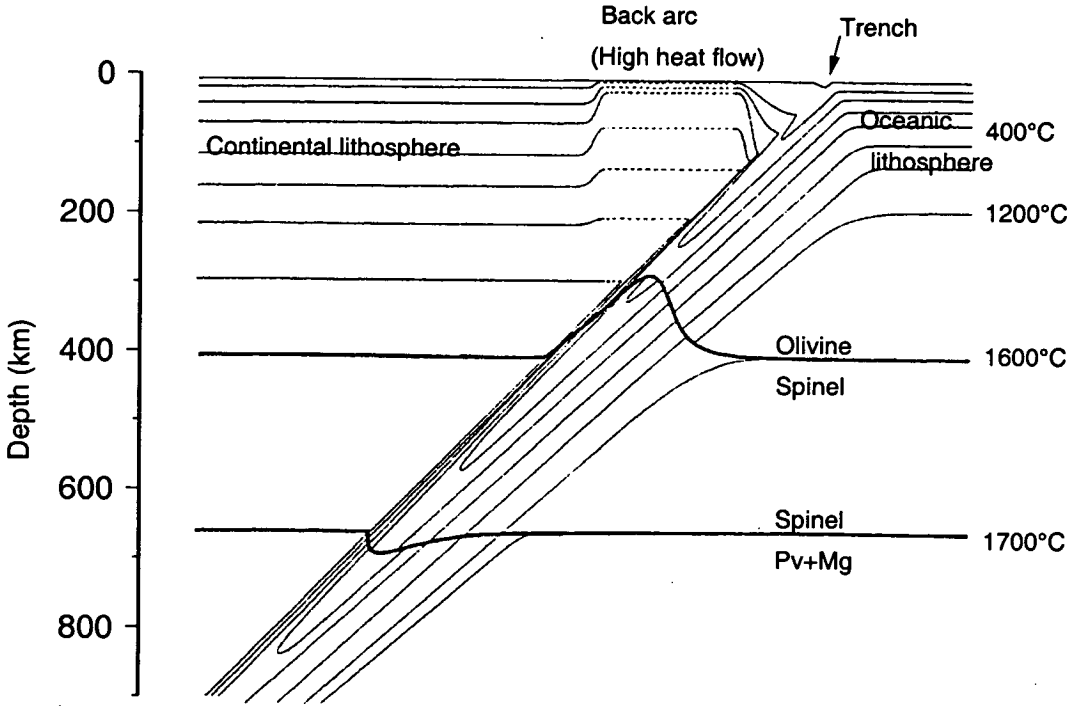

Figure 2.3.

Model of the thermal structure of a subduction zone. The fine lines are isotherms, joining points of equal temperature. The two heavy lines at 410 and 660 km depth indicate the solid–solid phase transformations which affect olivine and its high pressure forms and are thought to correspond to the seismically observed discontinuities at those depths. As can be seen from the pattern of the isotherms in the core of the slab, the olivine–spinel transformation releases heat, i.e. it is exothermic, whilst the spinel–perovskite transformation absorbs heat, it is endothermic. Redrawn from Schubert *et al.* (1975).

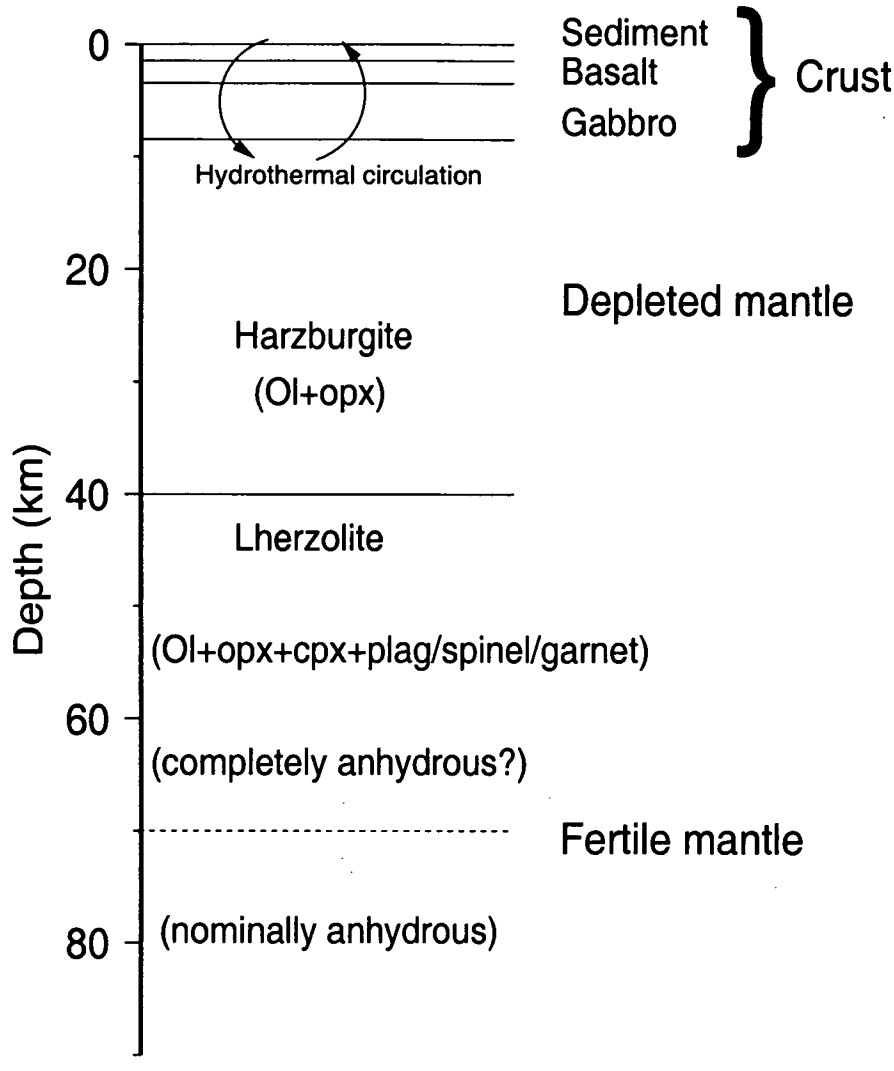

Figure 2.4.

Profile through typical oceanic lithosphere. Layers of intrusive gabbros, basaltic dykes and lavas and, on top, sediments, form the oceanic crust. The uppermost mantle has been depleted by partial melting during crust formation, whilst deeper mantle has been depleted less dramatically or not at all. The depleted harzburgite layer consists of olivine (ol) and orthopyroxene (opx), whilst at greater depth the fertile lherzolite also contains clinopyroxene and an aluminium bearing phase, either plagioclase, spinel or garnet with increasing depth. The water content of the lithosphere is poorly constrained, but the crust is known to be hydrated by hydrothermal circulation occurring near the mid–ocean ridges and hot spots. Beyond the depth of penetration of the hydrothermal circulation, the mantle may be completely dry, the small quantity of water which it would have held having been partitioned into the partial melt beneath the mid–ocean ridge (Hirth & Kohlstedt 1996). At greater depth still, this water may remain and the mantle is termed "nominally anhydrous." The depths of the different layers are poorly known and variable, so this figure is intended only as a schematic guide to the structure of the lithosphere.

temperatures above about 550 °C. The blueschist has a lower seismic velocity than either the lithospheric mantle or the convecting mantle, contrary to the first–order slab velocity structure presented above (Helffrich 1996, Helffrich & Abers 1997). Further deviations from the expected, simple velocity structure may be caused by flow–induced preferred orientation of olivine crystals, which results in an anisotropic velocity structure (Helffrich & Stein 1993), and the continued dehydration of hydrous minerals surviving to great depth in the cold slab, causing anomalously low S–wave velocities reflecting free H_2O above the slab in the mantle transition zone (Nolet & Zielhuis 1994).

Phase changes also occur in the subducting lithospheric mantle. Olivine is the most abundant mineral in the uppermost mantle and its phase diagram is shown in figure 2.5. Under equilibrium mantle conditions, olivine undergoes two solid–solid phase transformations to a denser, spinel type structure. In the Mg_2SiO_4 or Fe_2SiO_4 end member chemical systems, these phase changes are polymorphic, i.e. the crystal structure changes but the composition does not. However, in the solid solution $(Mg,Fe)_2SiO_4$, the reactions produce high–pressure phases with proportions of Mg and Fe which differ from the reactant olivine, so the reactions are not strictly polymorphic [see, for example, the pressure–composition diagrams shown by Jeanloz & Thompson (1983)]. At 410 km depth, the olivine transforms to denser wadsleyite, which further changes to ringwoodite at around 520 km (Ringwood & Major 1966, Akaogi, Ito & Navrotsky 1989). Ringwoodite is approximately 8% denser than olivine, occupies about 8% less volume and has a tetrahedral structure. At 660 km, it transforms to the orthorhombic perovskite structure [$(Mg,Fe)SiO_3$] plus magnesiowüstite [(Mg,Fe)O], again with an increase in density of around 8% and an associated decrease in volume. The olivine–wadsleyite transformation and the ringwoodite–perovskite transformation correlate with the seismically observed discontinuities at 410 and 660 km, respectively, and it is likely that the discontinuities are caused by the abrupt change in density across the zone of transformation. However, the wadsleyite–ringwoodite transformation predicted by the laboratory experiments is not observed seismically (Bock 1994). It may be that the transition zone structure is not as simple as figure 2.5 suggests. In experiments using realistic, multicomponent starting materials, Smyth & Kawamoto (1997) discovered a wadsleyite–type, hydrous phase which was stable at greater pressures than wadsleyite and may coexist with or

even instead of ringwoodite in parts of the transition zone, possibly explaining the lack of a coherent discontinuity at 520 km.

Any phase transformation requires a supply of energy to initiate it. Experiments by Wu *et al.* (1993) delimited the PT boundary that defines this "kinetic limit" for olivine under conditions of hydrostatic (i.e. isotropic) stress, and this is shown on figure 2.5. For large oversteps of the equilibrium olivine–spinel boundary, the limit is determined entirely by temperature, and transformation does not occur below 800 °C. When a shear stress was applied, they found that transformation began at 550 °C at pressures greater than 10 GPa, but did not reach completion until the hydrostatic kinetic boundary was reached. Also shown on figure 2.5 is their calculated minimum slab geotherm, which falls below the hydrostatic boundary throughout the transition zone, predicting the existence of metastable olivine at depths greater than 410 km in the subducting slab, a concept first proposed by Sung & Burns (1976). Such metastable olivine would be less dense than the surrounding mantle and would act to slow slab descent and force the slab into a state of compression, as is indicated by the majority of deep earthquake focal mechanisms in subduction zones, particularly at depths greater than 300 km (Isacks & Molnar 1969, Vassiliou 1984). At intermediate depths, the stress state varies from region to region, but is typically down–dip extensional or mixed (Isacks & Molnar 1969, Zhou 1990). In the metastable olivine model, the natural negative thermal buoyancy of the cold slab is the main force driving subduction. However, the observed stress state in slabs can be explained equally well by the occurrence of the $(Mg,Fe)_2SiO_4$ system phase transformations occurring at equilibrium PT conditions (Bina 1996), as will be described below.

The slope of a reaction in PT space is called its *Clapeyron slope.* As is shown on figure 2.5, the transition from olivine to wadsleyite or ringwoodite has a positive Clapeyron slope. Thus, at colder temperatures, the transformation occurs at lower pressures and hence shallower depth. Conversely, the ringwoodite to perovskite and magnesiowüstite transformation has a negative slope and occurs at greater depths at low temperatures. Hence, in a cold subducting slab, the equilibrium phase boundaries of these transformations develop considerable topography, as shown in figures 2.2 and 2.3. In the case of the olivine–spinel transformation, the effect is for the denser spinel phase to form at shallower depth in the slab

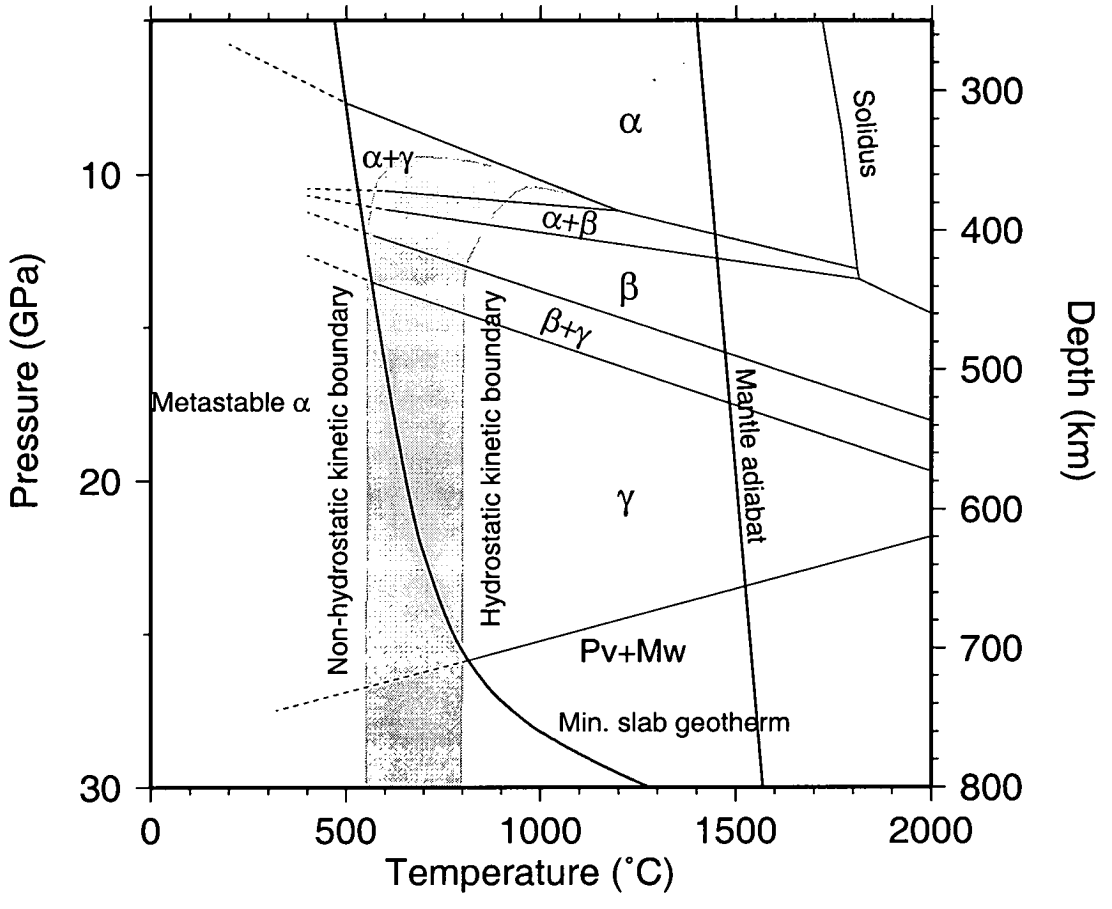

Figure 2.5.

Phase diagram for mantle olivine, $(Mg_{0.89}Fe_{0.11})_2SiO_4$. α olivine; β wadsleyite; γ ringwoodite; **Pv** perovskite; **Mw** magnesiowüstite. The equilibrium phase boundaries calculated by Akaogi *et al.* (1989) are shown. The transformation of olivine to its high pressure polymorphs is inhibited at low temperatures, but the transformation is promoted by the application of shear stress. The experimentally determined kinetic boundaries both with and without shear stress are shown (Wu *et al.* 1993), bounding the shaded region which shows the possible PT range of transformation of metastable olivine. An estimated minimum slab geotherm and the mantle adiabat are also shown. The slab geotherm converges more rapidly towards the mantle adiabat beyond the transition zone because the slab is assumed to descend more slowly through the lower mantle. Reproduced from Wu *et al.* (1993).

than in the surrounding mantle, providing a negative mineralogical buoyancy force in the slab (Isacks & Molnar 1969). The spinel–perovskite transformation has a negative Clapeyron slope and hence acts in the opposite sense, with ringwoodite surviving to greater depth in the slab than in the surrounding mantle and thus providing a positive buoyancy force. Christensen (1997) has shown that, although not dramatic, the magnitude of this buoyancy force is sufficient to influence the stress state in the slab. The net effect of these equilibrium transformations is to encourage a downdip extensional stress regime at depths less than ~350 km, and to force a downdip compressive stress regime at greater depth, consistent with many observed focal mechanisms. Therefore, mineral reactions can lead to accelerating or decelerating stress gradients, but may or may not be responsible for the microscopic instability mechanism required to produce deep earthquakes. Clearly, it is impossible to distinguish between the cases of equilibrium and metastable transformations of olivine using evidence of the stress state inferred from earthquake orientations alone. Whilst it is theoretically possible to distinguish between the two cases based on seismic travel times (Vacher, Spakman & Wortel 1999), results so far have proved ambiguous (Iidaka & Suetsugu 1992, Koper *et al.* 1998). Observations of an uplifted 410 km discontinuity all the way across the Izu–Bonin slab (Collier & Helffrich 1997) suggest that at least a partial transformation of olivine occurs near the equilibrium depth in this slab.

2.3 Earthquake Source Types and the Moment Tensor

Any rapid disturbance in the earth will excite elastic waves, which will propagate to the surface where, in places, they are recorded by seismographs. To invert these waveforms for information about the form of the disturbance which caused them, it is necessary to make some simplifying assumptions, since any given set of waveforms could be described by an infinite variety of complex sources. A reasonable assumption is to constrain the source to be an infinitesimal point disturbance which can be described by a sum of three orthogonal force dipoles and the six associated rotational force couples. These are illustrated in figure 2.6.

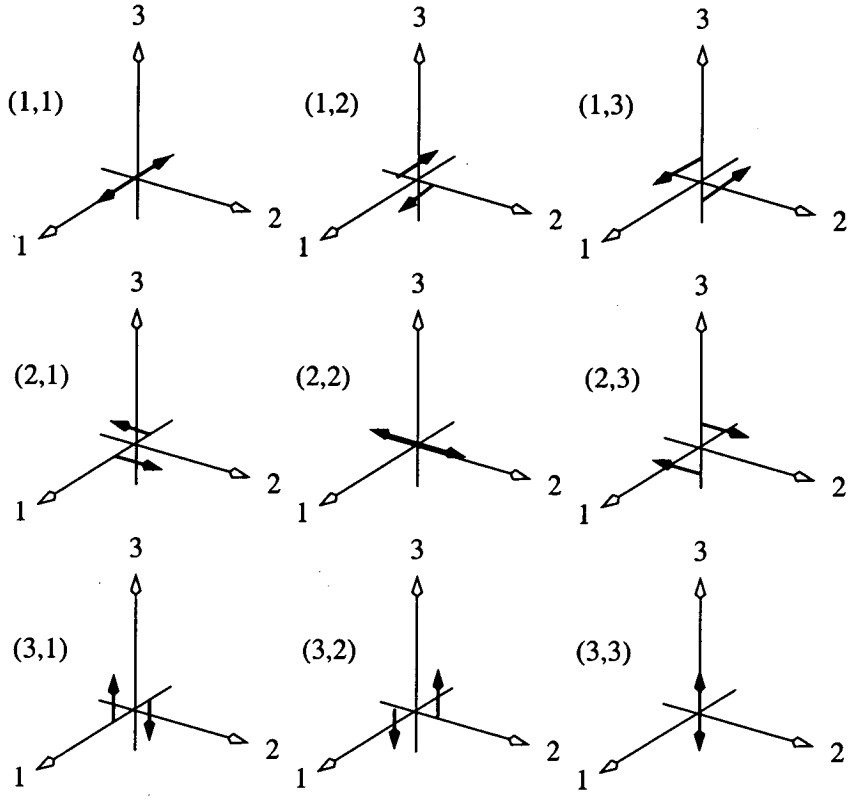

Figure 2.6.

The nine force couples which describe a general point source. The heavy black arrows indicate the equal and opposite forces. Couples (1,1), (2,2) and (3,3) are force dipoles, which produce volume change (positive = explosive, negative = implosive), whilst the remaining couples combine to produce constant volume shear deformation. After Aki & Richards (1980).

Inversion for an earthquake source must determine the sign and magnitude of each force couple. This is normally achieved by calculating synthetic waveforms for different sources and finding which source or sources match the observed waveforms. The resulting description of each source is known as the *seismic moment tensor* of an earthquake (Backus & Mulcahy 1976), and has the form of a symmetric 3×3 matrix, each element representing the corresponding force couple illustrated in figure 2.6. It describes the kinematics and the orientation of the source. Since a point source is assumed, then the wavelengths used for the inversion must be much longer than the real source.

The moment tensor can be manipulated to describe separately the un-oriented kinematics of the source, the *source type*, and its *orientation* (Hudson, Pearce & Rogers 1989). The source type is described by two variables, the amount of volume change, or volumetric component, and the type of constant volume deformation. The volumetric component describes the proportion of volume change in the source, with $+1$ corresponding to an explosion and -1 to an implosion. The constant volume component describes the type of shearing which occurs. Simple shear involves only lateral sliding across a fault, whilst pure shear describes the deformation which results from a body being compressed or extended whilst retaining its original volume. Figure 2.7 illustrates the range of constant volume deformation and how changes in the mode of deformation are reflected in an earthquake focal mechanism.

Hudson *et al.* (1989) introduced the source type plot on which to represent the different types of seismic point source. This is illustrated in figure 2.8. The volumetric component, k, is plotted on the vertical axis and the type of constant volume deformation, T, is represented on the horizontal axis. The shape of the plot is such that the area of a given region of (T,k) space is proportional to the probability that a randomly chosen, normalised sum of the nine force couples would plot in that area. For example, a purely explosive source can only be produced by one arrangement of dipoles, so the plot goes to a point at $k = 1$, $T = 0$. The point at the centre of the plot represents a *double couple* source. This is the classic earthquake source mechanism, with no volume change, solely simple shear and a single, planar rupture surface. Such a mechanism is thought to occur for all shallow, tectonic (as opposed to magmatic, geothermal or mining induced)

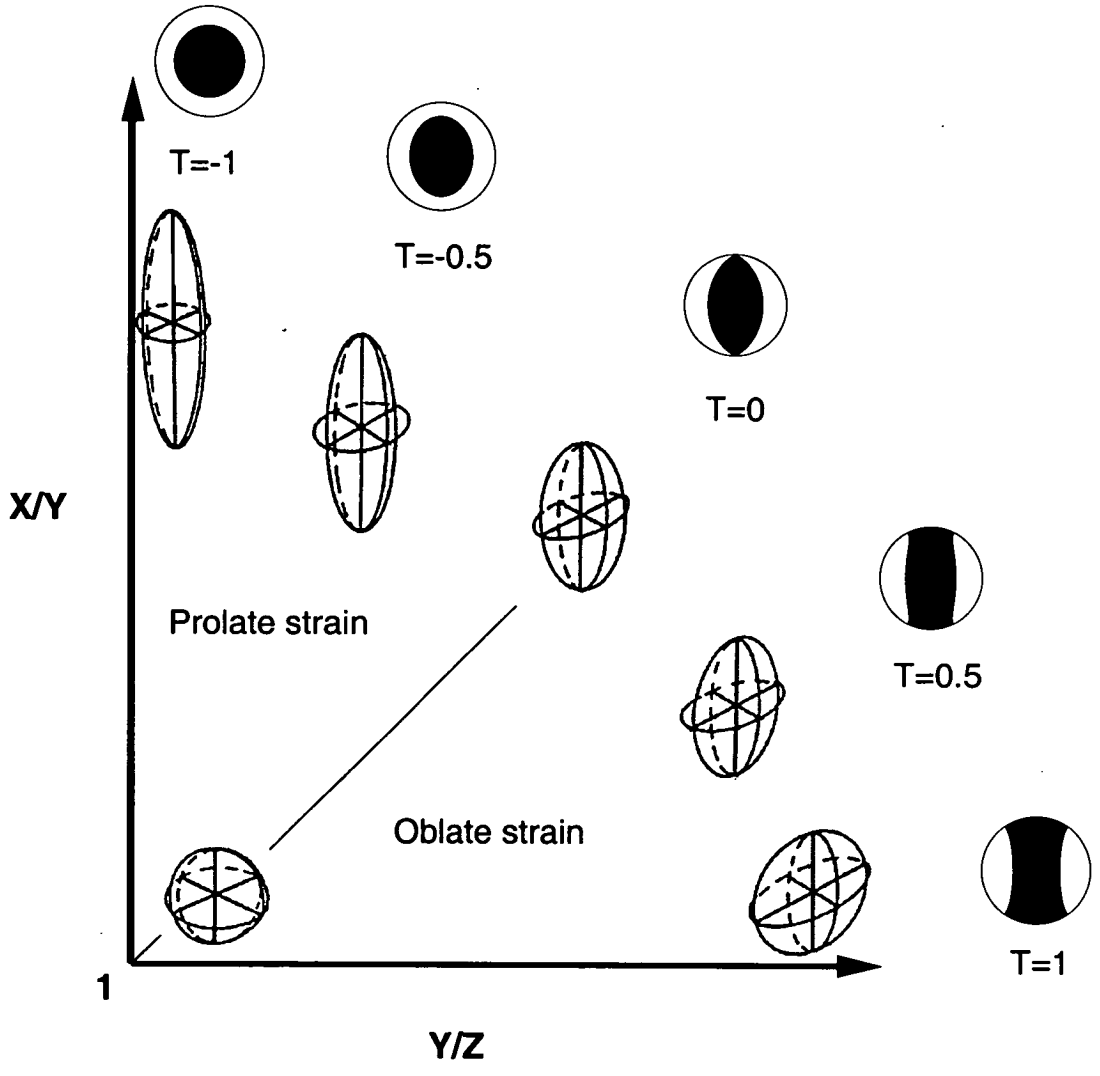

Figure 2.7.

Constant volume strain. Differing types of strain are illustrated by their effect on a sphere, with perpendicular axes X, Y and Z (X vertical). Large values of X/Y and small values of Y/Z define the field of prolate strain, whilst small X/Y and large Y/Z define the field of oblate strain. Plane strain lies on the 45° line which bisects the plot. Following Hudson *et al.* (1989), the type of strain is represented by the parameter T. Plane strain is caused by simple shear and corresponds to T=0, or the double couple earthquake mechanism. The mechanisms corresponding to T=−1 and T=+1 are called positive and negative compensated linear vector dipoles, respectively, and correspond to pure shear. A continuum of source types exists between these end members. Lower focal hemisphere projections show the polarity distribution of radiation emitted by the different constant volume sources with orientation equivalent to that of a 45° dip–slip reverse fault. The strain plot is after Flinn (1962), the focal mechanisms are after Pearce & Rogers (1989).

earthquakes, but this has not yet been demonstrated explicitly [e.g. Dziewonski & Woodhouse (1983), Pearce & Rogers (1989)].

The orientation of a seismic source is best described by considering a double couple mechanism. The double couple source is defined by three parameters, the strike (σ) and dip (δ) of the fault plane, and the direction of slip (ψ), as illustrated in figure 2.9. The orientation of other source types can be described equally well by these parameters, although they do not have the same physical meaning. As the volumetric component k approaches 1, then the orientation of the source becomes irrelevant, since purely volumetric sources are isotropic, i.e. the emitted radiation is identical in all directions.

2.4 Characteristics of Deep Earthquakes

The striking thing about deep earthquakes is how similar they appear to be to their shallow counterparts. Profiles through subduction zones often reveal a continuous zone of seismicity, extending without any apparent discontinuity or change in geometrical characteristics except for dip, from very shallow depths down into the transition zone at the base of the upper mantle. No systematic differences in rupture velocity or stress drop have been observed between shallow and deep earthquakes (Houston & Williams 1991), and they all appear to have shear dominated focal mechanisms (Stimpson & Pearce 1987, Stimpson 1987*a*). Certainly, any volumetric component is small, but some studies have found large, apparently well resolved components of pure shear in deep earthquake focal mechanisms (Giardini 1984, Kuge & Kawakatsu 1993). This issue is examined further in sections 2.8 and 6.5. Apart from the possible non–double couple components and the extraordinary depths at which deep earthquakes occur, only the depth distribution of seismicity and the low number of aftershocks for deep events suggest that the populations of shallow and deep earthquakes are fundamentally different.

Figure 2.10 shows the percentage of earthquakes occurring in depth bins of 10 km, from the surface down to 700 km depth. The vast majority of earthquakes occur at depths less than 70 km, with a smooth and rapid fall–off in activity to a local

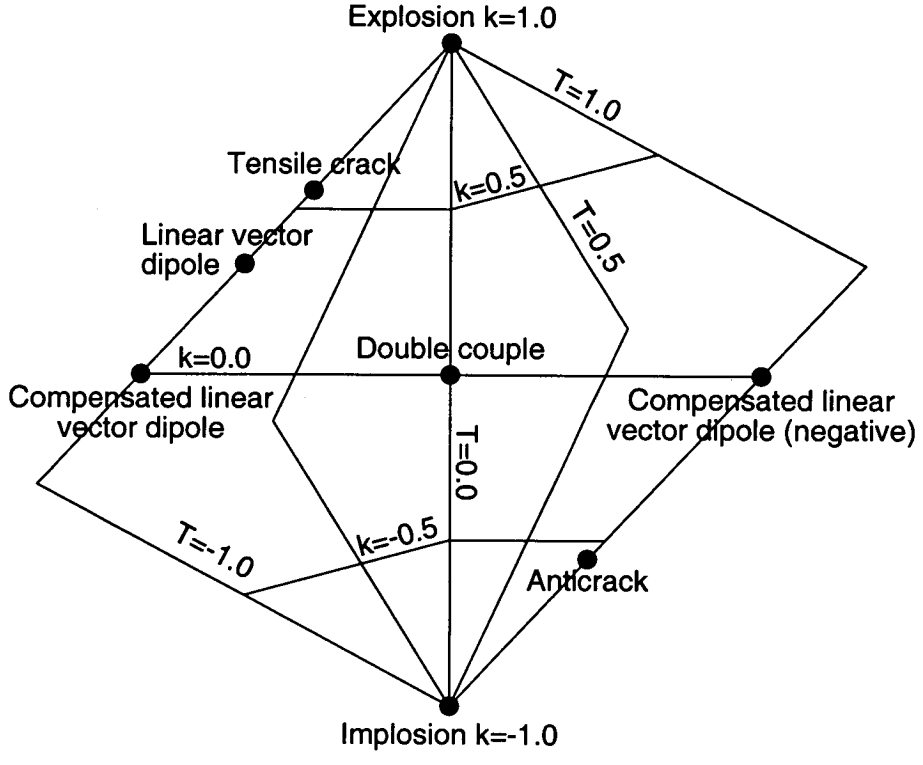

Figure 2.8.

Source type plot. The full range of source types that can be produced by the force couples of figure 2.6 plot on this diagram. The vertical axis shows the magnitude and sign of the volumetric component (k), whilst the horizontal axis shows the type of constant volume deformation (T). Simple shear (or plane strain) corresponds to $T = 0.0$, whilst pure shear corresponds to $T = +1.0$ (oblate strain) and $T = -1.0$ (prolate strain). Important source types are labelled and plotted as filled circles and T and k are contoured at intervals of 0.5. The anticrack source will be explained in section 2.6. After Hudson *et al.* (1989).

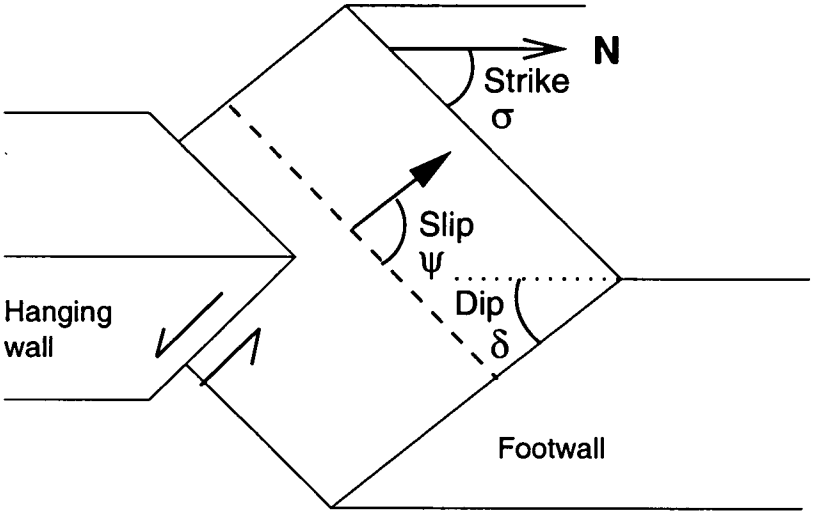

Figure 2.9.
Orientation parameters for a seismic source. The orientation of a double–couple source is described by the strike (σ) and dip (δ) of the fault plane on which the rupture occurred and the direction of slip (ψ). Strike is measured from north (N) and dip from the horizontal. The slip describes the direction of motion of the footwall relative to the hanging wall. This method of notation is consistent with that of the UK Atomic Weapons Establishment, but differs somewhat from the method of Aki & Richards (1980), who measure the slip on the hanging wall relative to the footwall.

minimum at around 300 km depth. A small, local maximum of activity occurs between 500 and 600 km depth, beyond which the seismicity decays to zero. The existence of increased seismic activity in the transition zone has been interpreted in many different ways. The simplest explanation that has been suggested is that a significant barrier to mass transfer exists at the interface between the transition zone and the lower mantle (McKenzie 1966). However, this is incompatible with the numerous observations of anomalously fast and, therefore, presumably cold material in the lower mantle [e.g. Creager & Jordan (1986), Suetsugu (1989), Grand (1994), van der Hilst, Widiyantoro & Engdahl (1997)]. Another possibility is that the peak in activity at 500–600 km reflects a different mechanism of deep seismogenesis. Alternatively, it may reflect variations in stress or strain rate within the slab. All these hypotheses are considered below.

O'Connell (1977) and Richter (1979) pointed out that a small increase in viscosity across the 660 km discontinuity would be sufficient to cause compression in the slab and increase the rate of seismicity, whilst still allowing material to sink into the lower mantle. The cessation of seismicity may represent the disappearance, due to heating, of slab material with sufficient strength to support the stresses required for an earthquake. Wortel (1986) and Wortel & Vlaar (1988) considered the buoyancy and resistive forces acting on a vertical slab and showed that the downdip force became compressive and increased with depth, whilst the strength of the slab decreased with depth. Where the slab strength was greater than the applied force, they deemed the slab to support stress elastically whilst, where the force was greater than the strength, the slab was considered anelastic. They proposed that seismicity occurred at the boundary of the anelastic and elastic regions, where the force equaled the slab strength. The rate of migration of this boundary should be proportional to the level of seismic activity, and it reaches a maximum just before the slab is brought to complete anelastic failure, just as the observed rate of seismicity increases before it falls to zero. This model takes no account of the feedback between stress state and failure and is unusual in that it assumes a constant strain rate whilst the loading force varies.

An alternative explanation for the mechanics governing the termination of seismicity was proposed by Willemann (1991). His model assumed a constant total load on the slab but allowed the stress and strain rates to vary. Earthquakes

were assumed to occur only above a certain strength (or differential stress), and once that strength was exceeded, then the rate of seismicity was proportional to the rate of strain. In his model, heating of the slab caused it to weaken, resulting in high strain rates and high seismicity just before the slab became too weak to support such catastrophic failure. Tao & O'Connell (1993) provide support for the idea that seismicity is proportional to strain rate. They used numerical models to investigate slab evolution and deformation, assuming a slab to behave as a weak, viscous fluid, rather than a strong, rigid solid. With an assumed moderate viscosity increase at 670 km, they found that the rate of deformation of their model slab varied with depth in much the same way as seismicity rates are observed to vary with depth. Models assuming the slab to be a viscous fluid also produce realistic slab profiles, similar to the shapes of observed Wadati–Benioff zones and tomographically imaged velocity structures (Kincaid & Olson 1987, Gurnis & Hager 1988, Tao & O'Connell 1992).

The final possible explanation for the depth distribution of earthquakes is that the shallow and intermediate events all occur by normal frictional sliding, whilst the deep earthquakes occur by a different mechanism. Some mechanism is required to reduce the normal stress on intermediate depth faults to allow sliding. Pressurised pore fluid resulting from dehydration has been widely suggested as one such potential mechanism, e.g. Green & Houston (1995), and this hypothesis is examined further in section 2.5. The theory proposes that the effectiveness of this mechanism decreases until it terminates or becomes negligible at around 300 km depth. At this point, the separate, deep mechanism begins to cause seismicity and its effectiveness increases with depth, until it is terminated by some characteristic of the base of the transition zone. The popular hypothesis of transformational faulting follows this logic, and it will be explained in detail in section 2.6.

The depth distribution of earthquakes provides only ambiguous evidence for a difference between shallow and deep earthquakes. However, the number of aftershocks triggered by an event does differ markedly between the two. Wiens *et al.* (1997) showed that the number of aftershocks for deep Tongan events is an order of magnitude less than for shallow events of comparable magnitude in California. Wiens & Gilbert (1996) demonstrated that the statistical behaviour

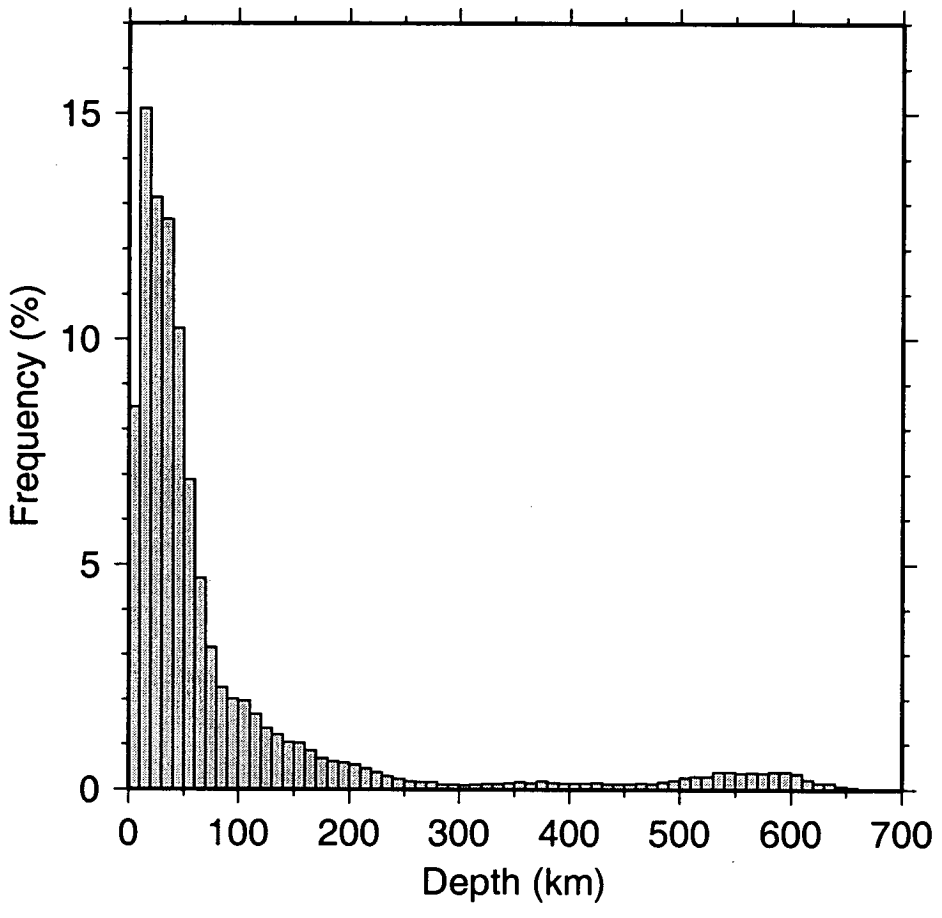

Figure 2.10.
Depth distribution of seismicity. Occurrence of earthquakes in 10 km depth bins, as a percentage of the total sample population. The dataset used was the entire catalogue of Engdahl *et al.* (1998), who determine earthquake depths from the arrival times of the surface reflection phases pP and sP.

of deep earthquakes is temperature dependent by showing that cold subduction zones have more smaller earthquakes relative to large ones, whilst the seismicity of warmer slabs is dominated by small numbers of large events. The three most plausible and most widely discussed groups of mechanisms by which deep earthquakes could occur are examined in the following sections.

2.5 Dehydration Induced Embrittlement

At shallow depths, fluids are thought to play a critical rôle in the occurrence of many earthquakes [e.g. Scholz (1990), Main *et al.* (1994), Miller (1996)], and it has been suggested that they may promote catastrophic failure at great depth (Raleigh 1967, Kirby 1995). In a saturated porous medium, a build up of pore fluid pressure counterbalances the normal stress (Terzaghi 1923, Terzaghi 1932) and so allows frictional sliding at lower shear stresses than would be necessary in a dry environment. In such a situation, the fluids are often described as being "overpressured" if they are pressurised beyond hydrostatic pressure. The notion that significant pore fluid pressure may permit unstable sliding has been used to explain the occurrence of intermediate depth earthquakes, most notably and recently by Kirby (1995) and Kirby *et al.* (1996), who cite dehydration reactions in the descending slab as a source of fluid. However, the extrapolation of the theory from shallow depths, where rock is porous, to greater depths, where the porosity approaches zero, may not be justified. In the case of a porous rock in a vacuum, the weight of its overburden is supported solely by the rock matrix, rather than by the pores. Removing the vacuum by filling the pores with fluid (i.e. saturating the rock) generates a pore fluid pressure which is exerted on the surrounding rock. This pressure counteracts the confining pressure and partially supports the overburden, reducing the effective pressure on the adjacent rock matrix and consequently promoting shear failure.

At greater depths, porosity is destroyed through compaction due to the increasing pressure. In this case also, the entire weight of the overburden is supported by the rock matrix. Fluids may be introduced to this system, but only via a dehydration reaction involving the transformation of a solid phase to a solid plus a fluid. If this reaction incorporates no change in volume, then the resulting fluid

will occupy space formerly occupied by a load–supporting solid. Provided the fluid is incompressible, then it must be at the same pressure as the surrounding solids, i.e. at lithostatic pressure. The effective pressure on the local rock mass has not been altered, since a solid at lithostatic pressure is replaced by an equal volume of fluid, also at lithostatic pressure. Thus, it can be seen that Terzaghi's principle of effective pressure being equal to the confining pressure minus the pore fluid pressure is valid only for *a priori* porous media. In the case of an initially non–porous medium described above, the theory predicts the effective pressure to be zero, when it is actually lithostatic for an incompressible fluid introduced by a reaction incorporating no volume change. Thus, a reduction in effective pressure in the rock adjacent to the pore due to "overpressured" fluids in a nominally non–porous medium requires the fluid to be pressurised *beyond* lithostatic pressure. However, this is unlikely ever to occur since, in the presence of even a small shear stress, the loss of traction across the fluid–rock interface concentrates shear stress at the tips of the inclusion and a fracture will propagate, forming a thin elliptical film of fluid and equalising the pressure. In such circumstances, the layer of fluid may be only of a few molecules thickness and its physical and chemical behaviour under such conditions is poorly known. Fluid inclusions could only exist at pressures greater than lithostatic in an isotropic stress field, where the pore–pressure is limited by the tensile strength of the rock.

Figure 2.11 shows the PT stability field of serpentine, as determined by Ulmer & Trommsdorff (1995). The general shape of the locus of dehydration is generic to all dehydration reactions which occur in the subducting slab, with a positive Clapeyron slope at low pressures and a negative slope at high pressures (Tatsumi & Eggins 1995). Through the release of fluid, these reactions increase the local entropy of the products compared to the reactant, so that the total volume change associated with the reaction may be determined from the Clapeyron equation,

$$\frac{dP}{dT} \approx \frac{\Delta S}{\Delta V}, \tag{2.1}$$

where P and T are pressure and temperature, ΔS is the change in molar entropy (positive) and ΔV is the total change in volume of both solids and any resulting

fluids. Thus, at low pressures where the Clapeyron slope is positive, the volume change upon dehydration is positive but, at higher pressures where the Clapeyron slope is negative, the volume change is negative.

Serpentine is formed when the mantle is hydrated by fluid circulation, typically by convective hydrothermal flow near the mid–ocean ridges, and so is expected to be present in the lithosphere just below the crust, in a depth range of approximately 7–20 km (Thompson 1992). Using any published estimate of slab geotherms and lateral thermal structure of the slab to estimate the temperature below the subducting crust [e.g. Creager & Boyd (1991)], it is clear that even the warmest geotherms are sufficiently cold for the dehydration of serpentine to have a negative volume change. Thus, there would be no immediate reduction in the effective pressure. Davies (1999, and references therein) observes that, over time, the pressure of the fluid would approach and maybe even exceed lithostatic, due to ductile flow of the rock surrounding the lens of fluid and because fluids expand more than solid rock for a given temperature increase. Once the fluid pressure is greater than lithostatic, then the effective stress on the surrounding rock is reduced and this may encourage either frictional sliding or tensile hydrofracturing. Alternatively, if widespread linkage of the fluid lenses occurs through self organisation by interaction of small stress perturbations at their edges, then frictional sliding may be promoted if the coefficient of friction at the rock–fluid interface is substantially lower than at the rock–rock interface. A mechanism by which dense inclusions may link up is described in section 2.6. Meade & Jeanloz (1991) showed that acoustic emissions may result from the amorphisation of serpentine as it dehydrates, but precisely how this mechanism would produce the shear failure characteristically observed during an earthquake is unclear. However, Irifune *et al.* (1996) demonstrated that amorphisation of serpentine occurs only at temperatures much lower than those found even in the cores of cold subducting slabs and so rejected this hypothesis as a cause of deep seismicity.

The upper part of the slab heats faster than the interior, by conduction of heat downwards from the overlying mantle and by frictional heating at the slab–mantle interface. Thus, the uppermost subducting crust is much hotter than the subducting mantle at a given depth, so dehydration reactions in the crust may have a positive volume change and could instantaneously promote earthquakes through

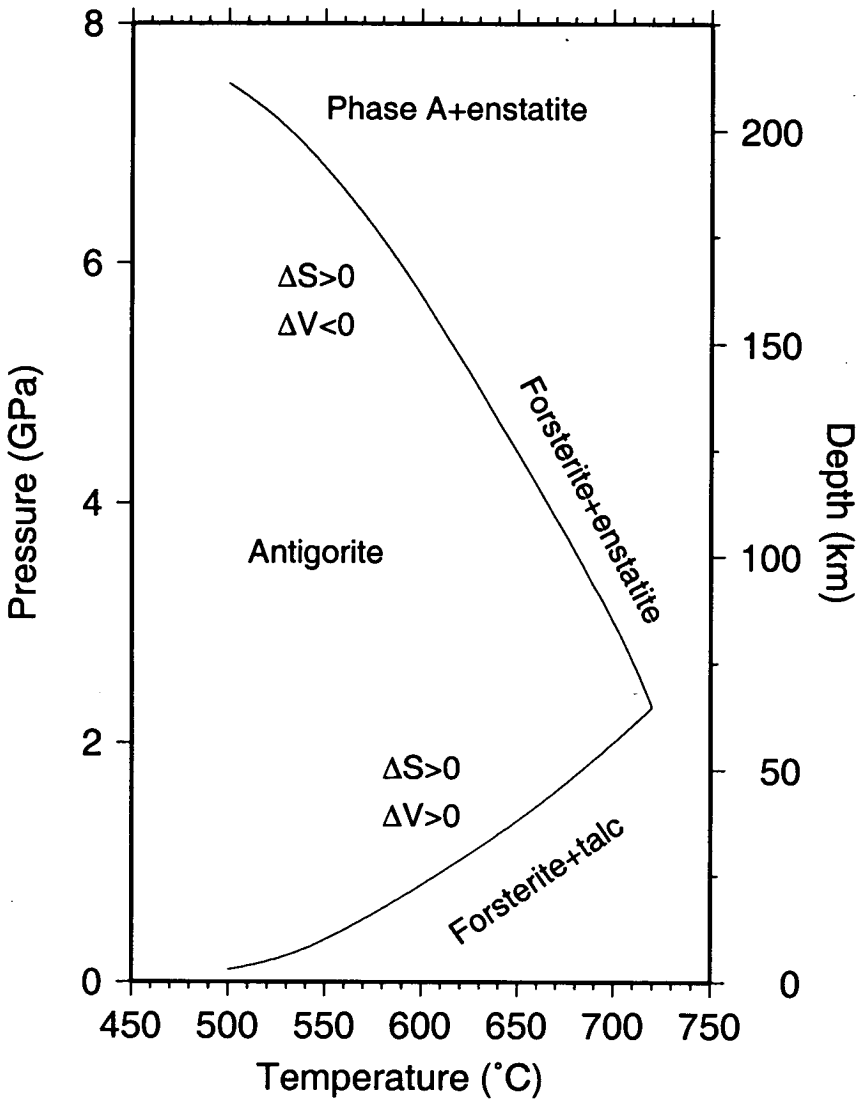

Figure 2.11.

Phase relations for serpentine. PT stability field for natural antigorite [a variety of serpentine, typical composition $Mg_{2.82}Si_2O_5(OH)_{3.64}$]. With increasing temperature, the serpentine dehydrates to form forsterite, the magnesium end member of olivine, and another solid phase plus water. However, at very high pressures, less water is released and a dense hydrous magnesium silicate called phase A is formed. The sign of the change in molar entropy between the products and reactants is shown by ΔS and the change in total volume associated with the reaction is shown by ΔV. Phase data from Ulmer & Trommsdorff (1995), figure plan after Tatsumi & Eggins (1995, p101).

a reduction in effective stress. Kirby, Engdahl & Denlinger (1996) fitted an exponential decay curve to the fall off in seismic activity between 50 and 90 km depth. Extrapolating the curve to greater depths, they found that the observed number of earthquakes was higher than that predicted by the extrapolation, and, following Kirby (1995), they attributed this to the occurrence of large scale dehydration causing high pore fluid pressures in the subducting crust. However, as was described in section 2.4, this depth distribution of seismicity can also be explained by the predicted strain rates in the slab, without requiring different embrittlement reactions to alter the percentage of deformation which occurs seismically, as is implied by Kirby, Engdahl & Denlinger (1996). In chapter 4, the predicted loci of dehydration reactions are compared to the observed distribution of seismicity, to determine whether or not deep earthquakes are directly associated with dehydration reactions.

2.6 Transformational Faulting

The mechanism of transformational faulting has been proposed to cause deep earthquakes at depths greater than around 350 km. The current hypothesis, described here, was first presented by Green & Burnley (1989), but the basic ideas of earthquakes being related to metastable phase transformations are much older (Dennis & Walker 1965, Vaisnys & Pilbeam 1976, McGarr 1977).

As described in section 2.2, phase data from experiments performed at the PT conditions relevant to subduction zones indicate that the estimated temperature in the core of cold slabs may be sufficiently low to inhibit the transformation from olivine to its high pressure forms at the equilibrium depths of these transformations. The phase change from the olivine to the spinel type structure also occurs in magnesium germanate, Ge_2SiO_4, but at much lower pressures than in silicate olivine, although the intervening modified spinel structure of wadsleyite does not occur. Using this germanate analogue for olivine, Green & Burnley (1989) and Burnley, Green & Prior (1991) observed unstable failure in laboratory experiments when the germanate was placed in metastable conditions. By first pressurising the sample to beyond the pressure of the equilibrium transformation, and then heating it, they simulated the temporal sequence of events which

might occur in a cold slab. Microscopic examination of the samples revealed fault zones filled with a very fine grained spinel phase, individual grains often being considerably smaller than 1 μm across (Burnley *et al.* 1991). Samples would fail only if a shear stress was applied, under which conditions the spinel nucleated preferentially along grain and sub–grain boundaries, forming ellipsoidal lenses. The fault zones appeared to be formed by the linking of these lenses of spinel.

That such transformation–induced faulting could occur in natural, silicate olivine was shown shortly afterwards (Green *et al.* 1990, Wu *et al.* 1993), at PT conditions up to but not beyond the equilibrium boundary for the ringwoodite to perovskite + magnesiowüstite transformation. The theory to explain this apparently brittle phenomenon at extremely high pressures depends upon the ideas of superplasticity and self–organising systems. When metastable olivine is subjected to shear stress, grains of the denser wadsleyite or ringwoodite will nucleate along the olivine grain boundaries, releasing heat due to the exothermic nature of the reaction. This extra heating promotes further nucleation of these "spinel" phases in the adjacent olivine (figure 2.5). The transformation incorporates a volume reduction, and the effect of a denser inclusion in a non–isotropic stress field, such as that of a slab in down–dip compression, is to concentrate stress at the edges of the inclusion which are normal to the principal compressive stress. This increase in stress forces the adjacent olivine further into the field of metastability, increasing the driving force for the transformation and resulting in preferential nucleation of the denser phase. Thus, a lens of the denser phase develops, its ellipsoidal shape maintained by the local concentration of stress at its tips, and further transformation encouraged by the local increases in pressure and temperature.

Such ellipsoidal lenses of a denser phase were termed "anticracks" by McGarr (1977), because they behave in an identical way to tensile cracks, except with the polarity of forces reversed. Thus, just as the stress fields formed at the tips of tensile cracks come to interact and link, resulting in a through going shear fracture (Segall & Pollard 1983), it is believed that such stress interaction also occurs between anticracks, eventually allowing many anticracks to link and form a thin, extensive planar surface of spinel. The dominant mechanism by which olivine transforms to spinel at the relatively cold, high pressure conditions

found in a subducting slab is nucleation, rather than growth of a pre–existing spinel grain. Thus, the grain size of the spinel is extremely small, many orders of magnitude smaller than the surrounding olivine. These tiny grains promote deformation by superplastic creep, a composite of diffusion related mechanisms, which allows the rapid redistribution of material around the grain boundaries. This results in grains which maintain approximately their initial shape and do not accumulate any permanent strain, whilst accommodating large strains at a scales many orders of magnitude greater than the grain scale. Very high strain rates are thought to be possible so, to apply the terminology usually reserved for frictional sliding, the "apparent", or "effective" coefficient of friction is reduced, thus enabling unstable slip.

This hypothesis does explain some of the observed characteristics of deep earthquakes. Once slip has occurred on a spinel fault, no aftershocks should occur on it since the fault would continue to have a low coefficient of friction and should encourage stable deformation. This is consistent with the observation that the majority of deep earthquake aftershocks occur in a volume surrounding the original hypocentre, and do not define a planar surface aligned with one of the nodal planes of the earthquake focal mechanism (Willemann & Frohlich 1987). However, not all deep earthquakes exhibit such behaviour, and Wiens *et al.* (1994) demonstrated that the most vigorous sequence of deep aftershocks recorded, for an event in Tonga, did lie in a common plane with one of the nodal planes of the mainshock. Over time, the spinel in a "transformational fault" should coarsen through crystal growth and become stronger than the surrounding olivine (Green & Burnley 1989), possibly concentrating stress in that region and encouraging failure nearby. Such a scenario is consistent with the observations of planar zones of earthquakes, well separated in time, that *do* lie on a plane common with other hypocentres and are aligned with a nodal plane of a nearby large earthquake (Giardini & Woodhouse 1984, Lundgren & Giardini 1992).

Work by Green & Zhou (1996) showed that transformational faulting could only occur for exothermic reactions, the transformation being inhibited by an endothermic reaction which would result in local cooling. They concluded that this explained the cessation of seismicity at the base of the transition zone, since the disassociation of ringwoodite to form perovskite and magnesiowüstite is an

endothermic reaction. However, olivine surviving metastably into the the lower mantle transforms first to a spinel phase, and not to Pv+Mw (Wang *et al.* 1997), but by a differing microstructural mechanism. Burnley (1995) showed that this mechanism, based on dislocation of the crystal structure rather than complete reconstruction, was pressure dependent and became dominant towards the base of the transition zone. Thus, she proposed that any olivine surviving to this depth would be transformed by the dislocation mechanism before entering the lower mantle.

To summarise, the metastable transformation of olivine to its spinel phase may result in the self–organised linkage of extremely fine–grained lenses of the spinel phase. Laboratory experiments have demonstrated that the fine grain size dramatically reduces the apparent coefficient of friction and so allows frictional sliding. Thus, the transformation of olivine to spinel can provide both a global external force on the slab, due to the vertical deflection of the phase boundaries, and a local mechanism of instability via self–organised superplasticity.

2.7 Adiabatic Instabilities

Deep earthquakes may be unrelated to mineral reactions, instead being a natural result of the manner in which rock deforms at high pressures and relatively low temperatures. At low pressures and temperatures, two surfaces moving against each other generate heat because the surfaces are not perfectly smooth, the well known effect of frictional heating. During ductile deformation, at higher PT conditions, there are no surfaces along which shear occurs, but the movement of dislocations within the material causes heating, an effect called *viscous dissipation.* Griggs & Baker (1968) proposed that deep earthquakes were caused by this process. A region with a slightly higher temperature than its surroundings would, they proposed, also be slightly weaker and hence deformation would occur preferentially in this region. An increased strain rate causes further heating due to viscous dissipation, whilst the surrounding area remains colder and experiences less strain, given a constant overall strain rate. Thus, a positive feedback is established, eventually leading to melting and a complete loss of strength in a narrow zone, at which point the release of stress is so rapid that an earthquake

occurs. This idea depends upon the rate of heat generation being considerably higher than the rate of thermal diffusion. The extreme case is where none of the generated heat is transferred to the surroundings, the *adiabatic case.* Heating of shear zones is a reasonable approximation to this case because of the very low thermal conductivity of rock, hence, although not strictly correct, the resulting instabilities are referred to as "adiabatic".

The ideas of Griggs & Baker (1968) were somewhat qualitative. A quantitative study by Ogawa (1987) assumed a power law rheology, where strain rate is proportional to around the third power of stress, a homogeneous lithology, typical slab temperatures (McKenzie 1970, Toksöz, Sleep & Smith 1973), and a constant spatially averaged strain rate. Shear concentrated on a small initial perturbation introduced to the model temperature field. Ogawa's results showed that the increase in temperature in the shear zone was slight for a long period, and then suddenly became extremely rapid, consistent with the occurrence of an earthquake. Instability developed only above a critical average strain rate. For a homogeneous starting material, the critical strain rate for a dry mantle was just within the estimated upper bound that may occur in a subducting slab. However, for a starting material that already contained low viscosity shear zones, with characteristics consistent with those observed by field geologists, the critical strain rate was around an order of magnitude lower, and less than that calculated for the Tonga slab by Giardini & Woodhouse (1986), showing that shear instability could be the cause of deep seismicity. For a wet mantle, shear instability was induced at even lower strain rates.

Ogawa (1987) did not consider that the rheological behaviour of the shear zone may alter as a function of the strain rate. An isothermal increase in strain rate will lead to a *strengthening* of the strained material, due to the generation and rearrangement of dislocations on the scale of the crystal lattice, an effect known as strain hardening. The complementary process, strain softening, is that considered by Ogawa (1987) where by viscous dissipation leads to a reduction in viscosity and strength. The balance of these two effects was investigated theoretically by Hobbs & Ord (1988). They found that instability occurred below a critical temperature, as long as the stress release was greater than the elastic stiffness of the surrounding system. Above this temperature, strain hardening became the

dominant process. Assuming the core of the slab to be strong and elastic, with a high stiffness due to its low temperature, they used the thermal models of Toksöz *et al.* (1973) to predict the locations in the slab at which plastic instabilities could occur. The zone of instability essentially bounded the strong core of the slab and, as in Wortel's analysis (section 2.4), predicted double zones of seismicity at intermediate depths and even in the transition zone for the coldest slabs. Such patterns of seismicity have been observed beneath Japan (Hasegawa, Umino & Takagi 1978), the Aleutians (Abers 1994) and at great depth beneath Tonga (Wiens, McGuire & Shore 1993), a pattern also predicted by the transformational faulting hypothesis due to the nucleation of earthquakes on either side of the wedge of metastable olivine. A further prediction of the Hobbs & Ord (1988) hypothesis is that the maximum stress drop should increase as the stiffness of the loading system decreases, since an infinitely stiff system would result in stable sliding across a fault. A stiff loading system is analogous to a cold slab, so this prediction is consistent with the observations that the largest earthquakes occur at great depth, where the slab is warmest (Lundgren & Giardini 1994), and in the warmer subduction zones (Wiens & Gilbert 1996).

Field studies of pseudotachylytes in exposed continental mantle peridotites partially support the idea of adiabatic instabilities causing deep earthquakes. Pseudotachylytes are zones of very fine grained or glassy material thought to result from melting in a fault zone during an earthquake (Scott & Drever 1953, McKenzie & Brune 1972, Sibson 1975). Obata & Karato (1995) found pseudotachylytes in the Balmuccia peridotite in the Italian Alps. The mantle fault zone had been almost completely melted , but was only 3 cm wide, suggesting an essentially adiabatic process. In a detailed investigation of the microstructures associated with this fault, Jin, Karato & Obata (1998) demonstrated that shear localisation had occurred at a temperature of around 800 °C, leading to a dramatic increase in stress and, therefore, strain in the shear zone, leading finally to a rapid phase of brittle or semi–brittle deformation which generated sufficient heat to cause melting and form the pseudotachylyte. The initial stage of self–sustaining localisation of deformation occurred due to grain size reduction by dynamic recrystallisation, rather than through viscous dissipation. This latter process may have become important in the final stage of deformation, resulting in instability. Alternatively, the melting may have occurred due to frictional heating as a result of unstable

sliding, the brittle instability having been initiated by the process of grain size reduction alone. Thus, it is possible that instability may be caused by mechanical processes at the grain scale, rather than by adiabatic heating.

Several differences between the geological setting of this process and that of subduction related deep earthquakes warrant caution in the extrapolation of the results. The deformation in the Balmuccia peridotite results from continental collision and uplift, thus the rock mass experienced decreasing pressures and temperatures before it failed catastrophically. In a subducting slab, pressures and temperatures are monotonically increasing. Also, Jin *et al.* (1998) estimated that shear instabilities could occur to a maximum depth of 80 km in the continental lithosphere, given a reasonable geological strain rate. The temperature at such a depth is around 900 °C, similar to that in the core of a cold subducting slab at great depth. However, the pressure at 80 km depth is only a fraction of that at 700 km depth, the maximum depth at which deep earthquakes occur.

A variation on the adiabatic instability hypothesis, involving the transformation of metastable olivine, has been suggested (Däβler & Yuen 1996). Shear localisation in metastable olivine would promote transformation of the olivine to spinel, by increasing the temperature. Däβler & Yuen (1996) showed that the amount of latent heat released by olivine increases as it survives further into the spinel PT stability field. Thus, they suggested, the released latent heat encouraged melting in the shear zone, resulting in an earthquake. Greater release of latent heat at greater depth should increase the number of earthquakes, consistent with the observed increase in seismicity deep in the transition zone.

2.8 Non–Double Couple Earthquakes

Bridgman (1945) suggested that deep earthquakes might be caused by volume change associated with phase transformations in mantle minerals. This idea raised the possibility that the earthquakes might have a detectable volumetric component. Indeed, Evison (1963) believed he had found events with implosive mechanisms, but these results have not subsequently been verified. As mentioned in section 2.4, the volumetric component of deep earthquakes is now constrained to be small, and is often referred to as "insignificant" [e.g. Kawakatsu (1991)]. However, even a very small volume change is significant if it reflects a fundamental source process. If the onset and propagation of an earthquake occurs instantaneously with a dehydration reaction, then the radiated wavefield may include an implosive component derived from the volume reduction of the reaction. Equally, if the process of transformational faulting involves a larger volume of the denser spinel phase than has been proposed, then it too may result in a small, but potentially resolvable, volumetric component. The behaviour of melt at high pressures is not well established, but experiments by Agee & Walker (1993) suggest that molten olivine should be denser than its solid between 300 and 500 km depth. Theoretical arguments also support the notion of heavy melts at high pressure (Stolper *et al.* 1981). The volume change produced by any of these mechanisms is likely to be smaller than the resolution of any previous seismic studies, which is typically about 10%. However, in the case of the uniquely large 9 June 1994 event beneath Bolivia (moment magnitude M_w=8.2), analysis of ultra–long periods allowed Okal (1996) to constrain the volume change to be less than 2%. In chapters 5 and 6 of this thesis, I show how the constraints that can be placed on the volumetric component of moderately large deep earthquakes ($6<M_w<7$) can be improved to $< 5\%$, given favourable circumstances.

Several studies using long–period seismic data have observed a component of pure shear (a constant volume non–double couple component), in focal mechanisms for deep earthquakes (Giardini 1983, Giardini 1984, Kuge & Kawakatsu 1993). In each case, the authors have observed that mechanisms including a component of oblate strain correlate with a state of down–dip compression in the slab, whilst mechanisms with a component of prolate strain correlate with down–dip extension. Giardini (1984) suggests that these observed non–double couple

components are true reflections of the source process, because of the correlation of the orientation of extension or compression with the stress state in the slab. Kuge & Kawakatsu (1993) consider this to be a possibility, but also note that the non–double components may be induced by the large scale, inhomogeneous and anisotropic near source velocity structure of the subduction zone, the type of apparent shear deformation being a function of how the velocity structure varies with depth, rather than being a function of stress state. Kuge & Lay (1994) showed that slip on several double couple subfaults of differing orientations also induces an apparent non–double couple component in the wavefield.

2.9 Summary

Subduction zones have a complex structure, reflected in the considerable variation of temperature, seismic velocity and anelastic attenuation found within them. On average, the subducting lithosphere, or slab, is colder, faster and less attenuating than the adjacent mantle. Olivine is the most abundant mineral in the slab and is known to undergo a series of equilibrium transformations to denser phases with increasing pressure. However, the intra–slab locations of these transformations under the non–equilibrium conditions of dynamic subduction are largely unknown, as is the extent of the depth interval over which they occur. Olivine may survive metastably into the transition zone, where a rapid phase change to its denser spinel form will result in a dramatic reduction in grain size and could allow unstable sliding due to the low coefficient of friction of the new phase. Alternatively, the release of latent heat from the reaction could promote melting, again with a dramatic fall in the coefficient of friction leading to instability. Equally, the transformation of olivine may occur near to its equilibrium depth at 410 km, and play no part in providing the local mechanism of instability for deep seismogenesis, although the elevated increase in density can explain the compressional forces inferred from the focal mechanisms.

The release of fluids via dehydration reactions may promote earthquakes at all depths by reducing either the effective stress or the coefficient of friction. Shear localisation might also occur by strain softening effects caused by heating during ductile deformation, again possibly leading to melting or a dramatic reduction in

grain size. All of these mechanisms may incorporate a small amount of volume change as part of the seismic source, although it is not an essential part of any of the hypotheses. Nevertheless, improved constraint on the amount of volume change associated with deep sources would be useful in trying to determine the mechanisms which allow brittle failure at such great depth. By assuming an earthquake to be a disturbance at a point, its mechanism can be described by the seismic moment tensor, from which the source type, including volumetric component, can be extracted. Any non–double couple component identified in the moment tensor is expected to be small, given the observed strong similarities between deep and shallow earthquakes.

Chapter 3

Thermal Structure of Subduction Zones

3.1 Introduction

The thermal structure of subduction zones has been an important research topic since they were identified as part of the earth's convection cycle during the 1960s. Initial efforts, which computed only the temperature in the subducting slab (McKenzie 1969, Griggs 1972), showed it to remain colder than the surrounding mantle at least as far as the base of the transition zone, a result which follows from the low rate of thermal assimilation of the subducted lithosphere compared to the velocity of subduction, as a consequence of the generically low thermal conductivity of rock. This feature of the models proved to be robust, and has been independently validated by inferences from seismic tomography studies [e.g. van der Hilst *et al.* (1991) and van der Hilst *et al.* (1997)], where slabs are delimited by positive velocity anomalies. Further thermal modelling work (Minear & Toksöz 1970*a*, Minear & Toksoz 1970*b*, Hasebe, Fujii & Uyeda 1970, Toksöz, Minear & Julian 1971, Turcotte & Schubert 1973) calculated the temperature distribution in both the slab and adjacent mantle, and considered the relative influences of a wide range of possible heat sources, namely adiabatic compression, shear heating at the slab–mantle interface, diffusion of heat from the mantle to the slab by both conduction and radiative transfer, radiogenic heating

and the release of latent heat by phase transformations. However, none of these models succeeded in explaining the observed high heat flows in back–arc regions without resorting to unfeasibly high levels of shear heating (Griggs 1972, Yuen *et al.* 1978).

This problem of high back–arc heat flow was addressed by Andrews & Sleep (1974) and Hsui & Toksöz (1979), who modelled induced flow in the mantle which overlies the slab. The flow is thought to be caused by coupling between the slab and mantle, so that chilled mantle material is dragged downwards by the slab, drawing new, hot mantle inwards towards the slab surface (as illustrated in section 3.3). Davies & Stevenson (1992) demonstrated that such a scenario was consistent with the occurrence of a volcanic arc, with melting of the convecting mantle being catalysed by the flux of hydrous fluids released from the slab. Induced mantle flow is probably an important influence on the thermal structure of subduction zones, preventing the mantle adjacent to the slab from becoming increasingly cold, and is now established as an integral part of slab thermal models. Such models are essential for the investigation of slab deformation and deep seismogenesis.

At very high temperatures, continuous ductile deformation inhibits the stress build up required to cause seismicity. The maximum depth extent of shallow seismicity in oceanic lithosphere appears to be approximately limited by the 600 °C isotherm (Denlinger 1992), whilst many studies have suggested that deep seismicity in subducting oceanic lithosphere is also inhibited solely by increasing temperature (McKenzie 1969, McKenzie 1970, Griggs 1972, Vlaar & Wortel 1976, Molnar, Freedman & Shih 1979, Wortel 1982, Wortel 1986, Wortel & Vlaar 1988). However, some of the current theories of deep seismogenesis, such as dehydration–induced embrittlement and transformational faulting (described in sections 2.5 and 2.6), predict that temperature is not the sole controlling variable, with the occurrence of seismicity being governed primarily by the stability limits of mineral reactions, which may vary with both pressure and temperature.

The investigation of these ideas at specific locations is necessary because the characteristics of subduction zones vary strongly from region to region. This requires the estimation of the thermal structure of individual subduction zone segments, rather than a single generic model. To this end, a well established numerical model based on that of Toksöz *et al.* (1971) is used here to model the

slab thermal structure of the specific subduction zones investigated in this thesis. The details of the method are described in section 3.3 and the relative importance of the various input parameters is assessed in section 3.4. The stability limits of different mineral reactions are superimposed onto the thermal models (section 3.5) and a comparison between their predicted behaviour and seismic observations is then used to assess the accuracy of a single model. Finally, the velocity structure of a subduction zone is predicted from its thermal profile, and the focusing effect on the short–period wavefield is investigated in section 3.6. However, before the discussion of these subjects, it is first necessary to consider the initial temperature distribution in oceanic lithosphere prior to subduction. This parameter influences all estimates of slab temperature, whichever technique is used, and there is little consensus about its details [e.g. McNutt (1995)].

3.2 Thermal Models of Oceanic Lithosphere

Constraints on the variation of temperature within the oceanic lithosphere come from observations of ocean depth, heat flow, elastic thickness and the geoid. The present thermal structure of any given volume of lithosphere depends upon the initial conditions at the ridge when it formed, its age (i.e. cooling time), and any subsequent flux of heat from the mantle. Analysis of ocean depths around the world has shown that ocean depth, almost universally, increases in proportion to the square root of the lithospheric age up to ages of at least 80 Ma (Marty & Cazenave 1989). This variation is consistent with the cooling of a half–space by conduction, whereby a half–space of initially constant temperature is instantaneously and continuously cooled at its surface to a much lower constant temperature (Turcotte & Oxburgh 1967). In this model, temperature at a given depth decreases indefinitely through time, and its applicability to lithosphere of age > 80 Ma varies from region to region. Ocean depths in the North American Basin of the western Atlantic are in agreement with the half–space model for lithospheric ages of up to 170 Ma (Marty & Cazenave 1989), whilst depth and heat flow measurements in much of the Pacific Ocean reach an apparent steady state after approximately 90 Ma (Renkin & Sclater 1988, Lister *et al.* 1990).

Figure 3.1 shows depths to the top of the basaltic crust in the Pacific, measured

from Deep Sea Drilling Project (DSDP) or Ocean Drilling Program (ODP) boreholes and collated by Carlson & Johnson (1994), plotted against the square root of lithospheric age. On such a plot, a half–space cooling model is represented by a straight line. The least squares fit to the data for ages < 90 Ma is shown as a solid line and has a correlation coefficient of 0.97, indicating that the data are very well modelled by a cooling half–space. For ages greater than 90 Ma, the ocean depth is approximately constant. Patterns like this led to the development of "plate models" for the thermal lithosphere, whereby a supposed background flux of heat from the mantle forced the overlying lithosphere to evolve to an equilibrium state, with a critical isotherm at a constant depth through time (McKenzie 1967, Parsons & Sclater 1977, Stein & Stein 1992). However, analysis of ocean depth data by Carlson & Johnson (1994) revealed that any single plate model could not provide a satisfactory fit to the data. They concluded that the cooling history of old lithosphere was not a simple extension of that of young lithosphere, proposing that the observed trends in ocean depth data resulted from the impact of mantle upwellings, or hot spots, on a background of a continuously cooling half–space, an extension of the ideas of Heestand & Crough (1981) and Schroeder (1984). I shall use a half–space model, but the plate models are described here to allow explicit comparison between my results and studies in which plate models have been used.

The rate of transfer of heat from a hot place to an adjacent cold place within a uniform material is governed by the *thermal diffusivity*, κ, of the material, where $\kappa = k/\rho C_p$ and k is the conductivity of the material, ρ the density and C_p the specific heat capacity at a given pressure. Both the normal half–space model and the plate models referred to above all assume that the thermal diffusivity remains constant. However, experimental studies (Kanamori, Fujii & Mizutani 1968, Fujisawa *et al.* 1968, Durham, Mirkovich & Heard 1987) have demonstrated that thermal diffusivity varies with both pressure and temperature. At temperatures below 1,200 °C , the variation of diffusivity with respect to temperature is 4–6 orders of magnitude larger than that with respect to pressure. At higher temperatures, there is almost no variation with temperature and only slow variation with pressure. Denlinger (1992) used the observed temperature dependence of the thermal diffusivity to recalculate the thermal structure of the lithosphere. His model still satisfies the observed dependence of heat flow and ocean depth

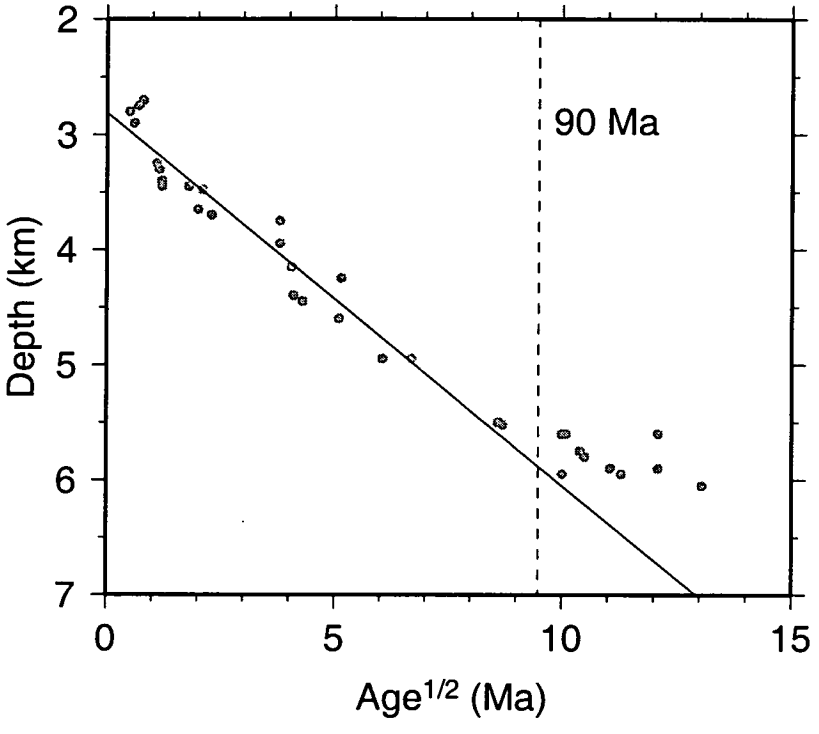

Figure 3.1.
Ocean depth–age relationship for the Pacific Ocean. The dots show depths to the basaltic crust below the sea surface, determined from DSDP/ODP boreholes in the Pacific Ocean. They are plotted against the square root of the lithospheric age. The solid line represents the half-space cooling model which best fits the data for ages less than 90 Ma. At older ages, the depth is approximately constant, an effect possibly due to heat flux into the lithosphere from mantle upwellings. After Carlson & Johnson (1994).

on the square root of the lithospheric age, but it is substantially cooler than the other models at depths of less than 60 km.

It is often convenient to use age as a proxy for the temperature structure of the oceanic lithosphere. Figure 3.2 illustrates the different thermal models, allowing comparison of the models at different depths and ages. The plate model of Stein & Stein (1992) is substantially hotter than the others and is close to equilibrium after only 50 Ma, whilst the plate model of Parsons & Sclater (1977) is in good agreement with the half–space model to an age of around 90 Ma. The model of Denlinger (1992), which uses a temperature–dependent thermal diffusivity, is not dramatically different from the normal half–space model when considered to 100 km depth. It converges with the Parsons & Sclater (1977) model at a temperature of 1,200 °C, close to the range of temperatures (1,250–1,450 °C) which have been proposed to define the base of the lithosphere.

The above observations show that, if age is to be used as a proxy for temperature, it must be done so with care and the specific history of the lithosphere must be considered. In parts of the Atlantic, for example, it would be appropriate to relate the real age of the lithosphere to its thermal structure. However, in the Pacific, the lithosphere appears, on average, to cool little after 90 Ma. Thus, no age greater than this should be used in a half–space model since, at greater ages, the thermal structure of the real lithosphere remains approximately constant, whilst the half–space model predicts continued cooling.

3.3 Numerical Modelling of the Thermal Structure of Subducting Lithosphere

The thermal structure of subducting lithosphere, and the adjacent mantle into which it subducts, is modelled here using a finite difference code written by Norman Sleep in 1982, and later modularised by John Brodholt in 1987. It is based upon the method of Toksöz *et al.* (1971) and assumes that the kinematics of the subduction zone are known and remain constant through time. Also, the model evolves until a steady state situation is reached. A recent global tomographic study (van der Hilst *et al.* 1997) identifies cold material at 900 km

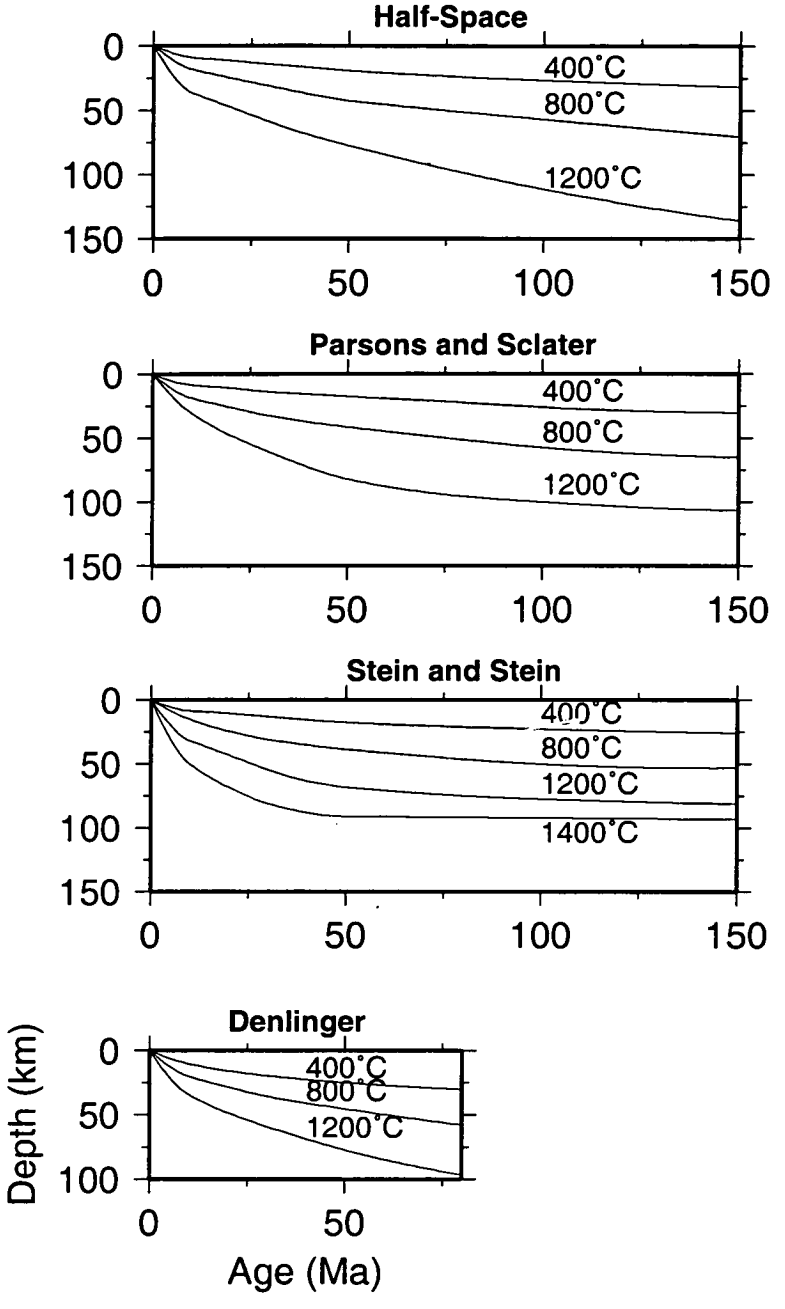

Figure 3.2.

Thermal models of the oceanic lithosphere. The variation with age (x–axis) and depth (y–axis) of four different models for the temperature structure of oceanic lithosphere are shown. The thin lines are isotherms. All of the models represent lithosphere which has evolved continuously from its time of formation at the mid–ocean ridge, and do not consider the possible influence of interaction with mantle upwellings away from the ridge. The Denlinger model, at the bottom of the figure, was calculated using a thermal diffusivity which varied with temperature, whilst the other models all assume a constant thermal diffusivity. The top three diagrams are after Stein & Stein (1996) and the bottom one is from Denlinger (1992).

depth beneath most of the subduction zones studied, showing that subduction has been active in these regions for some time. Thus, the assumption of a mature subduction zone seems appropriate, and it simplifies the modelling significantly by removing the need to examine the thermal structure at many different time steps.

The thermal structure of the lithosphere prior to subduction is calculated using a half–space cooling model. The majority of the subduction zones modelled in this study involve subduction of the Pacific plate, thus, following the arguments of section 3.2, a maximum age of 90 Ma is imposed for input into the thermal model. An initial temperature of 1,350 °C is used, which results in a half–space in excellent agreement with the best fitting half–space model found for the Pacific by Carlson & Johnson (1994) (and illustrated in figure 3.1), which is itself consistent, up to 90 Ma, with the plate model of Parsons & Sclater (1977) and is similar to that of Denlinger (1992), these latter two models being illustrated in figure 3.2. The half–space model is substantially different to the plate model of Stein & Stein (1992) (also shown in figure 3.2), which has been used elsewhere [e.g. Kirby *et al.* (1996)]. As an initial condition, the half–space temperature structure extends to 100 km depth across the entire model, essentially defining the thermal lithosphere. Below this depth, the temperature increases with an adiabatic gradient.

The thermal evolution of this prescribed temperature field is governed by the imposed kinematics and the relevant material constants, and it is modelled using an iterative numerical scheme (Minear & Toksöz 1970*a*). The initial subduction zone profile is discretised into a grid, with horizontal (x) and vertical (z) axes, typically with a vertical grid increment of 10 km. The horizontal increment is defined to be the vertical grid increment divided by the tangent of the dip, so that the diagonal across a grid square is always parallel to the dip of the slab. Subduction of the lithosphere into the mantle is modelled by translating the initial temperatures by two grid increments (in both x and z directions) down dip. The heat flux over a time interval defined by the rate of subduction is then calculated by solving the heat conduction equation using a finite difference method [due to L.H. Thomas in Peaceman & Rachford (1955)], such that the equation is solved first in the x direction and then in the z direction. Spatial temperature gradients are determined from the value of a given point and the points to which it is

immediately adjacent in the x and z directions. The heat conduction equation which is solved can be expressed analytically as

$$\frac{\partial T}{\partial t} = \kappa \bigtriangledown^2 T + \frac{H}{C_p \rho}, \tag{3.1}$$

where T is temperature, t is time, κ is the thermal diffusivity, H is the rate of heat production per unit volume, C_p is the specific heat capacity and ρ is the density. Thus, the variation of temperature through time is governed by the thermal diffusivity, the spatial temperature gradients and the influence of heat sources. The only source of heat generation considered in this study is that of adiabatic compression, an assumption which is justified below.

Three possible sources of heat generation within the subduction zone have been ignored. These are shear heating, radiogenic heating and the release of latent heat from phase transformations. The influence of radiogenic heating is negligible, since approximately 90% of the subducting lithosphere consists of mantle which is of similar composition to the convecting mantle into which it is subducting. Schubert *et al.* (1975) calculated the heating effect of the exothermic phase change from olivine to spinel, occurring at equilibrium conditions within the slab, and found the resulting maximum temperature increase to be less than 100 °C. The amount of heat generated by shear heating at the surface of the slab has been widely debated, and is reviewed in detail by Davies & Stevenson (1992) and Peacock (1996). Two particularly salient points have emerged from these discussions: (i) shear heating reduces both the strength and viscosity of the material, hence reducing the amount of heating which occurs for a given strain rate as time progresses, i.e. it is a negative feedback process; (ii) observations of heat flow, depth of seismic coupling, and the PT facies of exposed paleo–subduction zones all suggest relatively low values of shear stress of around 20 MPa or less. Anderson, Delong & Schwarz (1978) proposed that much of the heat generated by shear heating would be absorbed by endothermic dehydration reactions. Also, shear heating is likely to strongly influence only a narrow zone of the slab, its width determined by the rate of heat production and diffusion. Thus it appears likely that shear heating effects are of secondary importance when considering the

thermal evolution of the slab and that the decision to ignore them is justified.

The induced flow of the mantle adjacent to the slab is an important influence on the thermal structure of subduction zones. Above the slab, the mantle forms a wedge shape, or corner, bounded on two sides by the slab and the overlying lithosphere. By assuming that the mantle has a constant, temperature independent viscosity, then the form of the induced flow may be described analytically (Batchelor 1967, McKenzie 1969). Figure 3.3 shows the theoretical flow patterns for both a shallowly and steeply dipping slab, calculated using the expressions given by McKenzie (1969). These examples will be compared below with the flow approximation used in this study. Davies & Stevenson (1992) investigated the influence of allowing mantle viscosity to vary by up to five orders of magnitude and found it to be small. As they point out, the assumption of a constant velocity of subduction forces the slab to behave as if it has an infinite viscosity. In relation to this, any variations in mantle viscosity are small and of little significance. Thus, whilst temperature induced variations in viscosity may play a rôle in the earth, it is pointless considering them whilst using a model with kinematic boundary conditions. Rather, they must be investigated using a fully dynamic model. Such models are not sufficiently well developed to allow modelling of individual, real subduction zones, so we must make do with the assumption of constant mantle viscosity, an assumption which appears to produce reasonable thermal structures, as demonstrated by the widespread and successful use of kinematic models (Sleep 1973, Creager & Jordan 1984, Creager & Boyd 1991, Davies & Stevenson 1992).

To avoid the computational expense of determining the full corner flow analytically, a simple numerical approximation is used, as illustrated in figure 3.4. A non–convecting thickness of overriding mechanical lithosphere is defined, such that it is less than the 100 km thickness of the initial thermal lithosphere, thus allowing the original half–space thermal structure to evolve in response to heating by advection through the induced upwards mantle flow. The induced downward flow is defined to move parallel to and at the same speed as the slab. Its width increases with depth, such that the boundary between upgoing and downgoing flows has a dip, θ_c, which is always defined by

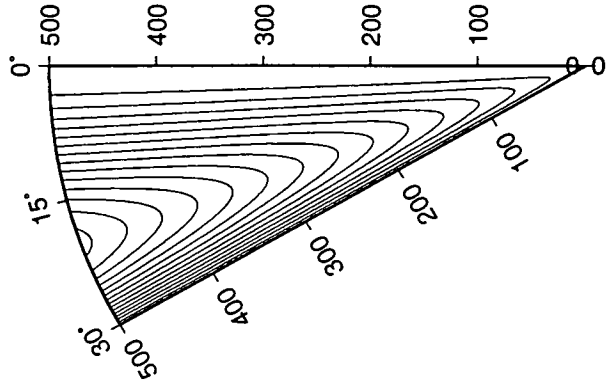

(a)

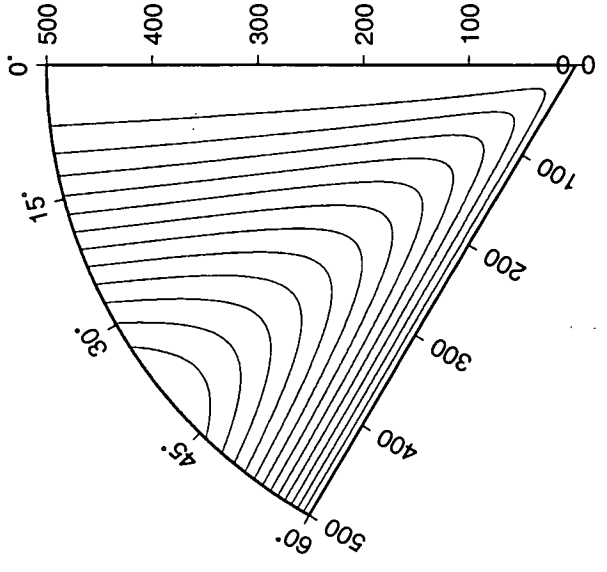

(b)

Figure 3.3.
Stream lines of flow induced in the mantle by the subducting slab. Analytical solutions for corner flow in the case of **(a)** a slab subducting at 30°, and **(b)** a slab subducting at 60°. The direction of induced flow is parallel to the contours and the lower boundary of the wedge is equivalent to the slab surface.

Table 3.1.
Comparison of models for mantle flow induced above the slab.

Slab dip	θ_c		Dip of upward flow	
	Analytical	Numerical approx.	Analytical	Numerical approx.
30°	20°	16°	3°	16°
45°	30°	27°	4°	27°
60°	39°	41°	5°	30°

$$\theta_c = \arctan \frac{\tan \theta_d}{2}, \tag{3.2}$$

where θ_d is the dip of the slab. For $\theta_d \leq 50°$, then the upward flow is parallel to the boundary between the two flow regimes, as shown in figure 3.4a. For $\theta_d > 50°$, then the dip of the upward flow is less than that of the flow boundary, as shown in figure 3.4b. The dips of the upward flows and of the boundaries between flow regimes for different slab dips are shown in table 3.1 for both the analytical flow solutions and the numerical approximations. Values of θ_c are in good agreement between the different models, with the difference never exceeding 5°. In the analytical models, the upward flow has a maximum dip of about 5°, whilst in the numerical model it can exceed 30°. Clearly, a more steeply dipping upward flow will advect material from greater depth, which will be hotter and will therefore increase the flux of heat to the slab. However, given the small gradient of the mantle geotherm, this effect is of only minor importance.

3.4 Input Parameters for the Thermal Model

To allow an estimation of the errors in the thermal models, it is necessary to investigate the relative influences of the different input parameters. Each parameter was varied within reasonable bounds so that its effect on the resulting model could be observed, and a brief summary of the results for the most significant parameters is presented here. Estimates of the effect of a parameter are based largely on how far the isotherms in the core of the slab are deflected. Such an approach is designed to provide a feel for how the model behaves, rather than to

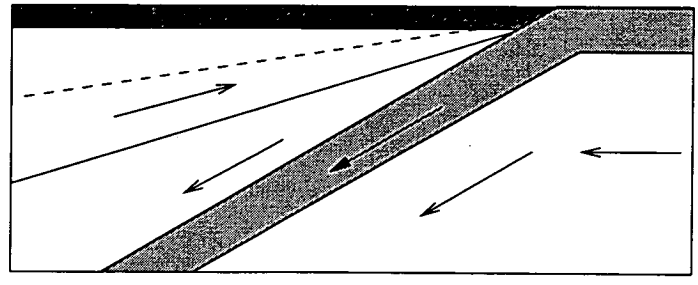

(a)

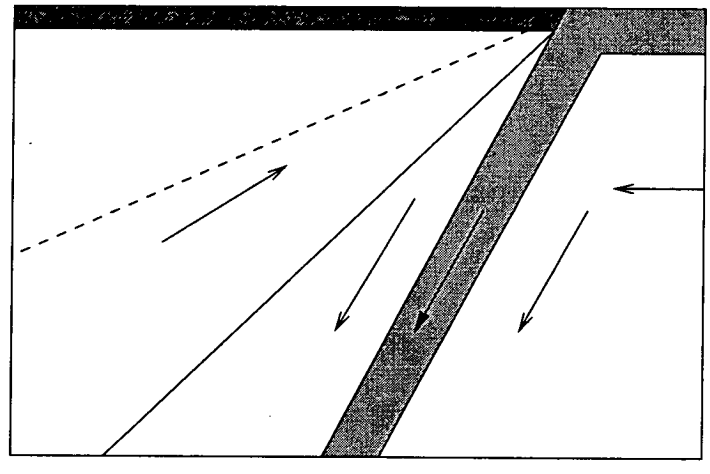

(b)

Figure 3.4.

Geometry and kinematics of the subduction model. The subducting slab is shaded light grey and the non–convecting, mechanical lithosphere is shaded dark grey. Arrows show the kinematics of the slab and the induced mantle flow for **(a)** a slab dipping at 30°, and **(b)** a slab dipping at 60°. The thin solid line in the mantle is the boundary between the upgoing and downgoing flow regimes and the thin dashed line marks the limit of flow, above which the mantle is assumed to be stationary.

generate precise comparisons between the parameters, since the model is complex and non–linear, and the results may vary somewhat for different combinations of parameters.

The rate of subduction is a strong controlling factor on the temperature distribution in the model. An increase in velocity of $2\,\mathrm{cm\,yr^{-1}}$ was observed to depress the maximum depth of a single isotherm by around 100 km. Fortunately, the rate of subduction is well constrained by plate motion reconstructions, such as that of Demets *et al.* (1990), which are used extensively in chapter 4. The thickness of lithosphere which is subducted is less well constrained, and estimates vary between 50 and 125 km, although most studies use thicknesses in the range 70–100 km (see table 3.2). The maximum depth of an isotherm varies by about 100 km over this range and the slab thickness probably represents the largest single source of uncertainty in the models.

Considerations regarding the age of the lithosphere have been discussed extensively in section 3.2, and it was concluded that no age greater than 90 Ma should be used in the calculation of the lithospheric thermal profile. Current knowledge of lithospheric age is good, with Müller *et al.* (1997) providing an up to date determination of ocean floor isochrons and the spatial distribution of errors associated with these estimates[1]. Age determines the amount of time for which the half–space model is allowed to cool, and the exact form of the solution is dependent upon the initial temperature. 1,350 °C provides an excellent fit to the observed ocean–depth data from the Pacific and is also a good approximation to the Parsons & Sclater (1977) plate model. In addition, this temperature also determines the model's adiabatic geotherm for the convecting mantle. The real mantle adiabat is estimated from experimental determinations of the PT phase relations of olivine and its denser polymorphs (Jeanloz & Thompson 1983, Akaogi *et al.* 1989). These solid–solid phase transitions are thought to be responsible for the seismically observed discontinuities at 410 and 660 km (Anderson 1967, Johnson 1967, Archambeau, Flinn & Lambert 1969). An estimate of the average current mantle adiabat is given by Thompson (1992) and it is very similar to that produced in the thermal model by assuming an initial half–space temperature of 1,350 °C, thereby validating the mantle geotherm predicted above.

[1]Their model is freely available at http://www-sdt.univ-brest.fr/jyroyer/Agegrid/.

Two important parameters which are assumed to be constant in every model are the specific heat capacity and the thermal conductivity. Both are also assumed not to change significantly between the slab and surrounding mantle. Various values have been used in previous studies, and these are summarised in table 3.2. In trials, I found that varying these parameters within a realistic range has little effect upon the resulting models, with changes being many times smaller than those caused by variation in the parameters described above. The values used in this study were suggested by George Helffrich (*personal communication*, 1997), and are also shown in table 3.2. Given the uncertainties in the values of these parameters, and the insensitivity of the model to such variations, the specific heat capacity and the thermal conductivity are assumed to remain constant at all depths and temperatures.

A further parameter which is assumed constant in all the models is the thickness of the overriding mechanical lithosphere. This is the thickness of material which is defined not to flow and in which, therefore, advection of heat is impossible. The crustal thickness of volcanic arcs provides a lower limit of about 30 km for this thickness (Davies & Stevenson 1992), whilst ablation of material via the induced mantle corner flow requires that the thickness be less than the 100 km used for the subducting slab. I use a value of 60 km, but varying the thickness between 30 and 80 km has negligible effect on the slab geotherm. It does alter the temperature structure of the wedge, resulting in higher temperatures at shallower depths, but the effect is not dramatic.

Values of the slab dip, thermal age and the convergence velocity must be determined for every location which is to be modelled. I assume that the observed Wadati–Benioff zone of seismicity represents the subducting slab and measure its dip from seismicity profiles perpendicular to the strike of the slab. Earthquake hypocentres from the EHB catalogue are used because they delimit the Wadati–Benioff zone more clearly than the ISC data, due to improved depth determinations resulting from the use of surface reflection phases. Slab dip may vary considerably along strike, even in a single subduction zone. To avoid this problem, the seismicity profiles extend for approximately 1° of latitude or longitude along strike, a distance within which there is likely to be little variation in

Table 3.2.
Fixed input parameters for the thermal model.

Parameter	Value	Selected values used elsewhere
Gravity	$9.8\,\mathrm{m\,s^{-2}}$	
Lith. density	$3{,}400\,\mathrm{kg\,m^{-3}}$	
Half–space temp.	1,350 °C	
Specific heat	$1.12 \times 10^3\,\mathrm{J\,kg^{-1}K^{-1}}$	1.05×10^3 (Däβler & Yuen 1996)
Conductivity	$3.34\,\mathrm{W\,m^{-1}\,K^{-1}}$	3.5 (Däβler & Yuen 1996) 2.5 (Peacock 1992) 2.5 (Toksöz *et al.* 1971)
Expansion coef.	$3 \times 10^{-5}\,\mathrm{K^{-1}}$	3.5×10^{-5} (Däβler & Yuen 1996) 3.6×10^{-5} (Toksöz *et al.* 1971)
Slab thickness	100 km	70–90 (Däβler & Yuen 1996) 90 (Davies & Stevenson 1992) 95 (Kirby *et al.* 1996) 100 (Helffrich, Stein & Wood 1989)
Over. lith. thick.	60 km	40 (Davies & Stevenson 1992)

slab morphology. Estimates of the age of the lithosphere at its point of subduction and of the convergence velocities come largely from Müller *et al.* (1997) and Demets *et al.* (1990). Where alternative sources have been used, these are explicitly referenced in the calculations presented in chapter 4. The model–specific values of dip, thermal age (≤ 90 Ma) and convergence velocity are shown in table 3.3.

3.5 Predicting the Locations of Mineral Reactions

Experimental determinations of the phase relations of a mineral assemblage at varying pressures and temperatures can be used, in conjunction with the thermal models of subduction zones, to predict the spatial distribution of specific mineral reactions within subduction zones. Phase boundaries, such as the one shown in figure 2.11 between serpentine and forsterite + enstatite, were discretised into straight line segments and described by simple linear equations. A series of such equations can then be developed to describe the PT locus of any given reaction.

Table 3.3.
Model–specific input parameters.

Location	Thermal Age	Dip	Convergence rate
Tonga	90 Ma	53°	13.0 cm yr^{-1}
Kurile	90 Ma	40°	8.2 cm yr^{-1}
Mariana	90 Ma	78°	7.0 cm yr^{-1}
Java	90 Ma	40°	7.4 cm yr^{-1}
N.E. Japan	90 Ma	30°	9.0 cm yr^{-1}
Izu 28°N	90 Ma	62°	5.7 cm yr^{-1}
Izu 32°N	90 Ma	47°	5.7 cm yr^{-1}
Shumagin	60 Ma	42°	7.5 cm yr^{-1}
Ryukyu	49 Ma	40°	4.0 cm yr^{-1}
Sumatra	50 Ma	50°	5.9 cm yr^{-1}

I wrote an algorithm which reads the temperatures from every grid point in the thermal model and calculates the corresponding pressures. It then evaluates each PT point, to determine on which side of the specific reaction boundary the point lies, and allocates a constant even number, e.g. 0 for serpentine and 2 for forsterite + enstatite. Contouring along the odd numbers, in this case 1, spatially delimits the equilibrium reaction boundary. This method is fast and simple, but has the disadvantage that the final contours of the phase boundary reflect the discrete, gridded nature of the thermal model. Thus, in figures showing thermal models with superimposed phase boundaries (such as figure 3.5), the step–like nature of the boundary is entirely a function of the contouring method. Such boundaries would, in reality, vary quite smoothly.

In chapter 4, the width of the stability field of serpentine in the subducting slab turns out to be a critical parameter. Thus, it is necessary here to constrain the error bars on this parameter and to show how variation in the input parameters affects the spatial location of dehydration loci. Two models were produced for a segment of the Japan subduction zone. Since the dip of the slab is well constrained by earthquake hypocentres, this was held constant at 30° in both models. The remaining input parameters were varied within reasonable bounds so as to produce the coldest and hottest models possible, using the parameter values shown in table 3.4. Estimates of "reasonable bounds" for the parameters were guided by previous studies and experimental data (Toksöz *et al.* 1971, Davies & Stevenson 1992, Stein 1995, Clauser & Huenges 1995, Däβler & Yuen 1996).

Table 3.4.
Values of parameters used in the sensitivity analysis, representing the range of realistic values.

Parameter	Cold slab	Hot slab
Lith. density	3,500 kg m^{-3}	3,300 kg m^{-3}
Half–space temp.	1280 °C	1450 °C
Specific heat	1.2×10^7 J kg^{-1} K^{-1}	1.0×10^7 J kg^{-1} K^{-1}
Conductivity	3.1×10^5 W m^{-1} K^{-1}	4.0×10^5 W m^{-1} K^{-1}
Expansion coef.	2.3×10^{-5} K^{-1}	4.0×10^{-5} K^{-1}
Slab thickness	130 km	70 km
Convergence vel.	10 cm yr^{-1}	8 cm yr^{-1}
Thermal age	100 Ma	70 Ma
Over. lith. thick.	90 km	30 km

The resulting two models, with serpentine stability fields delimited by the blue lines, are shown in figure 3.5. Earthquake hypocentres are included as points of reference. Although the thermal structures vary considerably, there is little difference in the extent of serpentine stability within the slab, showing that the predicted loci of dehydration within the slab are robust to errors in the input parameters for the thermal model. Such behaviour results from the dependence of mineral reactions on both temperature and pressure, the latter of which varies only with depth and is well constrained in the models, leading to this observed low sensitivity to temperature variation. However, there is a very large difference between the two temperature distributions in the mantle wedge and the overriding lithosphere and this does cause a considerable difference in the location of the stability limit of serpentine. So, whilst the location of this limit is well constrained within the slab, it is poorly known in the region directly above it.

Only errors in the actual method, such as the accuracy of the simulation of induced mantle flow, rather than in the model input, have not been considered. However, recent observations of an uplifted 410 km mantle discontinuity across the Izu–Bonin subduction zone (Collier & Helffrich 1997) allow the absolute accuracy of one thermal model to be assessed.

Collier & Helffrich (1997) observed seismic reflections and phase conversions from the 410 and 660 km mantle discontinuities by examining stacked records from the

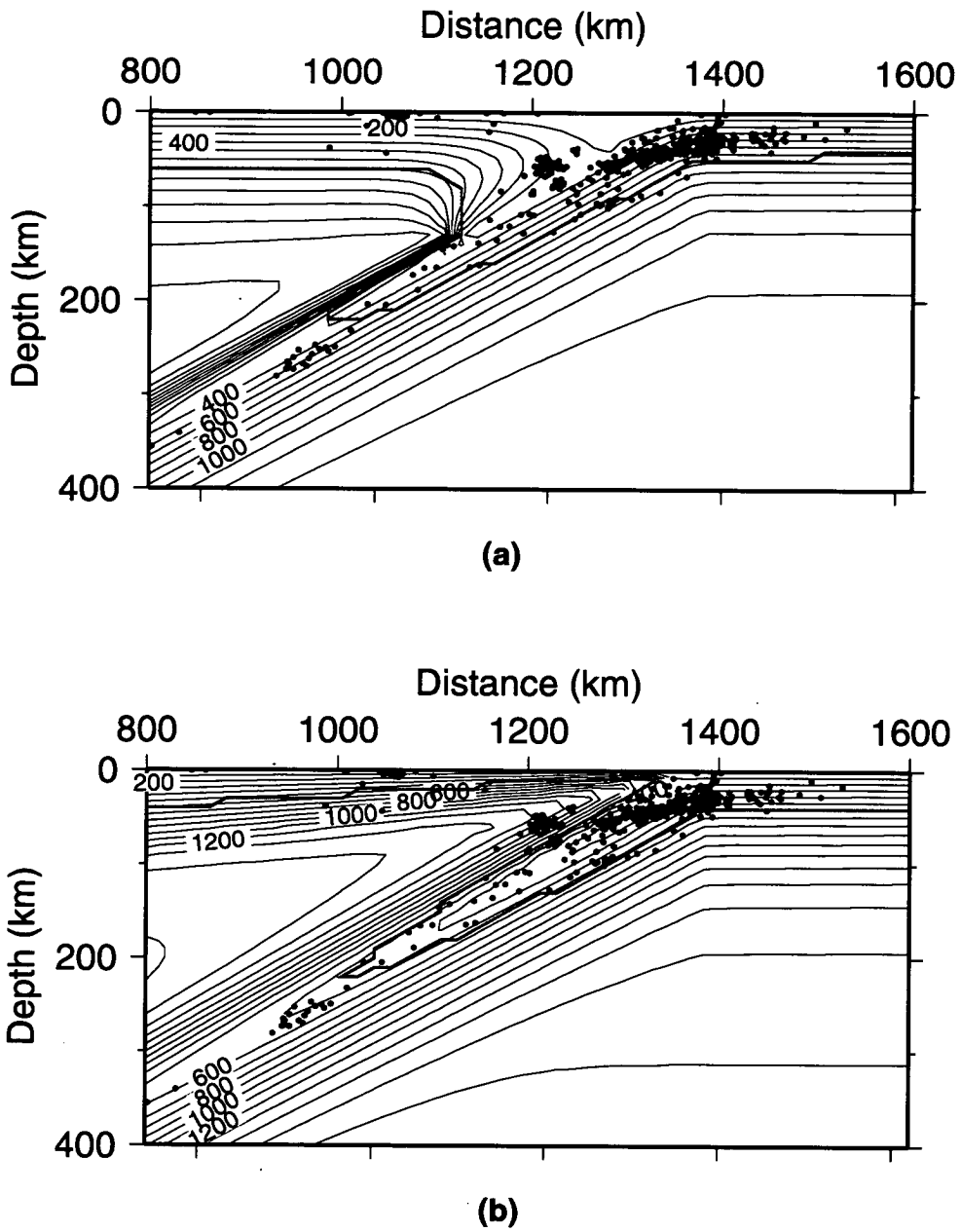

Figure 3.5.
Extreme thermal models for the Japan subduction zone, showing earthquake hypocentres (black dots) and the maximum stability limit of serpentine (blue line). **(a)** is the coldest realistic model and **(b)** is the warmest realistic model. The models were produced using the values shown in table 3.4 for the input parameters. The two models illustrate the degree of sensitivity of the predicted locus of dehydration to reasonable variations in temperature associated with the uncertainties in the input parameters.

United Kingdom's and the north–western United States' regional networks of seismometers. The 410 km discontinuity appeared to be uplifted to shallower depths in and near the subducting slab, whilst the 660 km discontinuity was depressed, behaviour consistent with the discontinuities representing phase changes from olivine to spinel and from spinel to perovskite and magnesiowustite, respectively. Assuming that these phase changes are the cause of the discontinuity [they are widely believed to be so, e.g. Wood (1997)], then the distance of perturbation in the subduction zone from their equilibrium depths can be used as a measure of temperature, since the Clapeyron (PT) slopes of the phase transformations are known from experimental data (Akaogi *et al.* 1989, Katsura & Ito 1989, Ito & Takahashi 1989, Ito *et al.* 1990) and the variation of pressure with depth is known.

Bina & Helffrich (1994) used the available experimental data to calculate best–fit Clapeyron slopes which were in agreement with the seismic observations of the discontinuities. I calculated a thermal model for the appropriate part of the Izu–Bonin subduction zone and superimposed both the predicted and the observed positions of the discontinuities, using the Clapeyron slopes of Bina & Helffrich (1994), as shown in figure 3.6. The maximum magnitudes of the observed displacements of the discontinuities were well modelled, particularly in the case of the "410", where the model is within 10 km of the observed discontinuity, which is within the reported error bounds (± 11 km) of the observations (based on a consideration of errors in the earthquake source location, the first–arrival time picks and in the velocity model). The "660" has been modelled as slightly too deep in the core of the slab, suggesting that the model may be around 100 °C too cold at this depth. Overall, it appears that the thermal model calculated here is a good first–order representation of the true thermal structure of the Izu–Bonin subduction zone, in the sense that it is validated quantitatively by independent seismic reflection and phase conversion data.

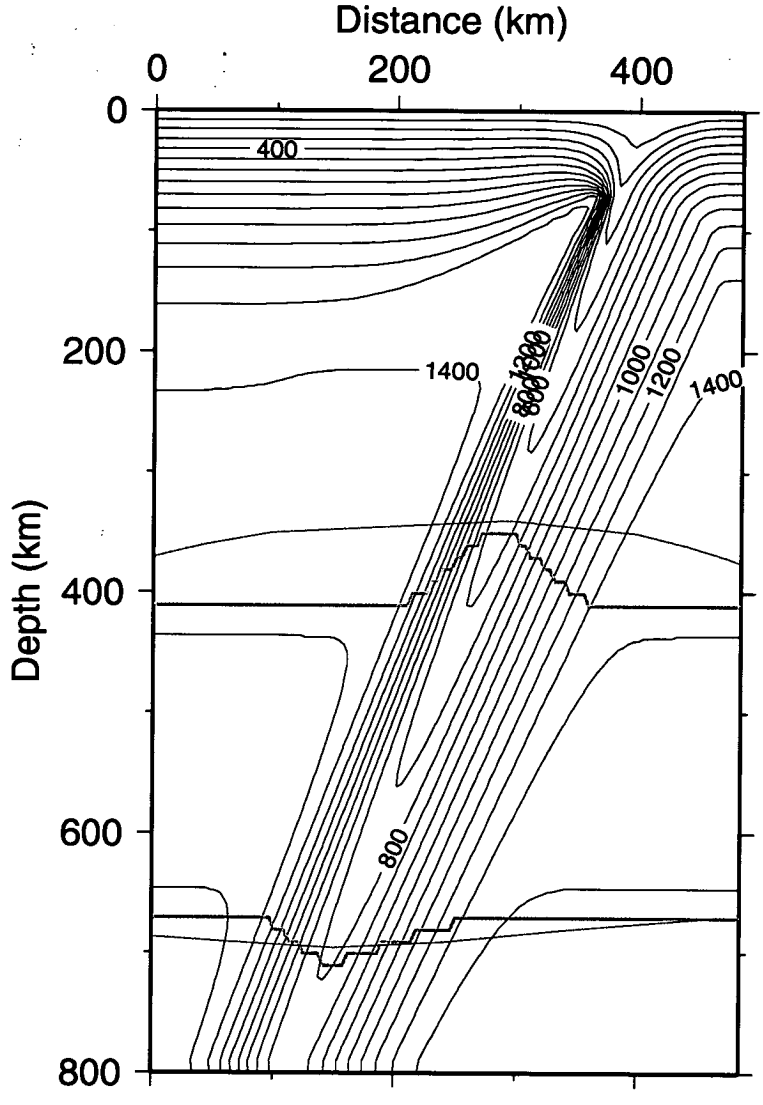

Figure 3.6.
Thermal model of the Izu–Bonin subduction zone, showing predicted and observed positions of the 410 and 660 km mantle discontinuities. The predicted positions of the olivine–wadsleyite (top) and ringwoodite–perovskite + magnesiowüstite (bottom) transformations are shown in red. The blue lines show the interpolated observations of the 410 and 660 km mantle discontinuities, from Collier & Helffrich (1997).

3.6 Slab Velocity Structures and Perturbations to the Short–Period Wavefield

The thermal structure of subduction zones is the primary cause of the significant velocity anomalies which are observed within them [see Lay (1994) for a detailed review of relevant studies], and this complicated velocity structure may affect the observed pattern of radiation from deep earthquakes. However, it is a relatively straight forward matter to examine how short period radiation might be affected by this velocity structure around the source. Following an approach adopted by many authors in the past (Toksöz *et al.* 1971, Sleep 1973, Engdahl, Sleep & Lin 1977, Fujita, Engdahl & Sleep 1981, Creager & Jordan 1984, Creager & Jordan 1986), I converted the modelled thermal structure of the Japan subduction zone into a P–wave velocity anomaly structure, using the conversion $\frac{\partial V_p}{\partial T} = 0.4$ $\mathrm{m\,s^{-1}\,K^{-1}}$, after the experimental work of Anderson *et al.* (1968) and the travel time calculations of Creager & Jordan (1986). The resulting anomaly structure was embedded into the spherically symmetrical IASP91 earth model, creating a composite model. This was then used to compute the ray paths for P–waves of period 1 s from a synthetic source at different depths in the slab, using an X–windows implementation (Davis & Henson 1993) of the Gaussian beam method (Cervený 1983, Weber 1988), which is computationally efficient and relatively easy to use.

Some of the results from this ray tracing exercise are shown in figure 3.7, for earthquake depths of 340 and 490 km, on a flat earth projection (Müller 1977). The calculations were carried out using a spheroidal earth model, but the results are presented on a flat earth projection for clarity, the alternative profiles through an oblate spheroid being somewhat difficult to interpret. A distinct asymmetry in the wavefield is visible, showing that the dipping slab does distort the short–period wavefield, even for sources located at great depth. The resulting pattern of asymmetry is different in each case and is governed by both depth and lateral location within the slab. It seems likely that the amount and form of this near–source distortion varies in a strongly non–linear fashion with location. Thus, how the wavefield will be perturbed at a given depth cannot be predicted accurately

and the distortion may therefore propagate into earthquake source inversions performed using high–frequency data, and produce artificial features in the results. The effect on inversions using low–frequency data cannot be predicted by ray tracing and would require full numerical modelling of the wavefield, a complex and computer intensive process [see, for example, Igel (1999)].

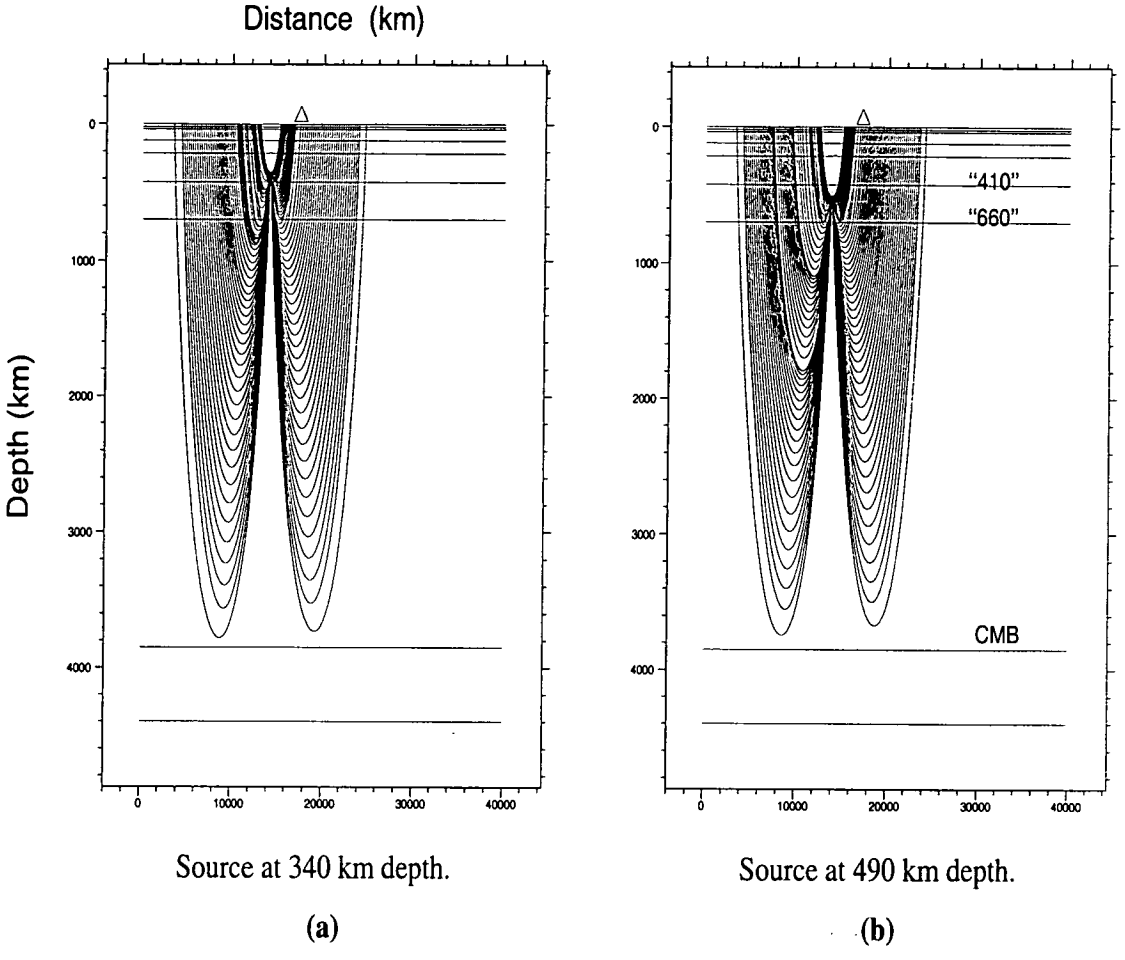

Figure 3.7.

Short–period ray paths from a seismic source in a two–dimensional slab velocity structure. The IASP91 global velocity model has been modified to include the velocity signature of a subduction zone, calculated from a thermal model of the Japan subduction zone, and converted to a cartesian coordinate grid using the earth flattening approximation of Müller (1977). **(a)** shows rays from a source at 340 km depth, **(b)** shows rays from a source at 490 km depth, both within the slab. Ray paths were calculated using the Gaussian beam method. for take–off angles between 0 and 90° from the downward vertical. The triangle at the top of each plot represents a receiver at 30° epicentral distance and the outermost rays reach a distance of approximately 100°. The model slab dips to the left at a true angle of 30° and the strike would be normal to the plane of the paper. Horizontal lines mark first–order velocity discontinuities in the IASP91 velocity model, and the 410 and 660 km seismically observed discontinuities are labelled, as is the core–mantle boundary (CMB).

3.7 Summary

The thermal structure of the Pacific lithosphere appears to reach a state of approximate thermal equilibrium, between conductive cooling and heat flux from the mantle, at an age of 90 Ma. It does not continue to cool indefinitely as predicted by a simple half–space cooling model. Thus, if the age of the Pacific lithosphere is to be used as a proxy for temperature, it should be capped at 90 Ma, as demonstrated in section 3.2.

A half–space cooling model, with an initial temperature of 1,350 °C, and which is limited to a maximum age of 90 Ma, provides a good approximation to the thermal models for lithosphere proposed by Parsons & Sclater (1977) and Carlson & Johnson (1994). Such a half–space model is used in the next chapter to provide an initial condition for models of the thermal structure of specific segments of subduction zones. As described in section 3.3, a kinematic description of the subduction zone is used as a constant boundary condition for an iterative numerical scheme which models the thermal evolution of the subduction zone from initiation to a steady state solution. It was shown in section 3.5 that a model of part of the Izu–Bonin subduction zone is in good agreement with independent seismic observations of displaced mantle discontinuities at that location, suggesting that the model does provide a good first–order approximation to the real thermal structure of that subduction zone.

Section 3.5 also demonstrated that the predicted positions of dehydration reactions *within* the subducting slab are relatively insensitive to uncertainties in the input parameters of the model. In contrast, the position of the same phase boundaries in the mantle wedge and overlying lithosphere are very sensitive to variation in the model input (see figure 3.5). This result is relevant to the interpretation of some of the results presented in section 4.6.

A thermal model of the Japan subduction zone was converted to a velocity model in section 3.6. Ray tracing through this velocity structure revealed the strong, non–linear focusing effect that a subducted slab may have on short–period radiation, which is relevant to results which are presented in section 6.3.

Chapter 4

The Rôle of Mineral Reactions in Seismogenesis

4.1 Introduction

Mineral reactions have been proposed as the mechanism by which to allow unstable sliding at unusually high pressure (see chapter 2 for a review of these arguments). In this chapter I use forward models of the thermal structure of subducted lithosphere to test two hypotheses. First, that deep earthquakes are caused by the dehydration of hydrous phases within the subducting slab. Second, that the depth of seismicity is limited by a critical temperature.

Investigating the rôle of temperature and pressure is important because it enables us to distinguish between the possibilities that seismogenesis is controlled either solely by a critical temperature or by the pressure–temperature (PT) locus of a mineral reaction. The method of Toksöz *et al.* (1971) (described in section 3.3) is used to estimate the spatial distribution of temperature within individual subduction zones. Experimentally determined equilibrium phase boundaries of subduction–related dehydration reactions are then superimposed on these models and the resulting loci of water release are compared with the distribution of earthquake hypocentres.

The double seismic zones of Japan and Shumagin (Eastern Aleutian Islands)

are investigated, as is unusually deep seismicity beneath the Izu trench. These locations form three case studies in sections 4.3, 4.4 and 4.5. A discussion of the individual results in relation to the generic dehydration hypothesis is given in section 4.6. In section 4.7, I use the thermal parameter concept of Molnar *et al.* (1979) to determine whether or not there is a simple relationship between the temperature of a slab and the maximum depth of seismicity. Finally, the thermal models are used to investigate how temperature limits seismicity with increasing depth (section 4.8) and also to investigate the extent to which it influences the location of the volcanic arc (section 4.9).

4.2 Dehydration Reactions

Hydrous minerals may exist in both the crust and mantle of oceanic lithosphere. Schmidt & Poli (1998) determined the phase assemblages of hydrated mid–ocean–ridge basalt (MORB) over a range of pressures and temperatures expected in subduction zones. A summary of their results is presented in figure 4.1. The stability limits of the most important hydrous minerals are shown but, for clarity, the different phase assemblages are omitted. Typically, basalt contains 5–6 wt% H_2O prior to subduction (Schmidt & Poli 1998). A variety of dehydration reactions are possible depending upon the exact PT conditions but, after the dehydration of amphibole and zoisite, only 0.1–1.1 wt% H_2O remains (Schmidt & Poli 1998), held in lawsonite. The decomposition of lawsonite with increasing depth marks the final dehydration of the subducting basaltic crust. Ono (1998) showed that, in cold subduction zones, a series of hydrous phases [in order of increasing pressure stability, phengite, topaz–OH and phase egg of Eggleton, Boland & Ringwood (1978)] will survive in the sedimentary layer of the crust to transition zone depths. However, the sediment layer experiences the highest slab temperatures and should be too weak to support the stresses necessary to cause seismic failure.

To determine the influence of water released from the basaltic crust in triggering intermediate depth seismicity, I calculated geotherms at a distance of 5 km perpendicularly below the slab surface for the coldest slab, Tonga; and Ryukyu, a relatively warm slab which exhibits seismicity to around 300 km depth. These

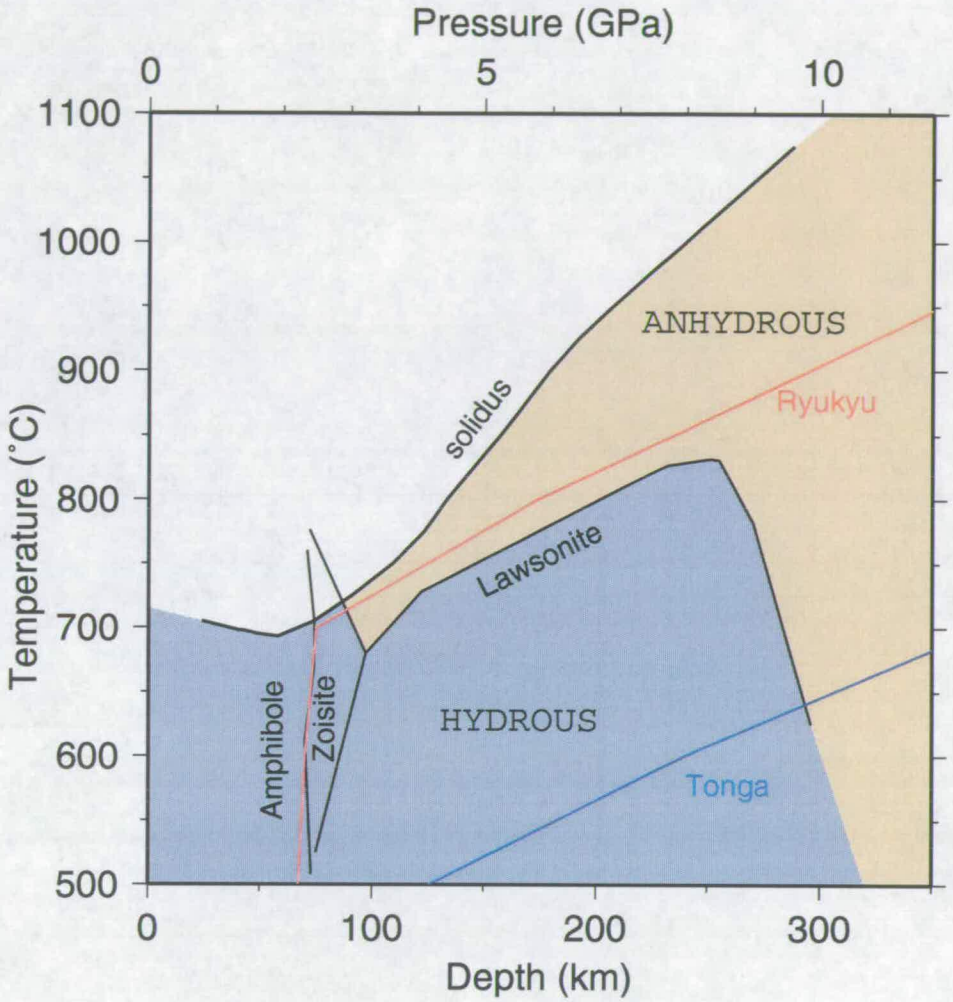

Figure 4.1.
Slab geotherms and their relation to the stability fields of hydrous minerals in the subducting basaltic crust. Phase diagram showing the stability limits of hydrous phases important in the subducting basaltic crust, as experimentally determined by Schmidt & Poli (1998). The linear phase boundaries are a function of the discrete sampling methods used in their experiments. Geotherms for the subducting crust, calculated in this study using the method described in chapter 3, at a distance of 5 km perpendicularly below the slab surface, are shown for Tonga (blue) and Ryukyu (red).

geotherms are also plotted on figure 4.1, illustrating the PT conditions experienced by the mid–crust during subduction. Ryukyu is sufficiently hot that lawsonite does not form on the breakdown of zoisite and so complete crustal dehydration is predicted to occur at a depth of around 100 km. In contrast, Tonga crust remains hydrated to the maximum pressure stability of lawsonite, at around 300 km depth. However, figure 4.2 shows that the patterns of intermediate depth seismicity are similar in each slab. The Tonga geotherm falls approximately 200 °C below anhydrous conditions at depths less than 300 km, a sufficiently large margin for this result to be robust with regard to errors in the thermal model. Errors in the Ryukyu geotherm mean that it could feasibly enter the lawsonite stability field, but the crust would still dehydrate completely at a depth above the deepest seismicity at 300 km owing to the negative Clapeyron (PT) slope of lawsonite dehydration reaction at high pressures. No change in seismicity pattern is apparent in either location, or at any other location studied, at the predicted depth of complete crustal dehydration. Thus, it appears that the occurrence of intermediate depth seismicity is not confined by and does not require the presence of hydrous minerals in the subducting oceanic crust. The current hypotheses of dehydration induced embrittlement do not require that earthquakes occur immediately following dehydration. Thus, if free fluids survive they may move and trigger seismicity away from the reaction boundary. However, this would require either saturation of the rock or very slow reaction kinetics for the absorption of water into nominally anhydrous minerals. The latter is unlikely, since the presence of water normally increases reaction rates, but it is possible that the former may occur in the slab, since the stable hydrous phases hold progressively less water with increasing depth. Hence, the above result does not exclude fluids as a cause of seismicity, but demonstrates that crustal dehydration reactions cannot cause directly all intermediate depth seismicity.

The subducting lithospheric mantle remains colder than the crust, and hydrous phases here can survive to greater depths. The dominant hydrous phase in the mantle in terms of both abundance and water content is serpentine. Experimental studies by Irifune *et al.* (1998), Frost & Fei (1998) and Shieh *et al.* (1998) delimit the stability fields of serpentine and the associated dense hydrous magnesium silicates stable at higher pressures. None of the studies used starting samples of natural mantle compositions, preferring instead samples of natural serpentine or

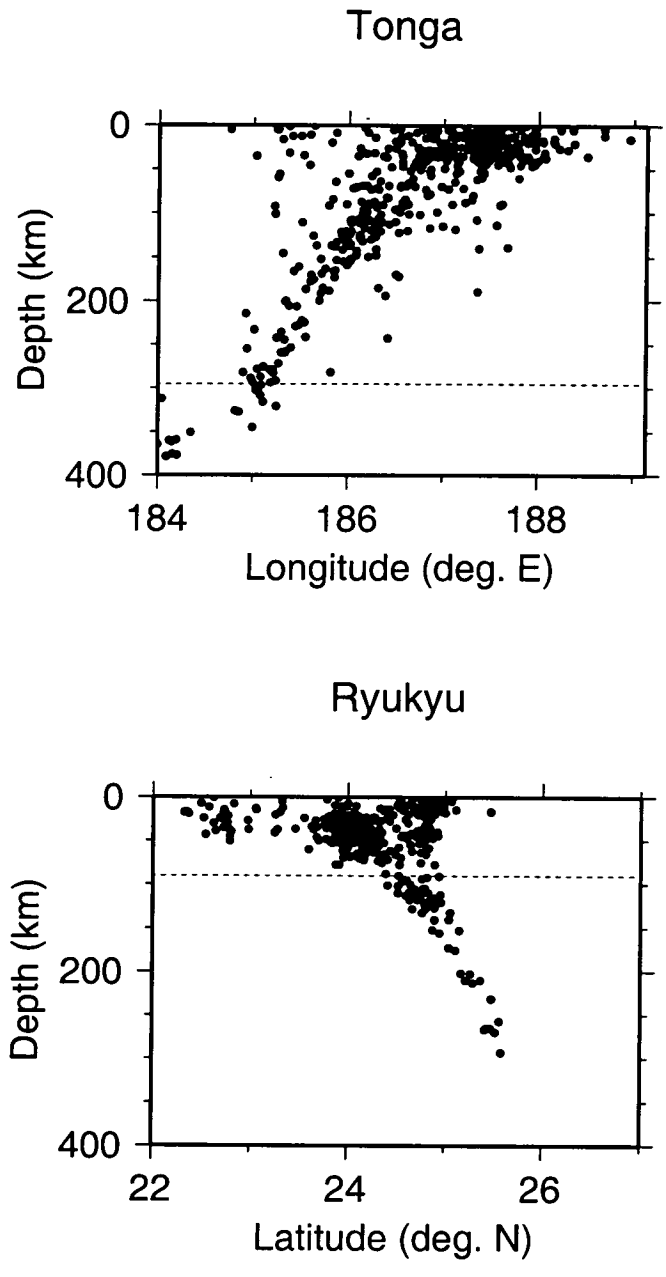

Figure 4.2.
Intermediate depth seismicity in Tonga and Ryukyu. Profiles showing earthquake hypocentres, plotted as black dots, from the EHB catalogue. In each case, the profiles are perpendicular to the strike of the subduction zone and extend over 1° along strike (122–123°E for Ryukyu and 15.5–16.5°S for Tonga). Dashed lines show the predicted depth of complete dehydration of the crust, taken from figure 4.1.

a synthetic mix of SiO_2 and $Mg(OH)_2 \pm MgO$. Thus, the results provide a general picture of the behaviour of hydrous phases in the mantle, rather than an accurate map of their occurrence in PT space. Figure 4.3 shows the phase diagram of Irifune *et al.* (1998), with superimposed slab geotherms for a distance of 15 km below the slab surface (i.e. in the lithospheric mantle). The three geotherms are from the Tonga, Shumagin and Sumatra thermal models. Although each geotherm is shown to a depth of 800 km, this is not intended to suggest that the model is reasonable to this depth. Tonga is the only one of the three slabs in which seismicity occurs in the mantle transition zone (~410–660 km depth). It is not known whether the other two slabs penetrate aseismically below the upper mantle or whether they accumulate atop the transition zone. Boyd & Creager (1991) used travel time residuals to suggest that the slab beneath Shumagin extends to 600 km depth. However, showing whether or not the slab was continuous or layered was beyond the resolution of their study. Any deviation from direct, constant velocity subduction must make the thermal models invalid below the depth at which it occurs.

Figure 4.3 shows that hydrous phases can be stable in the subducting lithospheric mantle even in the warmest slabs. For slabs which continue to descend, through the mantle transition zone into the lower mantle, hydrous phases in the lithospheric mantle remain stable beyond the depth of the deepest earthquakes. Thus, the hypothesis that dehydration causes deep seismicity is compatible with my calculated slab geotherms. This result is supported by the work of Frost & Fei (1998), who show phase D to be stable to even higher temperatures than those shown by Irifune *et al.* (1998).

To summarise, hydrous phases in the subducting lithospheric mantle can remain stable throughout the upper mantle and transition zone, for all slabs exhibiting intermediate and deep seismicity. However, this makes testing the dehydration hypothesis more difficult, since there is no predicted cessation of seismicity with depth (variation in one dimension alone). It is necessary, therefore, to examine well defined spatial patterns of seismicity (variations in two dimensions) to see if they correlate with the predicted loci of dehydration reactions. In this regard, it is useful to use intermediate depth double seismic zones, especially in Japan and the Aleutian Islands where local seismic networks improve the accuracy of

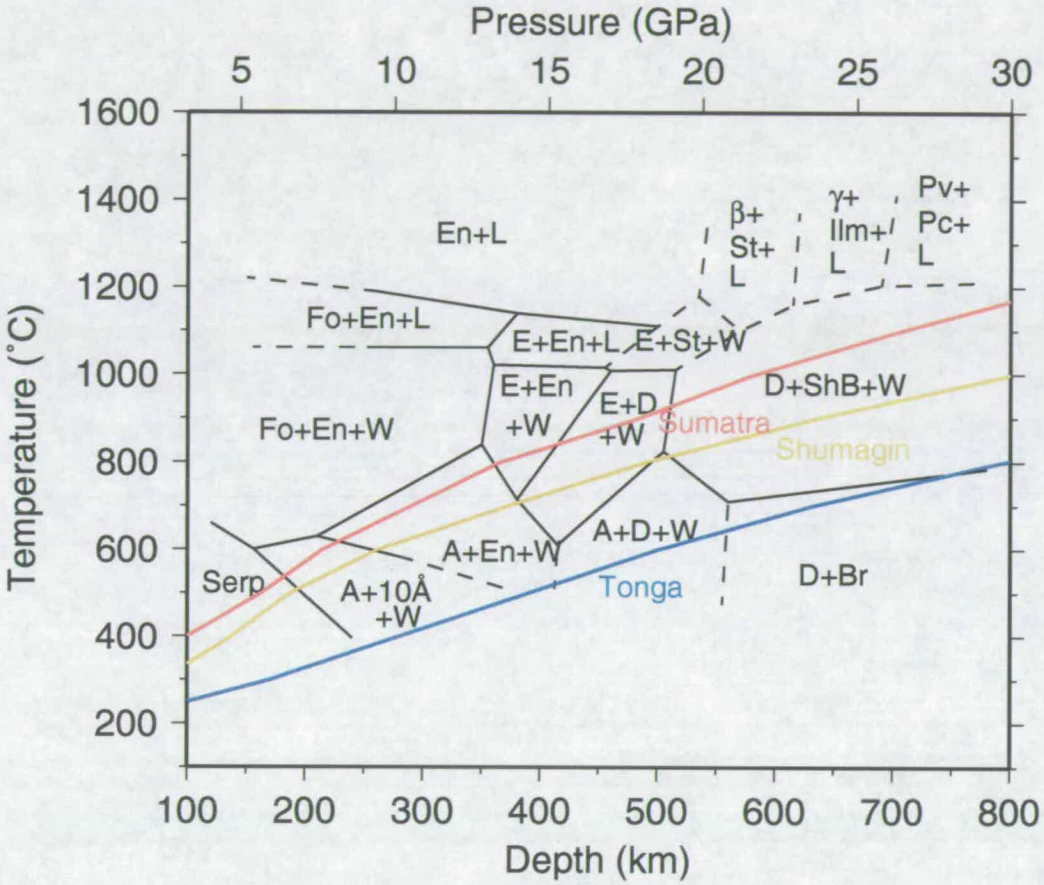

Figure 4.3.

Slab geotherms and their relation to mineral stability fields in the subducting lithospheric mantle. The experimentally determined phase boundaries of Irifune *et al.* (1998) are shown, determined using samples of natural antigorite (serpentine). Geotherms calculated at 15 km perpendicularly beneath the slab surface are shown for Tonga (blue), Shumagin (gold) and Sumatra (red) slabs. The phase abbreviations are: **Serp** serpentine; **Fo** forsterite; **En** enstatite; **W** water; **L** liquid (partial melt); **A** phase A (Akimoto & Akaogi 1980); **10Å** 10 Angstrom phase (Yamamoto & Akimoto 1977); **ShB** super–hydrous phase B (Gasparik 1990); **D** phase D (Liu 1987); **E** phase E (Kanzaki 1991); **Br** brucite; β wadsleyite (Ringwood & Major 1966); γ ringwoodite (Ringwood & Major 1966); **St** stishovite; **Ilm** ilmenite; **Pv** perovskite; **Pc** periclase.

earthquake location. For example, the convergent nature of some double seismic zones, notably in Japan, has led to the suggestion that they are caused by the progressive dehydration of a wedge of hydrous material located between the two planes of seismicity (Seno & Yamanaka 1996). Chlorite and serpentine are the two candidate minerals based upon their PT stability fields and natural occurrence. I plotted the equilibrium phase boundary for chlorite on thermal models for Japan and Shumagin and it bore little relation to the boundaries of the observed seismicity. The dehydration of serpentine does approximate the double seismic zone structure and is investigated in more detail in the following sections.

4.3 Japan Case Study

Figure 4.4 shows three sections perpendicular to the strike of the Japan subduction zone, with the thermal model, the maximum serpentine stability field (Ulmer & Trommsdorff 1995) and the seismicity distribution (from the EHB catalogue) for 1° latitude slices all superimposed. The convergence velocity is 9 cm per year, and all the input details for the model are listed in table 3.3. The double seismic zone is particularly clear in the southernmost (top) section of figure 4.4, but it is seen to some extent in all the sections. The equilibrium boundary of serpentine is shown by the blue line and it is clear that in all three sections the upper and lower planes of seismicity correspond well to this predicted locus of dehydration.

4.4 Shumagin, East Aleutian Islands, Case Study

In Shumagin, the observed double seismic zone is at a shallower depth than in Japan and earthquake locations from teleseismic data have greater scatter. I used earthquake locations from the East Aleutian Seismic Network, as given by Abers (1994, figure 6), which show a well defined double seismic zone beneath the Shumagin Islands. A convergence velocity of 7.5 cm per year (Creager & Boyd 1991), lithospheric age of 60 Ma (Minster & Jordan 1978) and slab dip of 42° were used. Lonsdale (1988) has shown that the age of subducting lithosphere through time at the trench is not constant, as might be expected, but is increasing. This

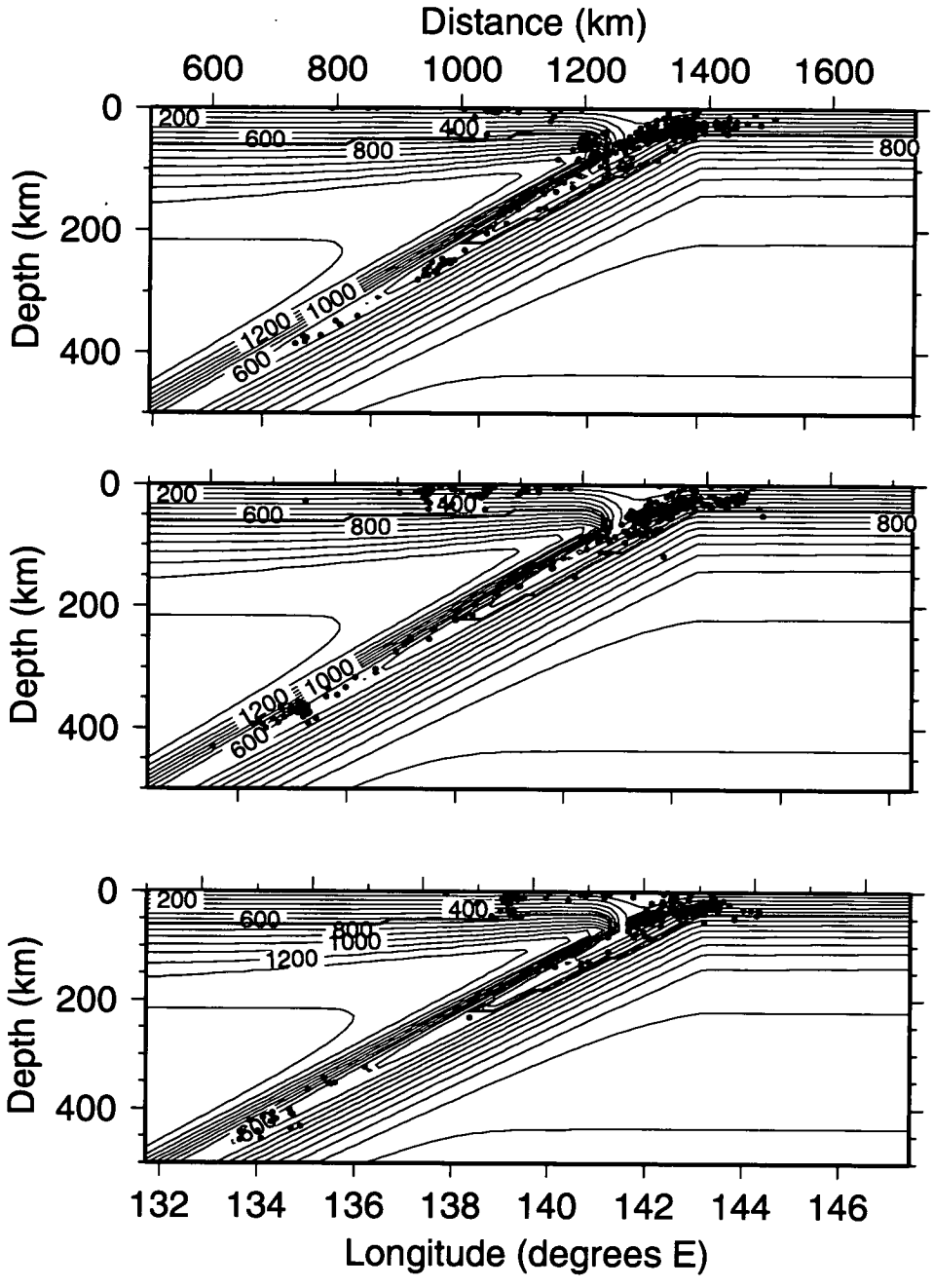

Figure 4.4.
Profiles through the Japan subduction zone. Each profile shows the modelled thermal structure, the predicted locus of serpentine dehydration and the distribution of seismicity. Black dots represent the earthquake hypocentres, taken from the EHB catalogue over 1° intervals of latitude. From top to bottom, the profiles show hypocentres from 36–37°N, 37–38°N and 38–39°N.

age variation was incorporated into a thermal model by Creager & Boyd (1991). Their minimum temperature geotherm for the Eastern Aleutians is in excellent agreement with mine, which assumes the age of the lithosphere at the trench to be constant at 60 Ma. This agreement implies that the variation through time of lithospheric age at the Aleutian trench does not exert a powerful influence on temperatures in the cold core of the slab.

Figure 4.5 shows the seismicity pattern and serpentine stability field overlain on the thermal model. The locations of the earthquakes relative to the slab are poorly constrained, so the seismicity is shown aligned with each side of the potentially hydrous zone. In each case, the plane of seismicity not coincident with serpentine dehydration is at least 200 °C colder than the equilibrium dehydration temperature. Given the shallow depth of < 150 km, and thermal gradients within the slab which are much lower than those near the slab–mantle interface, I suggest that this buffer of 200 °C is well outside the error bounds of the model. To check this, I altered the input parameters within reasonable bounds to produce a warmer slab model, but could not produce a significant thinning of the zone of serpentine stability. Even with a 30 km thickness of overriding lithosphere and a 50 km thick slab, the lower zone of seismicity is still significantly inside the zone of serpentine stability. The effect of the thin overriding lithosphere is to increase the temperature at a given depth in the mantle wedge. The temperature increase is sufficient that the lower zone of seismicity may be aligned with the lower limit of serpentine stability whilst a realistic maximum temperature of about 1,200 °C is present beneath the volcanic arc. However, this requires that the upper zone of seismicity occurs in the cold core of the slab, well away from any dehydration reactions. Independent information on the position of the earthquakes with respect to the slab would be useful, but they are too small, and hence insufficiently widely recorded, to allow the routine determination of their focal mechanisms or analysis of phases converted at the slab–mantle interface. In conclusion, it is very difficult to reconcile the Shumagin double seismic zone with the dehydration of a wedge of serpentinised mantle.

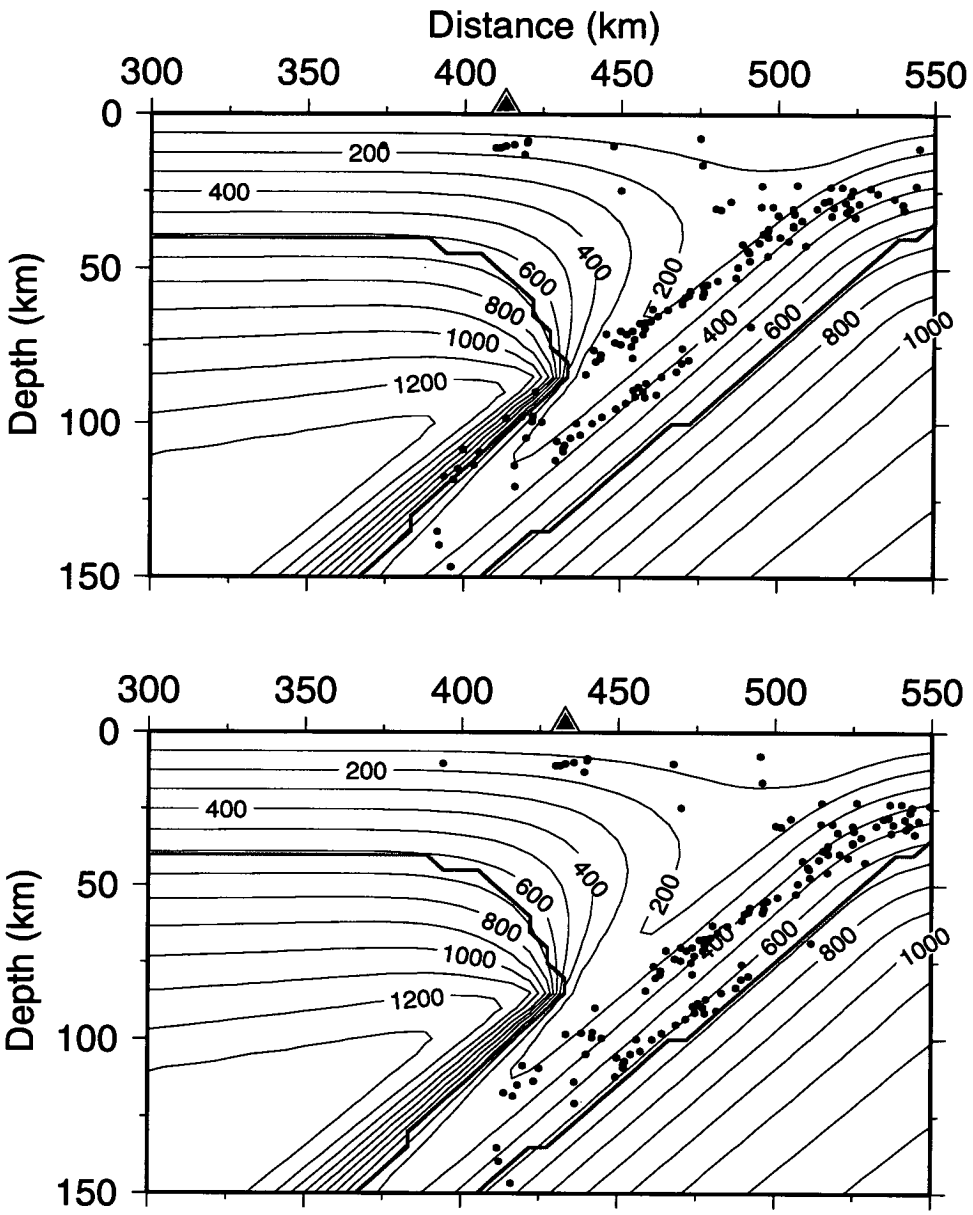

Figure 4.5.

Shumagin double seismic zone. Thermal model and superimposed seismicity for Shumagin, Eastern Aleutian Islands. The blue line shows the limit of serpentine stability and black dots are earthquake hypocentres from Abers (1994). The absolute locations of the earthquakes relative to the slab are not well known, so two possible relevant scenarios are shown — serpentine dehydration coinciding with the upper plane of seismicity (top) and the lower plane of seismicity (bottom). The profile is centred at 54°44'N, 162°W, and the location of the volcanic arc with respect to the seismicity is shown, for reference, by a red triangle.

4.5 Izu–Bonin Case Study

A population of earthquakes exists beneath the Izu trench which apparently occur at unusually high temperatures (700–1,200 °C), far outside the stability field of any hydrous mineral. This population is included in figure 4.6, which is a composite plot of the Izu subduction zone at 31–32°N (see figure 2.2 for the location). The convergence velocity here is less than for Japan and Shumagin, at 5.7 cm per year, and active back–arc extension is occurring, but its rate of 0.05–0.13 cm per year (Taylor *et al.* 1991), is smaller than the error bounds on the convergence rate and it is thus ignored. Earthquake hypocentres are from the EHB catalogue and clusters of events should have well constrained depths. A powerful constraint on hypotheses of intermediate depth seismogenesis would be provided by the unusually deep and, therefore, hot events beneath the trench area, if they are located correctly. The population is also seen if the locations of the Japanese Meteorological Agency (JMA) are used, determined using the Japanese regional network of seismometers. However, the 29 earthquakes are small, all with body wave magnitudes of 5 or less [as determined by the International Seismological Centre (ISC)]. They were not widely recorded at teleseismic distances, so the ISC solutions tend to have depths which have been fixed to be the same as the JMA depths. Travel time residuals in the ISC bulletin are large (up to 10 s) at teleseismic distances, whilst the local residuals are small. This apparent conflict between local and teleseismic times may be due to a considerable discrepancy between the local Jeffreys–Bullen (JB) model, used by the ISC, and the actual velocity structure of the north–west Pacific region, which would lead to mislocation of the earthquakes. This issue is examined in detail in appendix A.

By successfully modelling surface reflections, appendix A shows convincingly that one of the earthquakes from the anomalous population, the 8 July 1992 event, occurred within the oceanic crust, at a depth of around 6 km beneath the seabed. Other apparently deep events recorded at the arrays display similar complexity and arrival patterns and are also suggested to have occurred within the crust. Since the JMA depth estimates appear to have been based on predicted S–P times, we may conclude that the earth velocity models are insufficiently accurate to allow this to be a reliable method of depth determination in the north–west

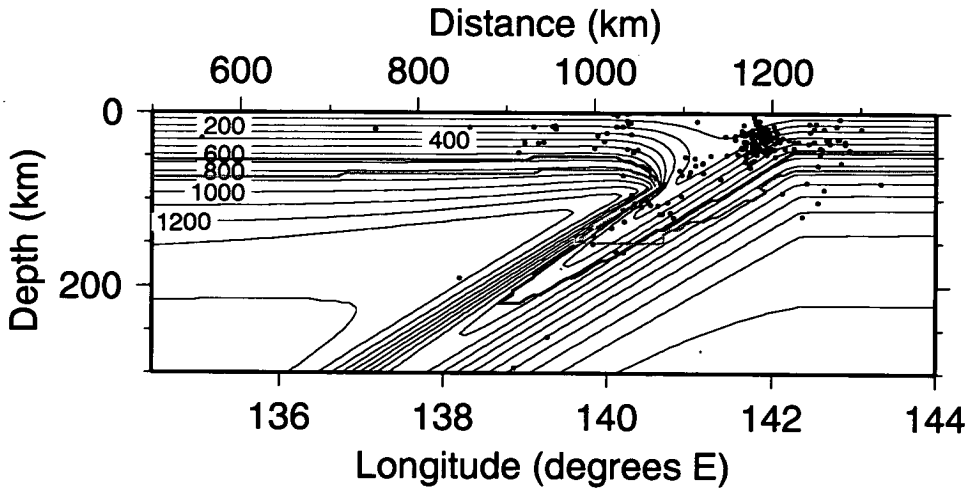

Figure 4.6.
Anomalously deep seismicity beneath the Izu trench. A 1° section of seismicity from the EHB catalogue (31–32°N) overlain on the relevant thermal model for Izu. Maximum stabilities of serpentine and chlorite are shown in blue and green respectively.

Pacific region. It is possible that all the surprisingly deep JMA hypocentres are a result of this systematic error. Equally, the EHB depth determination for 27 May 1992 has been shown (appendix A) to be the result of a phase mis–identification. Whilst occasional mispicks are an inherent part of the method (Engdahl *et al.* 1998, p727), it appears likely that, for a population of at least 10 events, the depth estimates are significantly in error. Strong water surface reflections and their multiples being identified as surface reflections seems the most likely explanation. Clearly, this population of events beneath the Izu trench almost certainly occurred at shallow depths and cannot be said to occur under hot, anhydrous conditions.

4.6 Dehydration–Induced Seismicity?

The case study of Japan shows that both the upper and lower planes of the double seismic zone are well modelled by the dehydration of serpentine. However, the Shumagin study shows that the double seismic zone there does not correlate with

serpentine dehydration. An alternative scenario is suggested by figure 4.5b, which shows that, if the lower plane of seismicity correlates with the stability limit of serpentine, then the upper plane would occur in the cold core of the slab. The applicability of this suggestion to Japan is investigated in figure 4.7. This is an enlarged plot of the top profile from figure 4.4, showing the statistical errors in the relative locations of the earthquakes. The true value of the relative errors will be somewhat larger than shown due to the difference between the complex subduction zone velocity structure and the assumed spherical earth model used to determine the locations. However, even taking this into consideration, it is clear that the earthquakes are well located and confirm that the double seismic zone is real. Despite the use of these hypocentres, it is not possible to distinguish confidently between the possibilities that the upper zone of seismicity corresponds to the cold core of the slab, the crust or surface of the slab, or to the limit of serpentine stability.

The lower plane of the Japan double seismic zone occurs around 40 km further into the slab than the upper zone. Water content of oceanic lithosphere at this depth is not well established, but a common viewpoint is that the oceanic lithosphere is hydrated only in the top 15–20 km [e.g. Thompson (1992)]. The impingement of water rich mantle plumes has been suggested as a mechanism for the hydration of the lithospheric mantle below this depth (Seno & Yamanaka 1996). The Cretaceous crust of the north–west Pacific is peppered by sea–mounts, a result of large amounts of past plume activity, so it is possible that the underlying mantle may have been hydrated by these plumes.

That the lithospheric mantle may be essentially dry appears equally feasible, with only small amounts of water bound in olivine and other nominally anhydrous minerals. To the best of my knowledge, there is no direct evidence of serpentinisation in the lithospheric mantle beneath the ocean basins. Minshull *et al.* (1991) showed that hydrothermal circulation can reach depths of at least 7 km in a fracture zone but, by its nature, this will be significantly more permeable than normal oceanic crust. Results from the Ocean Drilling Program (Juteau, Cannat & Lagabrielle 1990) proved the existence of serpentinised mantle near the slow–spreading Mid–Atlantic Ridge. However, analysis of seismic refraction profiles and laboratory measured seismic velocities by Carlson & Miller (1997)

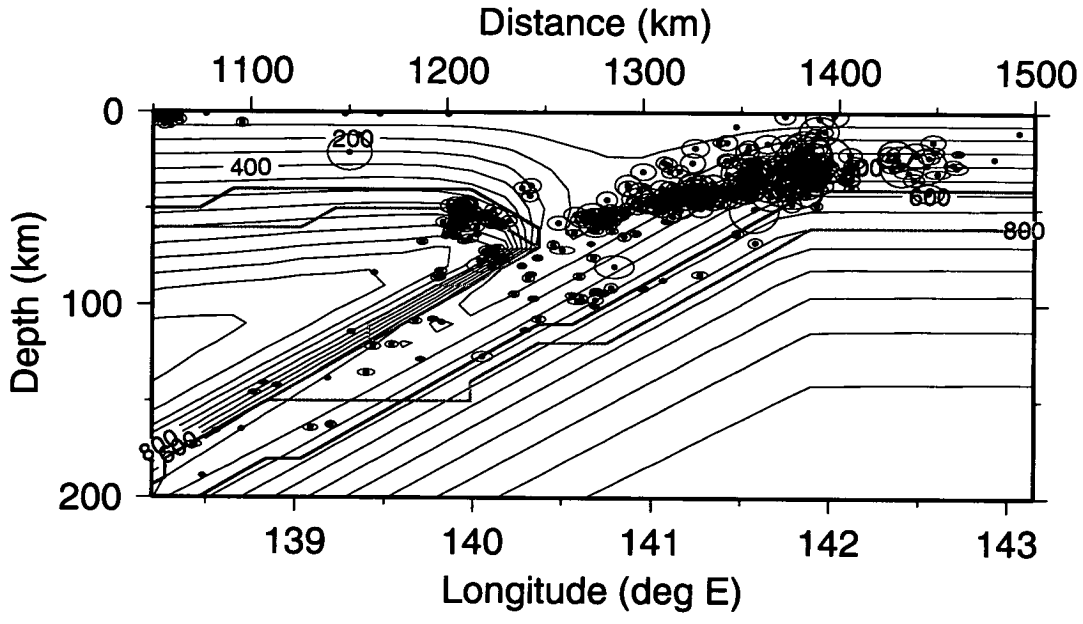

Figure 4.7.
Profile of the Japan subduction zone, showing earthquake hypocentres, thermal model and the predicted stability limits of hydrous minerals. The black dots are earthquake hypocentres from the EHB catalogue. Surrounding ellipses delimit the region of 95% confidence in the location, with respect to the surrounding seismicity. Maximum stability limits of serpentine and chlorite are shown in blue and green, respectively. The step–like, discrete nature of these limits is a function of the contouring technique and, in reality, they would be smooth. The profile extends for 1° along strike, 36–37°N.

demonstrated that serpentinite is not a volumetrically important constituent of the top 8 km of the Atlantic lithosphere. Owing to its more voluminous magma supply, the faster spreading Pacific plate should have a thicker, more coherent and probably less permeable crustal layer of basaltic composition, potentially reducing the depth of hydration by hydrothermal circulation. Observations of S–wave anomalies in the mantle transition zone adjacent to subduction zones have been interpreted as being due to the release of water from the slab (Nolet & Zielhuis 1994). Such water could not have survived in the basaltic crust (see figure 4.1), but may have been transported in the overlying sediment rather than the underlying mantle (Ono 1998).

Figure 4.7 also shows a concentration of seismicity directly above the slab, at 50–70 km depth. The earthquakes appear to occur only outside the stability fields of chlorite and serpentine. A strong seismic reflector above the subducting Nazca plate in Chile is interpreted by the ANCORP working group (ANCORP working group 1999) as being due to the accumulation of water against an impermeable barrier caused by the volume increase associated with the formation of serpentine in the overlying mantle. Following their results, it is a simple step to propose that the cluster of earthquakes in Japan is triggered by an increase in pore fluid pressure due to a similar accumulation of fluid released from the slab by dehydration. However, inspection of many seismicity profiles from all the major subduction zones has failed to find another convincing example of this phenomenon. Typically, seismicity above slabs extends to shallow depths and is more often than not confined to the region *within* which serpentine is stable. Thus, it appears that seismicity directly above the slab is probably not related to the occurrence of either hydration or dehydration reactions. Similarly, some earthquakes within the slab are located away from reaction boundaries. However, free fluids may survive and migrate if the local region is saturated, so they cannot be excluded as a possible explanation for intermediate depth seismicity.

To conclude, the results from the thermal modelling show that dehydration is not directly linked to the occurrence of intermediate depth earthquakes in the subducting slab. They provide no positive constraint on the hypothesis that deep (> 300 km) earthquakes are caused by dehydration. However, making the

assumptions that the experimentally determined DHMS phase boundaries provide a reasonable representation of their behaviour in a subducting slab, and that the slab subducts with approximately constant velocity and geometry, then some water will remain bound in hydrous minerals to at least the same depth as the deepest earthquakes (figure 4.3). The modelling provides no evidence in support of the hypothesis that earthquakes occurring in mantle above the slab are caused by increased pore fluid pressures, although this mechanism cannot be ruled out.

The hypothesis of dehydration–induced earthquakes fails to explain the observed spatial patterns of seismicity. The importance of temperature in limiting shallow seismicity [see, for example, Scholz (1990)] demands that its rôle in deep seismicity be investigated. In the following section, I examine the hypothesis that the maximum earthquake depth in a subducting slab varies as a linear function of slab temperature.

4.7 Thermal Parameter

Molnar *et al.* (1979) showed that the length of a Wadati–Benioff zone is proportional to the product of the square of the thickness of the subducting lithosphere and the convergence velocity. Assuming a half–space cooling model for the lithosphere, so that the square of the thickness was directly proportional to age and acted as an index of temperature, they defined the product of age and convergence rate as the thermal parameter, Phi (Φ). Φ varied linearly with the length of the seismic zone in different subduction zones. Later work (Kirby, Durham & Stern 1991, Kirby *et al.* 1996) used a larger database of earthquakes and determined convergence velocities from the NUVEL1 plate motion reconstruction (Demets *et al.* 1990). Φ was redefined slightly to be the product of the apparent vertical descent rate and age, the former being the convergence rate multiplied by the sine of the angle of dip of the Wadati–Benioff zone. Their results suggested a non–linear relationship between Φ and maximum earthquake depth. In slabs with $1,000 < \Phi < 5,000$ km, seismicity terminated at around 330 km depth. For colder slabs with $\Phi > 5,000$ km, seismicity terminated between 600 and 700 km depth.

There are two important limitations to these analyses. First, oceanic lithosphere often does not continue to cool indefinitely as a half–space, as shown in section 3.2. Second, in the later studies, the vertical descent rate of the lithosphere was calculated by multiplying the convergence rate by the sine of the average dip of the Wadati–Benioff zone. The thermal parameter thus calculated was then plotted against maximum earthquake depth within that subduction zone. The deepest earthquakes seem to occur in the coldest lithosphere at a given depth which, other parameters being equal, would have subducted with the steepest dip. The difference between steepest and average dip is small in many subduction zones (e.g. Tonga and Kermadec), but is particularly important in the case of Izu–Bonin, where both dip and depth extent of seismicity vary dramatically. Another possible complicating factor is the rate of trench rollback and back–arc spreading. This is incorporated into the convergence rate, but also affects the measure of rate of vertical descent of the lithosphere. If the point of subduction is moving oceanwards, then the observed dip of the Wadati–Benioff zone shallows, meaning that the vertical descent velocity is underestimated. Fortunately, the rate of trench roll–back is small compared to the rate of plate motion for present day subduction zones (with the possible exception of Tonga), so this effect is not usually significant.

Various models of cooling lithosphere were discussed in chapter 3. For the purpose of recalculating thermal parameters, I use 90 Ma as the age at which a half–space cooling model reaches a thermal structure approximating that of the Pacific oceanic lithosphere in thermal steady–state. This provides an upper bound to the lithospheric age used in the calculations. Subduction zone geometry is examined by plotting earthquakes from the EHB catalogue over 1° intervals along strike, thus associating the deepest earthquakes with the correct slab dip. Ages are from Müller *et al.* (1997) and convergence velocities are those calculated from NUVEL1 by Helffrich & Brodholt (1991), except for the rate for Kermadec, which is from Chase (1978). The thermal parameter of Tonga is the least well constrained (Wiens & Gilbert 1996). Tonga is the coldest slab and seismicity profiles show it deforming and layering at the base of the transition zone (Giardini & Woodhouse 1984), so simple models of its temperature become invalid at greater depth. Since Tonga has the largest thermal parameter of any present–day subduction zone, and the slab is warming whilst resting at a constant depth, the exact value of its

thermal parameter is not particularly significant to this investigation.

Figure 4.8 shows the results of Kirby *et al.* (1996) compared to the thermal parameters calculated in this study. The problem of using too great an age is unimportant for younger slabs so the parameters for these slabs calculated by Kirby *et al.* (1996) have been included on the new plot. The shift to generally lower values of Φ occurs as a result of capping the lithospheric age at 90 Ma. The new plot shows a number of points lying in between the distinct populations defined by Kirby *et al.* (1996). These are from the Japan and Izu–Bonin subduction zones, where dip and maximum depth of seismicity are variable. Apparent layering of the slab at the 410 km and 550 km mantle discontinuities is observed in parts of Izu–Bonin, so data were not taken from these areas (the observations of layering are discussed in section 7.2). Only sections of slab with undistorted, approximately planar Wadati–Benioff zones were used, ensuring that the temperature of the slab was proportional to depth, not the case for slabs which layer in the mantle and heat up whilst stationary at a constant depth.

The statistical significance of these results can be determined. For comparison, I shall examine first the characteristics of the results from Kirby *et al.* (1996), excluding the anomalous point for north Izu with $\Phi \approx 13,000$ km and maximum depth ≈ 350 km. Figure 4.9a considers intermediate depth and deep earthquakes to be separate populations, as proposed by Kirby *et al.* (1996). The least squares best fit lines, determined by linear regression, are shown, together with bounds which delimit the region within which we can be 95% certain lies the true best fit line[1]. Both populations can be fit by horizontal lines, in agreement with the hypothesis that seismicity terminates either at ~300 km or at ~700 km. However, no statistical validation has been presented to show that the results merit being divided into two populations. Considering them as a whole gives a correlation coefficient, **r**, of 0.78, a simple linear correlation significant at the 99% level[2]. Thus, the data are reasonably well fit by a linear relationship between thermal parameter and maximum earthquake depth (figure 4.9b). However, the level of significance is not a particularly appropriate criterion on which to judge the level at which the data fit a single linear relationship, since we know that maximum

[1]Determined using a t–test. See Kreyszig (1993, section 24.12) for details.

[2]The procedure for determining the significance of a correlation is described by Davis (1986).

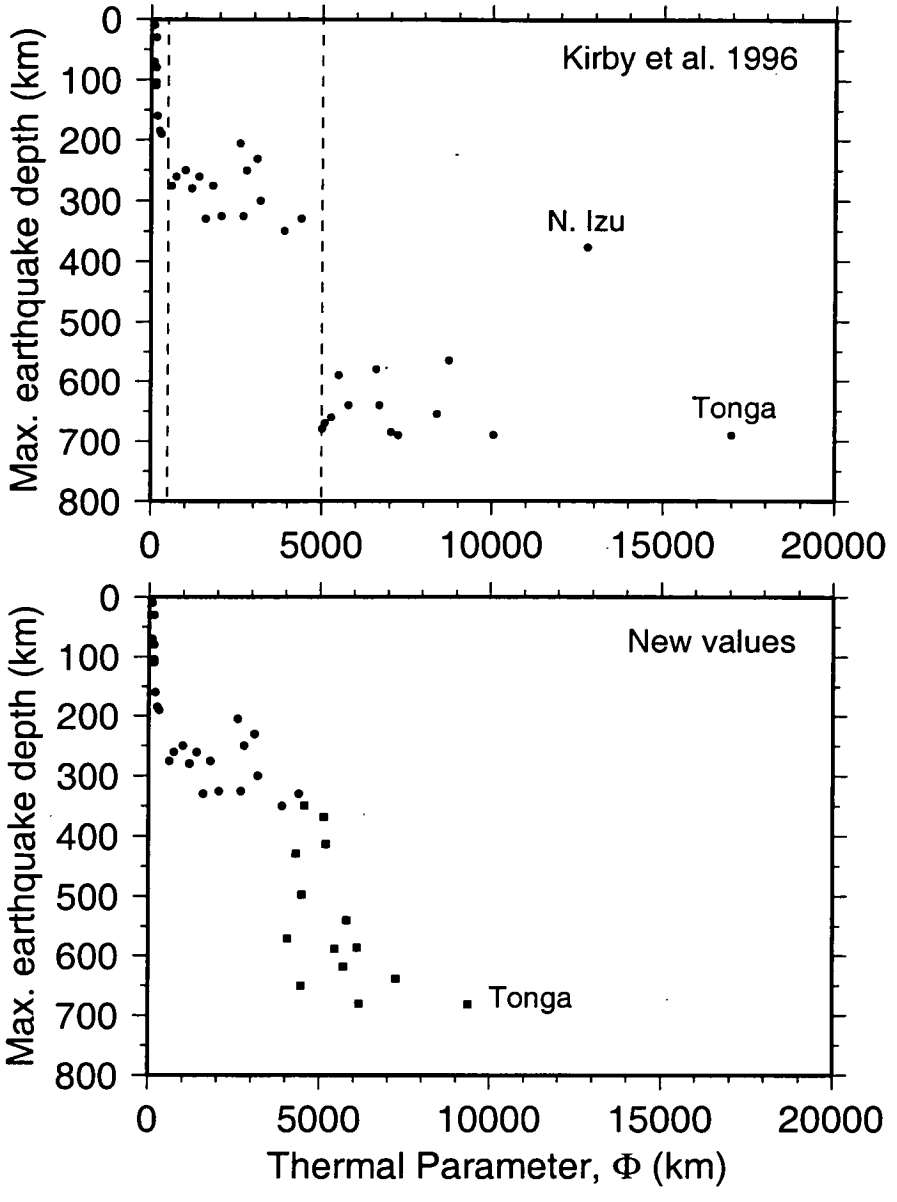

Figure 4.8.
Maximum earthquake depth as a function of the thermal parameter. The thermal parameter is a product of age and vertical descent rate. On the top graph, circles indicate the values calculated by Kirby *et al.* (1996) using the average dip and maximum earthquake depth observed in each separate subduction zone. Pecked lines mark their subdivisions into distinct populations. Points marked as squares on the lower graph were calculated using dips and earthquake depths from 1° segments of subduction zones and allowing a maximum age of 90 Ma (this study). Circles on the lower graph show the Kirby *et al.* (1996) results for hot subduction zones, which were not recalculated here, and are identical to the corresponding points on the upper graph.

earthquake depth does increase with the thermal parameter, and even a series of pressure–dependent horizontal lines on figure 4.8 may have a significant positive correlation. A more relevant statistic is the value of **r**, which determines to what extent the data points conform to a single linear relationship. The value of 0.78 shows that the fit is not especially good, introducing ambiguity into the interpretation of the thermal parameters.

Combining the intermediate depth data set of Kirby *et al.* (1996) with the results from this study, for subduction zones with deep seismicity, a similar analysis yields a higher correlation coefficient of 0.83. The best fit line is illustrated in figure 4.9c, again with 95% confidence intervals shown. A number of subduction zones have $\Phi < 500$ (see figure 4.8) and, as a separate population, these would have a best fit line considerably steeper than that for the population with larger values of Φ. However, considered as a single population, including the recalculated thermal parameters, the correlation coefficient is 0.90, showing that the population does conform to a simple linear relationship (figure 4.9d). These results show we cannot reject the hypothesis that maximum earthquake depth varies as a linear function of thermal parameter, and that this is the simplest interpretation of the results.

4.8 Critical Temperature Control on Seismicity

Shallow intraoceanic earthquakes do not occur at temperatures above about 600 °C (Denlinger 1992), which delimit the onset of crystal plasticity in olivine. Here I use the thermal models to estimate the temperature at which the deepest seismicity is occurring in several subduction zones. I assume that the deepest earthquakes occur in the coldest part of the slab. Figure 4.10 shows modelled minimum temperature geotherms and the maximum depths of seismicity. For the cases where seismicity terminates around 300 km depth, the predicted temperatures are ~600 °C. Where seismicity terminates near the base of the transition zone the predicted temperatures are ~700 °C. Errors in the model at this depth are large, with the possible range of temperatures probably varying between 600 and 900 °C.

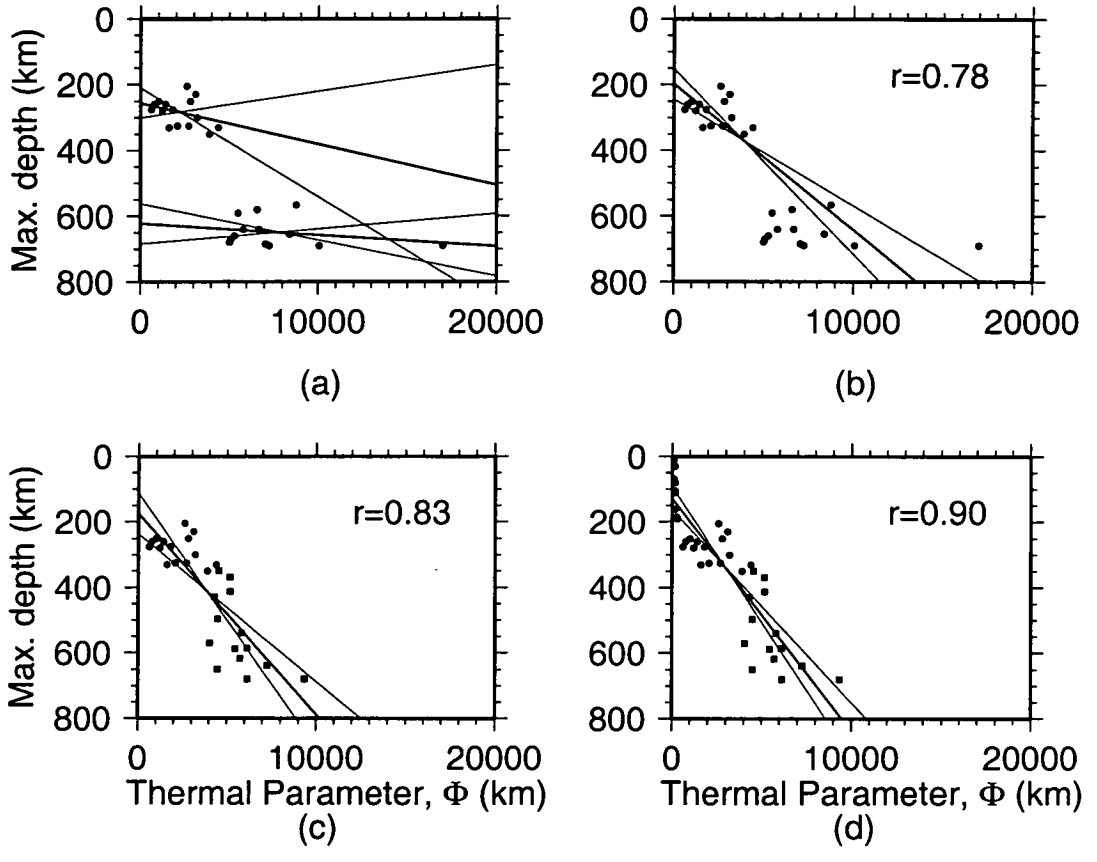

Figure 4.9.

Possible correlations between maximum earthquake depth and thermal parameter. Heavy lines show the least squares best fit, calculated by linear regression. Light lines delimit the regions of 95% confidence in that regression. **r** is the correlation coefficient, a measure of the extent to which the data conform to a linear relationship. **(a)** Two distict populations as defined by Kirby *et al.* (1996). Both populations may be fitted by horizontal lines. **(b)** Fitting the data in (a) with a single straight line. **(c)** A combined dataset of the thermal parameters calculated in this study (squares) and those of the intermediate depth population of Kirby *et al.* (1996) (circles). **(d)** Shallow and intermediate depth populations from Kirby *et al.* (1996) and the recalculated parameters for deep seismicity.

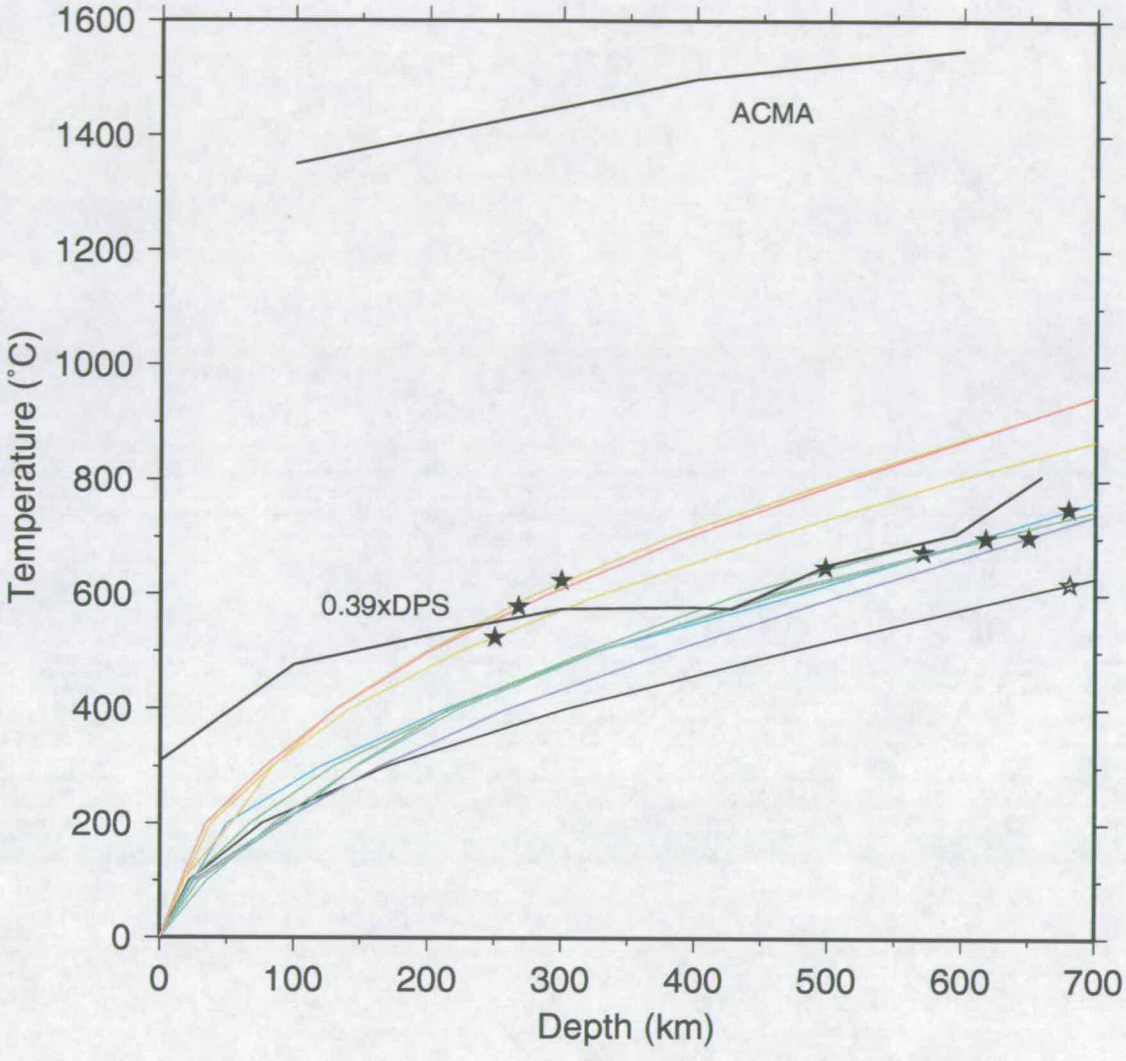

Figure 4.10.

Minimum slab geotherms and maximum earthquake depths. Each geotherm is colour coded for identification. From bottom to top, these are: Tonga (black), Kuril (dark blue), Mariana and Java (light blue), NE Japan (lime green), Izu 28°N (aquamarine), Izu 32°N (bright green), Shumagin (gold), Ryukyu (orange), Sumatra (red). Filled stars indicate the maximum depth of seismicity in each slab, the unfilled star for Tonga is to indicate that the slab layers at that depth and seismicity continues to higher temperatures. ACMA is the average current mantle adiabat (mantle geotherm in the convecting mantle) and 0.39×DPS is a fraction of the dry peridotite solidus, both after Thompson (1992).

In a study of the Aleutian subduction zone, Creager & Boyd (1991) showed that minimum slab temperatures at the maximum depth of seismicity coincided with 0.39 times the dry peridotite solidus[3] (DPS) as determined by Takahashi & Kushiro (1983). Their approach has been followed here, using a composite [due to Thompson (1992)] of more recent determinations of the DPS (Herzberg, Gasparik & Sawamoto 1990, Ito & Takahashi 1987, Scarfe & Takahashi 1986). Figure 4.10 shows that seismicity does not occur above a homologous temperature of approximately 0.39, in good agreement with Creager & Boyd (1991, figure 4). Errors in the model do not allow us to distinguish with absolute confidence between the hypothetical cases of seismicity being bounded by a constant absolute temperature and by a constant homologous temperature. However, given that the geotherms are minimum estimates of temperature, that the release of latent heat by the olivine–spinel transformation was ignored and that the true velocity of a slab probably falls in the transition zone, whilst the model assumes that it remains constant, then it seems likely that the estimated temperatures are a little low in the transition zone, as suggested by figure 3.6. If this is so, then the limiting temperature does increase somewhat with depth and is well modelled by a constant homologous temperature of about 0.4. The models do show robustly that the limiting temperature for seismicity does not increase rapidly with depth.

The assumption that the deepest earthquakes occur in the coldest part of the slab may be incorrect. If this is the case, then it is remarkable that seismicity always terminates when the core temperature of the slab exceeds about 700 °C. Such a situation would suggest that a cold, strong core resists deformation and allows stress to accumulate in the slab, leading to failure. A hot, weak core would allow the slab to deform in a ductile manner.

Figure 4.10 shows that the termination of seismicity is strongly temperature dependent. Remembering that the thermal modelling estimates temperatures not just in the subducting slab, but also in the surrounding mantle, it is now a simple matter to examine the extent to which temperature governs the location of the volcanic arc.

[3]The measure of temperature divided by melting temperature is known as the *homologous temperature.*

4.9 Location of the Volcanic Arc

The inclusion in the thermal models of induced mantle flow results in the generation of realistic temperature distributions in the wedge of mantle which overlies the subducting slab and is below the volcanic arc (see sections 2.2 and 3.3). Numerous workers have related the position of the volcanic arc to individual dehydration reactions causing melt generation, notably the breakdown of amphibole (Fitton 1971, Tatsumi 1986, Davies & Stevenson 1992, Inoue *et al.* 1998) and serpentine (Ulmer & Trommsdorff 1995). However, building on the ideas of Davies & Stevenson (1992), Schmidt & Poli (1998) prefer a scenario where the location of the volcanic arc is controlled by the position of a critical isotherm. They point out that the subducting slab contains several hydrous minerals which are present over a finite distance into the slab. High temperature gradients near the slab surface mean that the dehydration of any such mineral will occur over a considerable range of depths. Some of these phases dehydrate gradually through a series of reactions, and variations in composition also affect the PT conditions of dehydration. The cumulative effects of these factors led Schmidt & Poli (1998) to suggest that, whilst hydrous phases are still present, the release of water from the slab is continuous (although probably variable) with depth, a notion supported by Davies (1999). Thus, the mantle wedge directly above the slab is everywhere at least partially hydrated and the onset of partial melting is governed by its temperature. Schmidt & Poli (1998) postulate a critical isotherm of around 1,300 °C, based upon the inferred temperature of genesis for primitive island–arc magmas. The generalised thermal models for subduction zones of Davies & Stevenson (1992) and Furukawa (1993) are in approximate agreement with this hypothesis.

I tested the compatibility of the critical temperature hypothesis with my location–specific thermal models. The location of the volcanic front was determined from local highs in the ETOPO5 global topographic and bathymetric dataset[4], whilst

[4]Data Announcement 88–MGG–02, Digital relief of the the Surface of the Earth. NOAA, National Geophysical Data Center, Boulder, Colorado, 1988. Data available from http://www.ngdc.noaa.gov/mgg/global/seltopo.html.

Table 4.1.
Maximum predicted temperatures beneath volcanic fronts.

Location	Max. temp.	Dip	Min. depth to W–B zone
Japan 37°N	1200°C	28°	110 km
Izu 33°N	1200°C	33°	125 km
Tonga 20°S	1210°C	43°	90 km
Java 117°E	1260°C	40°	130 km
N. Chile 20°S	1230°C	27°	90 km
Aleutians 162°W	1200°C	42°	100 km

the thermal model was positioned to agree with the observed distribution of seismicity (from the EHB catalogue). Table 4.1 shows the maximum modelled temperatures directly beneath volcanic fronts from various subduction zones. Within the errors of the model, it is clear that all the volcanic fronts overlie mantle with an approximately constant maximum modelled temperature of around 1,200 °C. The depth to the Wadati–Benioff zone is well determined and exhibits considerable variation between 90 km and 130 km, suggesting that pressure alone is not a critical factor. The dehydration of amphibole is strongly pressure dependent so, for this reaction to be the source of fluids, the lateral transport of water through the mantle is required, a possible mechanism for which was described by Davies & Stevenson (1992). The volcanic fronts do lie approximately above the predicted onset of serpentine dehydration and this cannot be discounted as the controlling mechanism. However, the results are in excellent agreement with the critical temperature hypotheses of Davies & Stevenson (1992) and Schmidt & Poli (1998). The discrepancy in temperature between ~1,200 °C from my models and 1,300–1,350 °C from the genesis temperature of primitive magmas may be attributable to limitations in the simulation of mantle corner flow in the models used here. Indeed, reducing the thickness of the overriding lithosphere would remove much of this discrepancy without affecting the conclusion of a constant maximum temperature beneath the volcanic arcs. Alternatively, fluids may migrate laterally, as well as vertically, away from the slab to reach the hot mantle, and melt may migrate in the opposite lateral direction, a scenario suggested by Davies (1999) based on the predicted geometries of tensile fractures acting as conduits for the fluids. Equally, the most primitive magmas may be formed at greater depth and be focused towards the volcanic front as they migrate upwards.

4.10 Summary and Conclusions

Sections 4.2 through 4.6 showed that intermediate depth earthquakes are probably not directly related to the dehydration of hydrous minerals. Earthquakes at all depths appear to be strongly controlled by temperature. In section 4.7, it was shown that the depth extent of seismicity in a subduction zone may be governed solely by the minimum slab temperature. When a limiting temperature is exceeded, then seismicity will cease (section 4.8). It was shown from the thermal models that a homologous temperature equivalent to 0.39 times the dry peridotite solidus is a reasonable estimate of this limit. Not only is seismicity controlled by temperature but, in section 4.9, it was shown that the locations of volcanic arcs are compatible with a solely thermal control. Thus, temperature appears to be a critical governing factor within subduction zones.

All the work in this chapter has been based on predictions: the forward models of temperature distribution in subduction zones and the predicted behaviour of minerals in a complex environment at long time scales, extrapolated from experiments on simple starting materials at short timescales under laboratory conditions. Such work is valuable in helping us to distinguish between competing hypotheses. However, it is only ever as certain as the assumptions by which it is underpinned. In the following two chapters, I shall use one of the few methods of direct observation of subduction zones. Seismograms recorded at teleseismic distances from deep earthquakes will be used to constrain the physical processes happening at the earthquake source.

Chapter 5

Determination of Earthquake Source Characteristics: Methodology

5.1 Introduction

The hypothesis that deep earthquakes may be associated with mineral reactions implies that deep earthquake source mechanisms may include a volume change. However, no such change has yet been determined. In most cases, this is because the errors associated with a particular method are larger than the observed apparent volumetric component. However, in a study of the great Bolivian earthquake of 1994, Okal (1996) used very long data records (nearly 117 days) to jointly invert the fundamental and first normal modes (time period greater than 500 s) and constrained the volume change to be less than 2% of the total seismic moment. Hara, Kuge & Kawakatsu (1996) examined four more deep earthquakes using normal modes and concluded that the maximum volumetric component was less than 5%. However, they used very short data records of 10 hours or less, which is insufficient for proper sampling of the normal modes and may have increased the error bars beyond those quoted (Okal 1996).

Routine moment tensor inversions often show constant volume non–double couple mechanisms, consistent with a finite amount of pure shear. Such mechanisms

may be providing information about the source, or may be an artefact of the inversion, possibly caused by unmodelled, large scale velocity heterogeneity. A moment tensor inversion assumes that the observed wavefield radiated from a point source. However, earthquakes occur on fault planes of finite extent and extra information about the source can be obtained by assuming an "extended source" model. In this study, both point source and extended source methods are used to provide a kinematic description of the deep earthquake source.

Successful determination of earthquake moment tensors has been achieved by the application of many different methods to the inversion of various types of seismological data. The solutions most widely used in the literature are Harvard University's automated, routine inversions using the Centroid Moment Tensor (CMT) method of Dziewonski, Chou & Woodhouse (1981) and Dziewonski & Woodhouse (1983). The CMT method uses a least squares inversion procedure to match simultaneously the observed body wave arrivals and coda at time periods in the range 45–100 s, and the observed surface waves at periods greater than 135 s, with synthetic seismograms. The inversion is normally stabilised by forcing *a priori* the volumetric component to be zero. This approach is sensible for a whole waveform method, since the body wave coda contains large amounts of shear wave energy, which is not excited by a volumetric source component, and so only a relatively small amount of information is available about this source component (Stimpson & Pearce 1987). However, Kawakatsu (1991) showed that, for earthquakes recorded at a wide range of azimuths and epicentral distances, full moment tensors could be obtained by using the CMT method. The results of his analysis of 19 deep earthquakes are shown in figure 5.1. Circles show the least squares solutions and the error bars are at the 95% confidence level (two standard deviations away from the best fit). A source mechanism with no volume change falls within the error bars for all 19 events and the least squares solutions show no systematic trends. Thus, the deviations of the least squares solutions from a constant volume source are statistically insignificant and may be attributable to random errors.

Kikuchi & Kanamori (1994) used both the P–wave coda and the radial component of the 1,226 s period normal mode to investigate the volumetric component of the

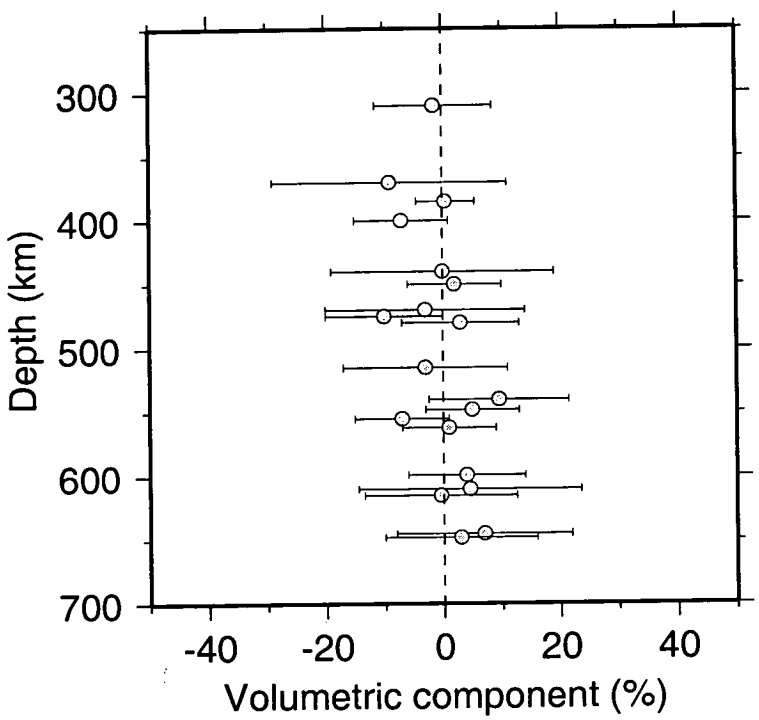

Figure 5.1.
Volumetric source components from CMT inversions. The results of Kawakatsu (1991) are shown, with volumetric component plotted against depth. Circles represent the volumetric component of the least squares CMT solution and the error bars indicate two standard deviations, or the 95% confidence limit, for these solutions.

great Bolivia event. Their body wave moment tensor inversion revealed a best–fit mechanism with a 10% implosive component, whilst the very–long–period analysis constrained $|k|$ to be less than 2%, in agreement with the normal mode analysis of Okal (1996). Kikuchi & Kanamori (1994) suggested that the apparent 10% volume change shown by their body–wave inversion may be an artefact of an insufficiently accurate earth model, but also speculated on the possibility of a time–variant, and hence frequency–dependent, moment tensor. This latter idea seems unfeasible, since both inversions assume a point source and hence determine the temporally averaged character of the source.

Analysis of normal modes has tightly constrained the volumetric component of the largest deep earthquake ever recorded. However, such an approach yields much less constraint when applied to smaller events (Okal 1996). Also, if deep earthquakes have a nucleation phase which includes a constant volumetric component, then this may represent a greater fraction of the moment release for a smaller event, and so be more easily detected from the pattern of radiation. To determine whether the lack of volume change associated with the Bolivia earthquake is typical of other deep events, a method is required which provides tight constraint on the volumetric component of smaller earthquakes. Previous work (Stimpson & Pearce 1987, Stimpson 1987*a*) using the relative amplitude method (Pearce & Rogers 1989), which uses the direct P–wave and its surface reflections, has demonstrated the powerful capability of this body–wave technique to constrain the volumetric component of the source, and it is applicable to events of any size. In chapter 6, I undertake a systematic study of deep earthquakes using the relative amplitude method. In this chapter, I discuss the method and necessary adaptations for its use in sections 5.2 to 5.6. A dynamic earthquake source cannot be described by a time invariant moment tensor alone and, in section 5.7, I describe a time domain method, due to Pearce & Stewart (1989), of estimating the rupture velocity and geometry of a source by analysing variations in pulse duration.

5.2 The Relative Amplitude Method

The type and orientation of a seismic source is reflected in the wavefield it generates. Perfect knowledge of the wavefield over a sphere immediately surrounding the source, the *focal sphere*, would in principle allow unique moment tensor inversion. In reality, we observe only the wavefield at the surface of the earth, after it has interacted with, and been altered substantially by, the earth's velocity and density structure. Much of this interaction is predictable and can be accounted for by the use of spherically symmetric earth models. However, the effects of lateral inhomogeneities, which are known to exist from the results of three–dimensional seismic tomography studies [e.g. van der Hilst *et al.* (1991)], remain largely unmodelled at present and introduce an added degree of noise into the inversion. Such effects can be minimised by using the *relative* amplitudes of two phases which have travelled similar paths and have therefore experienced approximately the same earth structure. Douglas *et al.* (1974) and Cullen & Douglas (1975) showed that the relative amplitudes of P and its surface reflections, pP and sP (figure 0.1), provide constraint on both the type and orientation of a seismic source. A formalised method of moment tensor inversion using these phases was developed (Pearce 1977, Pearce 1979, Pearce 1980, Pearce & Rogers 1989), known as the Relative Amplitude Moment Tensor Program. Henceforth, this will be referred to as the *relative amplitude method.*

The relative amplitude method depends upon the fact that moment tensor solutions are capable of describing any source that can be decomposed into a sum of nine force couples, derived from three orthogonal force dipoles. The theoretical radiation pattern of any such source is known, allowing values of the amplitude ratios and polarities on the focal sphere to be calculated for discrete values of T, k, σ, δ and ψ. For shallow sources, the P, pP and sP far field ray paths are so nearly identical that they are indistinguishable on a global cross–section showing the full ray path from source to receiver. Thus, they have truly sampled similar below source structure and the influence of this structure will be removed very effectively upon division. The observed amplitudes of these phases are assigned error bounds, within which the true amplitude must lie, and these bounds are compared to predicted relative amplitudes for a range of source types and orientations. Uncertainties in the measurements of amplitudes are introduced by

interference with other phases, background noise and differences in pulse morphology. If the polarity of a phase is unambiguous, then it is also specified. The amplitude of sP is further affected by a number of factors. The relative excitation of S to P radiation at the source is governed by the ratio of P– and S–wave velocities at the source (see section 5.4), which is poorly known because of the steep velocity gradients across subduction zones. Also, the reflection coefficient for S varies strongly with angle of incidence, magnifying the effect of small errors in the ray geometry, and shear energy attenuates more readily than compressional energy, especially in the presence of fluids, possibly leading to smaller amplitudes than would be predicted. Thus, wider amplitude bounds must be routinely allocated to the sP phase than to P and pP.

The name "relative amplitude method" may lead to some confusion since, in some cases, it is not the amplitude of a phase which is actually measured. For short period records of small earthquakes, then the amplitude observed on the seismogram is a fair representation of the amplitude predicted by a point source, hence this is the quantity which is measured. However, a broadband or long–period recording of a large earthquake will show individual phase arrivals which extend over many seconds, often with different pulse morphologies and durations at different locations. Such variation is caused largely by asymmetric rupture on the fault plane (which is discussed in section 5.7) and means that the observed amplitudes may not be the same as those predicted for a point source of the same mechanism. For a finite source, it is the *area under the pulse* which should be compared to the amplitude of a pulse from a point source. To continuously distinguish between the cases of amplitude and area is both laborious and somewhat confusing. In this study, the eight earthquake analyses presented in chapter 6 were all performed using areas measured from broadband and long–period data. The focal mechanism determination in Appendix A used amplitudes from short period array records. Henceforth, I shall refer only to amplitudes and amplitude bounds. When applied to measurements from broadband or long–period data, these terms will imply the use of pulse areas rather than amplitudes.

Ray tracing through a standard earth velocity model is used to map the amplitude observations at a receiver back to the appropriate location on the focal sphere. The amplitude bounds of the surface reflections are multiplied by a constant to

correct for the effect of energy loss experienced along their greater path length compared with that of the P–phase (see section 5.6 for details). The relative amplitude ranges and polarities are then compared to those calculated for the full range of different source types and orientations. Some of the predicted values will be incompatible with the observations and the corresponding sources are discarded. The remaining sources are then tested against data from another station, until the range of sources compatible with all the observations is found. Owing to the use of *relative* amplitudes, no determination of the earthquake moment is made. Thus, we invert for only five free parameters (two to describe the source type, three to describe its orientation), all of which are independent (Dufumier & Rivera 1997). The results can be rescaled by an independently determined scalar seismic moment to obtain full moment tensors where required.

In some cases, there may be no solutions which are compatible with all the data. Such a situation may be the result of several causes. Each of the five variables, T, k, σ, δ and ψ (defined in section 2.3) are continuous, so there are an infinite variety of possible source types. To forward model the characteristics of these sources, it is necessary to discretise the source type space and compute models at regular intervals within it. Since this space consists of five dimensions, a large number of calculations are required. With current computing capabilities and without adapting the code, it is possible to search for compatible solutions in all of source space at intervals of 5% in T and k and of 5° in the orientation parameters σ, δ and ψ. To search at higher resolutions, it is necessary to first limit the amount of source space, thus requiring *a priori* knowledge about the source. Initial searches at a coarser interval can provide such a constraint. As smaller search intervals are used, the probability of a population of compatible source types not coinciding with a grid point is reduced, but always remains finite. Experience has shown that intervals of 5% in T and k and of 5° in the orientation parameters tend to identify most of the populations of compatible source types, although the shape of the populations in source type space is not always well delimited at this level of resolution.

A more common cause of incompatible observations is the incorrect interpretation of a seismogram. Mis–identification of a phase as a surface reflection will most likely lead to the use of amplitude bounds which are not predicted by any of the

sources compatible with the rest of the data. For deep earthquakes, this problem is of minimal importance, since the long time separation of phases makes identification a relatively simple matter. The final possible explanation for incompatible observations is that the observed wavefield does not correspond to that predicted for any source type described by a sum of force couples (a "dipole source"). This may be as a result of distortion of the wavefield by unmodelled velocity structure, or of a source process including a single force or torque [e.g. Takei & Kumazawa (1994)].

5.3 The Importance of Directivity

A propagating rupture front that does not expand concentrically on a circular fault plane will give rise to azimuthal variation in the frequency content of the radiated P–waves, as first observed by Bollinger (1968). Owing to the Doppler effect, waves recorded in the direction of rupture will be of a higher frequency (blue–shifted), whilst those propagating in the opposite direction will be of a lower frequency (red–shifted). This effect has implications for the use of band–limited seismic records, where the proportion of energy which is recorded may vary with azimuth and epicentral distance. I investigated the magnitude of this effect using the following relationship between the observed (f_o) and true (f_s) frequencies:

$$f_o = \frac{V - V_o}{V - V_s} f_s. \tag{5.1}$$

V_s is the rupture velocity of the source, V_o is the velocity of the observer which, in this case, is zero, and V is the phase velocity. Considering a rupture propagating at $5\,\mathrm{km\,s^{-1}}$ towards a receiver (although not *directly* towards it, for then the receiver would lie on a nodal plane and would not record the P–phase!), the low–pass filtered record for periods greater than 20 s will only show waveforms of a true period of more than 40 s. There is an apparent shift of energy to higher frequencies, reducing the amplitudes on long period records. If the rupture was propagating away from the receiver, then more energy would be recorded at

lower frequencies, increasing the long period amplitudes. The effect of directivity is greatest for a line source in a vertical fault plane in which the rupture propagates in a vertical direction, for then P and the surface reflections experience Doppler effects of approximately equal magnitude but of opposite polarity. For a circular source, Doppler effects still occur but they are of similar magnitude and of common polarity and hence cancel out when amplitude ratios are calculated.

The relative amplitude method assumes a point source where, by definition, directional effects are not considered. Therefore, any variation in amplitude due to source directivity may propagate as a systematic error in the moment tensor determination. To eliminate this possibility, I chose initially to use records from digital broadband stations, which have a sufficiently wide frequency response to ensure that all the arriving energy is recorded. If band limited records are used, then wider amplitude bounds must initially be applied, until the ellipticity of the source has been determined and the magnitude of any potential Doppler effects can be evaluated.

A propagating fracture behaves as a point source only at wavelengths much greater than the maximum dimension of the source (Kostrov & Das 1988). Thus, at shorter wavelengths (higher frequencies), the observed full waveforms from large earthquakes will not be compatible with any of the source types which may be represented by the full moment tensor. This presents a problem with the use of broadband data, which includes the highest frequencies radiated by the source. At wavelengths less than or equal to the source dimension, the amplitude of a phase observed in the far–field is dependent upon the integration of multiple sources across the fault plane. For a horizontal or vertical fault plane, the take–off angles of P and pP are approximately equal (measured from the downwards and the upwards vertical, respectively), so the integrals are of approximately equal value since the phases have the same geometrical relationship to the source. Thus, the relative amplitude method should remove this problem because the integrals cancel out when the amplitudes are divided. Deep earthquakes in the mantle transition zone tend to have horizontal and vertical nodal planes [e.g. Estabrook & Bock (1995)] and so allow this idea to be tested. The relative amplitude method was designed for use with short–period data from small earthquakes, which have sufficiently small fault planes to satisfy the point

source approximation (Pearce 1977). It has never before been applied to large earthquakes using broadband data, so the broadband analyses presented in the following chapter are a new extension of the technique.

5.4 Rheological Considerations

To forward model the distribution of P, pP and sP amplitudes across the focal sphere, it is necessary to fix the relative excitation of shear and compressional waves in the source medium. This is determined by the values of the Lamé parameters, λ and μ (μ is also known as the shear modulus). For a Poisson solid $\lambda = \mu$ and the P– and S–wave velocities are related by $V_s = V_p/\sqrt{3}$. Global velocity models for P and S are independently determined from travel time data and so provide a measure of whether or not the earth behaves as a Poisson solid. Figure 5.2 shows the V_s profile from the IASP91 model, together with the profile of $V_p/\sqrt{3}$. Below the crust, $V_s < V_p/\sqrt{3}$, showing that the mantle does not behave as a Poisson solid. A general value for the relative excitation of shear to compressional radiation is given by $(V_p/V_s)^3$ [derived from Pearce (1980, appendix A)], thus it is important that we know both the S– and P–wave velocities at the source independently, rather than assuming a Poisson solid, so that this formulation can be used.

The occurrence of deep earthquakes in subduction zones, where the lateral velocity structure varies strongly, means that estimates of velocities at the source are subject to considerable errors. The source layer velocity may vary with the frequency of the radiation, with long wavelengths sampling a greater range of velocities within their first cycle. In view of these uncertainties, and the domination of deep earthquake spectra by low frequencies, the P– and S–wave velocities from the IASP91 model at the source depth are used as estimates for the source layer velocities. The influence of source and surface layer velocities upon the results of the inversion is investigated in section 6.3.

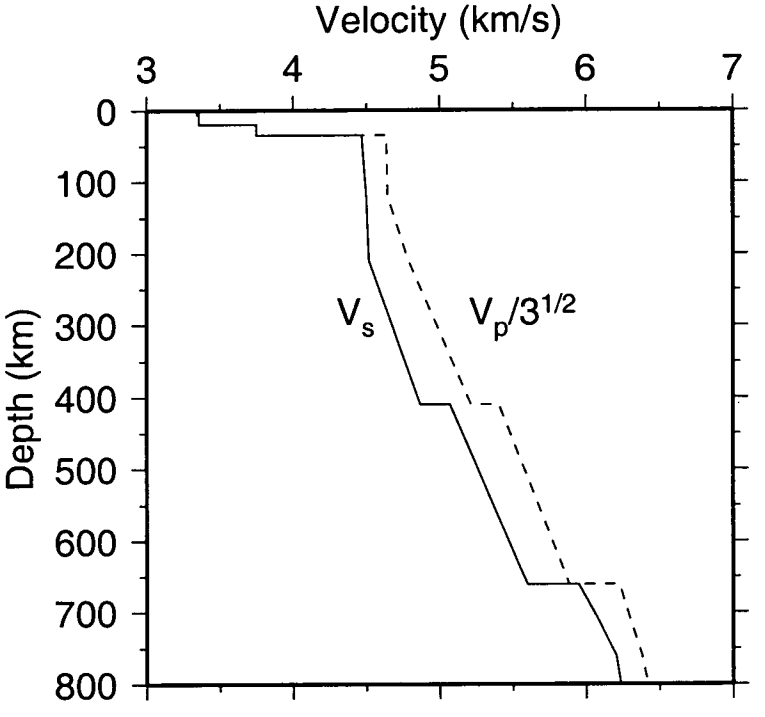

Figure 5.2.
Velocity profiles from the IASP91 earth model, for the crust, upper mantle and transition zone. The solid line shows the variation of the S–wave velocity with depth. The dashed line represents the S–wave velocity predicted for a Poisson solid from the model P–wave velocity.

5.5 Geometrical Adaptations Required for the Analysis of Deep Earthquakes

The application of the relative amplitude method to deep earthquakes invalidates some of the assumptions which are made when investigating shallow earthquakes. Figure 5.3 shows the geometry of P and pP waves leaving a 600 km deep source. α is the take–off angle of P, γ the take–off angle of pP and i its angle of incidence at the surface, also known as the emergent angle. The relative amplitude method is based upon the observation that P and the surface reflections have convergent ray paths which are separated by a small distance and hence sample essentially the same below source earth structure. Whilst this is a good assumption for shallow earthquakes, it is not the case for deeper sources, since the direct P–wave and the surface reflection paths may be up to 600 km apart in the lower mantle. This separation of paths means that each phase will experience a somewhat different amount of attenuation along its path and the use of relative amplitudes will not entirely remove the influence of path effects from the inversion for source parameters. Compensation for this possible source of error is made by assigning suitably wide amplitude bounds to the observations. For the data used in this study, the upper amplitude bound for P is typically a factor of two larger than the lower bound. Such bounds are wider than would be applied to phase observations from shallow earthquakes given data of equal quality [e.g. Douglas *et al.* (1999)], leading to a potential loss of resolving power in the data. However, large, deep earthquakes are recorded widely and the different phases are usually well separated in time, providing high quality, well distributed data at teleseismic distances. Thus, the loss of resolution due to the imposition of systematically wide amplitude bounds is balanced by the use of numerous clear observations.

The geometry associated with deep sources also invalidates three further assumptions which are usually made regarding the ray path near the source. To calculate the reflection coefficient of the free surface, it is necessary to know the angles of incidence of the upgoing legs of the pP and sP phases. For shallow focus events, good approximations are: (i) $\alpha = \gamma$; and (ii) $i = \arcsin[(V_{surf}/V_{srce})\sin(\gamma)]$, where V_{surf} is the surface velocity and V_{srce} is the velocity at the source. α and γ are very similar because the source and the pP bounce point at the surface are in

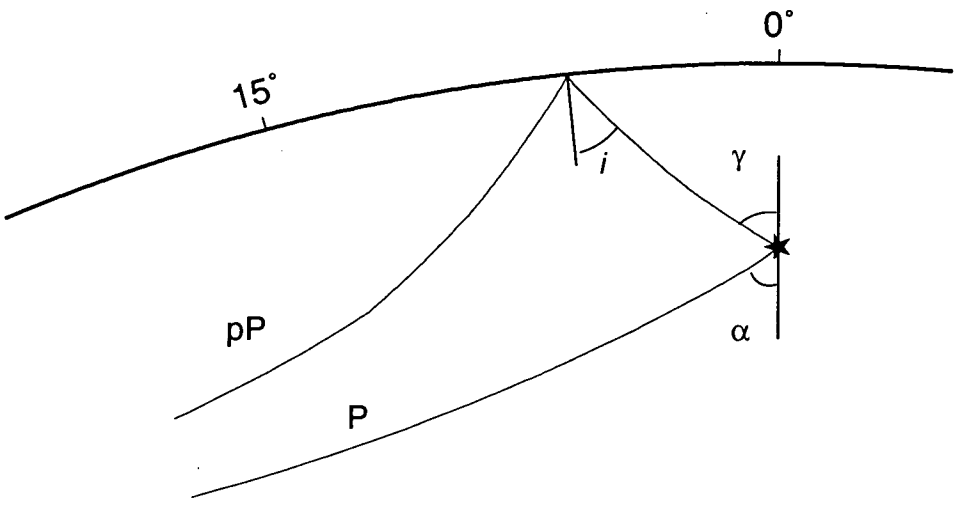

Figure 5.3.
Near source geometry of P and pP ray paths for a source at 600 km depth. The star marks the earthquake source. α and γ are the take–off angles of P and pP respectively, whilst i is the angle of incidence of pP at the earth's surface. The receiver at which these rays converge is at 40° epicentral distance. The ray paths were calculated using the TauP toolkit of Crotwell, Owens & Ritsema (1999).

close proximity, so that the rays have to leave at almost the same angle to reach a common point at the receiver. As can be seen from figure 5.3, this is not the case for deep events, where the pP bounce point is far removed from the source both horizontally and vertically. The same argument applies for sP, the take–off angle from the source for which is referred to as β. The second approximation accounts for refraction of the upgoing wave, but requires that the surface of the earth is flat. Again, for deep earthquakes, this is not a reasonable assumption, since the bounce point may be several degrees epicentral distance from the source, decreasing the expected angle of incidence. Finally, the angles of incidence of the three phases at the receiver are assumed to be equal. This angle i_r is normally calculated from a third assumption, that $i_r = \alpha$. Such an approximation is suitable for shallow, crustal earthquakes, where the direct ray path is almost symmetrical, but is not applicable to earthquakes occurring in high velocity material at great depth, for which the ray paths are strongly asymmetric.

Previous studies of deep earthquakes using the relative amplitude method (Pearce 1980, Stimpson 1987*b*, Rogers & Pearce 1987, Stimpson & Pearce 1987, Stimpson

1987*a*, Pearce & Rogers 1989) calculated the take–off angles, for P and the surface reflections, by ray–tracing through the earth velocity model of Herrin (1968), thereby dropping the assumption that $\alpha = \gamma$. However, the issue of the flat earth surface was not addressed and the angle of incidence of the upgoing phases at the surface was calculated as described above, using a surface velocity of $4.0\,\mathrm{km\,s^{-1}}$. The effect of considering a planar earth surface is to systematically overestimate the angle of incidence. However, given that large earthquakes radiate most of their energy at low frequencies, the surface velocity of $4\,\mathrm{km\,s^{-1}}$ which previous workers assumed seems somewhat low, since low frequency, long wavelength waves will not "see" thin, low velocity surface layers. This is reflected in both the Herrin (1968) and the IASP91 earth velocity models, which have surface velocities of $5.6\,\mathrm{km\,s^{-1}}$ and $5.8\,\mathrm{km\,s^{-1}}$, respectively. It may be that the lack of any apparent artefacts in the results of the previous studies is due to the trade–off between the effect of not considering the curvature of the earth's surface, which increases the angle of incidence at the surface, and using too low a surface velocity, which decreases it.

The last decade has seen the installation of many broadband seismometers, producing considerable improvements in both global coverage and the availability of high quality data. The potential of current global datasets to provide very high levels of resolution means that it is no longer acceptable to make such simplifying approximations and it is necessary, therefore, to calculate accurately all of the six ray path angles $\alpha, \beta, \gamma, i_{pP}, i_{sP}$ and i_r. I achieved this by ray tracing through the IASP91 continental earth model using the *spheray*[1] package of Henri–Claude Nataf. The angles so determined were used to calculate the surface reflection coefficients, substituting into the equations given by Pearce (1980, appendix A) [and derived from those of Knott (1899) and Zoeppritz (1919)]:

$$R_{pP} = \frac{2\sin 2\gamma \sin 2\beta - 3(\cos 4\beta + 1)}{2\sin 2\gamma \sin 2\beta + 3(\cos 4\beta + 1)}, \tag{5.2}$$

$$R_{sP} = \left(\frac{2\sqrt{3}\sin 4\beta}{2\sin 2\gamma \sin 2\beta + 3(\cos 4\beta + 1)}\right)\left(\frac{\cos\gamma}{\sqrt{3 - \sin^2\gamma}}\right). \tag{5.3}$$

[1]Freely available at http://geoscope.ipgp.jussieu.fr/.

For the sP phase, the angle of reflection is greater than the angle of incidence, because it undergoes a mode conversion from shear to the faster compressional radiation. This causes an increase in the amount of geometrical spreading, which is accounted for by the second term in equation 5.3. The effect of geometrical spreading on the upgoing radiation is small and Pearce (1980) calculated that the reduction in amplitude for a source at 500 km depth is less than 5%. Thus, no explicit corrections are applied for this effect, but it is considered when evaluating the width of the error bounds for the surface reflections.

The surface reflection coefficients were calculated for every surface reflection phase used in the investigation of the eight earthquakes. The results achieved using both this technique and the traditional method are reported in chapter 6 and displayed in appendix B. Appendix C includes the calculated reflection coefficients, the take–off angles and the angles of incidence at the receiver.

5.6 Quantification of Differential Attenuation Between P and the Surface Reflections

To determine an earthquake moment tensor using the relative amplitude method, the observed relative amplitude ranges of P, pP and sP are matched, at the relevant point on the focal sphere, with predicted amplitude ratios from different sources. The method assumes that the effect of earth structure between source and receiver will be removed by the use of amplitude ratios, and the merits of, and problems with, this assumption were discussed in sections 5.2 and 5.5, respectively. However, there exists a further problem — the surface reflections have a considerably longer ray path than the P–phase and experience extra attenuation. Thus, the observed amplitudes of the surface reflections are too small for correct moment tensor determination and an appropriate correction must be applied.

Excluding the reflection at the free surface and elastic attenuation due to geometrical spreading (both dealt with in section 5.5), radiation loses energy by interaction with interfaces (scattering attenuation) and by anelastic attenuation. To evaluate the effect of the former on the pP phase, energy partitioning at

the Moho[2] and Conrad[3] discontinuities was calculated for earthquake sources at 300 km and 635 km depth, using the method of Pearce & Young (1997) and velocities and densities from the IASP91 earth model. For both source depths, the maximum energy loss at teleseismic distances due to near–source, as opposed to near–receiver, interaction with these major interfaces was 5%, at an epicentral distance of 30°. The contribution of other intracrustal interfaces, with much lower contrasts in acoustic impedance, would be small. Thus, 5% is considered an approximate upper bound for near–source energy loss due to partitioning at interfaces other than the free surface.

The amount of anelastic attenuation experienced by a seismic wave is measured by the quantity t*, where t* is the total travel time T divided by the average quality factor Q_{AV} (Q is inversely proportional to anelastic attenuation, as described in section 2.2). The dependence of amplitude on the amount of attenuation is given by the relation:

$$A(f) \propto e^{-\pi f t^*}. \tag{5.4}$$

The distribution of Q within the earth is dependent upon the frequency at which it is observed (Sharrock, Main & Douglas 1995). As shown in figure 1.2, the amplitude spectra of the deep events examined in this study are dominated by low frequencies, which is fortunate since the average attenuation structure of the earth at long periods is reasonably well known [see, for example, the absorption band model of Anderson (1989, chapter 14)]. The deep lower mantle is thought to cause very little attenuation and has a a very high value of Q (> 1000). Conversely, the upper mantle does cause significant attenuation and has a lower value of Q of approximately 500 (Barazangi & Isacks 1971, Anderson 1989).

The important case to consider with respect to the relative amplitude method is when the amount of attenuation of pP (i.e. t^*_{pP}) is at its largest in proportion to the amount of attenuation of P (t^*_P). That is, the largest effect which will

[2]Boundary between the crust and mantle.
[3]Boundary between the upper and lower crust.

not cancel through the use of relative amplitudes. This occurs for ray paths to stations at near epicentral distances from the deepest earthquake, when the travel time for pP is at its largest relative to that of P. The deepest earthquake in this study is that of 9 June 1994, at 637 km depth, and the nearest record to it is from station SJG at 31.77° epicentral distance. The travel time for P is approximately 335 s and pP arrives 100 s later, at 435 s. It can be seen from figure 3.6 that at epicentral distances of around 30° the ray paths spend little time in the lower mantle, so its influence can be ignored. Assuming an average value of $Q = 500$, consistent with an upper mantle path, gives $t^*_P = 0.67$ s. Now, the upgoing pP phases all have relatively shallow take–off angles so, in almost all cases, their ray paths will not traverse the area of very high attenuation beneath the volcanic arc, whatever the station azimuth or dip of the slab (see figure 5.5 to help visualise this). The pP phase does, however, spend approximately three times longer than P in the low attenuation lithosphere, suggesting that $Q_{AV} = 500$ may be a slight overestimate of the amount of attenuation experienced by pP which will, therefore, provide an upper bound for the effect of differential attenuation. The amount of attenuation experienced by pP in this case is: $t^*_{pP} = 435\,\text{s}/500 = 0.87$ s.

The frequency spectra in figure 1.2 showed the amplitudes of the observed phases to be dominated by frequencies below about 0.5 Hz. Assuming that no energy is present above 0.7 Hz, the maximum effect of the differential attenuation on the relative amplitudes of P and pP is given by the expression:

$$\frac{A_{pP}(f)}{A_P(f)} = \frac{\int_0^{0.7} e^{-\pi f t^*_{pP}}\, df}{\int_0^{0.7} e^{-\pi f t^*_P}\, df} = \frac{0.31}{0.37} = 0.84\,. \tag{5.5}$$

The effect of anelastic attenuation is to reduce the amplitude of pP with respect to P by no more than 16%. This effect is significantly larger than that predicted for scattering attenuation (around 5% or less) and for geometrical spreading (also around 5% or less). The combined effect of all three sources of attenuation results in a maximum amplitude loss of around 26%. Given that the frequency spectra of every source and t^* for every path is different, to correct explicitly for the effect of attenuation on each specific amplitude ratio would require huge effort, with the majority of calculated corrections being small. The approach adopted here

is to consider the effect of attenuation when error bounds are assigned to each amplitude measurement. Systematically wider amplitude bounds will be applied to pP, typically being 25% wider for pP than for a similar recording of the P phase. Large differences in attenuation between P and pP manifest themselves as differences in the smoothness (frequency content) of the two pulses, a case which may occur if the surface reflection has sampled the highly attenuating mantle which is found above the slab at intermediate depths. When such a case is observed, larger error bounds will be applied. This argument is somewhat redundant with respect to sP, since much larger error bounds are always applied to this phase, as previously discussed in section 5.2.

Anelastic attenuation not only reduces the amplitude of a seismic phase, but also increases its duration, by preferentially removing the highest frequencies. This effect is perhaps most simply explained by consideration of a Dirac delta pulse, or time domain "spike" (infinite amplitude, infinitesimal duration). The amplitude spectrum of a delta pulse is a constant at all frequencies. Removing the highest frequencies, the pulse must necessarily broaden. As is described in section 5.7, the geometry of the source is to be determined by analysis of pulse durations, so it is necessary to examine the magnitude of the effect of differential attenuation on pulse lengths to determine whether or not the inversion may be contaminated.

Using the method of Douglas, Hudson & Blamey (1972), synthetic seismograms were produced for a range of t^* values. The P–waves from these calculations are shown in figure 5.4. For the range of t^* values calculated for P and pP above, the variation in pulse duration is around 0.5 s. This is sufficiently small to be accommodated within the error bounds imposed upon the observations of pulse duration, without the need to calculate and apply individual corrections to each phase.

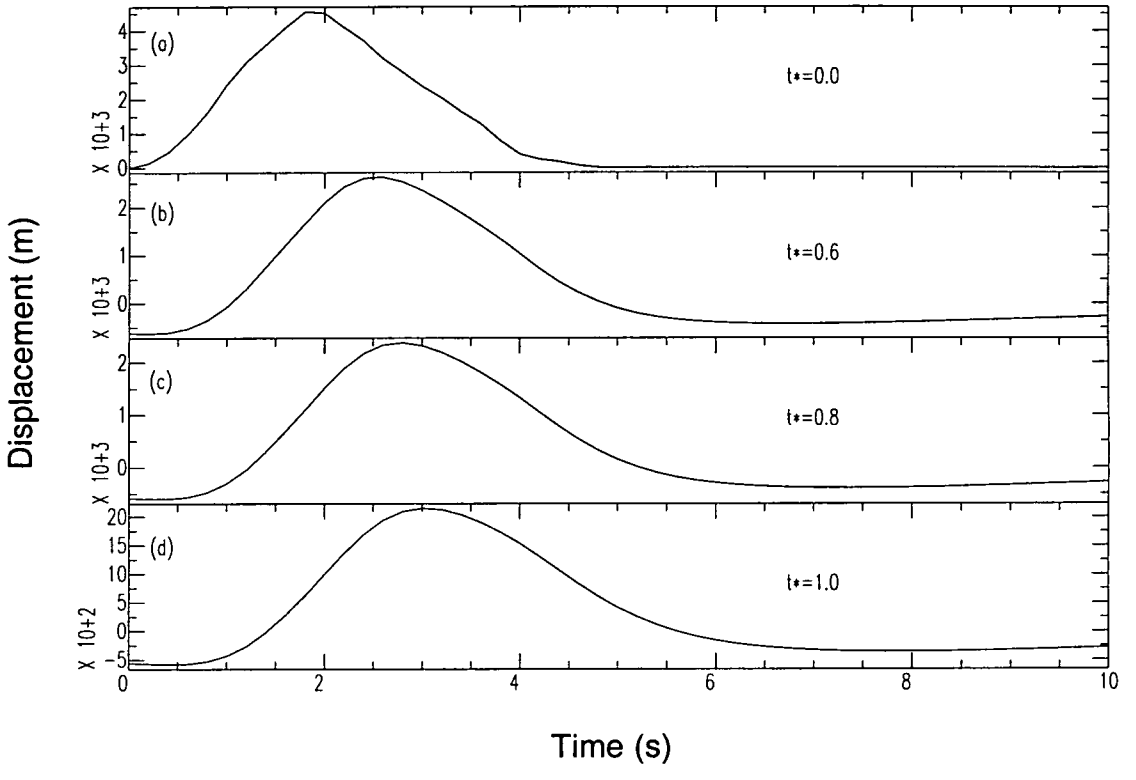

Figure 5.4.
Simple synthetic P waveforms from an ideal source, calculated for different values of t*. The horizontal axis is time in seconds, the vertical axis is displacement. The pulse duration varies from 4.7s with no attenuation (a), to about 6.0s with t*=1.0s (d). The waveforms were generated from a circular Savage (1966) type fault experiencing slip over a finite time interval, using the method of Douglas *et al.* (1972).

5.7 Source Geometry and Rupture Velocities From Time–Domain Waveform Analysis

As described in section 5.3, a rupture front propagating across a fault plane will give rise to Doppler shifts in the frequency content of the emitted radiation. This manifests itself on the recorded seismograms as a variation in pulse durations and amplitudes, dependent upon the azimuth of the receiver from the source, the take–off angle of the phase and the source geometry. Pulse durations are simple to measure on broadband displacement seismograms, allowing investigation of the geometry and speed of rupture and, potentially, to distinguish between the fault and auxiliary planes of a double couple mechanism. Pearce & Stewart (1989) adopted a grid search approach to this problem, predicting the pulse durations from different source geometries and comparing them to the observed durations. Although this approach is completely general and could, in theory, be applied to any source model, they chose the model of Savage (1966) on the basis that the radiated pulse durations could be expressed analytically and it is physically reasonable, with no discontinuities in stress across the fault surface.

In the Savage source model, slip is assumed to nucleate at the focus of an ellipse (the center of a circle and the end of a line, for these special cases), and decays smoothly with distance from the focus, falling to zero at the edge of the ellipse. The duration of radiation from such a source is dependent upon three parameters. Following Pearce & Stewart (1989), these are: a the semi–major axis of the ellipse; ϵ the eccentricity of the ellipse ($\epsilon = \sqrt{1-(b/a)^2}$, where b is the semi–minor axis); ζ the rupture velocity. All three parameters can be determined from analysis of pulse durations of body wave phases, assuming ϵ and ζ to be constant during rupture. This method assumes the source to be a double couple and requires prior knowledge of the focal mechanism. Thus, it should only be applied after the source type and orientation of an earthquake have been determined. Error bounds are placed on the pulse durations in the same manner as the amplitude bounds for use with the relative amplitude method, so that solutions compatible with the data are found, rather than a single, best–fit solution.

Shear energy is known to attenuate more rapidly than compressional energy and

increased attenuation broadens the observed pulse. Thus, observations of sP durations may be incompatible with the observed durations of P and pP, which experience less attenuation. Hence, although sP amplitudes are used in the relative amplitude method, where they are given wide amplitude bounds, I exclude them from the determination of source geometry because the required error bounds would be so wide as to render little useful constraint.

The theoretical maximum propagation velocity for a tensile crack is the Rayleigh wave speed of the failing medium (Freund 1990). However, in light of the uncertainty regarding the mechanism of failure for deep earthquakes, I search for compatible rupture velocities up to and including the absolute theoretical maximum for propagation of a shear crack, the P–wave velocity (Burridge, Conn & Freund 1979), thus making no *a priori* assumptions about the mechanics of the source.

5.8 Summary

The source parameters of eight deep earthquakes will be determined using the relative amplitude method and analysis of P and pP pulse durations. The use of broadband data removes the need to consider the effect of directivity on amplitudes and makes the direct measurement of pulse durations possible. In an advance on previous studies, the geometry of the P, pP and sP ray paths is to be calculated using the spherically symmetric IASP91 earth model, providing take–off angles and reflection coefficients of improved accuracy. The non–Poisson nature of the mantle is accounted for by using a general value for the relative excitation of P to S radiation, calculated using S– and P–wave velocities from the IASP91 model. The results of these investigations into source parameters are presented in the following chapter.

Chapter 6

Determination of Earthquake Source Characteristics: Results

6.1 Introduction

The seismograms excited by deep earthquakes are the most direct observations available of the source processes which occur during these disturbances. Even so, inverting these observations to provide a unique description of the source is a difficult and complex task. The problems associated with the methods chosen for use in this study were highlighted in chapter 5, and techniques to overcome these problems were proposed. Here, I present the results of this methodology and show that the developments of chapter 5 represent a useful advance of the relative amplitude method of moment tensor inversion.

Before attempting to invert for source characteristics, it is essential to confirm the predetermined conditions of the problem. Hence, in section 6.2, I check the published earthquake locations and search for unmodelled velocity anomalies, using teleseismic travel times. The results of the moment tensor determinations for different earth models and data of different frequency content are presented in section 6.3. The order in which these results are presented does not reflect the order in which the work was carried out. As discussed in the previous chapter, extended amplitude bounds should be used with band–limited data until the

magnitude of any Doppler effect has been assessed, in this study by analysis of pulse durations. Thus, the relative amplitude method was applied using broad-band data, followed by determination of the source geometry and then use of the relative amplitude method with long–period data. However, the results of the moment tensor determinations are presented together (section 6.3), before the results of the inversions for source geometries in section 6.6. All the rupture surfaces were shown to be nearly circular, resulting in small Doppler effects so, as it turned out, this strict methodology proved unnecessary and there was no need to use especially wide amplitude bounds with the long–period data.

An interpretation of the moment tensor results is given in section 6.4, with the emphasis on identification of factors which adversely influence the inversion for a moment tensor. They are compared to the relevant, independently determined, CMT solutions in section 6.5. The rupture velocities, and the size and shape of the rupture surfaces are constrained in section 6.6 and, finally, the specific implications of these results for rupture at great depth beneath the Peru–Bolivia border region are considered (section 6.7).

6.2 Earthquake Relocation and Travel–Time Residuals

When using the relative amplitude method to determine moment tensors, it is necessary to know the location of the earthquake. Results from the method are robust with respect to the normal errors associated with good quality earthquake locations. However, since any possible non–double couple component of deep earthquakes is expected to have a magnitude of less than 10% of the extremal source types, extra care is taken to ensure that the earthquakes in this study are located correctly, to prevent errors in location from propagating into errors in source type determination. For events prior to 1996, the ISC location was compared to the EHB and Harvard CMT locations. In all cases examined here, these locations were very similar and the EHB determination was preferred, since the estimation of depth by this method is superior, due to the use of surface reflected phases (Engdahl *et al.* 1998). For later events, only the National Earthquake

Information Center (NEIC) and Harvard CMT locations were available. In this case, I used hand picked arrival times from high quality records to relocate the events, using a least squares minimisation[1] and the NEIC location as an initial guess. The relocated hypocentres were always in good agreement with the initial locations.

It was shown in section 3.6 that a slab–like velocity structure is expected to distort the short–period wavefield produced by an earthquake. One way to test if the real wavefield interacts with the slab is to see if the distribution of travel–time residuals correlates with expected or known slab geometry. Zhou, Anderson & Clayton (1990) advise caution with this approach, since a small amount of diffuse heterogeneity along most of the ray path will produce the same effect as a strong near–source velocity anomaly. The results presented below must be considered in this context. However, the tomographic study of van der Hilst *et al.* (1997) shows cold material in the lower mantle beneath many current and palaeo–subduction zones, suggesting that at least some slabs do penetrate below the mantle transition zone. Thus, we might expect to observe slab induced travel–time anomalies at teleseismic distances even from the deepest earthquakes, which occur no deeper than the base of the transition zone. Previous work on this issue has looked only at the North–West Pacific subduction zones (Creager & Jordan 1984, Creager & Jordan 1986, Zhou *et al.* 1990), but numerous studies of travel times to local stations, looking at paths going up the slab, have shown a strong slab effect. The results of this body of work are summarised in detail by Lay (1994).

Davies & McKenzie (1969) examined travel times from the nuclear explosion Longshot, detonated above the Aleutian subduction zone. The location of this explosion is fixed and its origin time is known to within 0.1 s, making it an ideal source for the study of travel times. Their results revealed a band of negative residuals (fast ray paths) which could be fitted by a planar structure dipping at 65° with strike parallel to the subduction zone. Analysis of a nearby earthquake showed a similar, although less distinct, pattern of residuals. The fast ray paths are, presumably, along the subducting slab, and show that the wavefield from

[1] An in–house AWE Blacknest version called *speedy*, which includes corrections for the ellipticity of the earth.

a shallow source does interact measurably with the slab. Observing the effect of a slab using earthquake data is much more difficult than using travel times from an explosion, since the earthquake must first be located by minimising the travel–time residuals and hence partially compensating the effect of unmodelled velocity structure by mislocating the hypocentre. However, encouraged by the success of the earthquake analysis of Davies & McKenzie (1969), I examined the travel–time residuals for the deep earthquakes studied in this chapter.

Only the 29 March 1998 Tonga event, at a depth of approximately 500 km, was recorded at a sufficiently wide range of azimuths and epicentral distances, with respect to the subduction zone, to give a good chance of observing slab–induced travel–time anomalies. The event was relocated, as described above, producing a set of minimised travel–time residuals which were then plotted on the focal sphere and are shown in figure 6.1. A band of negative residuals is seen, which correspond to a plane dipping at 70° and striking at 44°. Seismicity profiles near the location of the event [e.g. Giardini & Woodhouse (1984)] show that the slab does dip steeply below 500 km depth. At the surface, the trench strikes at about 30°, correlating strongly with the observed pattern of residuals and suggesting that they are the result of fast ray paths within the slab. The large positive residuals either side of the fast plane mirror a pattern in the earthquake dataset of Davies & McKenzie (1969). It may be that the effect of the fast ray paths along the slab is to mis–locate the hypocentre down–dip so that, for ray paths passing either side of the slab, the travel time is greater than expected. This effect is not observed in the Longshot dataset, for which the location of the source is known independently and accurately.

The magnitude of the slab–induced negative residuals is 0.3–1.0 s. This is about 1 s less than the residuals predicted for a 500 km deep source in a slab extending to 1,000 km depth by the modelling of Kendall & Thompson (1993), a difference which may be caused by a small error in the source location. Putting the finer points of the interpretation aside, this result shows that the wavefield from this deep event probably did interact with a slab–like velocity structure, which may be important in distorting the characteristic shape of the radiated wavefield. Whether or not such distortion is of sufficient magnitude to affect the moment tensor inversion is discussed in section 6.4.

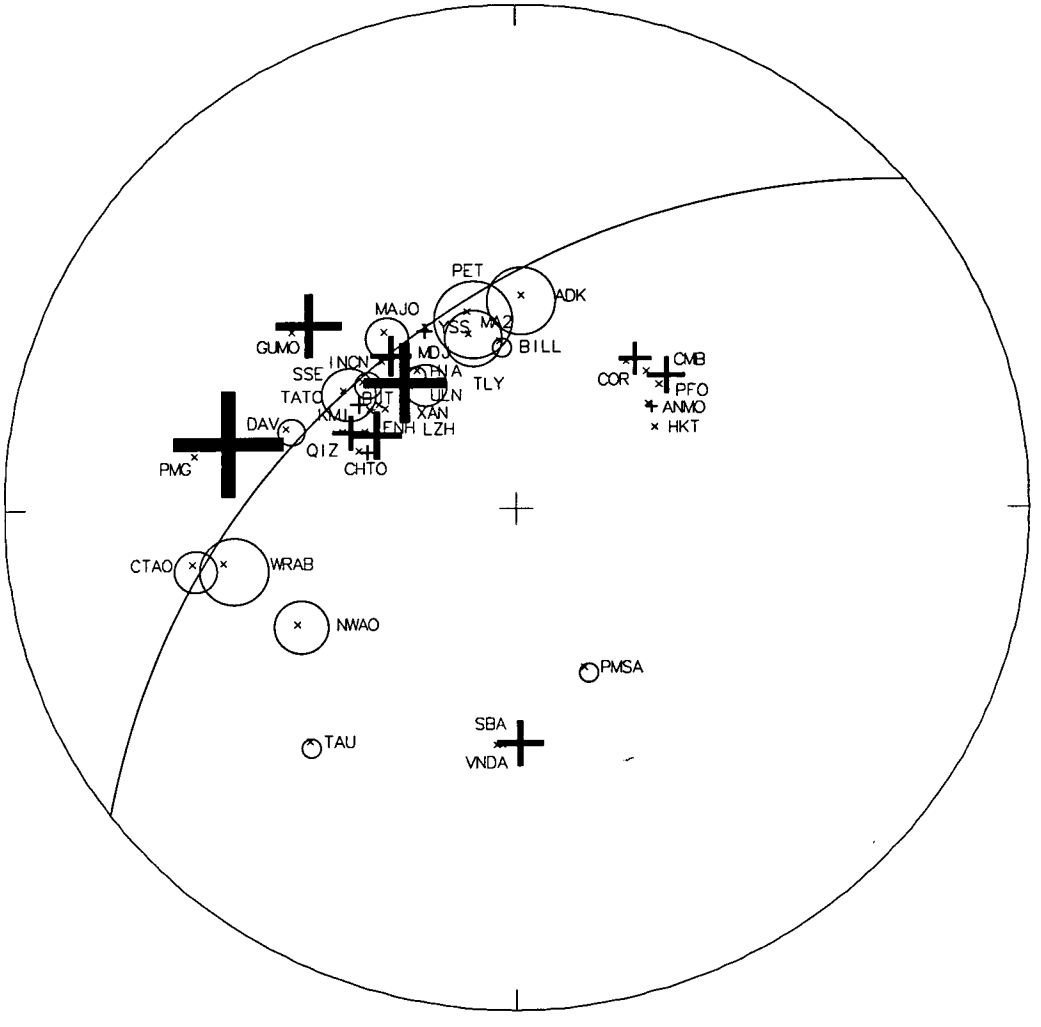

Figure 6.1.

Travel time residuals from the 29 March 1998, Tonga, earthquake. The travel time residuals are shown plotted on an equal area, lower focal hemisphere projection. Circles represent negative residuals (fast paths) and crosses show positive residuals (slow paths). The diameter of the symbol is proportional to the magnitude of the residual, with a scale of approximately 1 cm : 1 s. The text gives the identification code of each seismograph and the great circle indicates a plane which corresponds to the negative residuals, striking at 44° and dipping at 70°. Large positive residuals cluster on either side of this plane, an effect probably due to mislocation of the earthquake down-dip in the slab.

6.3 Moment Tensor Solutions

The eight events introduced in figure 1.1 were investigated using the relative amplitude method. Each was examined using three different models and using both broadband and long period data. The initial model is similar to that of previous workers [e.g. Stimpson & Pearce (1987)], using the earth velocity model of Herrin (1968) to calculate the take–off angles of the three key phases, P, pP and sP. Reflection coefficients were determined by assuming a flat earth surface and using the source and surface velocities from the IASP91 earth model. As discussed in section 5.5, this approach does not incorporate the curvature of the earth. Accordingly, ray paths and angles for a spherical earth were calculated using the more accurate IASP91 velocity structure in a second model. Both models assume that the relative excitation of S to P radiation is that of a Poisson solid, i.e $V_s = V_p/\sqrt{3}$. Although a common assumption, this is not the case for the averaged properties of the earth's mantle, as is shown in figure 5.2. The third model considers the case of a non–Poisson solid, using the IASP91 values of P– and S–wave velocities to calculate the relative excitation of these waves. All other parameters are as for the second model. Differences between models two and three were found to be extremely small, showing that the relative amplitude method responds in a stable manner to small variations in the ratio of the Lamé parameters.

The determination of source types is designed to test the hypothesis that deep earthquakes are consistent, within the error bounds of the observations, with a double–couple mechanism. Table 6.1 indicates whether or not a double couple was compatible with the observations for models one and two, using both broadband and long–period data. At long periods, using the IASP91 model, a double couple was compatible in every case. In table 6.2, one of the compatible focal mechanisms is illustrated on a lower focal hemisphere ("beach ball") projection for each event. The mechanisms are all well constrained, so a particular one shown in table 6.2 is representative of the whole population of compatible solutions. These focal mechanisms are in excellent agreement with the CMT determined mechanisms, as will be demonstrated explicitly in section 6.5. The full range of compatible source types and orientations for each earthquake is presented in appendix B, whilst the amplitude bounds used in each determination are given in appendix

C. To measure the constraint of the relative amplitude solutions on volumetric component (k), the constant volume source component was restrained to be solely simple shear (i.e. T=0) and k was searched in 1% increments over a full range of source orientations at an angular increment in σ, δ, and ψ of 2°. The resulting bounds on k are also shown in table 6.2. The solution with the greatest level of constraint is that for the Tonga earthquake of 4 September 1997. For T=0, k is shown to be less than +4% and greater than –2%.

The most uncertain parameters in the second model are the source and surface layer velocities. The IASP91 model is determined for continental areas, with a surface P–wave velocity of $5.8\,\mathrm{km\,s^{-1}}$. Figure 6.2 shows the area delimited by points of reflection for the pP and sP phases from the deepest of the three Bolivian events (9 June 1994). This "footprint" of the surface reflections lies entirely on continental crust, justifying the use of the IASP91 model. However, the Tongan events occur beneath an oceanic area and so, in theory, require a different model. Therefore, in an approach similar to that of Kennett (1992), I modified the IASP91 velocity and density model to approximate an oceanic setting, with a surface P–wave velocity of $6.4\,\mathrm{km\,s^{-1}}$. However, the effect on the inversions of using this oceanic model was small, with no change in source orientation and only minor variation in the range of compatible source types.

The main effect of errors in the source and surface velocities is to alter the angle of incidence of the upgoing phases at the surface and hence change the calculated reflection coefficients. Thus, the governing parameter is the *difference* between these velocities, which determines the total angle through which the rays will refract. To investigate the possible effect of such errors on the determination of k, I performed successive inversions holding the source velocity constant whilst changing the surface velocity. To avoid the time consuming business of ray tracing through many different velocity structures, the standard input model was used, with amplitude bounds from the long–period records of the 28 November 1997 event. Negative k components are of particular interest and hence k was restrained to be ≤ 0 to reduce the amount of computer time required. T was held constant at 0. The effect on the magnitude of k was small and is shown in figure 6.3. Minimum values of k varied between –7% and –2%, for $V_{surf} = 5.2$ and $V_{surf} = 6.2\,\mathrm{km\,s^{-1}}$ respectively. At velocities $\geq 6.4\,\mathrm{km\,s^{-1}}$ and $\leq 4.8\,\mathrm{km\,s^{-1}}$,

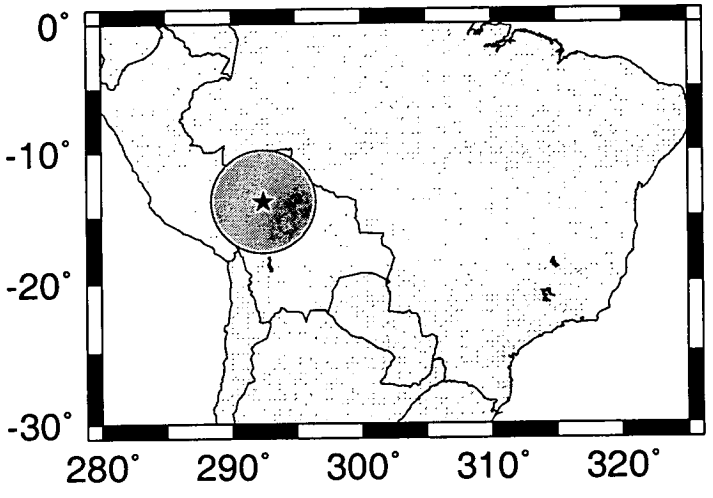

Figure 6.2.
Bounce points of the surface reflections from the 9 June 1994 earthquake. All the reflection points of the phases pP and sP lie within the shaded circle, which is centred on the epicentre of the 9 June 1994 event, close to the Peru–Bolivia border.

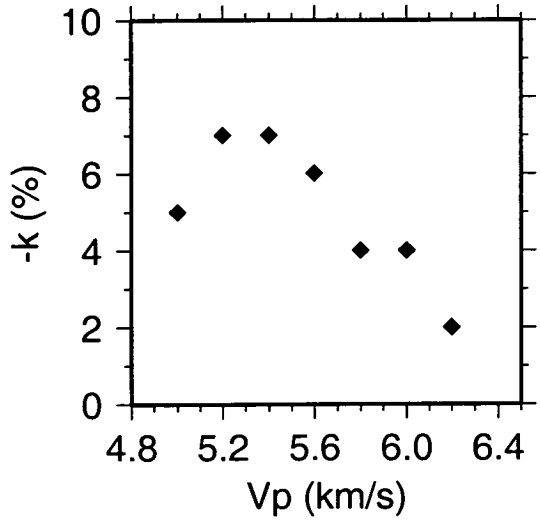

Figure 6.3.
Variation of the maximum negative volumetric component with change in the assumed surface P–wave velocity for the 28 November 1997 earthquake. The diamonds show the compatible solution with the largest negative volumetric component for each different value of the surface velocity. The standard input model was used and a Poisson solid was assumed, so that $V_S = V_P/\sqrt{3}$.

no compatible solutions were found.

The relative amplitude method also allows determination of source parameters using three component (vertical, north, east) observations of the direct S–wave polarities (Pearce & Rogers 1989). The use of S–wave data cannot distinguish any volumetric part of the source, but it does allow verification of the source orientations obtained from the P–wave data. The S–wave arrivals from the 28 November 1997 Bolivia earthquake were examined, with a view to demonstrating consistency with the focal mechanism determined using P–waves. Wherever possible, absolute polarities of the S–wave arrival were specified, but the onset of S was sometimes obscured by noise or S to P conversions. In such cases, the relative polarities of the three components were specified.

The S–wave inversion provided far less constraint on both source type and orientation than had the P–wave inversion. Most of the compatible S–wave solutions

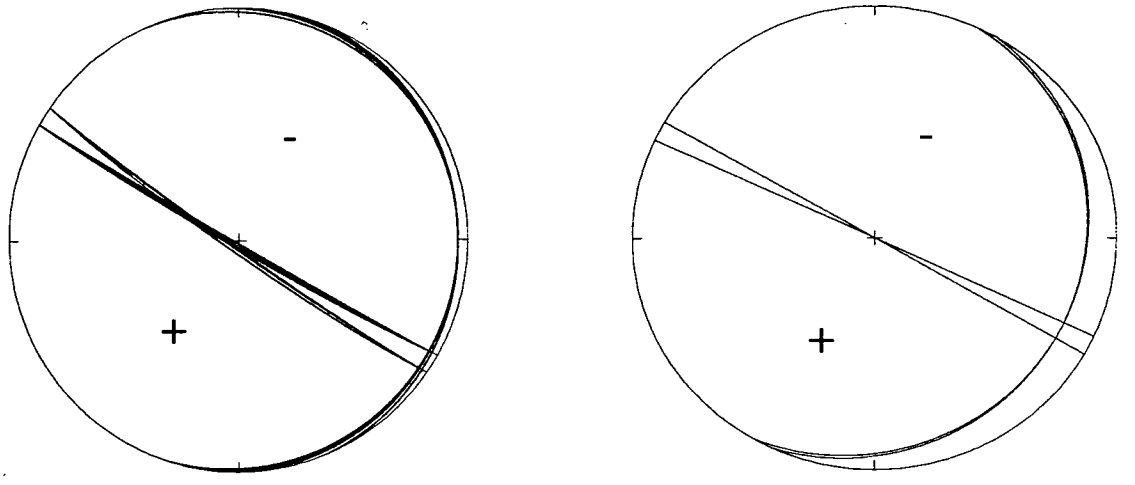

(a) (b)

Figure 6.4.
Double couple focal mechanisms for the 28 November 1997 Bolivia earthquake, determined using (a) P–wave observations, and (b) S–wave observations. Both focal mechanisms are plotted on the lower hemisphere of a Schmidt equal area projection and the + and – symbols indicate the compressional and extensional quadrants, respectively. The P–wave solution was determined from the polarities and relative amplitudes of P, pP and sP. The S–wave solution was determined from the polarities of S, recorded in three orthogonal directions, after the volume of possible mechanisms had been reduced by constraining the local stress regime to be extensional.

were reverse faults, suggesting that the data did have the potential to distinguish between normal faults of differing orientations. The P–wave focal mechanism showed the earthquake to be extensional, so I restrained the initial range of source orientations to include only normal (extensional) faults. With this condition, the S–wave polarities provided a tighter constraint on the focal mechanism, which was in excellent agreement with that determined from the P–waves. Figure 6.4 illustrates the ranges of orientations compatible with **(a)** the P and **(b)** the S observations with the pre–condition that the mechanism must be extensional. These results demonstrate internal consistency of the relative amplitude method, with both P– and S–wave inversions resulting in very similar focal mechanisms.

6.4 Interpretation of Moment Tensor Solutions

Using the standard input model for the relative amplitude method, as described in sections 5.5 and 6.3, with broadband data, six of the eight events appeared, at first sight, to be incompatible with a double–couple source mechanism (see column 2 in table 6.1). The two which were compatible (11/10/93 and 9/6/94) were also the two events which radiated most of their energy in the lowest frequency range. Using only long–period records and the standard model, only the 4 September 1997 event was incompatible with a double couple (column 3 in table 6.1). This incompatibility then disappeared when the IASP91 model was introduced with the long–period data (column 5). The third model, assuming a non–Poisson solid, gave slightly different ranges of source types (compare, for example, figures B.1 and B.2), but did not alter the source orientation or have any bearing on the compatibility of the observations with a double couple. Thus, for the eight events examined here, the most realistic model always produced a double couple solution compatible with the long period data.

In most cases, the range of source types compatible with the long period data is greater than that compatible with the broadband data. To investigate the cause of this variation, I define a simple parameter θ as a measure of the width of amplitude bounds (A_{min} and A_{max}), where

$$\theta = 1 - \frac{A_{min}}{(A_{min} + A_{max})/2}, \tag{6.1}$$

and then Θ is the sum of all values of θ for a given dataset. Analysis of the 31 March 1998 event provided a particularly spectacular example of how the long period data was compatible with a much greater range of source types than the broadband data. The source type plots for the IASP91 model, determined using both the broadband and long–period data, are shown in figure 6.5. For the amplitude bounds measured from the broadband data, $\Theta = 60.4$. For the long–period data, $\Theta = 52.3$. This somewhat surprising result shows that the amplitudes from the long–period records were bounded more tightly than those from the broadband records, whilst they provided less constraint on the source

Event	Std. BB	Std. LP	I91 BB	I91 LP	f_{max} (Hz)
10/1/94	NDC	DC	NDC	DC	0.3
9/6/94	DC	DC	DC	DC	0.06
28/11/97	NDC	DC	DC	DC	0.4
31/3/94	NDC	DC	NDC	DC	0.6
4/9/97	NDC	NDC	NDC	DC	0.6
29/3/98	NDC	DC	NDC	DC	0.6
13/5/97	NDC	DC	DC	DC	0.8
11/10/93	DC	DC	DC	DC	0.2

Table 6.1.
Earthquake source parameters I — results from the relative amplitude inversions for source type, assuming a Poisson solid at the source. BB broadband; **LP** long–period; **Std** standard input model; **I91** using the IASP91 earth model; **DC** compatible double couple (with no volumetric component) exists; **NDC** no compatible double couples; f_{max} frequency below which large amplitudes are present in the P–wave spectra. Long–period data was obtained by low–pass filtering the broadband records at $f = 0.05\,\mathrm{Hz}$ ($T = 20\,\mathrm{s}$).

type. Analysis for the 10 January 1994 event gave a similar result, with $\Theta_{BB} = 36.3$ and $\Theta_{LP} = 35.8$. The IASP91 source type plots for this event are also shown in figure 6.5. Using the terminology of Pearce & Rogers (1995), the long period records are of a higher *quality* than the broadband records, because they may be assigned narrower amplitude bounds, but provide less constraint and are therefore of lower *significance.*

The observations highlighted in the two preceding paragraphs have an important bearing on the issue of moment tensor inversion for deep earthquakes. The apparently higher significance of the broadband records suggests that they are in some way incompatible with a source described by a sum of force couples. Such incompatibility may result if the "high frequency point source" assumption justified in section 5.3 is incorrect. Alternatively, distortion of the short–period wavefield by the complex velocity structure of the subduction zone could result in the observed reduced compatibility of the high–frequency data with standard sources. A point source approximation breaks down for frequencies above which the wavelength is much larger than the maximum source dimension, whilst focusing effects should only become negligible for wavelengths much greater than the dimension of the subduction zone's complex velocity structure. The latter dimension will always be much larger than the former, so focusing of the wavefield is important to much lower frequencies than the validity of the point source assumption. As shown in figure 1.2, the amplitude of waves excited by deep earthquakes decays rapidly with increasing frequency, so the magnitude of any focusing effect should be much larger than the influence of a breakdown in the point source assumption. The two earthquakes which show the largest frequency dependent effect have sub–vertical and sub–horizontal fault planes so, following the argument of section 5.3 (page 102), the effect of the breakdown in the point source assumption should be negligible. Given the observations of section 6.2 and those of Barazangi & Isacks (1971), that the wavefields from deep earthquakes do interact measurably with the subduction zone velocity and attenuation structure, it seems likely that the cause of the non–double couple components at short periods is distortion of the wavefield by this unmodelled velocity structure, to which the longer period waves are less sensitive.

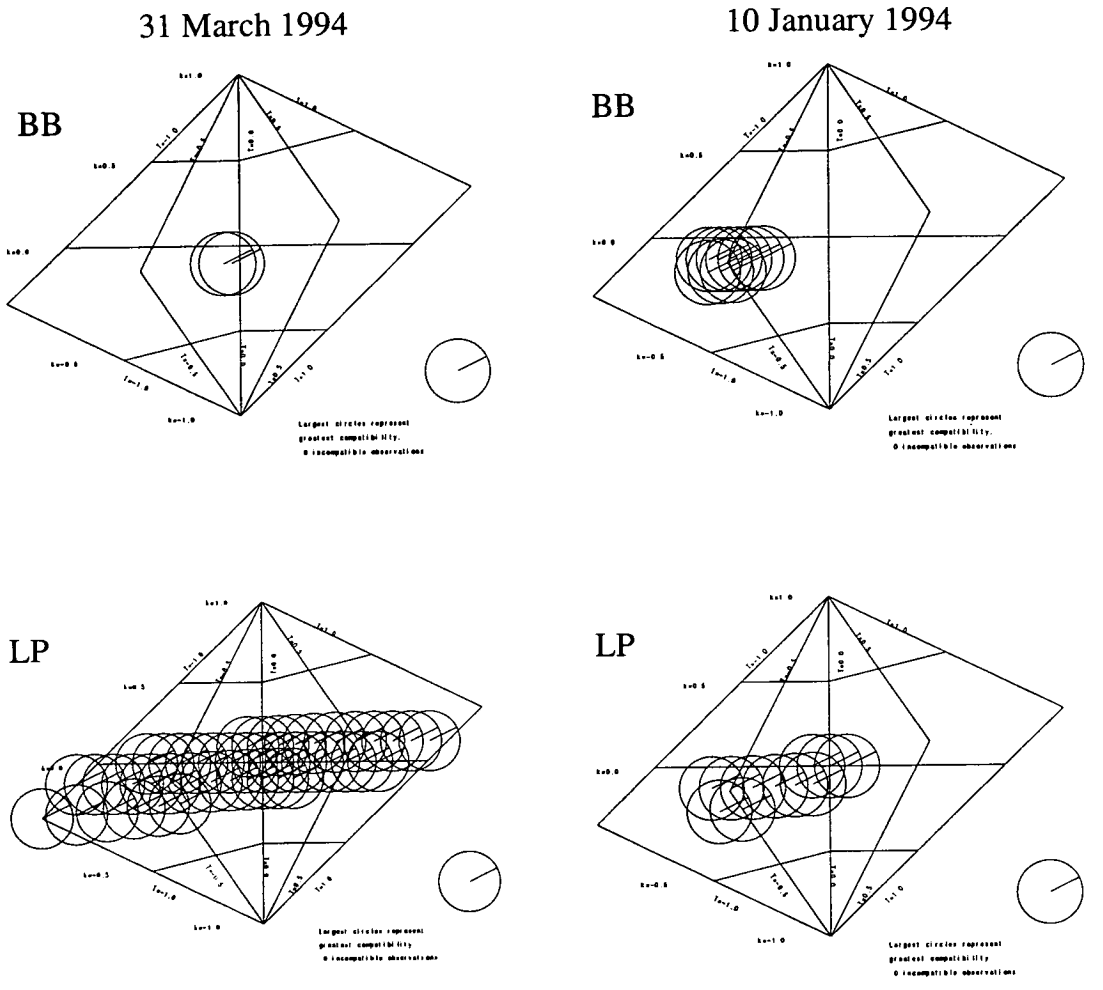

Figure 6.5.
Source type plots determined using the IASP91 model for the 31 March 1994, Tonga, event (left) and the 10 January 1994, Bolivia, event (right). k is plotted on the vertical axis, T on the horizontal axis. The upper plots show the source types compatible with relative amplitude observations from the broadband (BB) seismograms, whilst the lower plots show source types compatible with similar observations from the long–period (LP) seismograms. Excluding the difference in the frequency content of the data, the datasets are in every way identical, since the long–period records were obtained by low–pass filtering of the broadband records.

The long period seismograms contain untapered energy below 0.05 Hz (20 s period). For a velocity at the source of $10\,\mathrm{km\,s^{-1}}$, the minimum wavelength at the source is 200 km. With such large wavelengths, the first cycle of a wave samples the entirity of the subduction zone velocity structure and probably into the "normal" mantle beyond. The effect of the subduction zone velocity structure at these periods is impossible to predict without full numerical modelling of the wave propagation, but it seems unlikely that strong focusing effects would occur. Thus, the long–period results should not be strongly affected by the unmodelled near–source earth structure. These conclusions are in agreement with those of Tada & Shimazaki (1994), who examined the issue by forward modelling ray paths through a simple slab velocity structure and then inverted the synthetic far–field P–wave seismograms using a spherically symmetric velocity model. They found that at short periods, simple near–source velocity heterogeneity did induce apparent constant–volume non–double couple components in the results of the source inversion (the effect on k was not investigated), but suggested that such effects would not be important at long periods, for which the wavelength was much greater than the scale of the near–source heterogeneity. In summary, I find no evidence that the source mechanism of any of the eight events examined deviates from a double couple, after taking into account the possible distortions from (i) attenuation of the upgoing rays, (ii) unmodelled, asymmetric, near–source velocity structure, (iii) the assumption of a Poisson solid, and (iv) the individual geometries of each source–receiver ray path.

6.5 Comparison with CMT Solutions

The Centroid Moment Tensor (CMT) method finds the best–fit constant volume source, using very–long–period body and surface waves, as described in section 5.1. It is used to provide near real–time moment tensor determinations by the University of Harvard, who publish both the least–squares best–fit solution and, if that solution is not a double couple, the double couple which is obtained by forcing the amount of pure shear to be zero (i.e. $T = 0$). This is not, necessarily, the double couple which best fits the data. Figure 6.6 compares the double couple solutions determined in this study, using the relative amplitude method, with

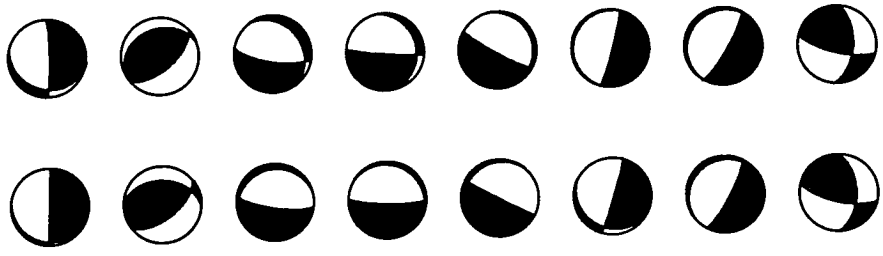

Figure 6.6.
Focal mechanisms determined by the relative amplitude method (top) and the CMT method (bottom). The focal mechanisms for the eight deep events studied in this thesis are shown. Of the solutions determined using the relative amplitude method, only one compatible solution is shown for each event. Other compatible source orientations were found, but they were all similar to the one shown. The CMT solutions shown are the double couple mechanisms derived from forcing the CMT least–squares solutions to include no component of pure shear.

the published CMT double couple solutions. The two are in excellent agreement, with only small differences. Most of these differences concern the orientation of shallowly dipping nodal planes, a parameter which is difficult to constrain accurately because the "equatorial" part of the focal sphere is poorly sampled at teleseismic distances. The range of source orientations compatible with the polarities and relative amplitudes of P and its surface reflections is, in all the cases examined here, small, and the alternative solutions cluster around that shown in figure 6.6. The agreement of these solutions with the independently determined CMT solutions suggests that the source orientation is determined accurately.

Figure 6.7 shows the constant volume source types determined using both methods. The single circles indicate the value of T for the best–fit CMT solution, whilst the error bars show the range of T values which are compatible with the relative amplitude data, assuming that $k = 0$. For seven of the eight earthquakes, the CMT solution lies within the bounds determined by the relative amplitude method, and only the solutions for the 10 January 1994 event are incompatible. Such a low incidence of incompatibility between the two sets of results does not show that the CMT determinations of T are incorrect. However, the absence of

any positively identified pure shear ($T \neq 0$) components in the relative amplitude solutions is consistent with a scenario where the non–double couple components in the CMT least–squares solutions may be an artefact, possibly induced by the propagation of errors from the earth model into the results of the source type inversion. Further investigation into the confidence bounds associated with the CMT solutions is required to help resolve this issue, and it is considered further in section 7.6.

6.6 Source Geometries

Analysis of the P and pP pulse durations found all the events to be compatible with a Savage (1966) fault model. The most pertinent results of the inversions are displayed in table 6.2. The fault plane was positively identified for six of the eight events and, in all six cases, it was found to be either sub–horizontal or sub–vertical. Individual rupture velocities ranged from less than $1.2\,\mathrm{km\,s^{-1}}$ to greater than $4.5\,\mathrm{km\,s^{-1}}$. The validity of such a wide range of rupture velocities is supported by examination of the seismograms. Figure 6.8 shows the P pulses from the three Bolivian events, all recorded at the same station. As expected, the pulse duration is longer for larger earthquakes. For a simple source model, the assumption of a constant rupture velocity means that the source duration is proportional to the linear dimension of the source. In turn, this is proportional to the cube root of the scalar moment, because it is itself proportional to the area of, and average slip on, the rupture surface. Hence, the rupture durations can be normalised by the cube root of the scalar moment to allow comparison of durations from earthquakes of different sizes. Figure 6.9 is a plot of the normalised P pulse durations against the reciprocal of the rupture velocity, for the five most well constrained events. It shows a positive correlation between the two, indicating that the observed pulse durations do scale inversely with the rupture velocity, and demonstrating internal consistency between the inversion results and the observations. Scatter is attributable to variations in the stress drop, errors in the estimation of the scalar moment, and variations in rupture velocity across the fault plane.

Some clarification is necessary regarding the measurement of the pulse durations,

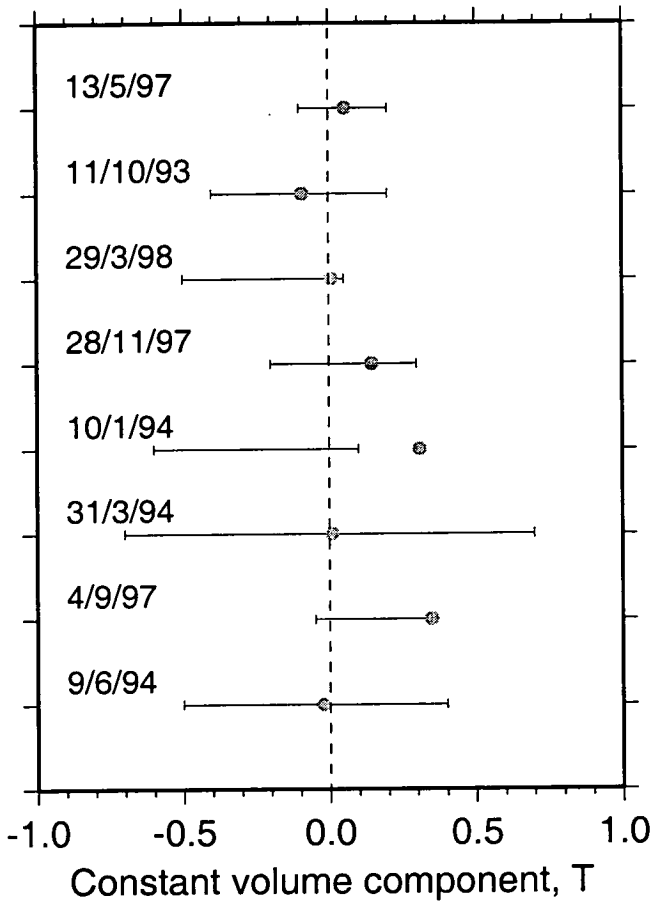

Figure 6.7.
Constant volume components of the source type determinations obtained using the CMT and relative amplitude methods. The earthquake solutions are arranged, from top to bottom, in order of increasing depth, but not on a linear depth scale. The amount of finite pure shear is indicated on the horizontal axis, ranging from a double couple at 0, to a negative or positive linear compensated dipole at +/−1. CMT least–squares solutions are indicated by a circle, and the range of compatible sources determined in this study using the relative amplitude method are indicated by the horizontal bars. Results from the non–Poisson solid, IASP91 model are shown. The date of each earthquake is shown on the left of the diagram.

Event	Fm	Fp	k (%)	V_r (km s^{-1})	A	ϵ
10/1/94		H	$-13 < k < 9$	$0.5 < V_r < 2.5$	13	0.3
9/6/94		H	$-6 < k < 10$	$0.8 < V_r < 1.2$	46	0.3
28/11/97		V	$-7 < k < 19$	$V_r > 4.5$	28	0.2
31/3/94		V	$-16 < k < 14$	$V_r > 4.0$	26	0.3
4/9/97		V	$-2 < k < 4$	$0.5 < V_r < 2.5$	18	0.5
29/3/98		U	$-18 < k < 6$	$V_r < 4$	(22)	(0.2)
13/5/97		U	$-8 < k < 10$	$0.8 < V_r < 5.8$	?	(0.2)
11/10/93		V	$-22 < k < 12$	$V_r < 2.3$	?	?

Table 6.2.

Earthquake source parameters II — results from inversions for source type, orientation and geometry. **Fm** focal mechanism, **Fp** orientation of fault plane, inferred from source directivity and described as **H**orizontal, **V**ertical or **U**nknown; k constraint on volume change, assuming T=0; $\mathbf{V}_r$ range of rupture velocities compatible with the observed pulse durations; **A** estimated length of the major axis of the fault ellipse; ϵ maximum compatible eccentricity of the rupture surface. The lengths and ellipticities for the 29 March 1998, 13 May 1997 and 11 October 1993 events are poorly constrained. See text for caveats regarding the dimensions of the 9 June 1994 event.

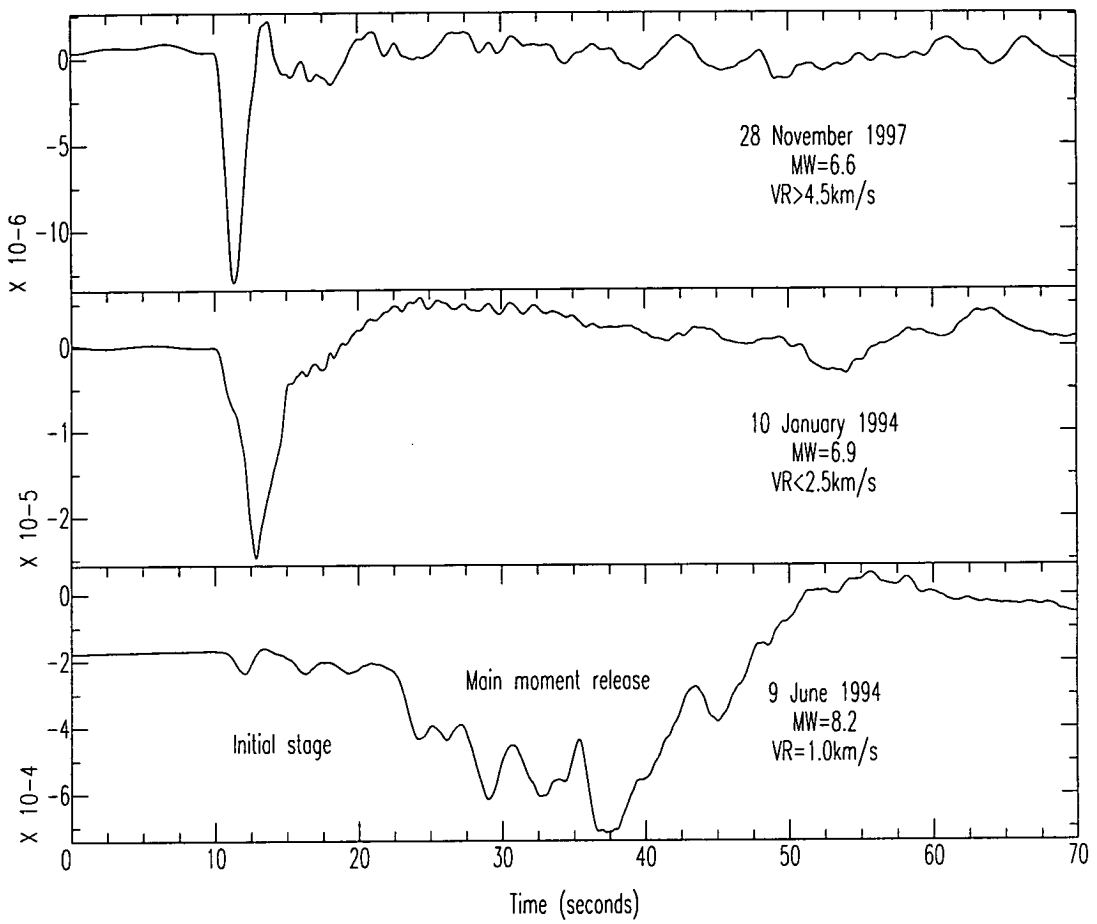

Figure 6.8.
P waveforms recorded at station ANMO, New Mexico, from three deep earthquakes beneath Bolivia. The seismograms are phaseless (instrument response removed) broadband displacement records. MW is the moment magnitude determined by Harvard University, VR is the rupture velocity determined in this study by the analysis of pulse durations. The vertical axis is displacement amplitude in metres.

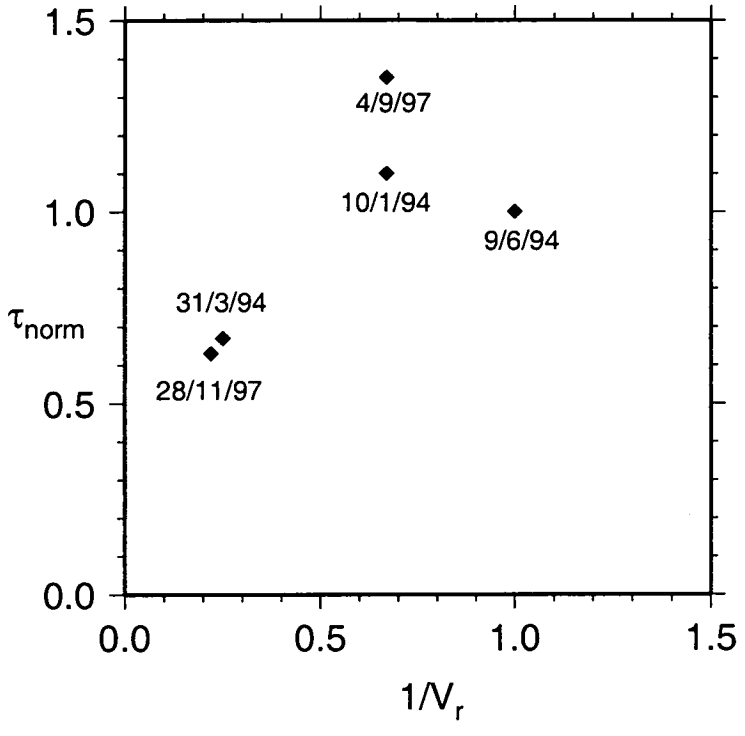

Figure 6.9.
Graph of P–pulse durations, normalised for magnitude, against the inverse of the rupture velocities. Only the results from the five most well constrained earthquakes are shown. Individual points are identified with the date of the earthquake. The positive correlation indicates that the source duration does increase for slower rupture velocities, confirming that the determinations of rupture velocity are reasonable and consistent with the data.

since it is essential that the same segment of waveform is measured at each station. For all the events except 9 June 1994, the duration of the complete P–pulse was measured, the onset and termination of the pulse providing clear markers between which to measure pulse duration. The 9 June 1994 event was much larger than the others and displayed an onset stage of low moment release, lasting around 10 s (see figure 6.8). Similarly, the end of the pulse is not clear, decaying gradually to zero. A distinct zone of high moment release lasting around 30 s is seen on all the records, so the duration of this was measured rather than the duration of the entire pulse. The implication of this technique is dependent upon the interpretation of the waveform. Most studies (Beck *et al.* 1995, Lundgren & Giardini 1995, Goes & Ritsema 1995, Chen 1995, Silver *et al.* 1995) interpret the peaks in the waveform to represent individual subevents, which are local maxima in the space–time distribution of moment release. Such an interpretation leads to the identification of the small initial onset phase as a separate precursory event [e.g. Antolik, Dreger & Romanowicz (1996)]. However, Ihmlé (1998) has shown that the observations are compatible with, and are well modelled by, a single propagating rupture with smooth variations in slip and moment release.

These two contradictory interpretations give two different estimates of the size of the fault plane. Subevent interpretations give areas of $30 \times 50\,\mathrm{km}^2$ (Beck *et al.* 1995) and $40 \times 60\,\mathrm{km}^2$ (Antolik *et al.* 1996). These are in good agreement with my determination of $46 \pm 6 \times 44 \pm 6\,\mathrm{km}^2$. The single rupture model gives an area of $100 \times 100\,\mathrm{km}^2$ (Ihmlé 1998). If this is the correct model, then my source dimensions will be too small because I considered only a fraction of the P–pulse. However, the determination of rupture velocity remains valid. My analysis revealed a rupture velocity of 0.8–$1.2\,\mathrm{km\,s}^{-1}$, in good agreement with the velocities determined by numerous previous studies (Silver *et al.* 1995, Lundgren & Giardini 1995, Beck *et al.* 1995, Antolik *et al.* 1996, Ihmlé 1998).

6.7 Bolivia Case Study

The three deep events which occurred beneath the Bolivia–Peru border region provide a unique opportunity to investigate the characteristics of deep earthquakes. All three events are large and well–recorded and occur within approximately 200 km of each other. The locations of the epicentres and deep background seismicity are shown in figure 6.10. A profile through the subduction zone, figure 6.11, shows the relative location of the hypocentres. All three events occur in an isolated region of seismicity, which appears to define a slab of subducted lithosphere lying sub–horizontally between 600 km and 700 km depth. Two of the fault planes have been shown to be sub–horizontal, the other sub–vertical. Estabrook & Bock (1995) proposed that such a pattern of faulting would result from the deformation of the slab above the 660 km mantle discontinuity. The observed situation deep beneath the Bolivia–Peru border region is entirely consistent with this hypothesis.

Rupture velocities were successfully determined for all three events. The 10 January 1994 earthquake, number 1 on figure 6.11, ruptured at less than $2.5\,\mathrm{km\,s^{-1}}$. The 28 November 1997 event, number 2, occurred very close to event 1 but ruptured at over $4.5\,\mathrm{km\,s^{-1}}$. I estimate the S–wave velocity at the source to be $5.4\text{–}6.0\,\mathrm{km\,s^{-1}}$, so the rupture velocity of this event was at least 75% of the S–wave velocity. Event 3, the very large 9 June 1994 earthquake, ruptured slowly at about $1\,\mathrm{km\,s^{-1}}$. Such a wide range of rupture velocities within the same segment of subducted lithosphere shows that the speed of rupture is governed neither by temperature nor slab morphology. Similar results from Tonga reveal that the dip of the fault plane is unimportant, with the 31 March 1994 and 4 September 1997 events both rupturing on sub–vertical fault planes but at very different velocities ($> 4\,\mathrm{km\,s^{-1}}$ and $< 2.5\,\mathrm{km\,s^{-1}}$, respectively).

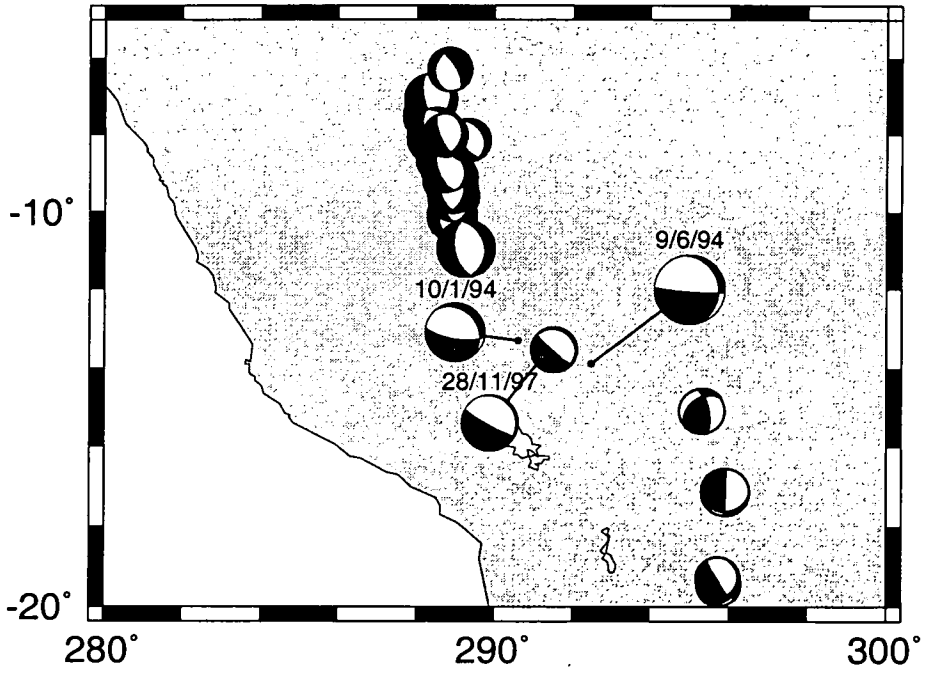

Figure 6.10.
Epicentres and focal mechanisms for deep seismicity beneath northern South America. The three focal mechanisms determined in this study are shown in grey and white and are labelled with the date of their occurrence. The black and white mechanisms are Harvard CMT determinations for nearby deep earthquakes. The radius of each lower focal hemisphere is proportional to the moment magnitude of the event (and hence to the log of the moment release).

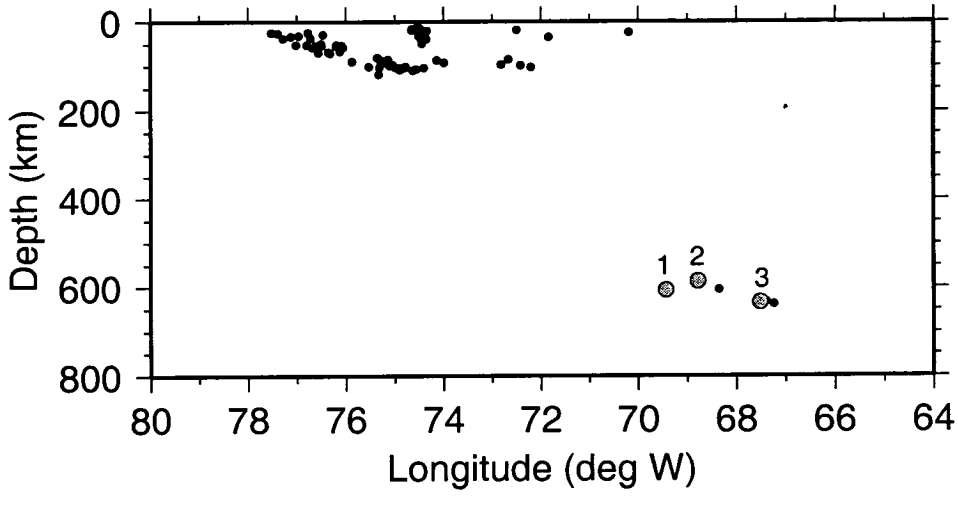

Figure 6.11.
Profile through the Andes subduction zone, 13–14°S. Black dots are earthquake hypocentres from the EHB catalogue. The three larger, grey dots indicate the hypocentres (also EHB) of the events for which source parameters were determined in this study. These are identified by numbers. 1: 10 January 1994; 2: 28 November 1997; 3: 9 June 1994. Event 1 ruptured at $< 2.5\,\mathrm{km\,s^{-1}}$, event 2 at $> 4.5\,\mathrm{km\,s^{-1}}$ and event 3 at $1\,\mathrm{km\,s^{-1}}$.

6.8 Conclusions

A number of important results have been presented in this chapter. Section 6.2 demonstrated that the subduction zone structure can have a significant effect on first arrival times at teleseismic distances, an effect probably caused by ray paths passing through colder, faster subducted material which extends into the lower mantle. However, the influence of differential attenuation between these phases was found in chapter 5 to be sufficiently small as not to require detailed corrections to the observed amplitudes and pulse durations used in the inversions in this study.

Moment tensor solutions for eight earthquakes in four different subduction zones revealed that the relative amplitudes and polarities of long–period P, pP and sP phases were consistent with the double couple source mechanism. Any consistent implosive component was constrained to be less than –2%, assuming that $T = 0$. These calculations used the IASP91 spherical velocity model. A simpler, less realistic model, assuming a flat earth surface and a Jeffreys–Bullen velocity model, resulted in a non–double component for the 4 September 1997 event, which can, therefore, be attributed to the propagation of the inappropriate assumptions into a systematic error in source type.

Moment tensor inversions performed using data of different frequency contents revealed components of the high frequency wavefield that were not compatible with any normal point source. These components are interpreted to be the result of refraction of the waves by the complex velocity structure of the subduction zone. In some cases, this distortion of the wavefield manifests itself as an apparent non–double couple component.

Analysis of the P and pP pulse durations from three closely spaced deep events beneath Boliva revealed a minimum range of rupture velocities of $1.2 \leq V_r \leq 4.5\,\mathrm{km\,s^{-1}}$. Results from all eight events showed that the rupture velocity is not dependent upon the slab temperature, morphology or dip. In the following chapter, the relevance of these conclusions to the mechanism of instability for deep earthquakes will be examined, in conjunction with the results from chapter 4 and the results of many investigations recorded in the literature.

Chapter 7

Discussion

7.1 Introduction

Two diverse lines of enquiry have yielded complementary results relevant to the source processes of deep earthquakes. The purpose of this discussion is to examine the implications of these results and to offer some relevant observations I have made during the course of this work. However, I first present a brief review of the most pertinent findings.

Two dimensional thermal models were calculated for many subduction zones (chapters 3 and 4). Section 4.4 shows that the observed double seismic zone in the Shumagin slab cannot be explained by the dehydration of serpentine, and section 4.6 suggests that the same is true for the Japan double seismic zone, although this could not be proved in section 4.3. Analysis of the temperatures at which the deepest seismicity occurs in individual subduction zones revealed that seismicity terminates once a critical temperature has been exceeded. This is probably best defined as an homologous temperature rather than an absolute temperature, although the errors in the models were sufficient to prevent a confident distinction being made between the two cases. No systematic pressure dependence was observed in any of the seismicity patterns, suggesting that deep seismogenesis does not require the occurrence of mineral reactions. However, this does not exclude the mechanism of transformational faulting, since the transformation of metastable olivine to spinel is entirely dependent on temperature below

a depth of about 400 km (see figure 2.5).

The amplitudes and polarities of the direct teleseismic P–waves and their surface reflections from eight deep earthquakes were all shown to be compatible with the double couple source model (section 6.3). Lots of high quality data, widely distributed over the focal sphere, resulted in well determined source types and orientations. For one event, it was shown that, assuming no component of pure shear, any implosive component contributed less than 2% to the total energy release. Rupture velocities were shown to vary widely, even within a single slab, and identification of the fault plane from variations in pulse durations revealed that rupture could occur on either the horizontal or vertical nodal plane of the "classic" deep earthquake focal mechanism (section 6.6).

The enigma of deep seismicity has puzzled earth scientists for the last 80 years. No individual study or method of investigation, past or present, has the capability to uniquely determine the answers to our questions regarding the nature of deep seismogenesis. Only by examining all the accumulated evidence can we hope to gain an understanding of the processes at work. The following discussion examines how my results relate to this body of work and deliberately highlights some of the relevant areas of research which have been largely ignored by the recent reviews of deep seismogenesis (Green & Houston 1995, Kirby *et al.* 1996), or have been published since those reviews were composed and since the work for this thesis was begun.

7.2 Depth Distribution of Earthquakes

The linear relationship between thermal parameter and maximum earthquake depth, demonstrated in section 4.7, suggests that both intermediate and deep earthquakes occur by a common mechanism. However, the argument used most widely to explain the characteristic depth distribution of deep earthquakes (illustrated in figure 2.10) requires that intermediate depth earthquakes occur due to some effect of dehydration, whilst deep earthquakes are related to a metastable wedge of olivine, via a process which peaks in its efficiency at generating earthquakes at about 600 km depth. The results of chapter 4, which suggest that

intermediate depth seismicity does not result from dehydration, are also at odds with this hypothesis.

Patterns of seismicity in the Izu subduction zone, just south of Japan, provide some insight into this problem. Figure 7.1 illustrates the seismicity of the Izu slab by way of six cross sections, parallel to the slab dip. On several sections, the slab appears to be deflected towards the horizontal near 400 km depth, and an increase in the seismic event rate is observed. Between 34 and 35 °N, the slab (as defined by earthquake hypocentres) appears to rest horizontally at 400 km. At 30–31 °N, layering begins at about 550 km depth, in the middle of the transition zone. No seismicity is observed at greater depth. These depths of layering correspond to the predicted and, in the case of the "410", seismically observed discontinuities due to solid–solid phase changes in Mg_2SiO_4, providing evidence that phase changes are altering sufficiently the rheology of the mantle to cause the deflection. The increase in seismicity at points of deflection, which must also be points of high strain, suggests that the seismic event rate is positively correlated to the strain rate.

Subducting slabs are frequently observed to layer horizontally at the base of the transition zone, at about 660 km depth (Ding & Grand 1994, van der Hilst 1995). I suggest that the increased strain rates resulting from this deflection cause the observed increase in seismicity at this depth (figure 2.10), consistent with the ideas of Willemann (1991) and Tao & O'Connell (1993). Layering at 410 and 550 km, as seen in the Izu slab, is not observed elsewhere, suggesting that perhaps the Izu slab is only just cold enough to possess sufficient negative buoyancy to subduct rapidly into the transition zone. The geotherms of figure 4.10 bear this out since, of the modelled slabs which exhibit deep seismicity, the model of Izu at 32 °N is the warmest and has the shallowest termination of seismicity. The lack of peaks in seismic activity in other subduction zones at these depths suggests that the changes in mantle rheology are minor and do not deflect colder, more rapidly descending slabs. Thus, it is unnecessary to invoke two different mechanisms of embrittlement to explain the observed variation of seismicity rates with depth, since the peak at the base of the transition zone appears to be due to the increased rate of deformation of the slab.

The observed deflections in seismicity patterns and slab velocity signatures in

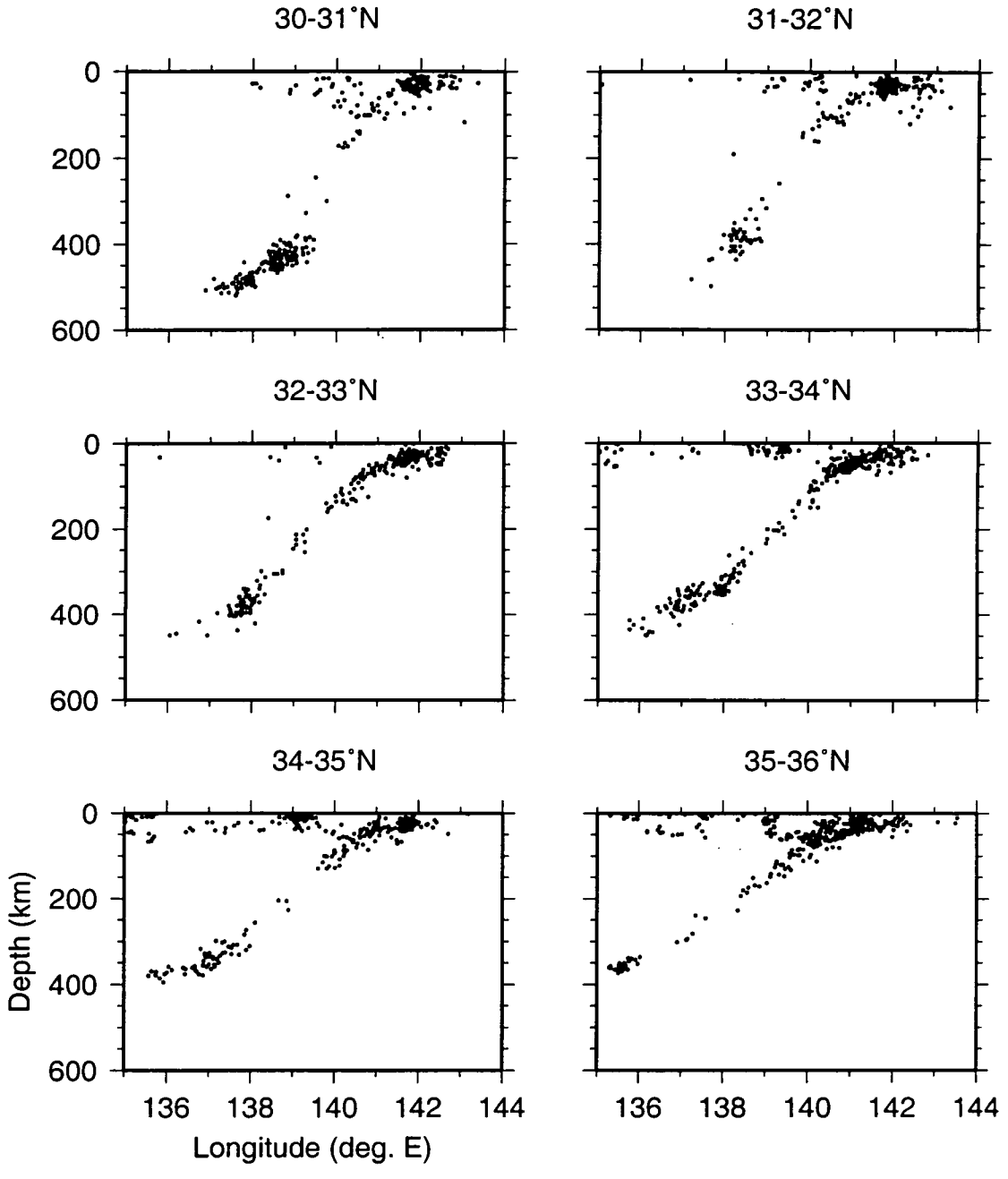

Figure 7.1.
Seismicity profiles across the Izu subduction zone. Earthquake hypocentres from the EHB catalogue are plotted as black dots. Each section shows events from a region extending 1° along strike and the range of longitudes shown is the same for all the sections. The horizontal and vertical scales are equal.

the transition zone suggest strongly that mantle viscosity increases with depth. Even a small increase in viscosity should provide sufficient resistance to slab penetration to generate down–dip compressive forces in the slab, as are observed in all slabs which exhibit deep seismicity (Zhou 1990). Indeed, an inversion of geoid and seismic travel time data by Cadek & van den Berg (1998) showed that the viscosity of the upper mantle must, in general, increase with depth. Their preferred model also included a dramatic reduction in viscosity directly above the 660 km discontinuity, which may explain why layering of slabs, and hence the increased rate of seismicity, at this depth is so widespread. No seismicity has ever been reliably located in the lower mantle. Even the coldest slab material may have warmed beyond the temperature at which seismicity ceases (about 800°C for typical slab strain rates in the upper mantle — an issue discussed in the following section) by the time it enters the lower mantle. Alternatively, higher viscosities in the lower mantle may reduce the maximum rate of deformation of the slab and so reduce the strain rate and hence lower the critical temperature for seismicity termination. This latter mechanism seems more likely, since it provides a reasonable explanation for termination of seismicity at a discrete depth. The former explanation might predict that a small amount of seismicity could occur in the lower mantle beneath Tonga, currently the coldest subduction zone (figure 4.10).

7.3 Pseudotachylyte Generation

From analysis of the frequency–moment distributions of seismicity in different depth ranges, Kagan (1999) proposed that the seismic efficiency in subducting slabs is at least an order of magnitude lower than for shallow earthquakes at plate boundaries. Seismic efficiency describes the proportion of the total tectonic strain which is accommodated by earthquakes. Hence, a low efficiency in subducting slabs implies that the majority of deformation is accommodated in a ductile manner, as predicted by the simple considerations of rock strength outlined in chapter 1. Thus, deep earthquakes must be occurring within a dominantly ductile deformation regime. Some insights into how this might occur can be gained from geological studies of pseudotachylytes within otherwise ductile shear zones, found

in areas of ancient and current continental collision, where rocks which were once part of the deep crust are today exposed at the surface.

Pseudotachylytes are thin veins of very fine grained material associated with melting during an earthquake (see section 2.7). Several studies have detailed their presence in dominantly ductile shear zones within continental crust and determined the physical conditions under which this apparently brittle deformation occurred (Clarke & Norman 1993, Austrheim & Boundy 1994, White 1996). The pseudotachylytes were inferred to have formed at temperatures of between 500 and 800 °C and at depths of 10 to at least 60 km, but the homologous temperatures have not been determined. In the studies of Clarke & Norman (1993) and White (1996), the instabilities are believed to have occurred in a nearly dry environment, with little or no free fluid. The pseudotachylytes of the Bergen Arc in Norway, studied by Austrheim & Boundy (1994), are associated with the fluid induced eclogitisation of anhydrous granulite (high temperature) facies rocks. However, the pseudotachylytes occurred only in the dry granulite rocks, rather than in the hydrous zones of eclogitisation. Dry rocks are stronger than rocks containing water and hence can support sufficiently high stresses for unstable failure to be a feasible mode of deformation. However, at significant depth, some mechanism of embrittlement is required to allow frictional sliding.

Obata & Karato (1995) described occurrences of pseudotachylytes in peridotite. They showed that the pseudotachylytes resulted from almost complete melting, and were not ultramylonites produced by extreme grain size reduction in a ductile deformation regime. However, analyses of the deformation microstructures by Jin *et al.* (1998) revealed that shear had been localised into a narrow zone through the ductile process of dynamic recrystallisation to progressively smaller grain sizes. At some point, the deformation became unstable and brittle failure occurred, associated with melting along the fault zone. This process was thought to have occurred under relatively high stresses and temperatures of up to about 800 °C, and the peridotite has been shown to be largely anhydrous (Brodie & Rutter 1987). Thus, all these studies suggest, or are consistent with, a common process of shear localisation in a ductile regime eventually leading to brittle failure, once a sufficiently high stress or strain rate is achieved. The conditions common to each example are dry and therefore strong rocks, temperatures no higher than

about 800 °C and high strain rates. Jin *et al.* (1998) showed that the grain size adjacent to the pseudotachylyte was only a few microns (μm). In laboratory experiments on magnesium germanate (which has the same crystal structure as olivine), Burnley *et al.* (1991) showed that grain sizes of less than 1 μm allowed frictional sliding at high pressures, apparently by reducing the effective coefficient of friction. Thus, it would seem reasonable to suggest that instability in the peridotite examined by Jin *et al.* (1998) also occurred due to a reduction in the effective coefficient of friction by extreme grain size reduction. Melting may have been caused by frictional heating after the onset of slip, or may have resulted largely from heating by viscous dissipation prior to the onset of slip.

Grain size reduction by dynamic recrystallisation occurs only when the dominant mechanism of deformation is dislocation creep [see for example, Twiss & Moores (1992)]. However, the influence of grain size on strength in a dislocation creep regime is small. The sort of feedback described above, where strain concentrates in a region of smaller grain size, requires active diffusional creep. However, in this regime, dynamic recrystallisation does not occur. Jin *et al.* (1998) suggest that the pseudotachylyte was produced under conditions near the boundary between the two mechanisms, with both diffusion creep and dislocation creep occurring simultaneously. This boundary is largely temperature, rather than pressure, dependent and so this mechanism of instability is a good candidate for causing deep seismicity which, as shown in section 4.8, is limited by a critical homologous temperature of 0.4 $\times$ the dry peridotite solidus. Figure 7.2 shows shear stresses and homologous temperatures at which different mechanisms of deformation occur for olivine with a grain size of 1 mm at pressures equivalent to 100 km depth. Whilst the typical grain size of the mantle may be of the order of 1 cm, examination of a deformation map for 0.1 mm grain size showed that the map changed significantly with grain size only at low shear stresses of less than 10 MPa, an order of magnitude below those found in slabs. Determination of a deformation map for a grain size of 1 cm has been prevented by the large scale of the experimental apparatus required so, given the lack of information, I extrapolate the behaviour observed between 0.1 and 1 mm and assume that the map at high shear stresses is largely unchanged. The range of conditions which occur within a slab are shaded and it can be seen that a homologous temperature of 0.4 lies just inside the field of diffusion creep but is close to the boundary with dislocation creep,

consistent with the deductions of Jin *et al.* (1998), based on direct observations of a pseudotachylyte in an exhumed mantle peridotite. If deep instability does require this interplay of different deformation mechanisms, then the nucleation of instability would be limited to a relatively narrow temperature range, predicting the occurrence of zones of seismicity on either side of the cold core of the slab in which only diffusion creep is active. Such double seismic zones are observed, at progressively greater depth in progressively colder subduction zones, in the Shumagin slab (figure 4.5), the Japan slab (figure 4.4) and in the Tonga slab (Wiens *et al.* 1993).

To test the consistency of this hypothesis with the observed earthquake patterns, I plotted the position of a homologous temperature of 0.4 onto the thermal profiles for the Japan and Aluetian subduction zones. The Japan double seismic zone does coincide approximately with the homologous temperature, but scatter in the hypocentres means that this result is inconclusive (recall that the Japan double seismic zone also coincided with the predicted stability limit of serpentine). However, the hypocentres defining the Aleutian double seismic zone are well located and provide a good test of the hypothesis. Figure 7.3 shows that both the lower zone of seismicity and the upper zone below a depth of about 90 km do coincide with the homologous temperature. At shallower depths, the upper zone of seismicity occurs at much lower temperatures, implying that the earthquakes may be caused by two different mechanisms. Most of the upper zone may be due to normal frictional sliding, enabled either by high stresses or the development of high pore–fluid pressures, whilst the lower zone, and possibly the deep upper zone, are consistent with the nucleation of a plastic instability during dominantly ductile deformation, normal brittle deformation being suppressed by the high confining pressures. The notion of separate mechanisms for deep and shallow earthquakes is supported by the observation that shallow crustal earthquakes do not terminate at a homologous temperature of 0.4. For a wet basaltic composition, the onset of plasticity at 450 °C corresponds to a homologous temperature of about 0.64. The corresponding homologous temperature for continental crust is 0.4 (dry) to 0.5 (wet).

The conditions described above of dry, strong rocks deforming in a ductile manner under high stresses at temperatures of less than 800 °C may be a good description

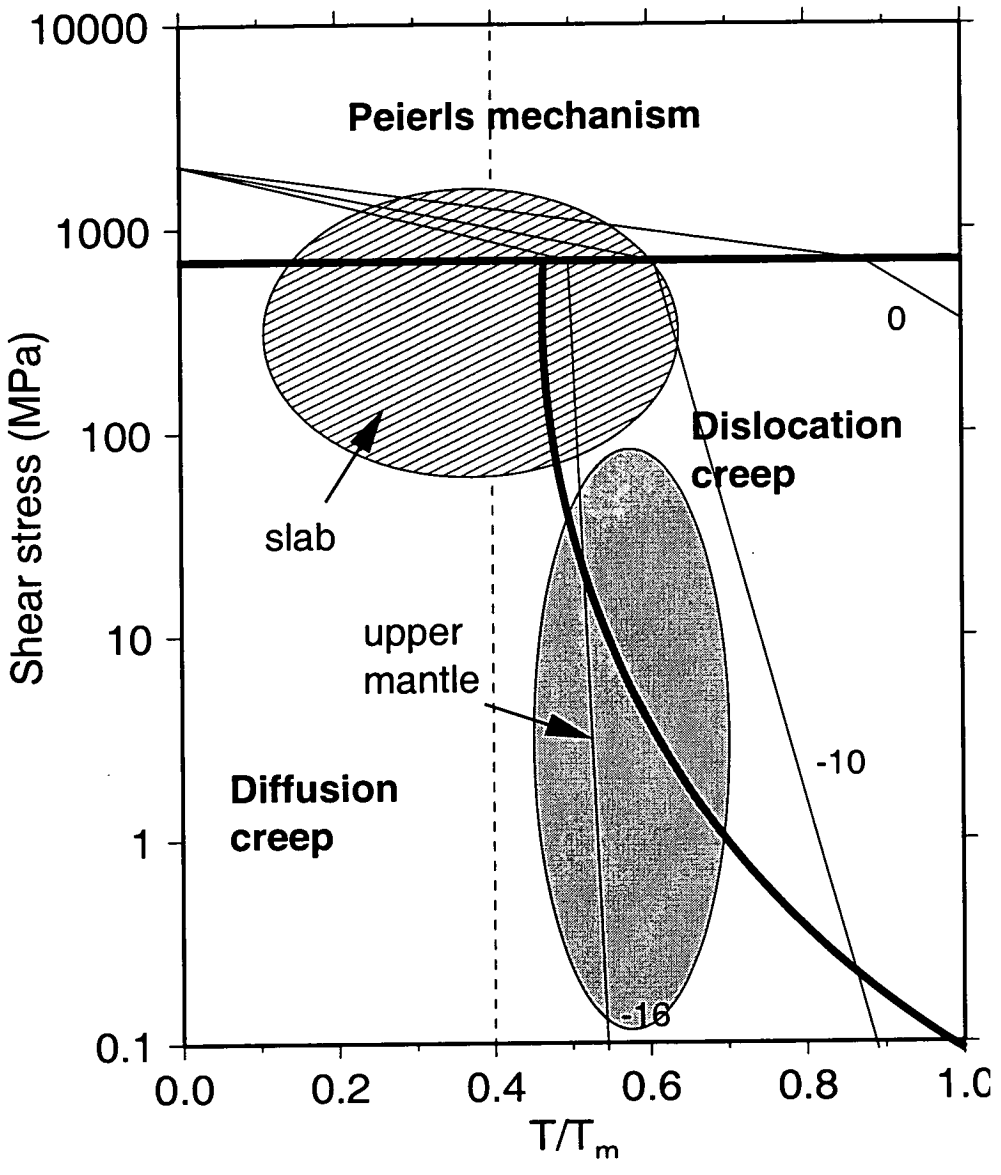

Figure 7.2.

Deformation mechanisms as a function of shear stress and homologous temperature. The domains of each different mechanism are calculated assuming an olivine rheology with a grain size of 1 mm, at a depth of 100 km. The shaded regions encompass the range of conditions which occur in the subducting slab (striped) and normal upper mantle (grey). A homologous temperature of 0.4 is indicated by the dashed line and approximate strain rates are illustrated schematically by the fine lines, labelled as powers of $10\,s^{-1}$. Redrawn from figures by Frost & Ashby (1982) and Karato, Paterson & Fitzgerald (1986).

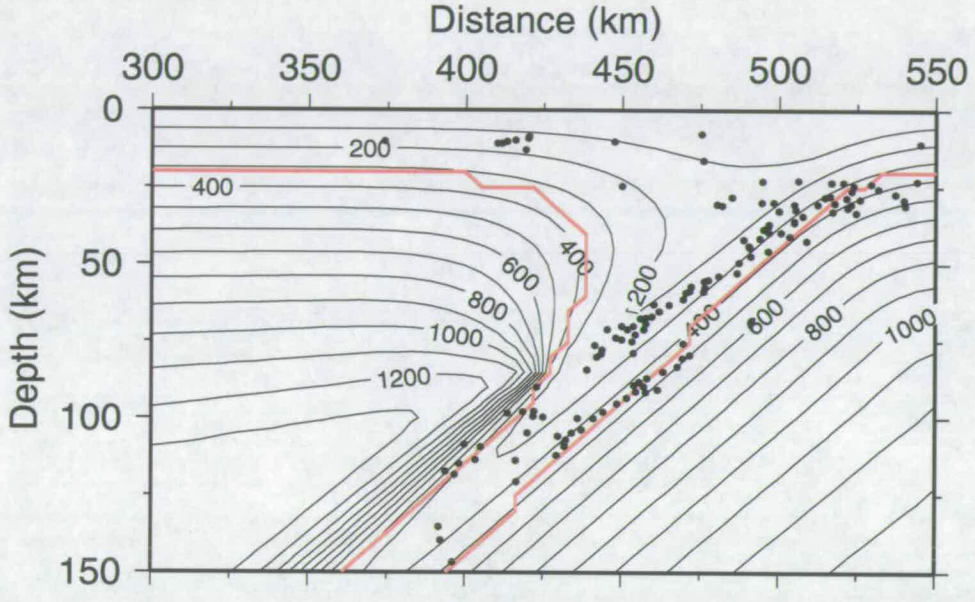

Figure 7.3.
Profile showing the Shumagin double seismic zone, thermal model and a homologous temperature of 0.4. The red line marks 0.4 × the dry peridotite solidus, whilst the black dots are earthquake hypocentres from Abers (1994). The lower zone of seismicity and the upper zone below about 90 km coincide with the homologous temperature.

of large parts of the subducting slab, particularly the lithospheric mantle. The most accurate earthquake locations with respect to position within the slab are those determined by the ANCORP working group (1999), who imaged the slab geometry beneath part of the Andes using artificial source, deep seismic reflection studies. Intermediate depth earthquake hypocentres were determined from a temporary deployment of a local network of seismometers. The locations show that a large majority of the earthquakes occur within the subducting lithospheric mantle. In a study of earthquakes between 300 and 400 km depth in the Izu–Bonin region, Nakamura, Ando & Ohkura (1998) identified a seismic phase arriving shortly after P as an S–to–P conversion from the upper slab–mantle interface. They used the arrival time of this phase to show that the earthquakes must have occurred about 20 km perpendicularly below the slab surface, in the lithospheric mantle. As described in section 4.6, the lithosphere may well be nominally or even completely anhydrous below the crust, so these observations are consistent with the idea of seismogenesis occurring in a relatively dry environment.

The results of my thermal modelling, presented in section 4.8, showed that deep seismicity could probably occur up to temperatures of at least 700 °C. The results from the field studies described above suggest that seismicity occurs up to about 800 °C. Given that my thermal models provide a minimum estimate of the temperature in a subducting slab, these two values are in good agreement and suggest that seismicity does terminate at around 800 °C at large scale geological strain rates, independently of pressure, and consistent with the hypothesis of grain size reduction with or without melting as an instability mechanism.

7.4 Seismicity in Subducting Continental Lithospheric Mantle?

Further evidence that deep earthquakes can occur in dry environments comes from the observed deep seismicity beneath the Hindu Kush and beneath the India–Myanmar (formerly Burma) border, at either end of the Himalaya (near the syntaxes, or points of termination, of this great mountain chain). Pegler & Das (1998) have relocated the seismicity beneath the Hindu Kush using the

method of joint epicentre determination (Douglas 1967), and the earthquakes clearly define a slab–like structure descending into the mantle. However, according to constraints on the age of continental collision and the convergence rate, any oceanic lithosphere subducted prior to the collision of India and Asia should now have sunk into the mantle transition zone or beyond [see, for example, the calculations in Pegler & Das (1998)]. Thus, the seismicity shown in figure 7.4, at depths of 100–300 km, is most unlikely to be occurring in oceanic lithosphere.

Continental crust is widely believed to be too buoyant to subduct, and figure 7.4 shows that there is little seismicity below the Hindu Kush at depths less than 80 km depth, i.e. at crustal depths (Mooney, Laske & Masters 1998). It appears that the crust in this collision zone is deforming with a low seismic efficiency, suggesting that it is weak, possibly due to the influence of heating and / or fluids, whilst the mantle is stronger and deforming with a much higher seismic efficiency. The simplest scenario which explains the observed patterns of seismicity is that the continental crust and mantle are separating, with the crust remaining at the surface and the mantle subducting, in agreement with the extensive study of geological structure by Meyer *et al.* (1998). If this is the case, then these deep earthquakes are occurring in the uppermost continental lithospheric mantle, which is probably anhydrous. The lack of deep seismicity beneath the central part of the Himalaya does not preclude subduction, but suggests that if it is occurring, then it is much slower than near the syntaxes, allowing the lithosphere to warm sufficiently to prohibit the occurrence of deep earthquakes.

7.5 Classifying Seismicity

I have shown in sections 4.7 and 4.8 that the termination of deep seismicity is strongly controlled by temperature. Such strong temperature control is also observed for shallow earthquakes, with seismicity in the continental crust usually being limited by the 300 °C isotherm, and in the oceanic crust by the 450 °C isotherm (Scholz 1998, and references therein). These temperatures represent the onset of plasticity at typical geological strain rates in quartz and feldspar respectively and, at higher temperatures, ductile deformation is dominant (Brace

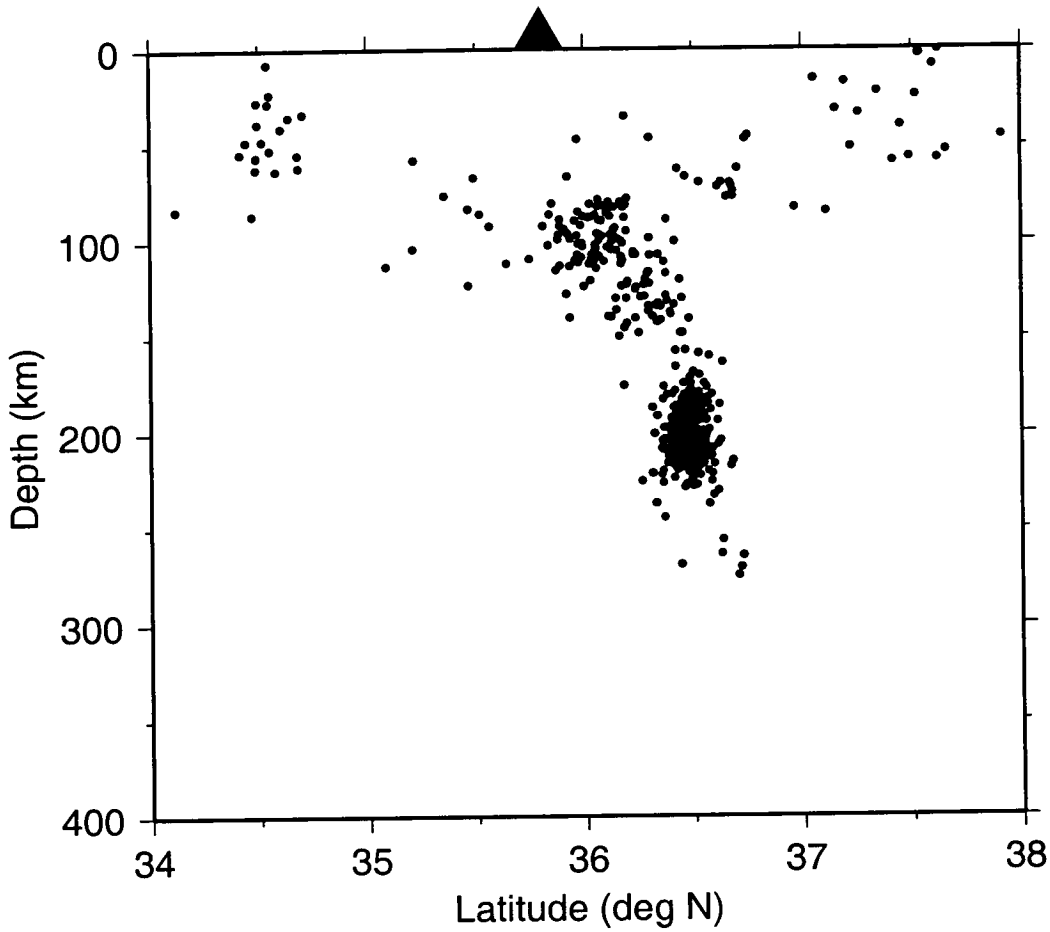

Figure 7.4.
Cross section showing seismicity beneath the Hindu–Kush, near the western syntaxis of the Himalaya. Black dots are earthquake hypocentres from the EHB catalogue. The large black triangle marks the approximate position of the topographic high of the Hindu–Kush mountains and the section is oriented north–south, parallel to the apparent direction of subduction at this point. The plot shows seismicity from the region 70–71 °E.

& Kohlstedt 1980). Some shallow earthquakes are observed to occur at depths corresponding to higher temperatures than these, up to about 600 °C, such as beneath Hawaii or beneath the central Indian Ocean (Wiens & Stein 1983, Denlinger 1992), and are discussed below.

Earthquakes beneath Hawaii cluster in a linear feature which extends to 60 km depth (Klein *et al.* 1987) and which is thought to coincide with a magma conduit (Ryan 1988). The earthquakes are probably encouraged by increased pore fluid pressure reducing the effective normal stress, since rising magmas release fluid in response to falling pressure. Beneath the Central Indian Ocean, seismicity occurs to 40 km depth (Buchanan 1998), where the confining pressure is approximately 1.2 GPa. There are at least three mechanisms which may be causing this seismicity and which I describe below. The actual mechanism responsible is not important for this discussion, since the example serves to highlight how it is theoretically possible to classify earthquake sources more precisely than simply describing the depths at which they occur and assuming that different depth populations correspond to different source processes.

The unusually deep seismicity beneath the Central Indian Ocean may be occurring by normal brittle failure. If the local strain rate is sufficiently high and the temperature sufficiently low, then the maximum shear stress applied to the lithosphere exceeds the confining pressure and failure by dry frictional sliding could result. Beekman (1994) showed that this may be the case if the strain rate is of the order of $10^{-15}\,s^{-1}$. However, if the lithosphere is sufficiently weak (i.e. the strain rate sufficiently low, the temperature sufficiently high or the rock wet) to prevent the build up of such high shear stresses, then some mechanism of embrittlement is required. Buchanan (1998) proposed that the large volume of fluid rich sediments forming the Bengal fan, deposited on the ocean floor above these unusually deep earthquakes, may develop high pore fluid pressures, which are transmitted to great depth. The resulting decrease in the effective stress would encourage seismicity. However, whether or not high pore fluid pressures could be transmitted to 40 km depth from the surface is unclear. The third possible mechanism is that of shear localisation in a dominantly ductile environment, as previously described in section 7.3. These three mechanisms correspond to three general categories into which earthquakes can be divided based upon their source

processes: i) those that occur at shallow depths by dry frictional sliding; ii) those which are enabled by a reduction in the effective stress, caused by an increase in pore fluid pressure; iii) those which are enabled by a decrease in the coefficient of friction along a shear zone, either by adiabatic heating or by grain size reduction. The latter two categories can, in theory, occur at any depth, although the details of the high pore fluid pressure mechanism will vary with depth as described in section 2.5.

I propose that deep seismicity occurs in material that is essentially cold and dry. At typical geological strain rates, the maximum temperature at which rocks can support seismicity appears to be no more than about 800 °C. Under such conditions, only a small fraction of the total deformation can occur by seismic slip, and it seems likely that this slip will result from a reduction in the coefficient of friction along a shear zone by grain size reduction and heating through viscous dissipation. Certainly, there is no compelling evidence for the occurrence of either dehydration induced embrittlement or of transformational faulting, as has been demonstrated throughout this thesis. The association of earthquakes with melt generation along the fault plane (section 7.3) is compatible with the kinetic descriptions of the eight deep earthquakes analysed in chapter 6. The wide variation in rupture velocities may be related to the extent of melting along the fault plane, although whether extensive melting would favour fast or slow rupture speeds relative to those produced by a fault zone consisting of extremely fine grained solids is unknown. Such a fault zone is predicted by the transformational faulting hypothesis and it is unclear how this mechanism could lead to the wide range of observed rupture velocities without also invoking the formation of a partial or complete melt. Melting may result in a small negative volume change, but it is likely that such a change would be compensated by thermal expansion associated with the heating of the shear zone. Thus, the proposed mechanism of ductile shear localisation leading to brittle failure is consistent with the observed double couple focal mechanisms of deep earthquakes.

Despite the considerable body of evidence presented here, it would be presumptuous to discount the rôle which fluids and solid–solid phase transformations may play in encouraging some deep seismicity. None of the results presented in this thesis categorically reject the hypotheses of dehydration induced embrittlement

or transformational faulting occurring at depth, and it is plausible that not all deep earthquakes are enabled by the same grain–scale mechanism. Thus, further studies are required to advance our understanding of catastrophic shear failure and the conditions under which it may occur. However, the simplest hypothesis consistent with the available data is that only one mechanism, that of dynamic grain size reduction, is required.

7.6 Further Work

One of the key difficulties which hinders progress in the understanding of deep earthquakes is the lack of knowledge about their exact location in relation to the slab. We can be fairly confident that they occur within it, but little detail is available beyond that. Two recent studies, Nakamura *et al.* (1998) and the ANCORP working group (1999), have improved this situation by using converted phases and deep seismic reflection studies, respectively, to locate seismicity with respect to the slab. To improve this situation further, high resolution regional tomographic studies are required to determine slab geometries and locations *independently* from earthquake hypocentres. In the past, the latter have sometimes been used to locate the former, making the results unsuitable for the type of work undertaken here.

Detailed tomographic studies may also shed some light on another very important issue. In many slabs, seismicity is observed to terminate at intermediate depths in the upper mantle (see figure 4.2, for example, which illustrates the case for the Ryukyu slab). We do not know whether this is because the slab becomes too hot to support seismicity, or whether the slab itself simply does not extend beyond that depth. However, the complex velocity structure of subduction zones makes accurate ray tracing difficult and so may limit the resolution of such regional and local tomographic investigations.

The results of chapter 6 showed that the eight earthquakes investigated could all have been caused by a double couple source mechanism. However, the constant volume component of deformation was not especially well constrained and the possibility of a component of pure shear remains. In fact, many CMT solutions

for deep earthquakes do suggest such a component. If this component is real, then the relative amplitude method should be capable of detecting it, although the loss of resolution through the various adaptations required for its application to deep earthquakes may reduce its capacity to do so. If the pure shear shown by the CMT solutions is not a reflection of the source, then its existence is surprising. Given the low frequencies used in the CMT inversion, distortion of the wavefield by local, unmodelled velocity structure should not be an important issue. An investigation of the effect of small scale, widely distributed heterogeneity on source type inversion may be warranted, possibly using a methodology similar to that of Vasco & Johnson (1989). Their method allows the *significance* of certain moment tensor components, such as the value of T, to be determined.

To take a wider view, little is known independently about the distribution of fluids in the lithosphere. Developments in this field probably require the combined use of both deep seismic and electromagnetic techniques, in conjunction with careful examination of the petrological evidence available from large exposures of rocks uplifted from great depth and from mantle xenoliths.

Chapter 8

Conclusions

The predicted envelope of serpentine dehydration determined for the Shumagin slab appears not to correlate with the well located twin zones of seismicity observed within the slab. Assuming that the upper zone of seismicity occurs at, or near to, the surface of the slab, then the lower zone of earthquakes occurs 200 °C inside the equilibrium stability limit of serpentine and, thus, is almost certainly not caused by dehydration. Analysis of geotherms for both very cold and hot subduction zones showed that dehydration reactions are also unrelated to any seismicity occurring in the crust of the subducting slab. However, if hydrous phases exist in the lithospheric mantle, then some of the water they contain may be retained by dense hydrous magnesium silicates to at least the base of the transition zone, and possibly into the lower mantle.

Calculation of the thermal parameters, an index of slab temperature, for many different subduction zone segments revealed a linear relationship between the thermal parameter and the maximum depth of seismicity, suggesting a strong thermal control on the termination of seismicity. Minimum slab geotherms measured from two dimensional thermal models of specific sections of subduction zone showed that the deepest seismicity always occurred at a temperature equivalent to about 0.4 $\times$ the dry peridotite solidus, i.e. at a constant homologous temperature, independent of depth. This suggests that all deep seismicity may be attributable to a single, thermally controlled, mechanism, rather than the separate mechanisms which have often been proposed to explain different depth

populations of seismicity. The predicted position of 0.4 × DPS accurately coincides with the observed intermediate depth double seismic zone in the Shumagin slab. The thermal models also showed that the volcanic arc was always located above mantle with an approximately constant maximum temperature, suggesting that the process of melting in the mantle wedge above the slab is also governed entirely by temperature, rather than pressure. Thus, thermal controls appear to dominate the major subduction zone processes of melting and seismogenesis, implying that pressure–dependent mineral reactions can be ruled out as a possible local mechanism for instability.

Moment tensor inversion for the source type and orientation of eight deep earthquakes revealed that teleseismic records of the phases P, pP and sP were, for all eight events, consistent with a double couple source. The inversions were performed using the relative amplitude method, which provided high resolution of any potential volumetric component. The most well constrained source volumetric component was explicitly shown to be greater than –2% and less than +4%, assuming no component of pure shear. Various additions and alterations to the method were necessary to adapt it for use with deep earthquakes, and excellent agreement of the resulting relative amplitude solutions with the Harvard CMT solutions, independently determined using different data and a different method, proved that these adaptations were successful.

Variations in the duration of the seismic phases P and pP provided good constraint on the geometry and velocity of rupture. Deep earthquakes may occur on both horizontal and vertical faults, and the speed of rupture may vary dramatically even within a single segment of slab. Rupture velocities were shown to have a minimum range of $1.2 \leq V_r \leq 4.5\,\mathrm{km\,s^{-1}}$ and showed no correlation with pressure, temperature or fault plane geometry.

The results presented in this thesis do not positively identify the process by which deep seismogenesis occurs. However, they suggest that deep seismicity is unrelated to mineral reactions because its occurrence is entirely governed by temperature. A mechanism of brittle instability occurring in a dominantly ductile deformation regime (a plastic instability), which incorporates a reduction in the coefficient of friction along the fault plane either by melting or by grain size reduction, is entirely consistent with both the results presented here and

with published observations of pseudotachylytes in ductile shear zones which are exposed in the field. Such a mechanism requires a dry environment, with reasonably high strain rates and low temperatures. Deep seismicity, then, is predicted to terminate once the temperature exceeds the homologous limit of 0.4 described above.

Bibliography

Abers, G. (1994), 'Three–dimensional inversion of regional P and S arrival times in the East Aleutians and sources of subduction zone gravity highs', *Journal of Geophysical Research* **99**(B3), 4,395–4,412.

Agee, C. & Walker, D. (1993), 'Olivine floatation in mantle melt', *Earth and Planetary Science Letters* **114**, 315–324.

Akaogi, M., Ito, E. & Navrotsky, A. (1989), 'Olivine—modified spinel—spinel transitions in the system Mg_2SiO_4–Fe_2SiO_4: calorimetric measurements, thermochemical calculation, and geophysical application', *Journal of Geophysical Research* **94**(B11), 15,671–15,685.

Aki, K. & Richards, P. (1980), *Quantitative Seismology: theory and methods*, Vol. 1, W.H. Freeman & Co., San Francisco.

Akimoto, S. & Akaogi, M. (1980), 'The system Mg_2SiO_4–MgO–H_2O at high pressures and temperatures; possible hydrous magnesian silicates in the mantle transition zone', *Physics of the Earth and Planetary Interiors* **23**(4), 268–275.

ANCORP working group (1999), 'Seismic reflection image revealing offset of Andean subduction–zone earthquake locations into the oceanic mantle', *Nature* **397**, 341–344.

Anderson, D. (1967), 'Phase changes in the upper mantle', *Science* **157**, 1,165–1,173.

Anderson, D. (1989), *Theory of the Earth*, Blackwell Scientific Publications.

Anderson, O., Schreiber, E., Liebermann, L. & Soga, N. (1968), 'Some elastic constant data on minerals relevant to geophysics', *Rev. Geophys. Space Phys.* **6**, 491–524.

Anderson, R., Delong, S. & Schwarz, W. (1978), 'Thermal model for subduction with dehydration in the downgoing slab', *Journal of Geology* **86**, 731–739.

Andrews, D. & Sleep, N. (1974), 'Numerical modelling of tectonic flow behind island arcs', *Geophys. J.R. Astron. Soc.* **38**, 237–251.

Antolik, M., Dreger, D. & Romanowicz, B. (1996), 'Finite fault source study of the great 1994 deep Bolivia earthquake', *Geophysical Research Letters* **23**, 1,589–1,592.

Archambeau, C., Flinn, E. & Lambert, D. (1969), 'Fine structure of the upper mantle', *Journal of Geophysical Research* **74**(25), 5,825–5,866.

Austrheim, H. & Boundy, T. (1994), 'Pseudotachylytes generated during seismic faulting and eclogitization of the deep crust', *Science* **265**, 82.

Backus, G. & Mulcahy, M. (1976), 'Moment tensors and other phenomenological descriptions of seismic sources — I. Continuous displacements', *Geophys. J.R. Astron. Soc.* **46**, 341–361.

Barazangi, M. & Isacks, B. (1971), 'Lateral variations of seismic–wave attenuation in the upper mantle above the inclined earthquake zone of the Tonga island arc: deep anomaly in the upper mantle', *Journal of Geophysical Research* **76**(35), 8,493–8,516.

Batchelor, G. (1967), *An introduction to fluid dynamics*, Cambridge University Press.

Beck, S., Silver, P., Wallace, T. & James, D. (1995), 'Directivity analysis of the deep Bolivian earthquake of June 9, 1994', *Geophysical Research Letters* **22**(16), 2,257–2,260.

Beekman, F. (1994), Tectonic modelling of thick–skinned compressional intraplate deformation, PhD thesis, Vrije Universiteit Amsterdam.

Bina, C. (1996), 'Phase transition buoyancy contributions to stresses in subducting lithosphere', *Geophysical Research Letters* **23**(24), 3,563–3,566.

Bina, C. & Helffrich, G. (1994), 'Phase transition Clapeyron slopes and transition zone seismic discontinuity topography', *Journal of Geophysical Research* **99**(B8), 15,853–15,860.

Bock, G. (1994), 'Synthetic seismogram images of upper mantle structure: no evidence for a 520 km discontinuity', *Journal of Geophysical Research* **99**(B8), 15,843–15,851.

Bollinger, G. (1968), 'Determination of earthquake fault parameters from long–period P waves', *Journal of Geophysical Research* **73**(2), 785–807.

Boyd, T. & Creager, K. (1991), 'The geometry of Aleutian subduction: three dimensional seismic imaging', *Journal of Geophysical Research* **96**(B2), 2,267–2,291.

Brace, W. & Kohlstedt, D. (1980), 'Limits on lithospheric stress imposed by laboratory experiments', *Journal of Geophysical Research* **85**(B11), 6,248–6,252.

Bridgman, W. (1945), 'Polymorphic phase transitions and geological phenomena', *American Journal of Science* **243a**, 90–97.

Brodie, K. & Rutter, E. (1987), 'Deep crustal extensional faulting in the Ivrea Zone of northern Italy', *Tectonophysics* **140**, 193–212.

Buchanan, S. (1998), Seismicity and tectonics of the Central Indian Ocean Basin, PhD thesis, University of Edinburgh.

Burnley, P. (1995), 'The fate of olivine in subducting slabs: a reconnaissance study', *American Mineralogist* **80**, 1,293–1,301.

Burnley, P., Green, H. & Prior, D. (1991), 'Faulting associated with the olivine to spinel transformation in Mg_2GeO_4 and its implications for deep earthquakes', *Journal of Geophysical Research* **96**(B1), 425–443.

Burridge, R., Conn, G. & Freund, L. (1979), 'The stability of a rapid mode II shear crack with finite cohesive traction', *Journal of Geophysical Research* **85**(B5), 2,210–2,222.

Byerlee, J. (1968), 'Brittle-ductile transition in rocks', *Journal of Geophysical Research* **73**(14), 4,741–4,750.

Cadek, O. & van den Berg, A. (1998), 'Radial profiles of temperature and viscosity in the Earth's mantle inferred from the geoid and lateral seismic structure', *Earth and Planetary Science Letters* **164**, 607–615.

Carlson, R. & Johnson, H. (1994), 'On modeling the thermal evolution of the oceanic upper mantle: An assessment of the cooling plate model', *Journal of Geophysical Research* **99**(B2), 3,201–3,214.

Carlson, R. & Miller, D. (1997), 'A new assessment of the abundance of serpentinite in the oceanic crust', *Geophysical Research Letters* **24**(4), 457–460.

Cervený, V. (1983), 'Synthetic body wave seismograms for laterally varying layered structures by the Gaussian beam method', *Geophys. J.R. Astron. Soc.* **73**, 389–426.

Chase, C. (1978), 'Plate kinematics: The Americas, East Africa and the rest of the World', *Earth and Planetary Science Letters* **37**, 355–368.

Chen, W. (1995), 'En echelon ruptures during the great Bolivian earthquake of 1994', *Geophysical Research Letters* **22**(16), 2,261–2,264.

Christensen, U. (1997), 'Influence of chemical buoyancy on the dynamics of slabs in the transition zone', *Journal of Geophysical Research* **102**(B10), 22,435–22,443.

Clarke, G. & Norman, A. (1993), 'Generation of pseudotachylite under granulite facies conditions, and its preservation during cooling', *Journal of Metamorphic Geology* **11**, 319–335.

Clauser, C. & Huenges, E. (1995), Thermal conductivity of rocks and minerals, *in* T. Ahrens, ed., 'Rock physics and phase relations: a handbook of physical constants', number 3 *in* 'AGU Reference Shelf', AGU, Washington, DC., pp. 105–126.

Collier, J. & Helffrich, G. (1997), 'Topography of the "410" and "660" km seismic discontinuities in the Izu-Bonin subduction zone', *Geophysical Research Letters* **24**(12), 1,535–1,538.

Creager, K. & Boyd, T. (1991), 'The geometry of Aleutian subduction: three dimensional kinematic flow model', *Journal of Geophysical Research* **96**(B2), 2,293–2,307.

Creager, K. & Jordan, T. (1984), 'Slab penetration into the lower mantle', *Journal of Geophysical Research* **89**(B5), 3,031–3,049.

Creager, K. & Jordan, T. (1986), 'Slab penetration into the lower mantle beneath the Mariana and other island arcs of the northwest Pacific', *Journal of Geophysical Research* **91**(B3), 3,573–3,589.

Crotwell, H. P., Owens, T. & Ritsema, J. (1999), 'The TauP toolkit: Flexible seismic travel–time and ray–path utilities', *Seismological Research Letters* **70**(2), 154–160.

Cullen, E. & Douglas, A. (1975), 'P–wave seismograms from three seismic sources in SW USSR', *Geophys. J.R. Astron. Soc.* **41**, 11–28.

Däβler, R. & Yuen, D. (1996), 'The metastable olivine wedge in fast subducting slabs: Constraints from thermo-kinetic coupling', *Earth and Planetary Science Letters* **137**, 109–118.

Davies, D. & McKenzie, D. (1969), 'Seismic travel time residuals and plates', *Geophys. J.R. Astron. Soc.* **18**, 51–63.

Davies, J. (1999), 'The role of hydraulic fractures and intermediate–depth earthquakes in generating subduction–zone magmatism', *Nature* **398**, 142–145.

Davies, J. & Stevenson, D. (1992), 'Physical model of source region of subduction zone volcanics', *Journal of Geophysical Research* **97**(B2), 2,037–2,070.

Davis, J. (1986), *Statistics and data analysis in geology*, 2nd edn, John Wiley & Sons, Inc.

Davis, J. & Henson, I. (1993), Development of an X–windows tool to compute Gaussian beam synthetic seismograms, Technical Report TGAL-93-03, Phillips Laboratory, Hanscom AFB, MA, USA.

Demets, C., Gordon, R., Argus, D. & Stein, S. (1990), 'Current plate motions', *Geophysics Journal International* **101**(2), 425–478.

Denlinger, R. (1992), 'A revised estimate for the temperature structure of the oceanic lithosphere', *Journal of Geophysical Research* **97**(B5), 7,219–7,222.

Dennis, J. & Walker, C. (1965), 'Earthquakes resulting from metastable phase transitions', *Tectonophysics* **2**(5), 401–407.

Ding, X.-Y. & Grand, S. (1994), 'Seismic structure of the deep Kurile subduction zone', *Journal of Geophysical Research* **99**(B12), 23,767–23,786.

Douglas, A. (1967), 'Joint epicentre determination', *Nature* **215**, 47–48.

Douglas, A., Bowers, D., Marshall, P., Young, J., Porter, D. & Wallis, N. (1999), 'Putting nuclear–test monitoring to the test', *Nature* **398**, 474–475.

Douglas, A., Hudson, J. & Blamey, C. (1972), 'A quantitative evaluation of seismic signals at teleseismic distances III — computed P and Rayleigh wave seismograms', *Geophys. J.R. Astron. Soc.* **28**, 385–410.

Douglas, A., Marshall, P., Young, J. & Hudson, J. (1974), 'Seismic source in East Kazakhstan', *Nature* **248**, 743–745.

Dufumier, H. & Rivera, L. (1997), 'On the resolution of the isotropic component in moment tensor inversion', *Geophysical Journal International* **131**, 595–606.

Durham, W., Mirkovich, V. & Heard, H. (1987), 'Thermal diffusivity of igneous rocks at elevated pressure and temperature', *Journal of Geophysical Research* **92**(B11), 11,615–11,634.

Dziewonski, A. & Woodhouse, J. (1983), 'An experiment in systematic study of global seismicity: centroid moment tensor solutions for 201 moderate and

large earthquakes of 1981', *Journal of Geophysical Research* **88**(B4), 3,247–3,271.

Dziewonski, A., Chou, T.-A. & Woodhouse, J. (1981), 'Determination of earthquake source parameters from waveform data for studies of global and regional seismicity', *Journal of Geophysical Research* **86**(B4), 2,825–2,852.

Eggleton, R., Boland, J. & Ringwood, A. (1978), 'High pressure synthesis of a new aluminium silicate: $Al_5Si_5O_{17}(OH)$', *Geochemical Journal* **12**, 191–194.

Engdahl, E., Sleep, N. & Lin, M.-T. (1977), 'Plate effects in north Pacific subduction zones', *Tectonophysics* **37**, 96–116.

Engdahl, E., van der Hilst, R. & Buland, R. (1998), 'Global teleseismic earthquake relocation with improved travel times and procedures for depth determination', *Bull. Seismol. Soc. Am.* **88**(3), 722–743.

Estabrook, C. & Bock, G. (1995), 'Rupture history of the great Bolivian earthquake: slab interaction with the 660km discontinuity?', *Geophysical Research Letters* **22**(16), 2,277–2,280.

Evison, F. (1963), 'Earthquakes and faults', *Bull. Seismol. Soc. Am.* **53**, 873–891.

Fitton, J. (1971), 'The generation of magmas in island arcs', *Earth and Planetary Science Letters* **11**, 63–67.

Flinn, D. (1962), 'On folding during three-dimensional progressive deformation', *Quart. J. Geol. Soc. London* **118**, 385–433.

Freund, L. (1990), *Dynamic fracture mechanics*, Cambridge University Press, New York.

Frost, D. & Fei, Y. (1998), 'Stability of phase D at high pressure and high temperature', *Journal of Geophysical Research* **103**(B4), 7,463–7,474.

Frost, H. & Ashby, M. (1982), *Deformation Mechanism Maps*, Pergamon Press, Oxford.

Fujisawa, H., Fujii, N., Mizutani, H., Kanamori, H. & Akimoto, S. (1968), 'Thermal diffusivity of Mg_2SiO_4, Fe_2SiO_4, and NaCl at high pressures and temperatures', *Journal of Geophysical Research* **73**(14), 4,727–4,733.

Fujita, K., Engdahl, E. & Sleep, N. (1981), 'Subduction zone calibration and teleseismic relocation of thrust zone events in the central Aleutian Islands', *Bull. Seismol. Soc. Am.* **71**, 1,805–1,828.

Furukawa, Y. (1993), 'Magmatic processes under arcs and formation of the volcanic front', *Journal of Geophysical Research* **93**(B5), 8,309–8,319.

Gasparik, T. (1990), 'Phase relations in the transition zone', *Journal of Geophysical Research* **95**(B10), 15,751–15,769.

Giardini, D. (1983), Regional deviation of earthquake source mechanisms from the double couple model, *in* H. Kanamori & E. Boschi, eds, 'Earthquakes: Observations, Theory and Interpretations', North Holland Publishing Company.

Giardini, D. (1984), 'Systematic analysis of deep seismicity: 200 centroid–moment tensor solutions for earthquakes between 1977 and 1980', *Geophys. J.R. Astron. Soc.* **77**, 883–914.

Giardini, D. & Woodhouse, J. (1984), 'Deep seismicity and modes of deformation in Tonga subduction zone', *Nature* **307**, 505–509.

Giardini, D. & Woodhouse, J. (1986), 'Horizontal shear flow in the mantle beneath the Tonga arc', *Nature* **319**, 551–555.

Goes, S. & Ritsema, J. (1995), 'A broadband P wave analysis of the large deep Fiji Island and Bolivia earthquakes of 1994', *Geophysical Research Letters* **22**(16), 2,249–2,252.

Grand, S. (1994), 'Mantle shear structure beneath the Americas and surrounding oceans', *Journal of Geophysical Research* **99**(B6), 11,591–11,621.

Green, H. & Burnley, P. (1989), 'A new self organising mechanism for deep focus earthquakes', *Nature* **341**, 733–737.

Green, H. & Houston, H. (1995), 'The mechanics of deep earthquakes', *Annu. Rev. Earth Planet. Sci.* **23**, 169–213.

Green, H. & Zhou, Y. (1996), 'Transformation–induced faulting requires an exothermic reaction and explains the cessation of earthquakes at the base of the mantle transition zone', *Tectonophysics* **256**, 39–56.

Green, H., Young, T., Walker, D. & Scholz, C. (1990), 'Anticrack associated faulting at very high pressure in natural olivine', *Nature* **348**, 720–722.

Griggs, D. (1972), The sinking lithosphere and the focal mechanism of deep earthquakes, *in* E. Robertson, ed., 'The nature of the solid earth', McGraw-Hill Inc., pp. 361–384.

Griggs, D. & Baker, D. (1968), The origin of deep–focus earthquakes, *in* 'Properties of matter under unusual conditions', John Wiley, New York, pp. 23–42.

Gurnis, M. & Hager, B. (1988), 'Controls on the structure of subducted slabs', *Nature* **335**, 317–321.

Gutenberg, B. & Richter, C. (1954), *Seismicity of the earth and associated phenomena*, 2nd edn, Princeton University Press, New Jersey.

Hara, T., Kuge, K. & Kawakatsu, H. (1996), 'Determination of the isotropic component of deep focus earthquakes by the inversion of normal mode data', *Geophysics Journal International* **127**(2), 515–528.

Hasebe, K., Fujii, N. & Uyeda, S. (1970), 'Thermal processes under island arcs', *Tectonophysics* **10**, 335–355.

Hasegawa, A., Umino, N. & Takagi, A. (1978), 'Double-planed structure of the deep seismic zone in the northeastern Japan Arc', *Tectonophysics* **47**, 43–58.

Heestand, R. & Crough, S. (1981), 'The effect of hot spots on the oceanic age–depth relation', *Journal of Geophysical Research* **86**(B7), 6,107–6,114.

Helffrich, G. (1996), Subducted lithospheric slab velocity structure: observations and mineralogical inferences, *in* G. Bebout, D. Scholl, S. Kirby & J. Platt, eds, 'Subduction: Top to Bottom', Vol. 96 of *Geophysical Monographs*, AGU, pp. 215–222.

Helffrich, G. & Abers, G. (1997), 'Slab low velocity layer in the eastern Aleutian subduction zone', *Geophysical Journal International* **130**(3), 640–648.

Helffrich, G. & Brodholt, J. (1991), 'Relationship of deep seismicity to the thermal structure of subducted lithosphere', *Nature* **353**, 252–255.

Helffrich, G. & Stein, S. (1993), 'Study of the structure of the slab-mantle interface using reflected and converted seismic waves', *Geophysical Journal International* **115**(1), 14–40.

Helffrich, G., Stein, S. & Wood, B. (1989), 'Subduction zone thermal structure and mineralogy and their relationship to seismic wave reflections and conversions at the slab / mantle interface', *Journal of Geophysical Research* **94**(B1), 753–763.

Herrin, E. (1968), '1968 seismological tables for P phases', *Bull. Seismol. Soc. Am.* **58**, 1,193–1,241.

Herzberg, C., Gasparik, T. & Sawamoto, H. (1990), 'Origin of mantle peridotite: Constraints from melting experiments to 16.5 GPa', *Journal of Geophysical Research* **95**(B10), 15,779–15,803.

Hirth, G. & Kohlstedt, D. (1996), 'Water in the oceanic upper mantle: implications for rheology, melt extraction and the evolution of the lithosphere', *Earth and Planetary Science Letters* **144**, 93–108.

Hobbs, B. & Ord, A. (1988), 'Plastic instabilities: implications for the origin of intermediate and deep focus earthquakes', *Journal of Geophysical Research* **93**(B9), 10,521–10,540.

Houston, H. & Williams, Q. (1991), 'Fast rise times and the physical mechanism of deep earthquakes', *Nature* **352**, 520–522.

Hsui, A. & Toksöz, M. (1979), 'The evolution of thermal structures beneath a subduction zone', *Tectonophysics* **60**, 43–60.

Hudson, J. (1969), 'A quantitative evaluation of seismic signals at teleseismic distances II — body waves and surface waves from an extended source', *Geophys. J.R. Astron. Soc.* **42**, 117–130.

Hudson, J., Pearce, R. & Rogers, R. (1989), 'Source type plot for inversion of the moment tensor', *Journal of Geophysical Research* **94**(B1), 765–774.

Igel, H. (1999), 'Wave propagation in three-dimensional spherical sections by the Chebyshev spectral method', *Geophysical Journal International* **136**(3), 559–566.

Ihmlé, P. (1998), 'On the interpretation of subevents in teleseismic waveforms: The 1994 Bolivia deep earthquake revisited', *Journal of Geophysical Research* **103**(B8), 17,919–17,932.

Iidaka, T. & Suetsugu, D. (1992), 'Seismological evidence for metastable olivine inside a subducting slab', *Nature* **356**, 593–595.

Iidaka, T., Mizoue, M. & Suyehiro, K. (1992), 'Seismic velocity structure of the subducting Pacific plate in the Izu–Bonin region', *Journal of Geophysical Research* **97**(B11), 15,307–15,319.

Inoue, T., Irifune, T., Yurimoto, H. & Miyagi, I. (1998), 'Decomposition of K–amphibole at high pressures and implications for subduction zone volcanism', *Phys. Earth Planet. Inter.* **107**, 221–231.

Irifune, T., Kubo, N., Isshiki, M. & Yamasaki, Y. (1998), 'Phase transformations in serpentine and transportation of water into the lower mantle', *Geophysical Research Letters* **25**(2), 203–206.

Irifune, T., Kuroda, K., Funamori, N., Uchida, T., Yagi, T., Inoue, T. & Miyajima, N. (1996), 'Amorphization of serpentine at high pressure and high temperature', *Science* **272**, 1,468–1,470.

Isacks, B. & Molnar, P. (1969), 'Mantle earthquake mechanisms and the sinking of the lithosphere', *Nature* **223**, 1121–1124.

Ito, E. & Takahashi, E. (1987), 'Melting of peridotite at uppermost lower–mantle conditions', *Nature* **328**, 514–517.

Ito, E. & Takahashi, E. (1989), 'Postspinel transformations in the system Mg_2SiO_4—Fe_2SiO_4 and some geophysical implications', *Journal of Geophysical Research* **94**(B8), 10,637–10,646.

Ito, E., Akaogi, M., Topor, L. & Navrotsky, A. (1990), 'Negative pressure-temperature slopes for reactions forming $MgSiO_3$ perovskite from calorimetry', *Science* **249**, 1,275–1,278.

Jarrard, R. (1986), 'Relations among subduction parameters', *Reviews of Geophysics* **24**(2), 217–284.

Jeanloz, R. & Thompson, A. (1983), 'Phase transitions and mantle discontinuities', *Rev. Geophys. Space Phys.* **21**(1), 51–74.

Jin, D., Karato, S. & Obata, M. (1998), 'Mechanisms of shear localization in the continental lithosphere: Inferences from the deformation microstructures of peridotites from the Ivrea zone, northwestern Italy', *Journal of Structural Geology* **20**, 195–209.

Johnson, L. (1967), 'Array measurments of P velocities in the upper mantle', *Journal of Geophysical Research* **72**(24), 6,309–6,325.

Juteau, T., Cannat, M. & Lagabrielle, Y. (1990), 'Serpentinized peridotites in the upper oceanic crust away from transform zones: a comparison of the results of previous DSDP and ODP legs', *Proceedings of the Ocean Drilling Program, Scientific Results* **106/109**, 303–308.

Kagan, Y. (1999), 'Universality of the seismic moment–frequency relation', *Pure and Applied Geophysics* **155**(2-4), 537–573.

Kanamori, H., Fujii, N. & Mizutani, H. (1968), 'Thermal diffusivity measurement of rock-forming minerals from 300 to 1000 K', *Journal of Geophysical Research* **73**(2), 595–605.

Kanzaki, M. (1991), 'Stability of hydrous magnesium silicates in the mantle transition zone', *Phys. Earth Planet. Inter.* **66**, 307–312.

Karato, S., Paterson, M. & Fitzgerald, J. (1986), 'Rheology of synthetic olivine aggregates: influence of grain–size and water', *Journal of Geophysical Research* **91**(B8), 8,151–8,176.

Katsura, T. & Ito, E. (1989), 'The system Mg_2SiO_4—Fe_2SiO_4 at high pressures and temperatures: Precise determination of stabilities of olivine, modified spinel, and spinel', *Journal of Geophysical Research* **94**(B11), 15,663–16,670.

Kawakatsu, H. (1991), 'Insignificant isotropic component in the moment tensor of deep earthquakes', *Nature* **351**, 50–53.

Kendall, J.-M. & Thompson, C. (1993), 'Sesimic modelling of subduction zones with inhomogeneity and anisotropy—I. Teleseismic P–wavefront tracking', *Geophysical Journal International* **112**(1), 39–66.

Kennett, B. (1992), 'Locating oceanic earthquakes — the influence of regional models and location criteria', *Geophysical Journal International* **108**(3), 848–854.

Kennett, B. & Engdahl, E. (1991), 'Traveltimes for global earthquake location and phase identification', *Geophysical Journal International* **105**(2), 429–465.

Kikuchi, M. & Kanamori, H. (1994), 'The mechanism of the deep Bolivia earthquake of June 9, 1994', *Geophysical Research Letters* **21**(22), 2,341–2,344.

Kincaid, C. & Olson, P. (1987), 'An experimental study of subduction and slab migration', *Journal of Geophysical Research* **92**(B13), 13,832–13,840.

Kirby, S. (1995), 'Intraslab earthquakes and phase changes in subducting lithosphere', *Reviews of Geophysics, Supplement, U.S. National Report to the I.U.G.G. 1990–1994* pp. 287–297.

Kirby, S., Durham, W. & Stern, L. (1991), 'Mantle phase changes and deep earthquake faulting in subducting lithosphere', *Science* **252**, 216–225.

Kirby, S., Engdahl, E. & Denlinger, R. (1996), Intermediate depth intraslab earthquakes and arc volcanism as physical expressions of crustal and uppermost metamorphism in subducting slabs, *in* G. Bebout, D. Scholl, S. Kirby & J. Platt, eds, 'Subduction: Top to Bottom', Vol. 96 of *Geophysical Monographs*, AGU, pp. 195–214.

Kirby, S., Stein, S., Okal, E. & Rubie, D. (1996), 'Metastable phase transformations and deep earthquakes in subducting oceanic lithosphere', *Reviews of Geophysics* **34**(2), 261–306.

Klein, F., Koyanagi, R., Nakata, J. & Tanigawa, W. (1987), The seismicity of Kilauea's magma system, *in* R. Decker, T. Wright & P. Stauffer, eds, 'Volcanism in Hawaii', United States Geological Survey, pp. 1,019–1,186.

Knott, C. (1899), 'Reflection and refraction of elastic waves with seismological applications', *Philisophical Magazine* **48**, 64–97. Series 5.

Koper, K., Wiens, D., Dorman, L., Hildebrand, J. & Webb, S. (1998), 'Modeling the Tonga slab: Can travel time data resolve a metastable olivine wedge?', *Journal of Geophysical Research* **103**(B12), 30,079–30,100.

Kostrov, B. & Das, S. (1988), *Principles of Earthquake Source Mechanics*, Cambridge Monographs on Mechanics and Applied Mathematics, Cambridge University Press, Cambridge.

Kreyszig, E. (1993), *Advanced Engineering Mathematics*, 7th edn, John Wiley & Sons, Inc.

Kuge, K. & Kawakatsu, H. (1993), 'Significance of non-double couple components of deep and intermediate depth earthquakes: implications from moment tensor inversions of long period seismic waves', *Phys. Earth Planet. Inter.* **75**, 243–266.

Kuge, K. & Lay, T. (1994), 'Systematic non–double–couple components of earthquake mechanisms: The role of fault zone irregularity', *Journal of Geophysical Research* **99**(B8), 15,457–15,467.

Lay, T. (1994), *Seismological structure of slabs*, Vol. 35 of *Advances in Geophysics*, Academic Press, San Diego.

Lister, C., Sclater, J., Davis, E., Villinger, H. & Nagihara, S. (1990), 'Heat flow maintained in ocean basins of great age: Investigations in the north–equatorial West Pacific', *Geophysical Journal International* **102**(3), 603–630.

Liu, L.-G. (1987), 'Effects of H_2O on the phase behaviour of the forsterite–enstatite system at high pressures and temperatures and implications for the Earth', *Phys. Earth Planet. Inter.* **49**, 142–167.

Lonsdale, P. (1988), 'Paleogene history of the Kula plate: Offshore evidence and onshore implications', *Geological Society of America Bulletin* **100**, 733–754.

Lundgren, P. & Giardini, D. (1992), 'Seismicity, shear failure and modes of deformation in deep subduction zones', *Phys. Earth Planet. Inter.* **74**, 63–74.

Lundgren, P. & Giardini, D. (1994), 'Isolated deep earthquakes and the fate of subduction in the mantle', *Journal of Geophysical Research* **99**(B8), 15,833–15,842.

Lundgren, P. & Giardini, D. (1995), 'The June 9 Bolivia and March 9 Fiji deep earthquakes of 1994: I. Source processes', *Geophysical Research Letters* **22**(16), 2,241–2,244.

Main, I., Meredith, P., Henderson, J. & Sammonds, P. (1994), 'Positive and negative feedback in the earthquake cycle: the role of pore fluids on states of criticality in the crust', *Annali di Geofisica* **37**, 1,461–1,479.

Marty, J. & Cazenave, A. (1989), 'Regional variations in subsidence rate of oceanic plates: a global analysis', *Earth and Planetary Science Letters* **94**, 301–315.

McGarr, A. (1977), 'Seismic moments of earthquakes beneath island arcs, phase changes and subduction velocities', *Journal of Geophysical Research* **82**(2), 256–264.

McKenzie, D. (1966), 'The viscosity of the lower mantle', *Journal of Geophysical Research* **71**(16), 3,995–4,010.

McKenzie, D. (1967), 'Some remarks on heat flow and gravity anomalies', *Journal of Geophysical Research* **72**(24), 6,261–6,273.

McKenzie, D. (1969), 'Speculations on the consequences and causes of plate motions', *Geophys. J.R. Astron. Soc.* **18**, 1–32.

McKenzie, D. (1970), 'Temperature and potential temperature beneath island arcs', *Tectonophysics* **10**, 357–366.

McKenzie, D. & Brune, J. (1972), 'Melting on fault planes during large earthquakes', *Geophys. J.R. Astron. Soc.* **29**, 65–78.

McNutt, M. (1995), 'Marine geodynamics: Depth–age revisited', *Reviews of Geophysics* **33**, S413–418.

Meade, C. & Jeanloz, R. (1991), 'Deep focus earthquakes and recycling of water into the Earth's mantle', *Science* **252**, 68–72.

Meyer, B., Tapponier, P., Bourjot, L., Métivier, F., Gaudemer, Y., Peltzer, G., Shunmin, G. & Zhitai, C. (1998), 'Crustal thickening in Gansu–Qinghai, lithospheric mantle subduction, and oblique, strike–slip controlled growth of the Tibet plateau', *Geophysical Journal International* **135**(1), 1–47.

Miller, S. (1996), 'Fluid–mediated influence of adjacent thrusting on the seismic cycle at Parkfield', *Nature* **382**, 799–802.

Minear, J. & Toksöz, M. (1970*a*), 'Thermal regime of a downgoing slab', *Tectonophysics* **10**, 367–390.

Minear, J. & Toksoz, M. (1970*b*), 'Thermal regime of a downgoing slab and new global tectonics', *Journal Geophysical Research* **75**(8), 1,397–1,419.

Minshull, T., White, R., Mutter, J., Buhl, P., Detrick, R., Williams, C. & Morris, E. (1991), 'Crustal structure at the Blake Spur Fracture Zone from expanding spread profiles', *Journal of Geophysical Research* **96**(B6), 9,955–9,984.

Minster, J. & Jordan, T. (1978), 'Present–day plate motions', *Journal of Geophysical Research* **83**(B11), 5,331–5,354.

Molnar, P., Freedman, D. & Shih, J. (1979), 'Lengths of intermediate and deep seismic zones and temperatures in down–going slabs of lithosphere', *Geophys. J.R. Astron. Soc.* **56**, 41–54.

Mooney, W., Laske, G. & Masters, T. (1998), 'CRUST 5.1: A global crustal model at 5 degrees × 5 degrees', *Journal of Geophysical Research* **103**(B1), 727–747.

Müller, G. (1977), 'Earth flattening approximation for body waves derived from geometric ray theory — improvements, corrections and range of applicability', *Journal of Geophysics* **42**, 429–436.

Müller, R., Roest, W., Royer, J., Gahagan, L. & Sclater, J. (1997), 'Digital isochrons of the world's ocean floor', *Journal of Geophysical Research* **102**(B2), 3,211–3,214.

Nakamura, M., Ando, M. & Ohkura, T. (1998), 'Fine structure of deep Wadati–Benioff zone in the Izu–Bonin region estimated from S–to–P conversions', *Phys. Earth Planet. Inter.* **106**, 63–74.

Nolet, G. & Zielhuis, A. (1994), 'Low S–velocities under the Tornquist–Teisseyre zone — evidence for water injection into the transition zone by subduction', *Journal of Geophysical Research* **99**(B8), 15,813–15,820.

Obata, M. & Karato, S. (1995), 'Ultramafic pseudotacylyte from the Balmuccia peridotite, Ivrea Verbano zone, northern Italy', *Tectonophysics* **242**, 313–328.

O'Connell, R. (1977), 'On the scale of mantle convection', *Tectonophysics* **38**, 119–136.

Ogawa, M. (1987), 'Shear instability in a visco-elastic material as the cause of deep focus earthquakes', *Journal of Geophysical Research* **92**(B13), 13,801–13,810.

Okal, E. (1996), 'Radial modes from the great 1994 Bolivian earthquake: No evidence for an isotropic component to the source', *Geophysical Research Letters* **23**(5), 431–434.

Ono, S. (1998), 'Stability limits of hydrous minerals in sediment and mid–ocean ridge basalt compositions: Implications for water transport in subduction zones', *Journal of Geophysical Research* **103**(B8), 18,253–18,267.

Parsons, B. & Sclater, J. (1977), 'An analysis of the variation of ocean floor bathymetry and heat flow with age', *Journal of Geophysical Research* **82**(5), 803–827.

Peaceman, D. & Rachford, H. (1955), 'The numerical solution of parabolic and elliptical differential equations', *J. Soc. Ind. Appl. Math.* **3**, 28–41.

Peacock, S. (1992), 'Blueschist-facies metamorphism, shear heating, and P–T–t paths in subduction zones', *Journal of Geophysical Research* **97**(B12), 17,693–17,707.

Peacock, S. (1996), Thermal and petrologic structure of subduction zones, *in* G. Bebout, D. Scholl, S. Kirby & J. Platt, eds, 'Subduction: Top to bottom', Vol. 96 of *Geophysical Monograph*, American Geophysical Union, Washington DC, pp. 119–133.

Pearce, R. (1977), 'Fault plane solutions using relative amplitudes of P and pP', *Geophys. J.R. Astron. Soc.* **50**, 381–394.

Pearce, R. (1979), Earthquake focal mechanisms from relative amplitudes of P, pP and sP: Method and computer program, Technical Report O 41/79, Atomic Weapons Research Establishment, Aldermaston, Berks.

Pearce, R. (1980), 'Fault plane solutions using relative amplitudes of P and surface reflections: further studies', *Geophys. J.R. Astron. Soc.* **60**, 459–487.

Pearce, R. & Rogers, R. (1989), 'Determination of earthquake moment tensors from teleseismic relative amplitude observations', *Journal of Geophysical Research* **94**(B1), 775–786.

Pearce, R. & Rogers, R. (1995), Seismic source discrimination at teleseismic distances using radiation patterns: Concepts and feasibility study, Technical Report O 4/94, Atomic Weapons Establishment, Aldermaston, Berks.

Pearce, R. & Stewart, R. (1989), 'Interpretation of seismic pulse durations in terms of a propagating rupture: a method and case histories', *Tectonophysics* **166**, 115–132.

Pearce, R. & Young, J. (1997), Amplitude versus offset (AVO) and the Zoeppritz equations for partioning of seismic waves at an interface: theory, new computer program, examples and review of past errors, Technical Report O 3/96, Atomic Weapons Establishment, Aldermaston, Berks.

Pegler, G. & Das, S. (1998), 'An enhanced image of the Pamir–Hindu Kush seismic zone from relocated earthquake hypocentres', *Geophysical Journal International* **134**(2), 573–595.

Raleigh, C. (1967), 'Tectonic implications of serpentinite weakening', *Geophys. J.R. Astron. Soc.* **14**, 113–118.

Renkin, M. & Sclater, J. (1988), 'Depth and age in the North Pacific', *Journal of Geophysical Research* **93**(B4), 2,919–2,935.

Richter, F. (1979), 'Focal mechanisms and seismic energy release of deep and intermediate earthquakes in the Tonga–Kermadec region and their bearing on the depth extent of mantle flow', *Journal of Geophysical Research* **84**(B12), 6,783–6,795.

Ringwood, A. & Major, A. (1966), 'Synthesis of Mg_2SiO_4–Fe_2SiO_4 solid solutions', *Earth and Planetary Science Letters* **1**, 241–245.

Rogers, R. & Pearce, R. (1987), 'Application of the relative amplitude moment–tensor program to three intermediate–depth IASPEI earthquakes', *Phys. Earth Planet. Inter.* **47**, 93–106.

Ryan, M. (1988), 'The mechanics and three–dimensional internal structure of active magmatic systems: Kiluaea Volcano, Hawaii', *Journal of Geophysical Research* **93**, 4,213–4,248.

Savage, J. (1966), 'Radiation from a realistic model of faulting', *Bull. Seismol. Soc. Am.* **56**(2), 577–592.

Scarfe, C. & Takahashi, E. (1986), 'Melting of garnet peridotite to 13 GPa and the early history of the upper mantle', *Nature* **322**, 354–356.

Schmidt, M. & Poli, S. (1998), 'Experimentally based water budgets for dehydrating slabs and consequences for arc magma generation', *Earth and Planetary Science Letters* **163**, 361–379.

Scholz, C. (1990), *The Mechanics of Earthquakes and Faulting*, Cambridge University Press.

Scholz, C. (1998), 'Earthquakes and friction laws', *Nature* **391**, 37–42.

Schroeder, W. (1984), 'The empirical age–depth relation and depth anomalies in the Pacific Ocean Basin', *Journal of Geophysical Research* **89**(B12), 9,873-9,883.

Schubert, G., Yuen, D. & Turcotte, D. (1975), 'Role of phase transitions in a dynamic mantle', *Geophys. J.R. Astron. Soc.* **42**, 705–735.

Scott, J. & Drever, H. (1953), 'Frictional fusion along a Himalayan thrust', *Royal Society of Edinburgh Proceedings* **65**(B2), 121–140.

Segall, P. & Pollard, D. (1983), 'Nucleation and growth of strike slip faults in granite', *Journal of Geophysical Research* **88**(B1), 555–568.

Seno, T. & Yamanaka, Y. (1996), Double seismic zones, compressional deep trench – outer rise events and superplumes, *in* G. Bebout, S. Kirby, J. Platt & D. Scholl, eds, 'Subduction: Top to Bottom', Vol. 96 of *Geophysical Monographs*, AGU.

Sharrock, D., Main, I. & Douglas, A. (1995), 'A two layer attenuation model for the upper mantle at short periods', *Geophysical Research Letters* **22**(19), 2,561–2,564.

Shieh, S., Mao, H., Hemley, R. & Ming, L. (1998), 'Decomposition of phase D in the lower mantle and the fate of dense hydrous silicates in subducting slabs', *Earth and Planetary Science Letters* **159**, 13–23.

Sibson, R. (1975), 'Generation of pseudotachylyte by ancient seismic faulting', *Geophys. J.R. Astron. Soc.* **43**, 775–794.

Silver, P., Beck, S., Wallace, T., Meade, C., Myers, S., James, D. & Kuehnel, R. (1995), 'Rupture characteristics of the deep Bolivian earthquake of 9 June 1994 and the mechanism of deep focus earthquakes', *Science* **268**, 69–73.

Sleep, N. (1973), 'Teleseismic P–wave transmission through slabs', *Bull. Seism. Soc. Am.* **63**, 1,349–1,373.

Smyth, J. & Kawamoto, T. (1997), 'Wadsleyite II: A new high pressure hydrous phase in the peridotite–H_2O system', *Earth and Planetary Science Letters* **146**, E9–E16.

Stein, C. (1995), Heat flow of the earth, *in* T. Ahrens, ed., 'Global Earth Physics: A handbook of physical constants', number 1 *in* 'AGU Reference Shelf', AGU, Washington, DC, chapter 9, pp. 144–158.

Stein, C. & Stein, S. (1992), 'A model for the global variation in oceanic depth and heat flow with lithospheric age', *Nature* **359**, 123–129.

Stein, S. & Stein, C. (1996), Thermo-mechanical evolution of oceanic lithosphere: implications for the subduction process and deep earthquakes, *in* G. Bebout, D. Scholl, S. Kirby & J. Platt, eds, 'Subduction: top to bottom', Vol. 96 of *Geophysical Monographs*, AGU.

Stimpson, I. (1987*a*), 'The relative amplitude moment tensor method applied to the IASPEI deep earthquakes', *Phys. Earth Planet. Inter.* **47**, 150–158.

Stimpson, I. (1987*b*), Teleseismic studies of earthquake source mechanisms using complete seismograms, thesis, University of Wales, Cardiff.

Stimpson, I. & Pearce, R. (1987), 'Moment tensors and source processes of three deep Sea of Okhotsk earthquakes', *Phys. Earth Planet. Inter.* **47**, 107–124.

Stolper, E., Walker, D., Walker, B. & Hays, J. (1981), 'Melt segregation from partially molten source regions: The importance of melt density and source region size', *Journal of Geophysical Research* **86**(B7), 6,261–6,271.

Suetsugu, D. (1989), 'Lower mantle high–velocity zone beneath the Kurils as inferred from P–wave travel time and amplitude data', *Journal of Physics of the Earth* **37**, 265–295.

Sung, C. & Burns, R. (1976), 'Kinetics of high pressure phase transformations: Implications to the evolution of the olivine–spinel transition in the downgoing lithosphere and its consequences on the dynamics of the mantle', *Tectonophysics* **31**, 1–32.

Tada, T. & Shimazaki, K. (1994), 'How much does a high velocity slab contribute to the apparent non–double–couple components in deep focus earthquakes?', *Bull. Seismol. Soc. Am.* **84**(4), 1,272–1,278.

Takahashi, E. & Kushiro, I. (1983), 'Melting of a dry peridotite at high pressures and basalt magma genesis', *American Mineralogist* **68**, 859–879.

Takei, Y. & Kumazawa, M. (1994), 'Why have the single force and torque been excluded from the seismic source model?', *Geophysical Journal International* **118**(1), 20–30.

Tao, W. & O'Connell, R. (1992), 'Ablative subduction: a two sided alternative to the convectional subduction model', *Journal of Geophysical Research* **97**(B6), 8,877–8,904.

Tao, W. & O'Connell, R. (1993), 'Deformation of a weak subducted slab and variation of seismicity with depth', *Nature* **361**, 626–628.

Tatsumi, Y. (1986), 'Formation of the volcanic front in subduction zones', *Geophysical Research Letters* **13**(8), 717–720.

Tatsumi, Y. & Eggins, S. (1995), *Subduction zone magmatism*, Frontiers in Earth Sciences, Blackwell Science, Cambridge, MA.

Taylor, B., Klaus, A., Brown, G., Moore, G., Okamura, Y. & Murakami, F. (1991), 'Structural development of Sumisu Rift, Izu–Bonin Arc', *Journal of Geophysical Research* **96**(B10), 16,113–16,129.

Terzaghi, K. (1923), 'Calculation of the porosity index of clay from hydrodynamic tension conditions', *Sitzbericht (Abt. IIa) Akademie der Wissenschaften* p. 132. In German.

Terzaghi, K. (1932), 'Bearing capacity of shallow foundations', *Prelim. Pub. 1st Congr. Int. Ass. Bridge Struct. Eng.* pp. 659–672. In German.

Thompson, A. (1992), 'Water in the Earth's upper mantle', *Nature* **358**, 295–302.

Toksöz, M., Minear, J. & Julian, B. (1971), 'Temperature field and geophysical effects of a downgoing slab', *Journal of Geophysical Research* **76**(5), 1,113–1,138.

Toksöz, M., Sleep, N. & Smith, A. (1973), 'Evolution of the downgoing lithosphere and the mechanisms of deep focus earthquakes', *Geophys. J.R. Astron. Soc.* **35**, 285–310.

Turcotte, D. & Oxburgh, E. (1967), 'Finite amplitude convective cells and continental drift', *Journal of Fluid Mechanics* **28**, 29–42.

Turcotte, D. & Schubert, G. (1973), 'Frictional heating of the descending lithosphere', *Journal of Geophysical Research* **78**(26), 5,876–5,886.

Twiss, R. & Moores, E. (1992), *Structural Geology*, W.H. Freeman & Co., New York.

Ulmer, P. & Trommsdorff, V. (1995), 'Serpentine stability to mantle depths and subduction related magmatism', *Science* **268**, 858–861.

Vacher, P., Spakman, W. & Wortel, M. (1999), 'Numerical tests on the seismic visibility of metastable minerals in subduction zones', *Earth and Planetary Science Letters* **170**(3), 335–349.

Vaisnys, J. & Pilbeam, C. (1976), 'Deep earthquake initiation by phase transformations', *Journal of Geophysical Research* **81**(5), 985–988.

van der Hilst, R. (1995), 'Complex morphology of subducted lithosphere in the mantle beneath the Tonga trench', *Nature* **374**, 154–157.

van der Hilst, R., Engdahl, R., Spakman, W. & Nolet, G. (1991), 'Tomographic imaging of subducted lithosphere below northwest Pacific island arcs', *Nature* **353**, 37–43.

van der Hilst, R., Widiyantoro, S. & Engdahl, E. (1997), 'Evidence for deep mantle circulation from global tomography', *Nature* **386**, 578–584.

Vasco, D. & Johnson, L. (1989), 'Inversion of waveforms for extreme source models with an application to the isotropic moment tensor component', *Geophysical Journal* **97**, 1–18.

Vassiliou, M. (1984), 'The state of stress in subducting slabs as revealed by earthquakes analysed by moment tensor inversion', *Earth and Planetary Science Letters* **69**, 195–202.

Vlaar, N. & Wortel, M. (1976), 'Lithospheric aging, instability and subduction', *Tectonophysics* **32**, 331–351.

Wadati, K. (1928), 'Shallow and deep earthquakes', *Geophysical Magazine* **1**, 162–202.

Wang, Y., Martinez, I., Guyot, F. & Liebermann, R. (1997), 'The breakdown of olivine to perovskite and magnesiowustite', *Science* **275**, 510–513.

Weber, M. (1988), 'Computation of body–wave seismograms in absorbing 2–D media using the Gaussian beam method: comparison with exact methods', *Geophysical Journal* **92**, 9–24.

White, J. (1996), 'Transient discontinuities revisited: pseudotachylyte, plastic instability and the influence of low pore fluid presure on deformation processes in the mid–crust', *Journal of Structural Geology* **18**(12), 1,471–1,486.

Wiens, D. & Gilbert, H. (1996), 'Effect of slab temperature on deep earthquake aftershock productivity and magnitude–frequency relations', *Nature* **384**, 153–156.

Wiens, D. & Stein, S. (1983), 'Age dependence of oceanic intraplate seismicity and implications for lithospheric evolution', *Journal of Geophysical Research* **88**(B8), 6,455–6,468.

Wiens, D., Gilbert, H., Hicks, B., Wysession, M. & Shore, P. (1997), 'Aftershock sequences of moderate–sized intermediate and deep earthquakes in the Tonga subduction zone', *Geophysical Research Letters* **24**(16), 2,059–2,062.

Wiens, D., McGuire, J. & Shore, P. (1993), 'Evidence for transformational faulting from a deep double seismic zone in Tonga', *Nature* **364**, 790–793.

Wiens, D., McGuire, J., Shore, P., Bevis, M., Draunidalo, K., Prasad, G. & Helu, S. (1994), 'A deep earthquake aftershock sequence and implications for the rupture mechanisms of deep earthquakes', *Nature* **372**, 540–543.

Willemann, R. (1991), 'A simple explanation for the depth distribution of deep earthquakes', *Geophysical Research Letters* **18**(6), 1,123–1,126.

Willemann, R. & Frohlich, C. (1987), 'Spatial patterns of aftershocks of deep focus earthquakes', *Journal of Geophysical Research* **92**(B13), 13,927–13,943.

Wood, B. (1997), 'The composition and structure of the Earth's mantle', *Terra Nova* **9**(Abstract Supplement No. 1), 25.

Wortel, M. (1982), 'Seismicity and rheology of subducted slabs', *Nature* **296**, 553–556.

Wortel, M. & Vlaar, N. (1988), 'Subduction zone seismicty and the thermo-mechanical evolution of the downgoing lithosphere', *Pure and Applied Geophysics* **128**, 625–659.

Wortel, R. (1986), 'Deep earthquakes and the thermal assimilation of the subducting lithosphere', *Geophysical Research Letters* **13**(1), 34–37.

Wu, T.-C., Bassett, W., Burnley, P. & Weathers, M. (1993), 'Shear-promoted phase transformations in Fe_2SiO_4 and Mg_2SiO_4 and the mechanism of deep earthquakes', *Journal of Geophysical Research* **98**(B11), 19,767–19,776.

Yamamoto, K. & Akimoto, S.-I. (1977), 'The system MgO–SiO_2–H_2O at high pressures and temperatures — stability field for hydroxyl chondrodite, hydroxyl clinohumite and 10Å phase', *American Journal of Science* **277**, 288–312.

Yuen, D., Fleitout, L., Schubert, G. & Froidevaux, C. (1978), 'Shear deformation zones along major transform faults and subducting slabs', *Geophys. J.R. Astron. Soc.* **54**, 93–119.

Zhou, H. (1990), 'Observations on earthquake stress axes and seismic morphology of deep slabs', *Geophysical Journal International* **103**(2), 377–401.

Zhou, H., Anderson, D. & Clayton, R. (1990), 'Modeling of residual spheres for subduction zone earthquakes 1. Apparent slab penetration signatures in the NW Pacific caused by deep diffuse mantle anomalies', *Journal of Geophysical Research* **95**(B5), 6,799–6,827.

Zoeppritz, K. (1919), 'Erdbebenwellen VIIB: Uber Reflexion und Durchgang seismicher Wellen durch Unstetigkeitsflächen', *Nachr der Koniglichen Gesell d Wiss Göttingen. math. phys.* **K1**, 66–84. In German.

Appendix A

Relocation of Earthquakes Beneath the Izu Trench

In section 4.5, considerable importance was attached to accurate depth determination for earthquakes located beneath the Izu trench in the northwest Pacific. According to the JMA hypocentres, these 29 events occurred away from the slab at depths of up to 150 km. In order to re–evaluate the hypocentral locations, a subset of the earthquake population was studied using records from the short period seismic arrays at Yellowknife (YKA) in Canada, Warramunga (WRA) in Australia and at Gauribidanur (GBA) in India. The events were not detected at the fourth UK type array, at Eskdalemuir (EKA), in Scotland. Summation of the array components produces a higher signal to noise ratio than is available from a single three–component station. The arrays consist of 20 short period instruments arranged in two perpendicular lines of 10 instruments each. This geometry allows the source direction of arriving energy to be determined and cross correlation of energy from the desired direction across all 20 components picks out coherent arrivals, which may be much smaller than the detection threshold for a single station. The events examined are detailed in table A.1.

All the events show considerable complexity in the first 40 s after the initial P–wave arrival, suggesting a shallow crustal source. An exceptionally clear record at WRA for the 8 July event shows 6 discrete arrivals making up the P–wave coda. All the earthquakes occurred beneath the Izu trench, where the ocean depth is

Table A.1.
Anomalous earthquakes beneath Izu Trench

Date	Time	Lat.	Lon.	Depth	m_b	Array data
24/05/92	13:58:41.7	31.63N	142.34E	142km	4.3	YKA WRA GBA
27/05/92	19:28:00.3	31.41N	142.17E	52km	4.5	YKA WRA GBA
30/05/92	17:22:13.3	31.49N	142.67E	93km	4.2	YKA
31/05/92	11:20:00.9	30.74N	141.99E	87km	4.3	YKA WRA
5/06/92	12:02:45.1	31.29N	142.71E	109km	4.2	YKA WRA
8/07/92	20:26:15.5	31.23N	142.68E	73km	4.2	YKA WRA GBA

Data from the ISC bulletin. Locations shown are those determined by the JMA. Detection at arrays determined by inspection of the individual records.

around 6 km. Thus, it would be reasonable to expect to see reflections from the water surface in the coda, at least 8 s after the first arrival (P–wave velocity in water is 1.5 $km\,s^{-1}$). Possible pwP and pwwP phases are seen at approximately 10 and 20 seconds.

Following the methodology of Buchanan (1998), synthetic seismograms were used to match the arrival times of predicted and observed phases and hence to identify the different phases and determine the above source velocity structure and source depth. Amplitudes of surface reflections were measured and used to determine the focal mechanism using the relative amplitude method (described in chapter 5). Recalculating the synthetic seismograms using this focal mechanism allowed comparison of the observed and synthetic waveforms at different stations. A high degree of similarity indicates that the model was correct, whilst significant differences point to errors in the phase identifications, velocity structure or source model.

The synthetic seismograms were produced using the method of Hudson (1969) and Douglas *et al.* (1972), which uses horizontal, plane layers to represent earth structure near the source and receiver. An initial velocity and density model for oceanic crust was taken from Douglas *et al.* (1972). A source located in the lower part of the oceanic crust, at a depth of 6.3 km below the sea bed, produced arrivals in good agreement with those observed. The time between pwP and pwwP varied at the different stations and could not be accurately reconciled with the pwP–P time, an effect probably caused by a dipping ocean floor and water depth which varied over the trench. The modelling incorporated above source

reflections from the interfaces between intrusive and extrusive basalts, extrusive basalt and sediment, sediment and water, and the water surface. Many of these were identified on the clear WRA record.

The relative amplitude method requires amplitudes from different points *on the focal sphere* of an earthquake. Hence it is possible to use amplitudes from any reflected phase as long as they are corrected for energy loss above the source. Here I chose to use reflections from the extrusive basalt–sediment interface. These reflections are large and have interacted with a small number of boundaries, making calculation of energy loss simpler. The equations which govern energy partitioning at an interface (Knott 1899, Zoeppritz 1919) are applied to the crustal model from the synthetic seismogram calculations using the method of Pearce & Young (1997). The calculated proportions of energy remaining in the downgoing P–wave after reflection were similar for all the array stations and common factors of 0.46 for pP and 0.11 for sP were adopted. The sP factor must be further corrected for the change in geometrical spreading caused by the angle of reflection being larger than the angle of incidence (Pearce 1980, appendix A), giving a value of 0.06.

The search for focal mechanisms compatible with the observations was constrained to look only for double couple mechanisms. Compatible mechanisms formed two clusters in orientation space, representing the fault and auxiliary planes, as shown in figure A.1. A solution was chosen arbitrarily (strike 90°, dip 50°, slip 160°) and used to compute new synthetic seismograms. These were in good agreement with the observed seismograms, as shown in figure A.2, strongly supporting the interpretation that this earthquake occurred at a shallow depth of about 6 km within the oceanic crust. Synthetics computed for the JMA depth of 73 km failed to match the observed phase arrival times.

The other five events recorded at the arrays show similar arrivals to the 8 July event, but are either more complex or have a poorer signal to noise ratio. The complex nature of all the seismograms almost guarantees that these events occurred at shallow depth, either in or just below the oceanic crust. To try and show this explicitly, the Joint Epicentre Determination method of Douglas (1967) was used to compute the relative locations of the events. First, the location of the 8 July event was recalculated by a least squares minimisation of the picked

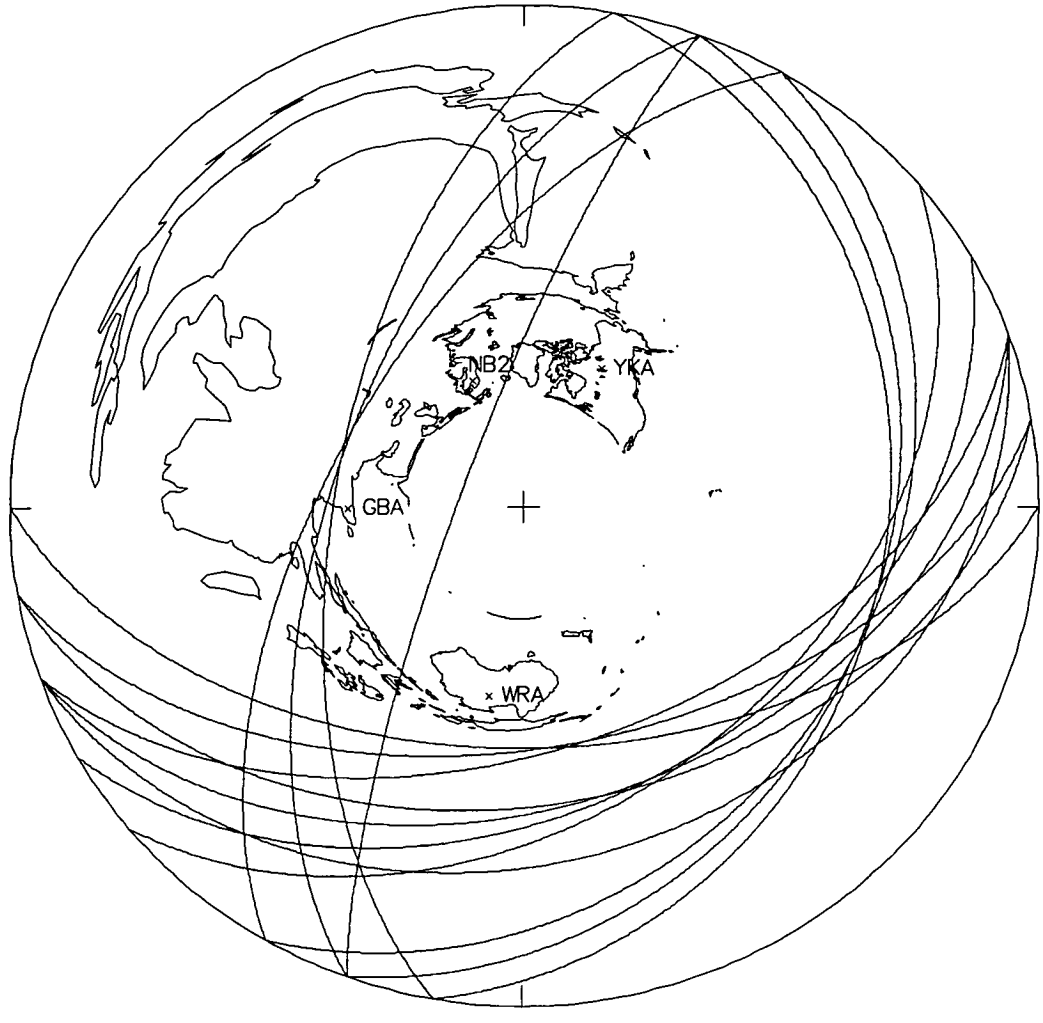

Figure A.1.
Possible focal mechanisms for 8 July 1992 earthquake. Fault planes compatible with the relative amplitude observations are shown on the lower half of the focal sphere on a Schmidt equal area projection. The locations of the three seismic arrays used in the focal mechanism determination are also shown projected onto the lower focal hemisphere. These are Yellowknife (YKA), Warramunga (WRA) and Gauribidanur (GBA). NB2 marks the location of the NORSAR array in Norway, an arrival time from which was used in the relocation of this earthquake.

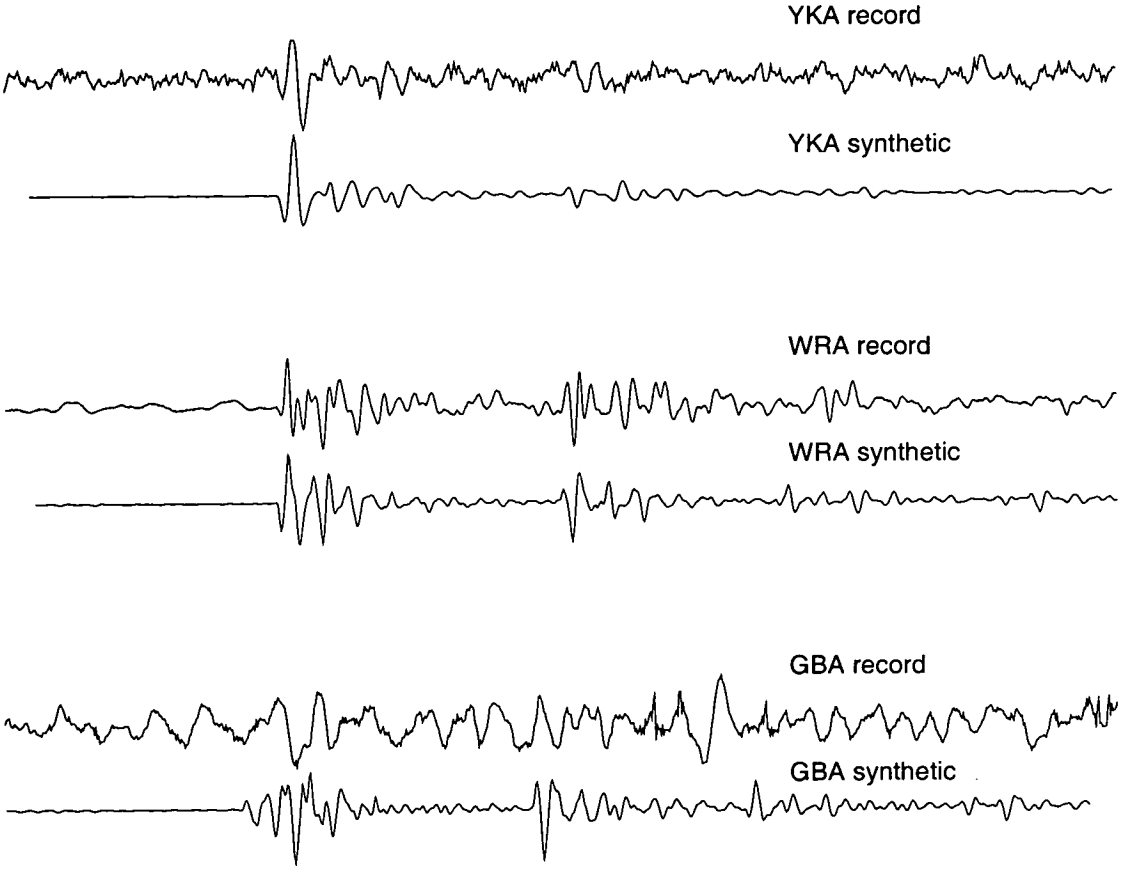

Figure A.2.
Observed and synthetic seismograms for the 8 July 1992 event beneath the Izu trench. Records are from the seismic arrays at, from top to bottom, YKA, WRA and GBA. The synthetics were produced using a 6 km water layer and a source at 6.3 km depth beneath the sea bed, in the basaltic layer of the oceanic crust. The timescale is approximately 1 cm : 3.0 s.

arrival times at YKA, WRA and GBA and of the ISC reported arrival time at the NORSAR array, Norway. The regional JMA data were not used, since the earthquakes of interest all lie outside of the network, which therefore suffers from a systematic directional bias, and the four array stations provide good azimuthal coverage, as shown in figure A.1. The JMA epicentre and origin times were used as an initial guess and the depth was fixed at 6.3 km. Perturbations of origin time and location to minimise the squares of the travel times shifted the epicentre by 37 km in an ESE direction and the origin time became 1.8 s earlier. This new location was fixed in the joint epicentre determination, to tie the other epicentres to an absolute reference frame. Unfortunately, the data were insufficient to distinguish between the effects of variation in focal depth and origin time, so the depths could not be constrained.

Having failed to show explicitly that the whole population of earthquakes occurred at shallow depth, it is necessary to examine why they were located at considerable depth by two different and independent methods. The JMA depths appear to have been based on S–P times. Predicted S–P times in an IASP91 earth model for intermediate depth hypocentres are consistently closer to the observed times than predictions for shallow events. For the 8 July event, the S–P time at local station HJJ was 38.2 s. For the JMA epicentre, this gives a depth of 73 km, the JMA reported depth. With all the Japanese stations lying to the north of Izu, then the S–P time will be similar at them all. Using my recalculated epicentre, the S–P times are best fit by a 50 km source, giving a time of 39.7 s at HJJ. However, this event has been located above at a depth of 6.3 km. The most likely cause of the anomalous S–P times, and hence also the anomalous depth determination, is a significant departure of the regional velocity structure from the IASP91 model. Such a departure is unsurprising and is probably related to the large volume of old, cold lithosphere which has been subducted in the north–west Pacific region.

The EHB method of depth determination relies on an automated phase picking algorithm to identify surface reflections. Of the subset of events for which array data is available, only the 27 May 1992 earthquake is present in the EHB catalogue. Records from this event are noisy at YKA and GBA, but the WRA record is clearer. An IASP91 earth model was used to predict phase arrival times at

WRA for the EHB hypocentre (31.703 °N, 142.125 °E, 91.8 km depth). There was little correlation between the predicted and observed arrivals except in one case. Predicted pP coincides with the observed second water reverberation, pwwP. It appears that this phase has been mis–identified as pP by the EHB algorithm, although why this has occurred is not clear.

Appendix B

Moment Tensor Solutions

The full results of the moment tensor inversions described in chapter 6 are presented here. Compatible source types and orientations are displayed on source type plots and lower focal hemisphere projections, respectively. When a double couple source mechanism is compatible, only the double couple orientations are shown. Otherwise, all the compatible non–double couple solutions are illustrated.

The solutions for each earthquake are presented together, in a consistent order. First are the results from the standard, Jeffreys–Bullen model, with separate broadband and long–period analyses. Second are the results from the new model incorporating the IASP91 velocity structure, also with separate broadband and long period analyses. Both models assumed the source to occur in a Poisson solid. Finally, the long period results from the new model after dropping the assumption of Poisson solid are shown. Only broadband solutions are shown for the 11 October 1993 (Izu–Bonin) and 9 June 1994 (Bolivia) events because they radiated energy at such low frequencies that low pass–filtering at 0.05 Hz would have had no effect.

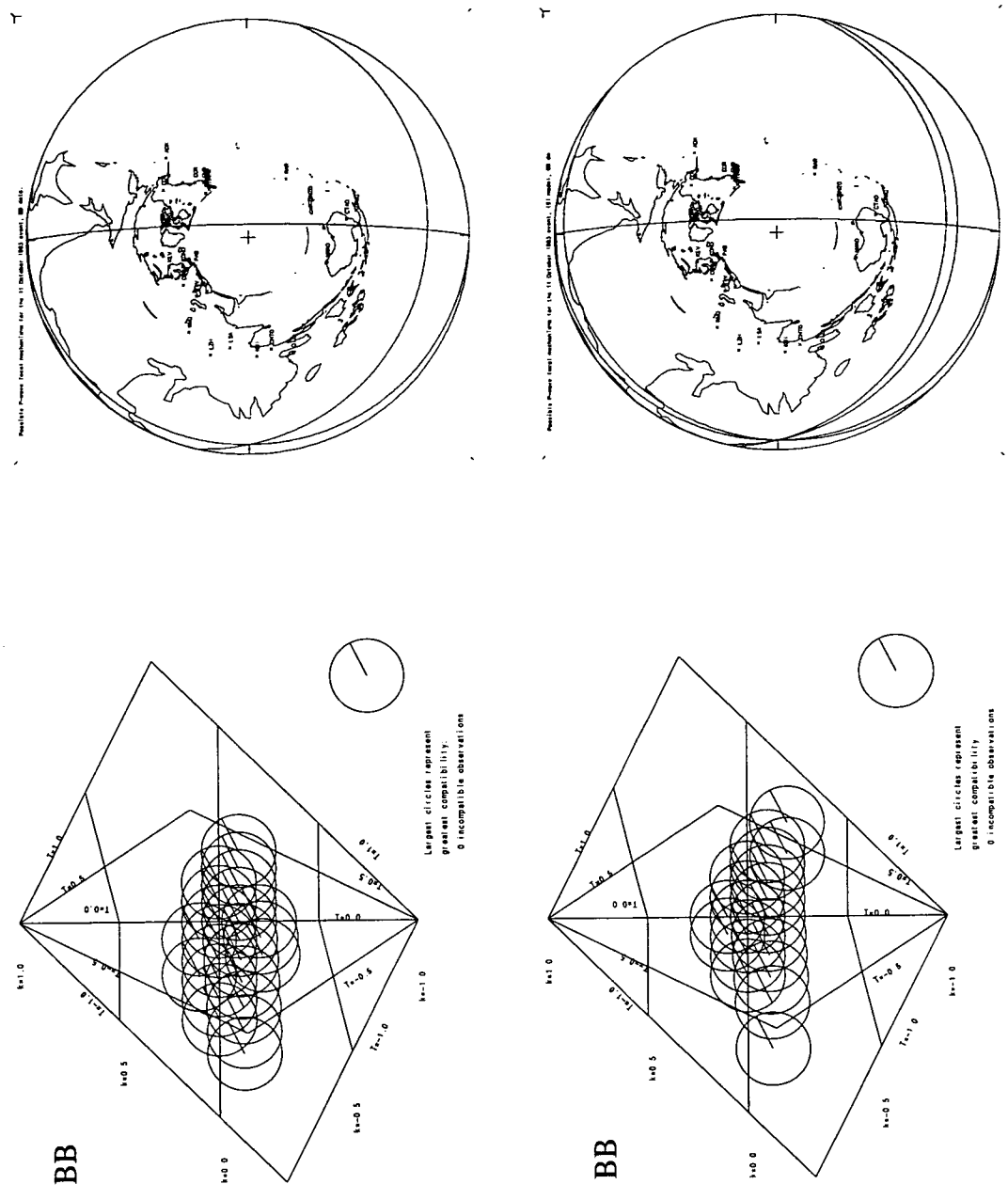

Figure B.1.

Source type and focal mechanism determinations for the 11 October 1993, Izu–Bonin earthquake. The top set are the results obtained using the earth velocity model of Herrin (1968) to calculate take–off angles, and assuming a flat earth surface to calculate reflection coefficients, henceforth known as the "standard model". The bottom set were obtained using an IASP91 earth model in the calculation of both take–off angles and reflection coefficients. Only the fault plane solutions for compatible double–couples are shown.

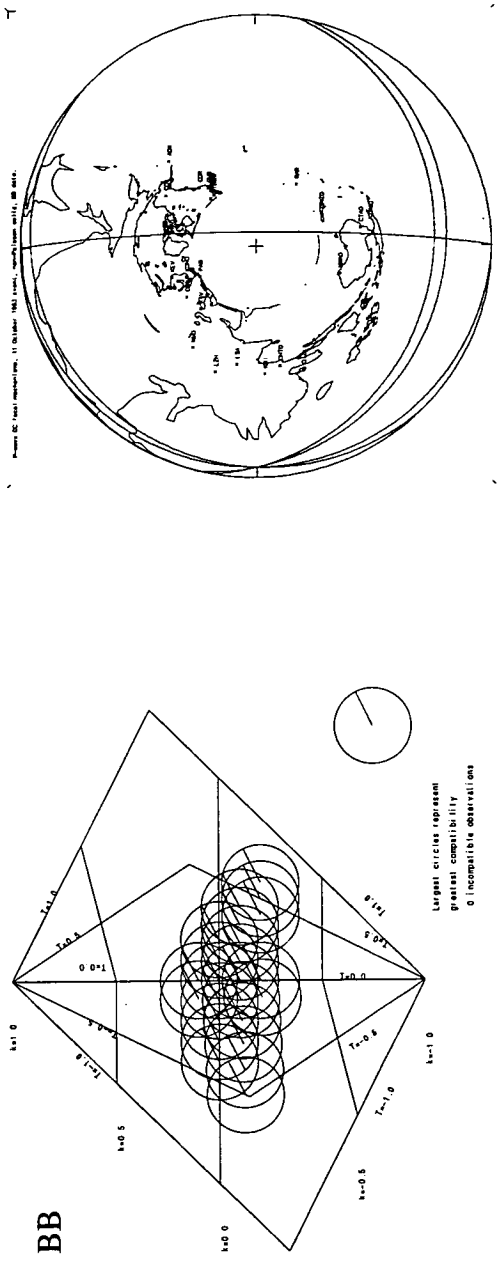

Figure B.2.
Source types and double–couple orientations compatible with data from the 11 October 1993 Izu–Bonin earthquake, determined assuming a non–Poisson source material. For this inversion, the relative excitation of S to P radiation was given the general value $(V_p/V_s)^3$. The IASP91 earth velocity model and the same set of observations as for figure B.1 were used.

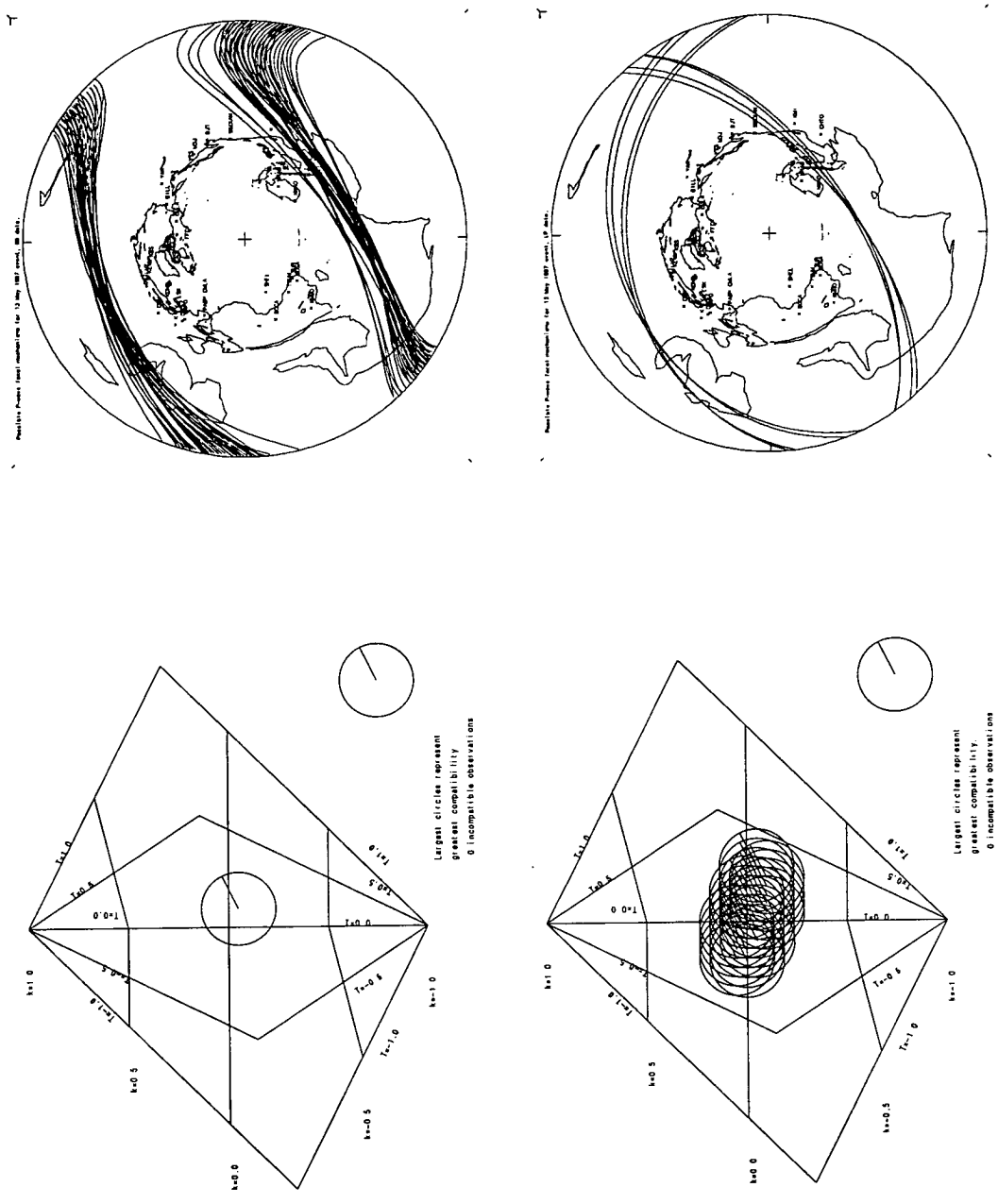

Figure B.3.
13 May 1997 Hindu Kush earthquake, standard model. Results obtained using the standard model with broadband (top) and long period (bottom) data.

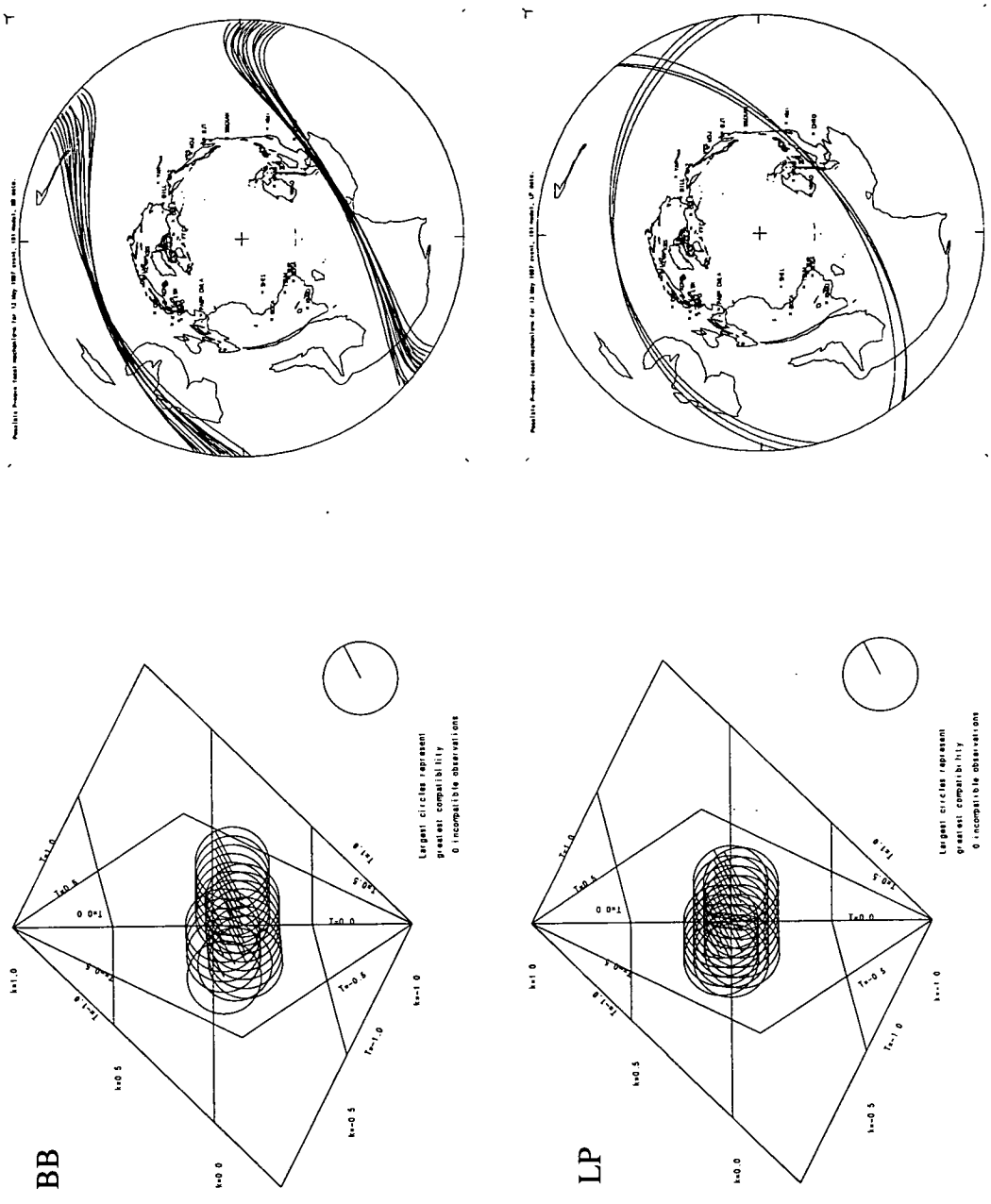

Figure B.4.
13 May 1997 Hindu Kush earthquake, IASP91 model. Results obtained using the IASP91 model with broadband (top) and long period data (bottom).

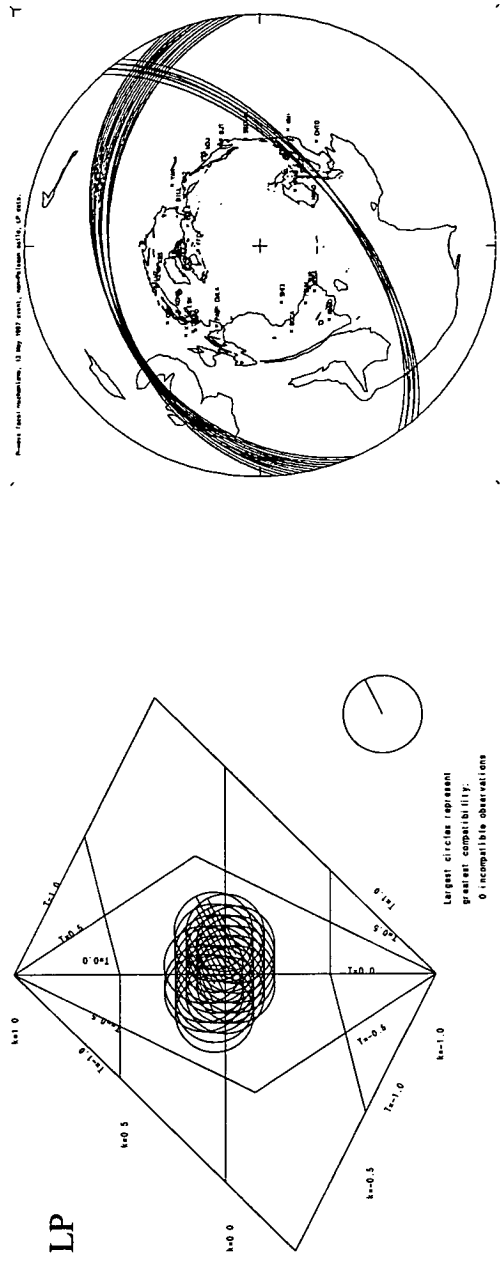

Figure B.5.
13 May 1997 Hindu Kush earthquake, assuming a non-Poisson source material. Compatible source types and double couple orientations are shown.

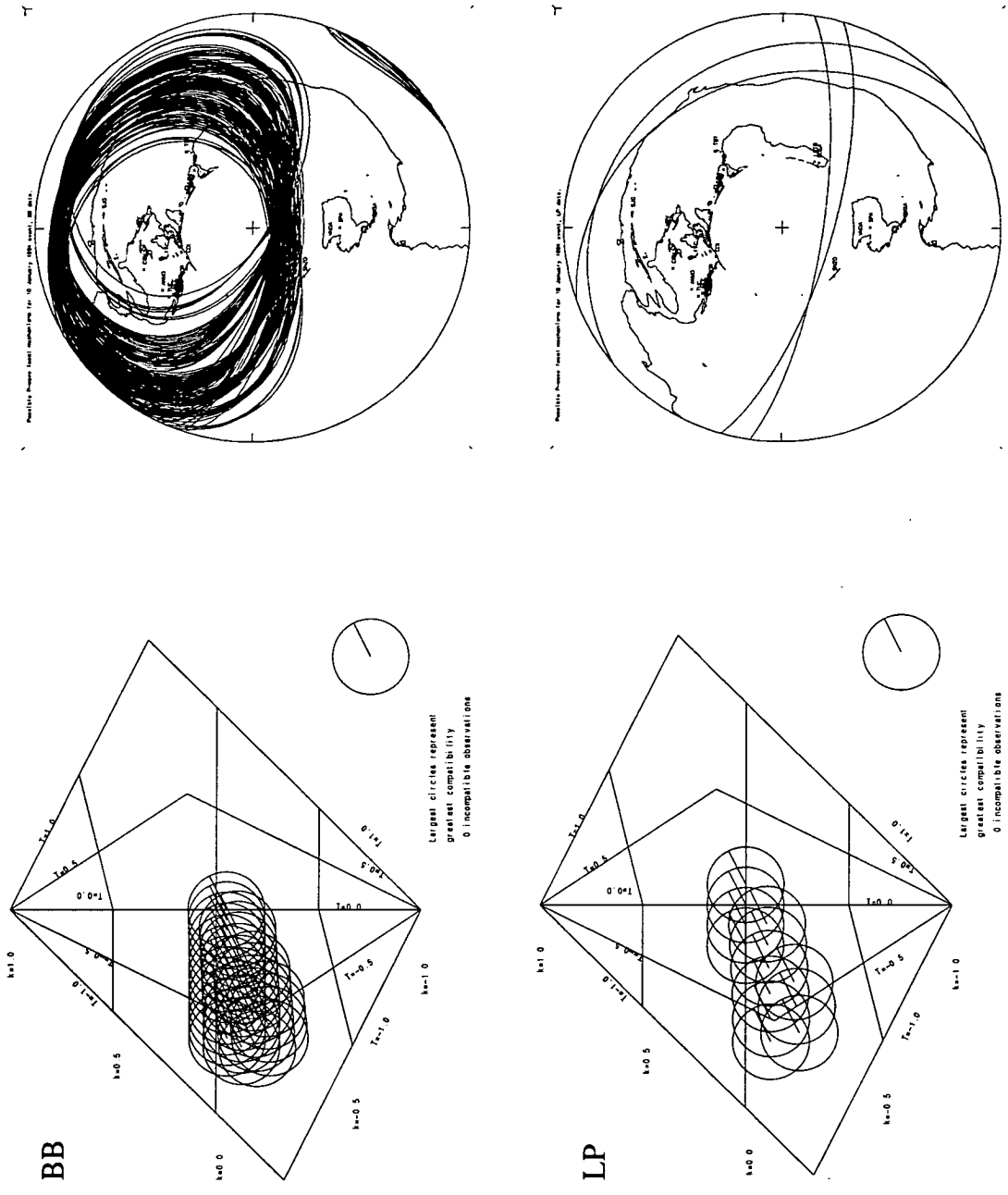

Figure B.6.
10 January 1994 Bolivia earthquake, standard model. Results obtained using the standard model with broadband data (top) and long period data (bottom).

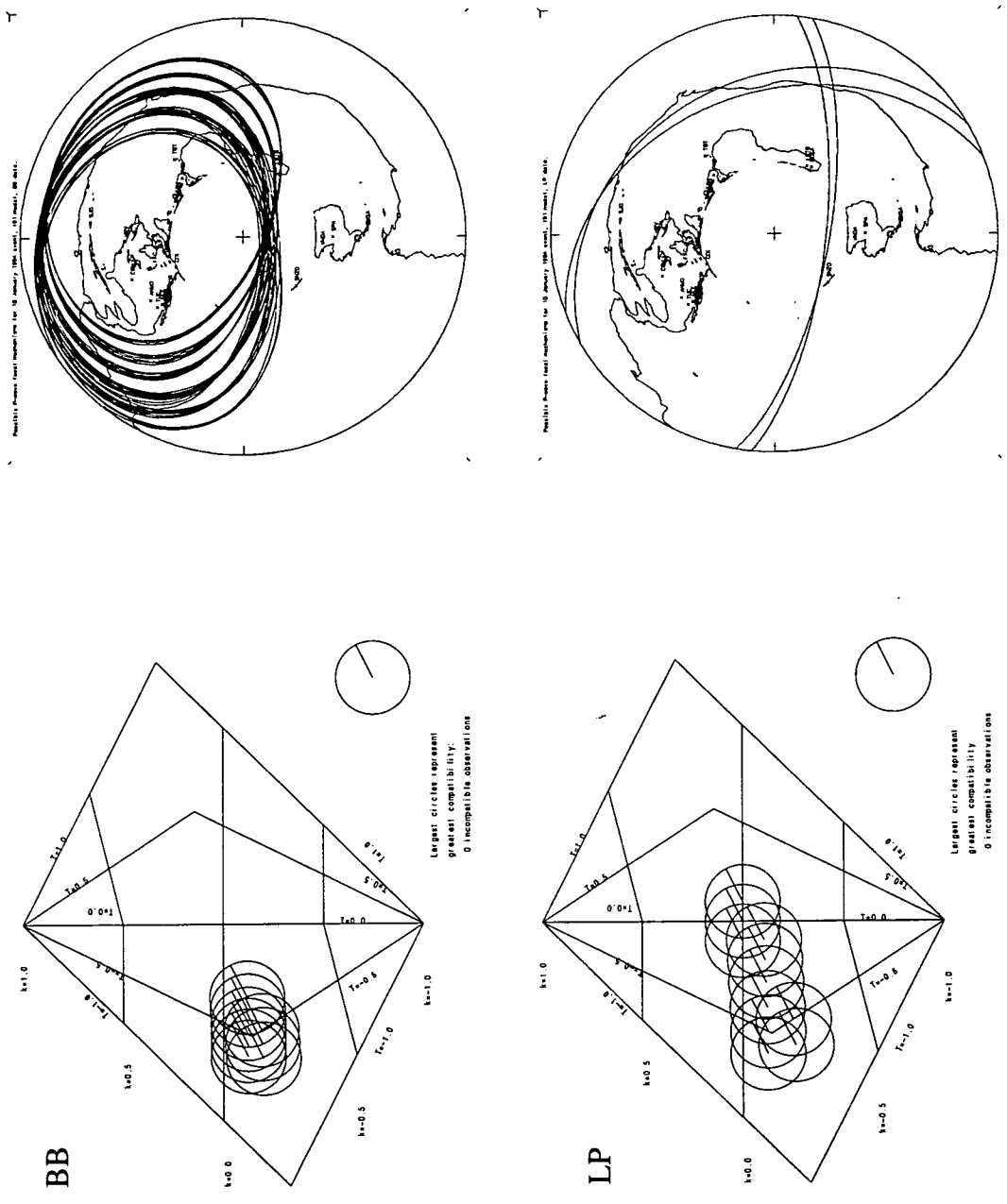

Figure B.7.
10 January 1994 Bolivia earthquake, IASP91 model. Results obtained using the IASP91 model for broadband data (top) and long period data (bottom).

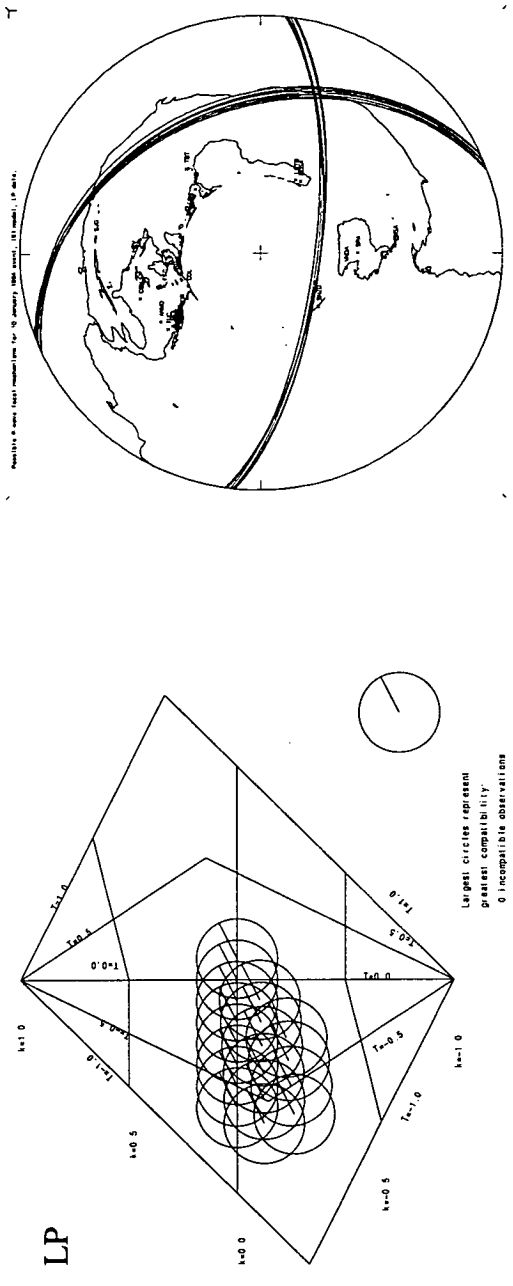

Figure B.8.
10 January 1994 Bolivia earthquake, assuming a non–Poisson solid. Compatible source types and double couple mechanisms are shown.

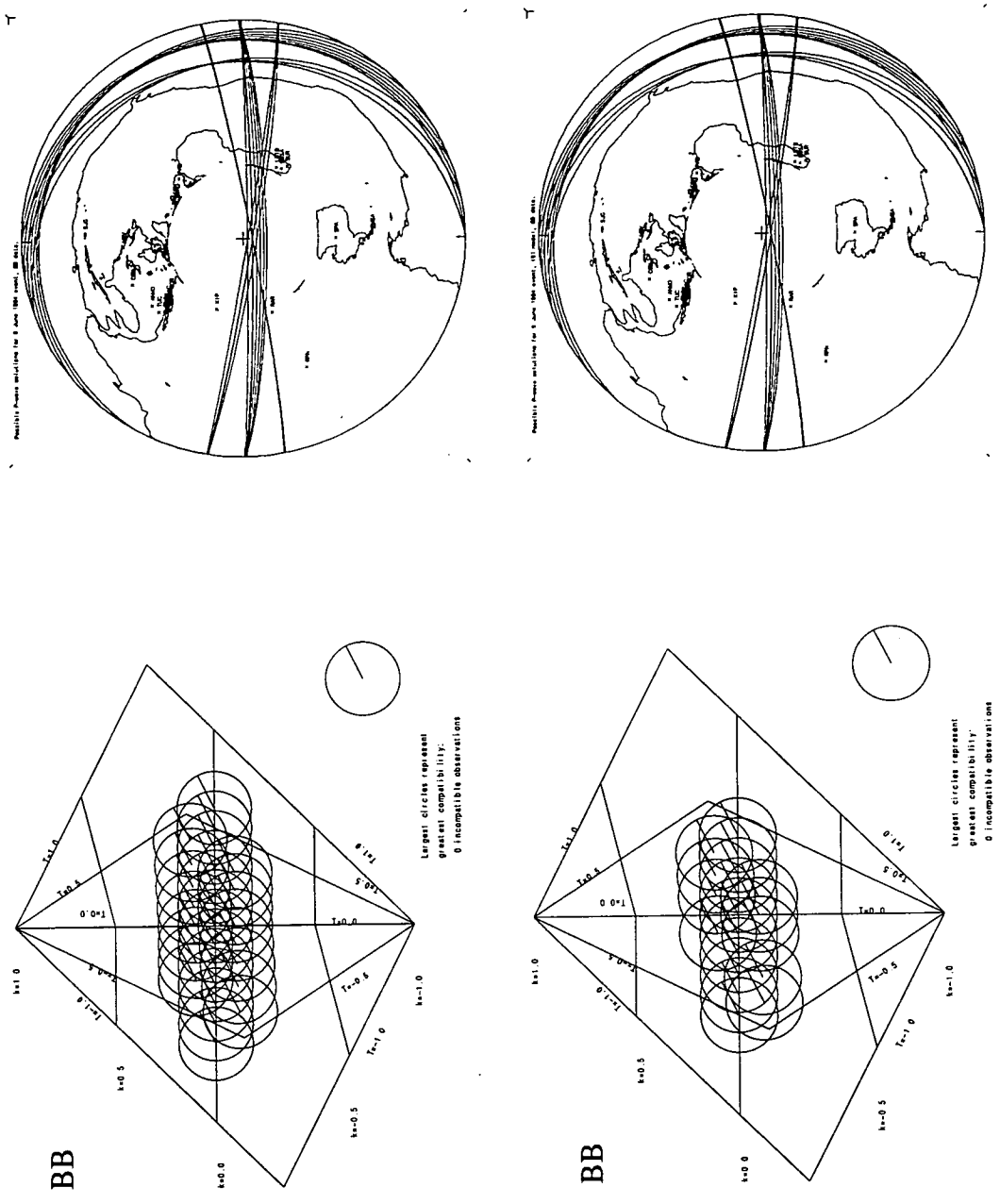

Figure B.9.

9 June 1994 Bolivia earthquake. Broadband data was used with both the standard (top) and IASP91 (bottom) models. The source spectrum of this event was dominated by very low frequencies, so low pass filtering to provide long period data was unnecessary.

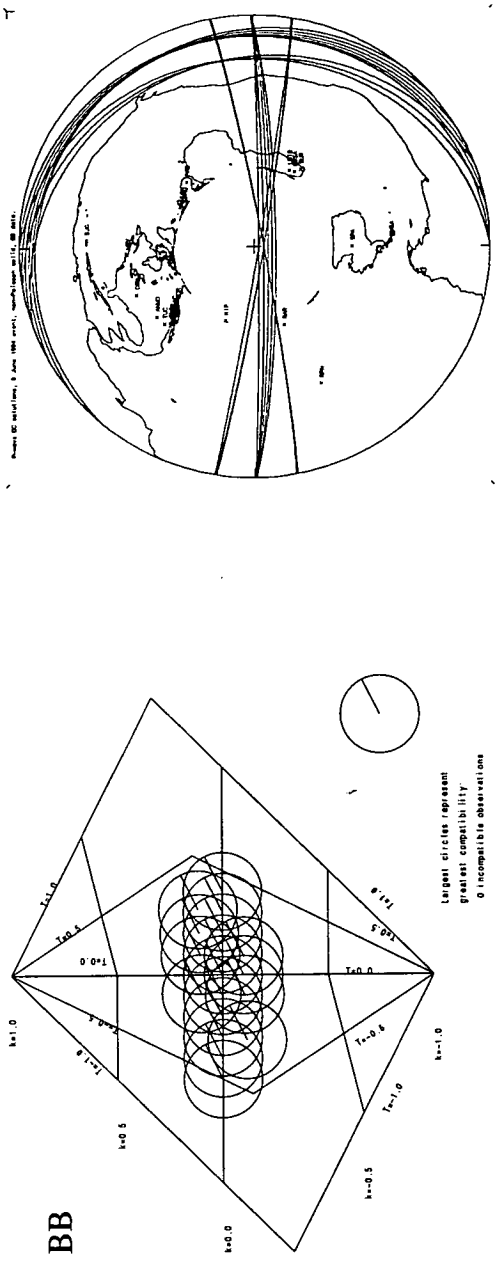

Figure B.10.

9 June 1994 Bolivia earthquake, assuming a non–Poisson source material. Compatible source types and double couple mechanisms are shown. Low pass filtering was unnecessary due to the domination of the source spectrum by low frequencies.

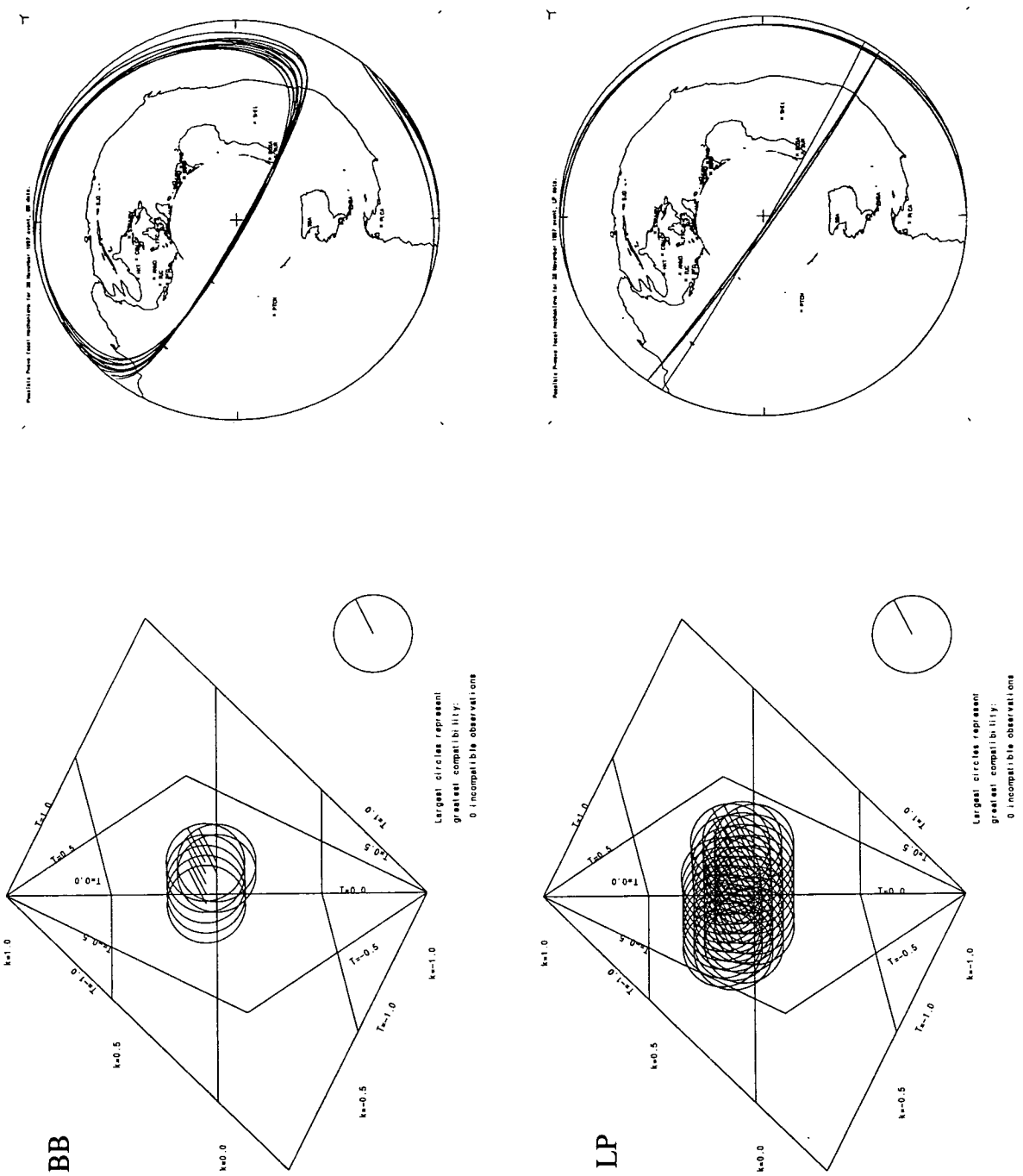

Figure B.11.
28 November 1997 Bolivia earthquake, standard model. Results determined using the standard model with broadband (top) and long period data (bottom).

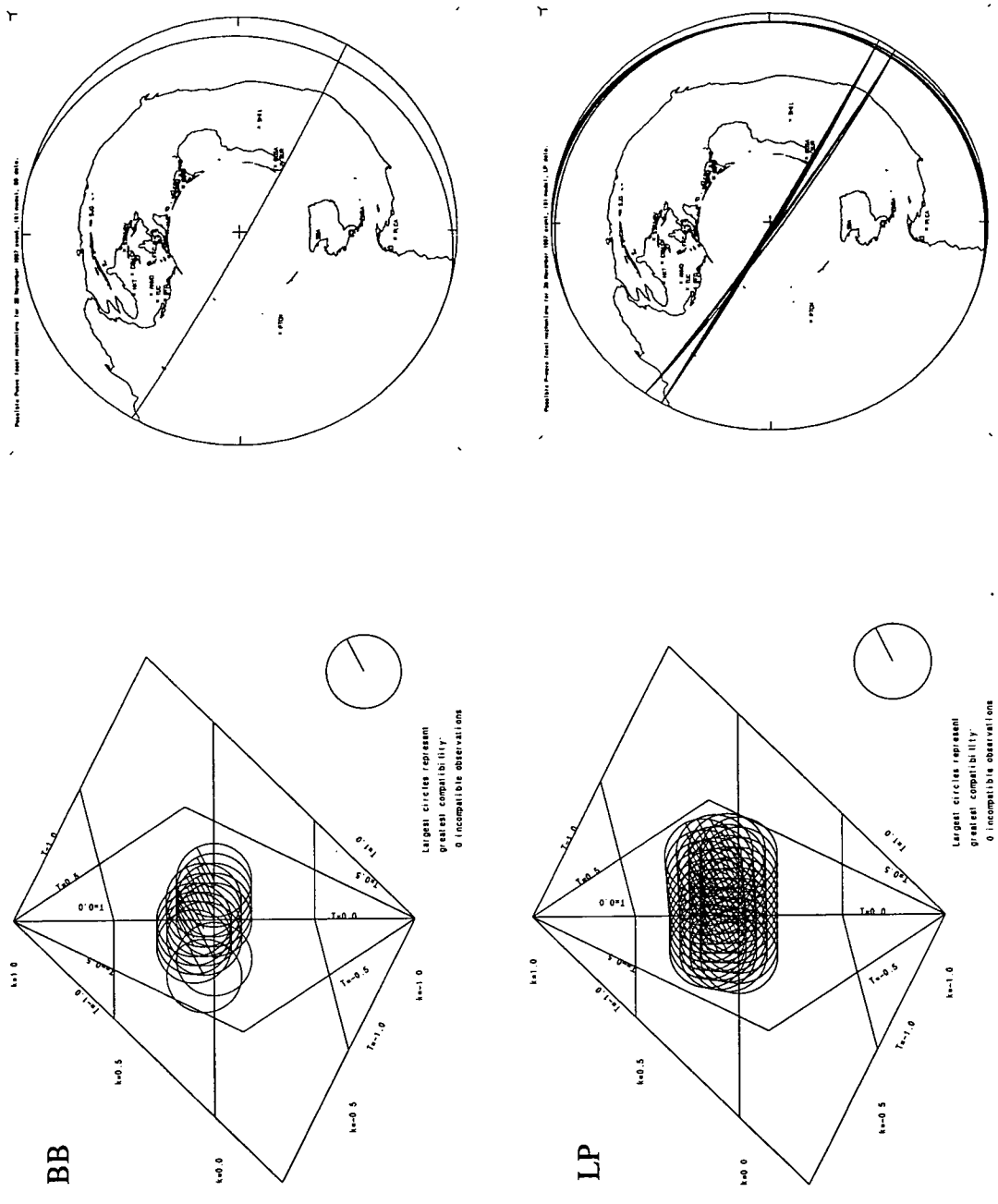

Figure B.12.
28 November 1997 Bolivia earthquake, IASP91 model. Results determined using the IASP91 model with broadband (top) and long period data (bottom).

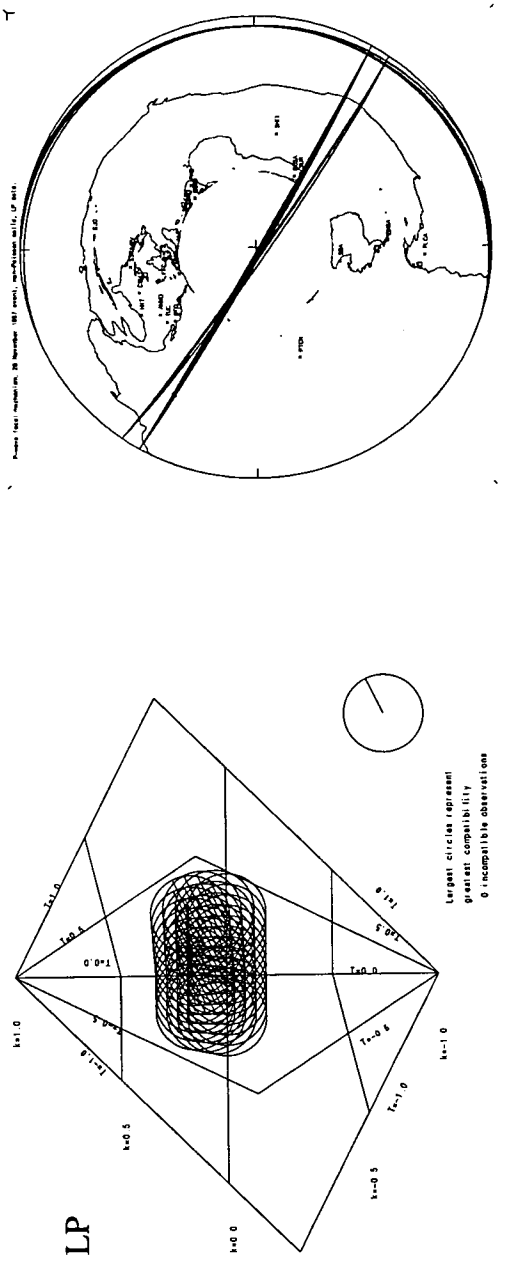

Figure B.13.
28 November 1997 Bolivia earthquake, assuming a non–Poisson source material. Compatible source types and double couple orientations are shown.

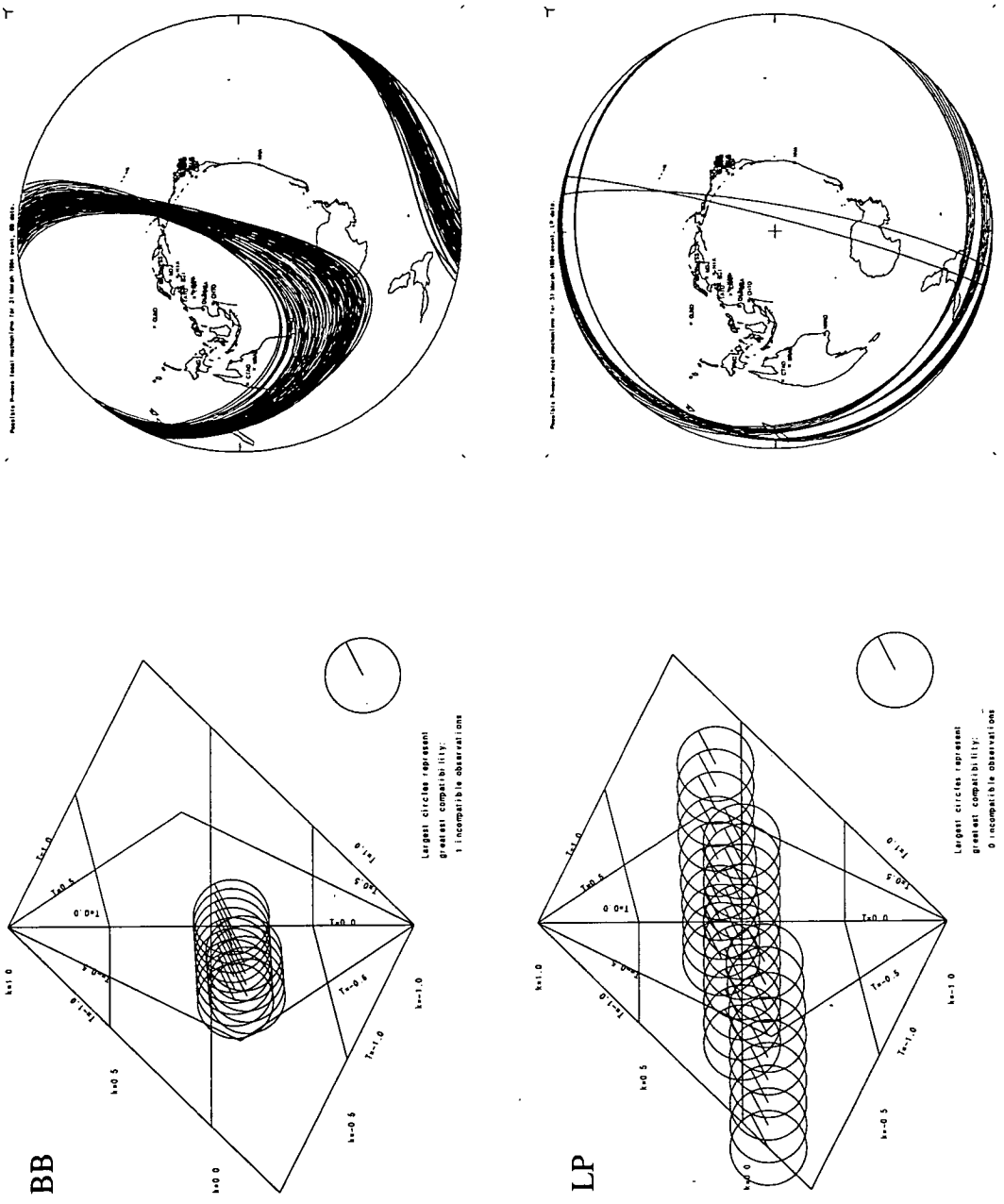

Figure B.14.
31 March 1994 Tonga earthquake, standard model. Results obtained using the standard model for broadband (top) and long period data (bottom).

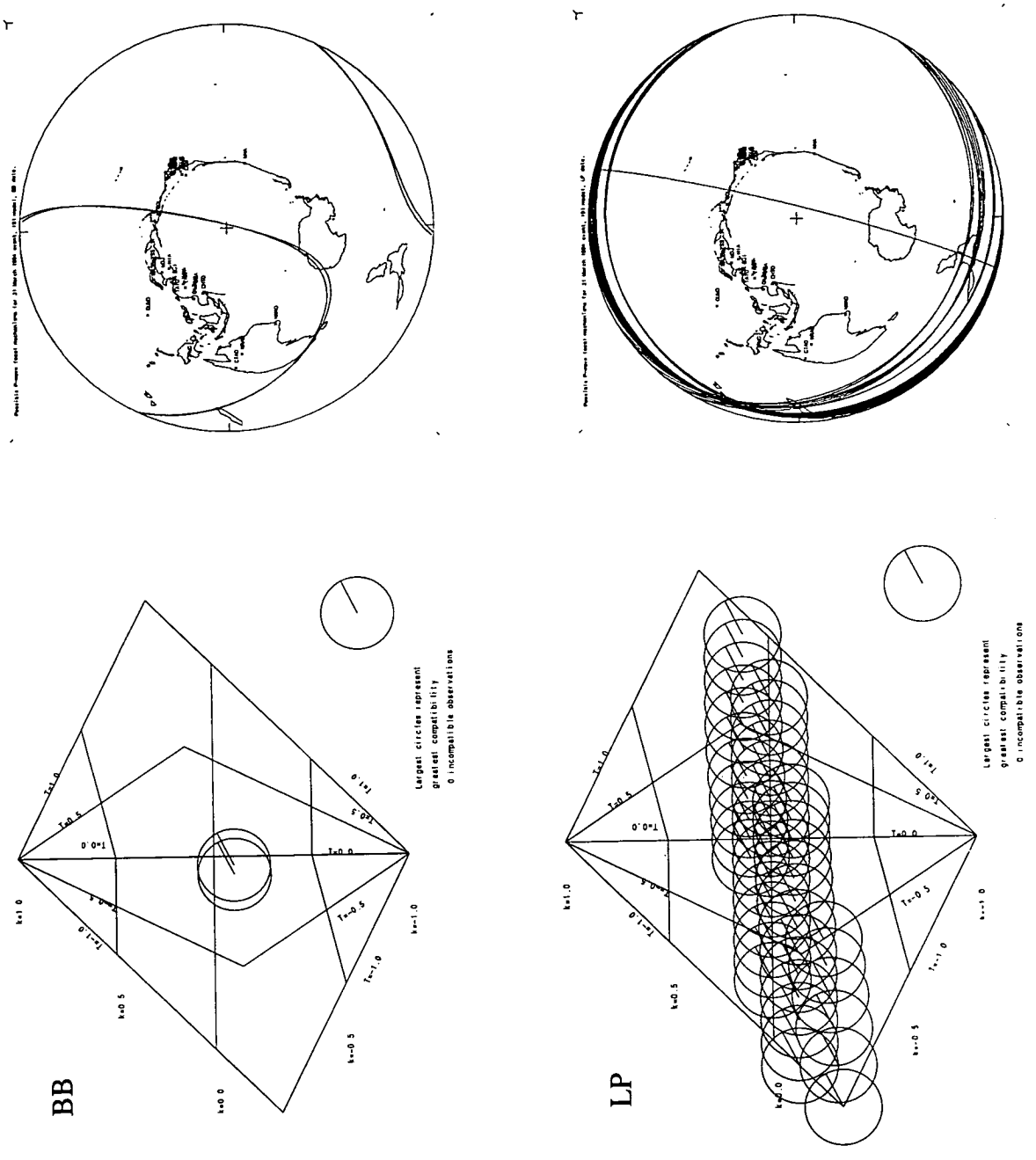

Figure B.15.
31 March 1994 Tonga earthquake, IASP91 model. Results obtained using the IASP91 model for broadband (top) and long period data (bottom).

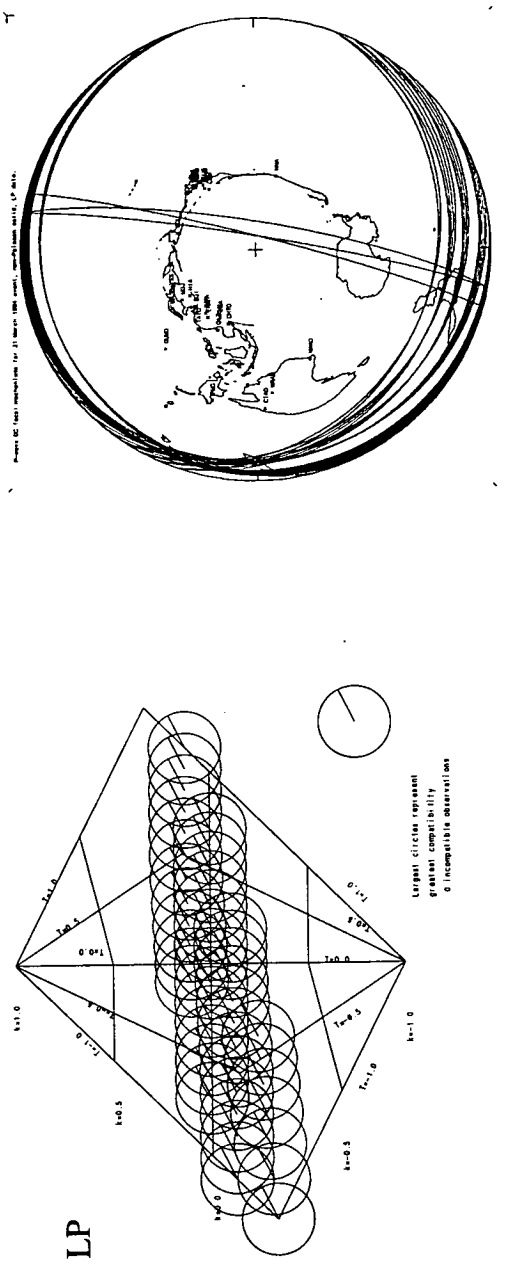

Figure B.16.
31 March 1994 Tonga earthquake, assuming a non–Poisson source material. Compatible source types and double couple orientations are shown.

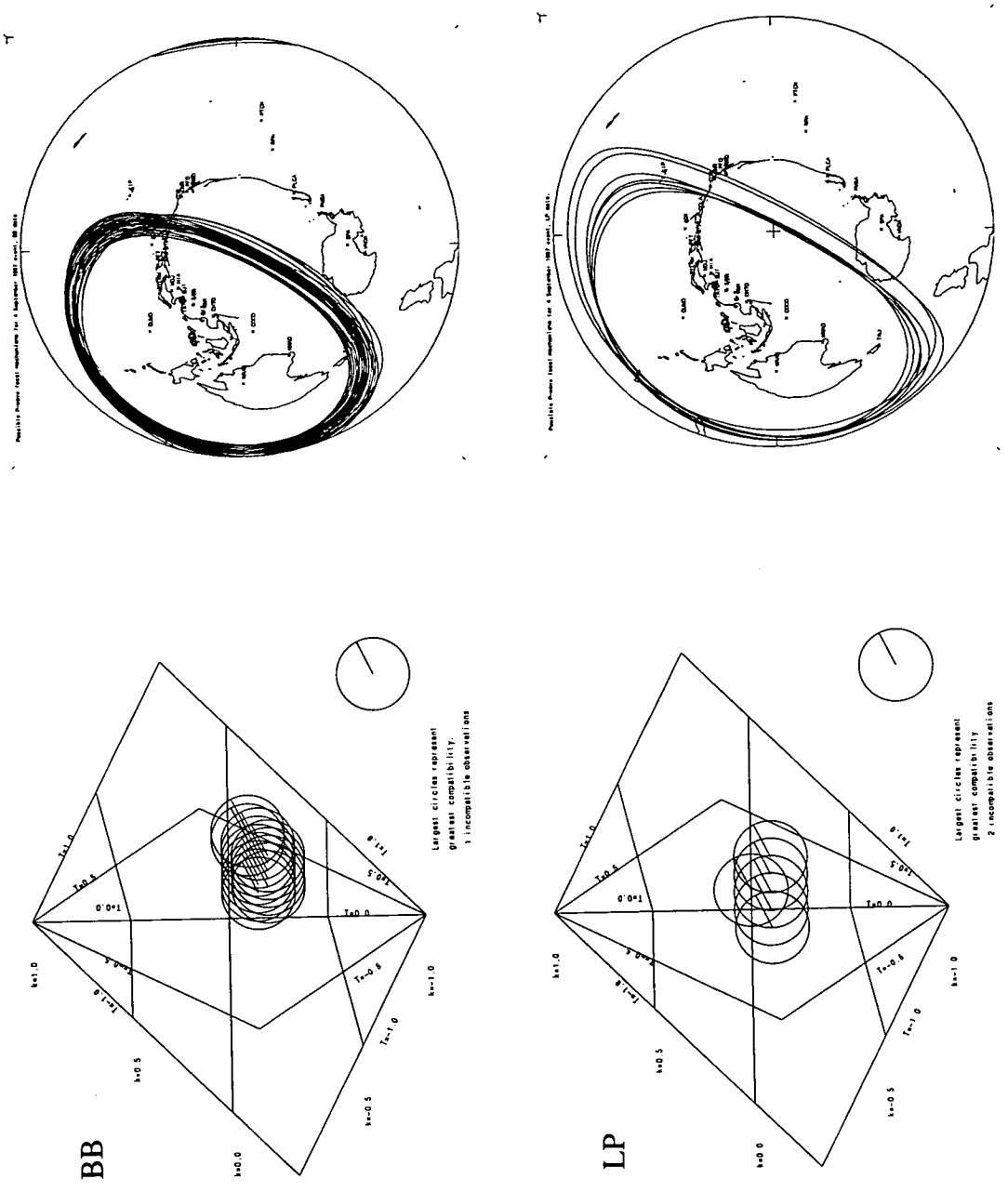

Figure B.17.
4 September 1997 Tonga earthquake, standard model. Results obtained using the standard model for broadband (top) and long period data (bottom).

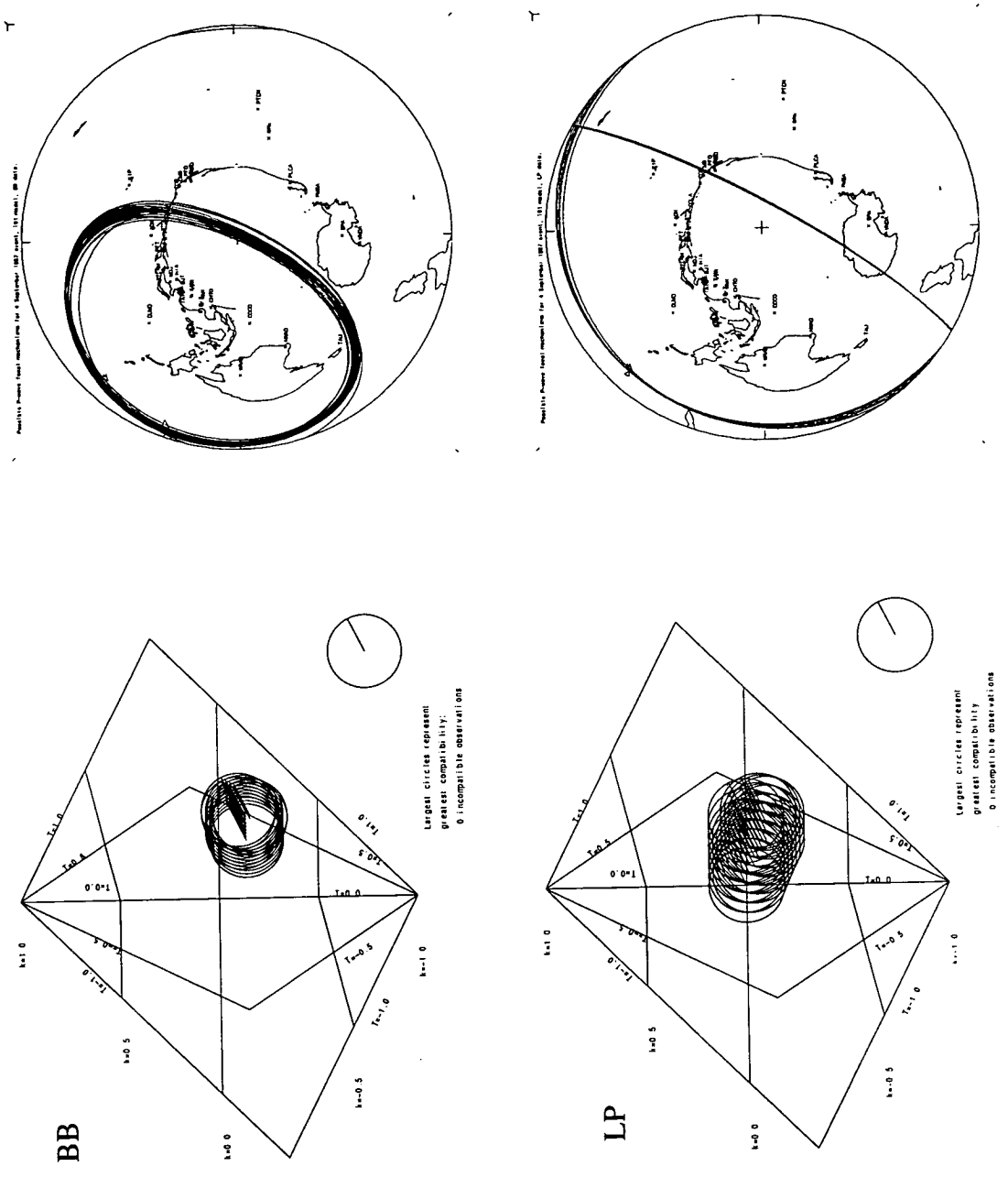

Figure B.18.
4 September 1997 Tonga earthquake, IASP91 model. Results obtained using the IASP91 model for broadband (top) and long period data (bottom).

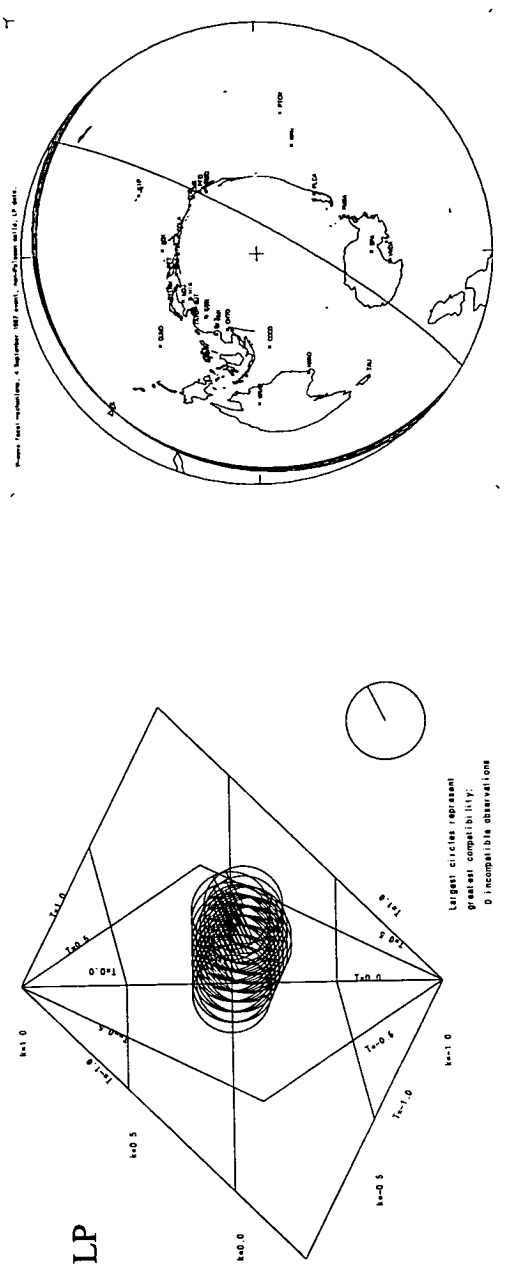

Figure B.19.
4 Spetember 1997 Tonga earthquake, assuming a non–Poisson source material. Compatible source types and double couple orientations are shown.

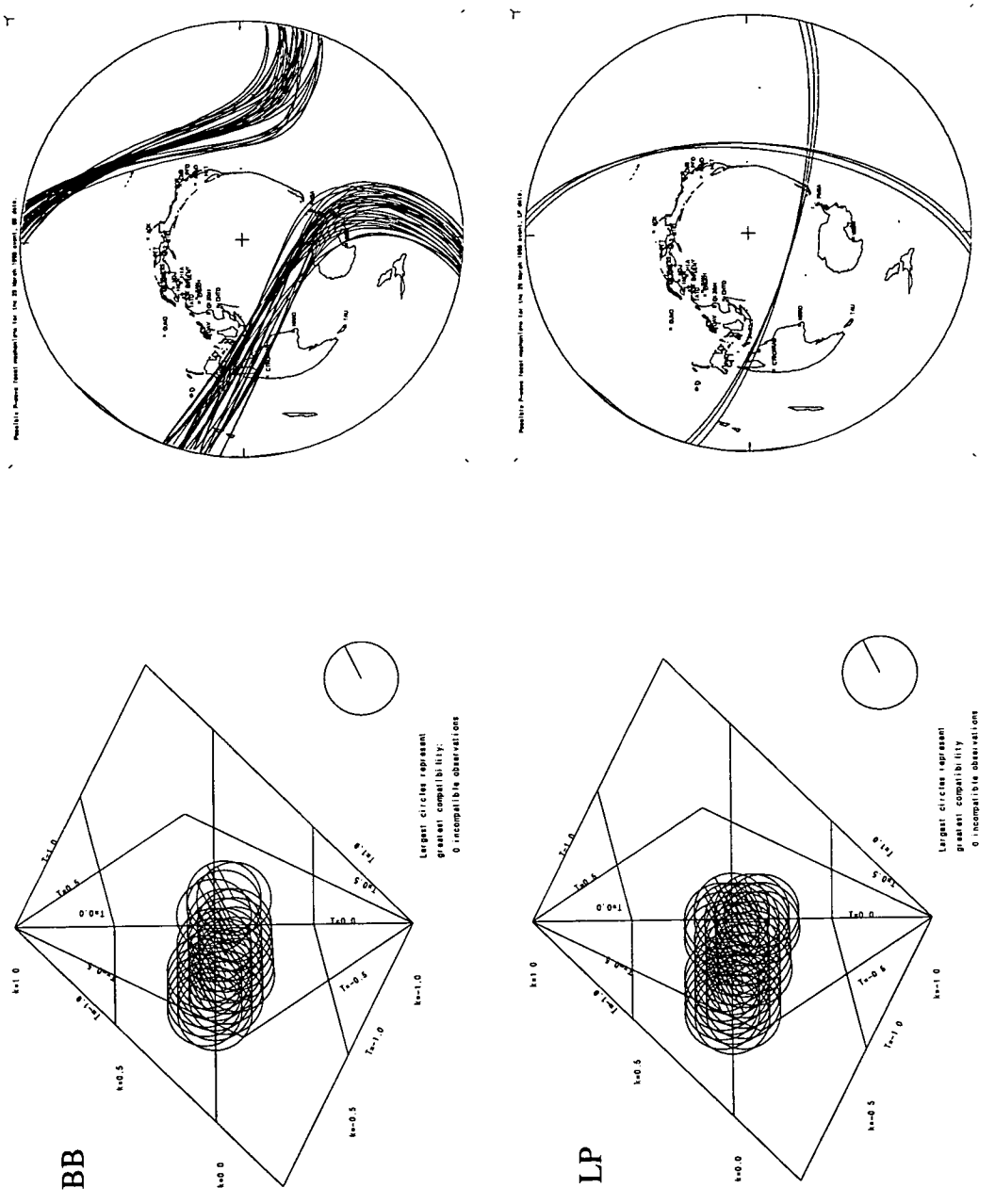

Figure B.20.
29 March 1998 Tonga earthquake, standard model. Results obtained using the standard model for broadband (top) and long period data (bottom).

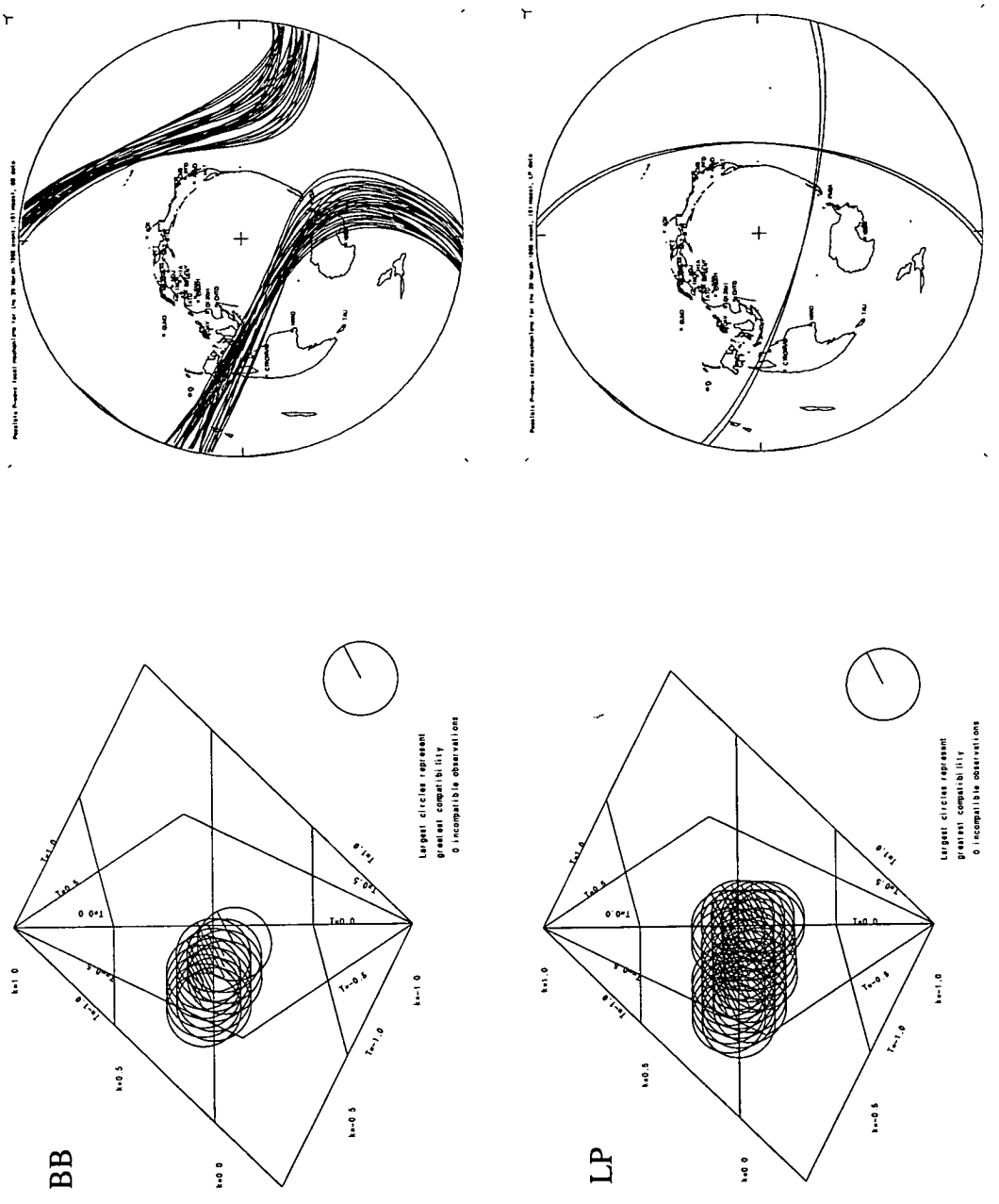

Figure B.21.
29 March 1998 Tonga earthquake, IASP91 model. Results obtained using the IASP91 model for broadband (top) and long period data (bottom).

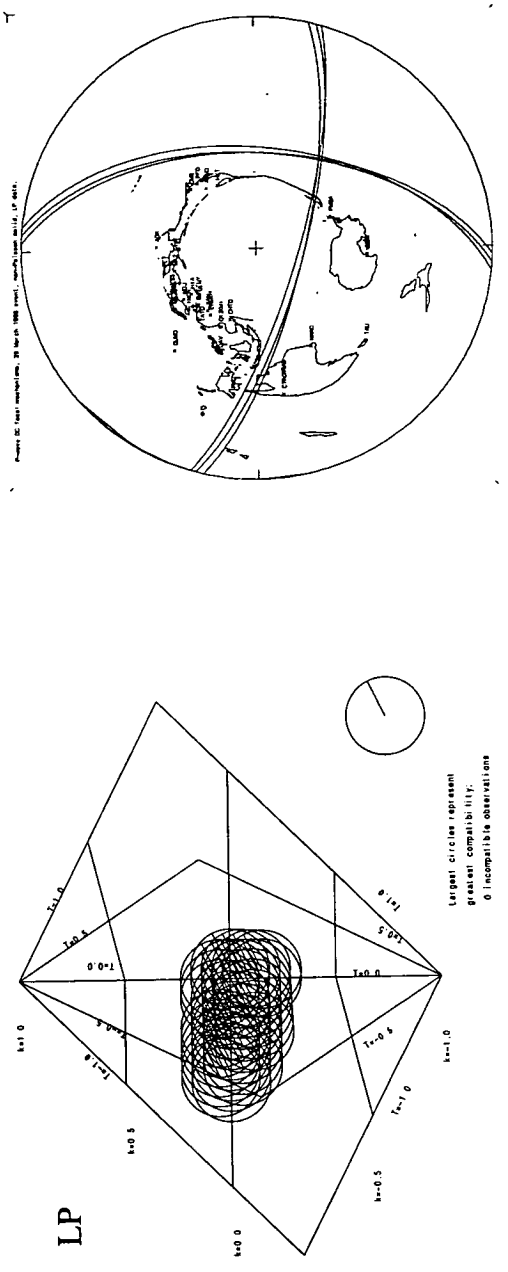

Figure B.22.
29 March 1998 Tonga earthquake, assuming a non–Poisson source material. Compatible source types and double couple orientations are shown.

Appendix C

Amplitude Bounds

The following tables provide details of the input data for the relative amplitude inversions, used to determine the earthquake source types and orientations in chapter 6. Six of the eight events have three tables each. The first shows the polarities and amplitude bounds for P, pP and sP measured from the broadband seismograms. The second shows the polarities and amplitude bounds measured from the long–period seismograms. The third table contains the take–off angles (α, γ and β), the angle of incidence of P at the receiver (i) and the surface reflection coefficients for pP (R_{pP}) and sP (R_{sP}), as calculated by ray tracing through the IASP91 earth velocity model. The earthquakes of 11 October 1993 (Izu–Bonin) and 9 June 1994 (Bolivia) excited waves of particularly low frequencies, removing the need to low pass filter the broadband records. These events have only two tables, the broadband amplitude bounds and the IASP91 parameters.

Polarities are described using the following convention:–

- + positive
- – negative
- U unknown
- O1 opposite to the polarity of P
- S1 same as the polarity of P

O and S may be followed by the numbers 2 or 3, referring to pP and sP, respectively, rather than to P (1).

11 October 1993, 15:54:21.2 UT, Broadband records											
Station			P			pP			sP		
Code	Δ	Az.	Pol.	Min.	Max.	Pol.	Min.	Max.	Pol.	Min.	Max.
ADK	38.28	45.3	+	4.0	10.0	U	0.0	6.0	–	2.0	30.0
PMG	42.14	166.5	+	1.0	3.0	+	1.0	6.0	–	2.0	12.0
CTAO	52.45	170.3	+	6.0	10.0	+	10.0	50.0	–	12.0	60.0
COL	54.78	30.1	+	3.0	5.0	+	1.0	5.0	–	2.0	12.0
WMQ	40.83	301.5	–	7.0	15.0	U	0.0	10.0	U	0.0	30.0
LSA	40.08	279.3	–	10.0	20.0	U	0.0	10.0	U	0.0	50.0
CMB	79.06	52.0	+	3.0	7.0	+	2.0	6.0	–	3.0	15.0
GSC	82.97	52.7	+	3.0	7.0	+	2.0	8.0	–	3.0	12.0
PFO	84.16	53.9	+	3.0	6.0	+	2.0	6.0	–	3.0	12.0
KIV	72.05	310.9	–	5.0	7.0	–	1.0	5.0	+	3.0	11.0
OBN	70.37	323.3	–	4.0	8.0	–	1.0	4.0	+	2.0	10.0
RAR	79.65	123.0	+	3.0	6.0	+	3.0	6.0	–	3.0	9.0
CHTO	37.49	259.0	–	8.0	16.0	U	0.0	12.0	+	5.0	50.0
LZH	28.53	287.6	–	15.0	27.0	–	4.0	28.0	+	8.0	40.0
QIZ	28.47	249.7	–	5.0	20.0	–	2.0	25.0	+	10.0	70.0
KMI	31.66	266.5	–	8.0	30.0	–	1.0	17.0	+	10.0	50.0
KEV	67.10	339.3	–	3.0	5.0	–	0.2	2.0	+	1.0	7.0
ISA	81.64	53.2	+	3.0	6.0	+	2.0	5.0	–	2.0	10.0
TUC	88.78	52.2	+	2.0	4.0	+	1.0	5.0	–	1.0	10.0
NWAO	67.56	198.9	–	1.0	3.0	U	0.0	3.0	+	0.30	8.0
ANMO	89.94	47.9	+	2.0	4.0	+	1.0	5.0	–	2.0	10.0
COR	73.84	47.3	+	3.0	6.0	+	2.0	6.0	–	3.0	14.0
SNZO	80.46	152.9	+	1.0	4.0	+	1.0	6.0	–	1.0	15.0
KONO	79.23	336.1	–	3.0	5.0	U	0.0	2.0	+	1.0	7.0
TLY	31.84	318.2	–	10.0	20.0	U	3.0	20.0	+	8.0	50.0
AAK	50.54	301.2	–	12.0	24.0	–	4.0	10.0	+	10.0	80.0
ABKT	63.85	299.8	–	10.0	20.0	–	2.0	8.0	+	8.0	40.0
NRIL	46.51	338.3	–	7.0	14.0	–	2.0	5.0	+	3.0	20.0
ARU	58.30	320.0	–	7.0	14.0	–	1.0	6.0	+	5.0	30.0
ALE	65.22	2.9	–	5.0	16.0	+	8.0	30.0	U	0.0	50.0

continued on next page

continued from previous page

Station			P			pP			sP		
Code	Δ	Az.	Pol.	Min.	Max.	Pol.	Min.	Max.	Pol.	Min.	Max.
FFC	79.38	30.7	+	5.0	10.0	+	2.0	10.0	–	3.0	20.0
MLA	58.88	35.8	+	5.0	10.0	+	4.0	12.0	–	4.0	20.0
USC	82.67	54.5	+	5.0	10.0	+	4.0	20.0	–	5.0	30.0
RPV	82.74	54.7	+	5.0	10.0	+	5.0	10.0	–	5.0	25.0
SBC	81.45	54.8	+	5.0	10.0	+	4.0	12.0	–	4.0	25.0
BAR	84.54	54.8	+	5.0	10.0	+	4.0	11.0	–	5.0	25.0
VTV	83.02	53.6	+	5.0	10.0	+	5.0	10.0	–	5.0	25.0
NEE	84.73	52.1	+	5.0	10.0	+	5.0	12.0	–	5.0	25.0
PAS	82.68	54.3	+	5.0	10.0	+	4.0	10.0	–	5.0	25.0
SVD	83.44	53.8	+	5.0	10.0	+	4.0	11.0	–	5.0	20.0
GDH	78.63	4.2	–	5.0	10.0	U	5.0	50.0	U	2.0	50.0

11 October 1993, IASP91 parameters						
Stn.	α	γ	β	i	R_{pP}	R_{sP}
ADK	44.2	133.3	157.1	25.5	-0.70	-0.30
PMG	42.4	135	157.9	24.6	-0.72	-0.29
CTAO	38.0	140.1	160.0	22.3	-0.77	-0.27
COL	36.9	141.1	160.4	21.8	-0.78	-0.27
WMQ	42.9	134.4	157.6	24.8	-0.71	-0.29
LSA	43.3	134.1	157.4	25.0	-0.71	-0.30
CMB	26.9	151.8	165.4	16.2	-0.87	-0.21
GSC	25.3	153.5	166.2	15.3	-0.89	-0.20
PFO	24.9	154	166.4	15.0	-0.89	-0.20
KIV	29.8	148.8	163.9	17.8	-0.85	-0.23
OBN	30.4	148.1	163.6	18.2	-0.84	-0.23
RAR	26.7	152	165.5	16.1	-0.87	-0.21
CHTO	44.5	132.9	157.0	25.6	-0.70	-0.30
LZH	48.1	129.8	155.7	27.3	-0.67	-0.31
QIZ	48.1	129.8	155.7	27.3	-0.67	-0.31
KMI	47.0	131.2	156.2	26.8	-0.68	-0.31

continued on next page

continued from previous page

Stn.	α	γ	β	i	R_{pP}	R_{sP}
KEV	31.8	146.6	162.9	19.0	-0.83	-0.24
ISA	25.9	152.9	165.9	15.6	-0.88	-0.20
TUC	23.1	156	167.4	14.0	-0.90	-0.18
NWAO	31.6	146.8	163.0	18.8	-0.83	-0.24
ANMO	23.0	156.5	167.7	14.0	-0.91	-0.18
COR	29.1	149.6	164.3	17.4	-0.85	-0.22
SNZO	26.4	152.4	165.7	15.9	-0.88	-0.21
KONO	26.9	151.9	165.4	16.2	-0.87	-0.21
TLY	47.0	131.2	156.2	26.8	-0.68	-0.31
AAK	38.8	139.1	159.6	22.7	-0.76	-0.28
ABKT	33.1	145.2	162.2	13.9	-0.81	-0.25
NRIL	40.5	137.3	158.7	23.6	-0.74	-0.28
ARU	35.3	142.7	161.1	20.9	-0.82	-0.23
ALE	32.6	145.8	162.5	19.4	-0.82	-0.25
FFC	26.8	151.9	165.4	16.1	-0.87	-0.21
MLA	35.1	143.0	161.3	20.8	-0.79	-0.26
USC	25.5	153.3	166.1	15.4	-0.88	-0.20
RPV	25.4	153.4	166.1	15.4	-0.88	-0.20
SBC	26.0	152.8	165.9	15.7	-0.88	-0.20
BAR	24.7	154.1	166.5	15.0	-0.89	-0.20
VTV	25.3	153.5	166.2	15.3	-0.89	-0.20
NEE	24.6	154.2	166.5	14.9	-0.89	-0.20
PAS	25.5	153.3	166.1	15.4	-0.88	-0.20
SVD	25.2	153.7	166.3	15.2	-0.89	-0.20
GDH	27.1	151.6	165.3	16.3	-0.87	-0.21

13 May 1997, 14:13:47.8 UT, Broadband records											
Station			P			pP			sP		
Code	Δ	Az.	Pol.	Min.	Max.	Pol.	Min.	Max.	Pol.	Min.	Max.
XAN	30.96	83.0	+	3.0	7.0	–	8.0	40.0	–	1.0	30.0
BJT	35.40	70.2	+	5.0	10.0	–	5.0	25.0	–	2.0	20.0
KEV	40.87	338.3	+	5.0	10.0	+	2.0	8.0	–	3.0	30.0
KMBO	48.76	227.6	+	10.0	20.0	–	0.50	7.0	–	7.0	30.0
YSS	52.85	54.6	+	5.0	10.0	–	4.0	20.0	U	0.0	15.0
SFJ	67.83	338.8	+	5.0	10.0	U	0.0	3.0	–	2.0	18.0
SSE	41.71	82.2	+	5.0	10.0	–	10.0	40.0	–	4.0	25.0
KONO	45.14	321.0	+	5.0	10.0	+	2.0	9.0	–	7.0	30.0
SHEL	89.04	249.4	+	10.0	20.0	–	6.0	25.0	–	6.0	30.0
CMLA	73.26	304.7	+	10.0	20.0	U	0.0	5.0	–	6.0	35.0
BILL	58.75	25.9	+	5.0	10.0	–	2.0	10.0	–	2.0	18.0
COLA	74.56	16.1	+	10.0	20.0	–	5.0	20.0	–	4.0	30.0
BOSA	77.67	220.1	+	10.0	20.0	–	6.0	20.0	–	4.0	30.0
NWAO	81.41	142.1	+	5.0	10.0	–	6.0	25.0	U	1.0	15.0
OBN	29.99	319.6	+	5.0	10.0	U	2.0	12.0	U	0.0	50.0
CHTO	30.20	118.0	U	5.0	20.0	–	15.0	80.0	–	10.0	100.0
KIEV	32.99	308.9	+	5.0	10.0	+	3.0	9.0	–	3.0	25.0
GRFO	44.50	306.8	+	5.0	10.0	+	1.0	7.0	–	5.0	25.0
KMI	29.40	103.5	U	2.0	10.0	–	10.0	120.0	–	4.0	90.0
MA2	54.44	38.0	+	5.0	10.0	–	2.0	15.0	–	3.0	20.0
BGCA	57.22	250.1	+	10.0	20.0	U	0.0	5.0	–	4.0	25.0
LVZ	37.53	338.4	+	10.0	20.0	+	4.0	14.0	–	8.0	60.0
ESK	52.33	316.0	+	10.0	20.0	+	1.0	7.0	–	9.0	50.0
MDJ	44.47	60.5	+	5.0	10.0	–	4.0	18.0	–	1.0	12.0
TSUM	74.85	231.8	+	10.0	20.0	–	3.0	16.0	–	3.0	25.0
KBS	48.69	347.2	+	5.0	10.0	+	2.0	7.0	–	5.0	50.0
PAB	57.80	297.9	+	6.0	12.0	+	0.10	6.0	–	2.0	40.0
YAK	44.06	35.4	+	6.0	12.0	–	2.0	20.0	–	3.0	25.0
DPC	41.11	307.5	+	5.0	30.0	U	0.0	8.0	–	3.0	100.0
SUR	82.98	220.9	+	10.0	20.0	–	5.0	22.0	–	4.0	30.0
FFC	89.02	355.9	+	10.0	20.0	–	7.0	30.0	–	5.0	35.0

13 May 1997, 14:13:47.8 UT, Long–period records											
Station			P			pP			sP		
Code	Δ	Az.	Pol.	Min.	Max.	Pol.	Min.	Max.	Pol.	Min.	Max.
XAN	30.96	83.0	+	2.0	8.0	–	10.0	40.0	–	0.10	10.0
BJT	35.40	70.2	+	10.0	20.0	–	25.0	70.0	–	1.0	20.0
KEV	40.87	338.3	+	10.0	20.0	+	1.0	15.0	–	15.0	50.0
KMBO	48.76	227.6	+	20.0	40.0	–	1.0	15.0	–	18.0	80.0
YSS	52.85	54.6	+	10.0	20.0	–	9.0	45.0	U	0.0	5.0
SFJ	67.83	338.8	+	10.0	20.0	U	0.0	5.0	–	10.0	40.0
SSE	41.71	82.2	+	10.0	20.0	–	20.0	50.0	–	1.0	20.0
KONO	45.14	321.0	+	10.0	20.0	+	2.0	15.0	–	8.0	40.0
SHEL	89.04	249.4	+	10.0	20.0	–	4.0	25.0	–	4.0	40.0
CMLA	73.26	304.7	+	10.0	20.0	U	0.0	5.0	–	6.0	35.0
BILL	58.75	25.9	+	10.0	20.0	–	0.01	7.0	–	10.0	50.0
COLA	74.56	16.1	+	10.0	20.0	–	1.0	10.0	–	8.0	40.0
BOSA	77.67	220.1	+	15.0	30.0	–	5.0	25.0	–	8.0	40.0
NWAO	81.41	142.1	+	10.0	20.0	–	18.0	150.0	U	0.0	30.0
OBN	29.99	319.6	+	5.0	10.0	U	1.0	13.0	U	0.0	50.0
CHTO	30.20	118.0	U	0.0	10.0	–	5.0	20.0	–	5.0	40.0
KIEV	32.99	308.9	+	10.0	20.0	+	2.0	12.0	–	8.0	40.0
GRFO	44.50	306.8	+	10.0	20.0	+	0.50	5.0	–	5.0	40.0
KMI	29.40	103.5	U	0.0	10.0	–	15.0	40.0	–	2.0	50.0
MA2	54.44	38.0	+	15.0	30.0	–	10.0	35.0	–	10.0	50.0
BGCA	57.22	250.1	+	15.0	30.0	–	1.0	6.0	–	10.0	50.0
LVZ	37.53	338.4	+	10.0	20.0	+	0.10	10.0	–	8.0	40.0
ESK	52.33	316.0	+	10.0	20.0	+	1.0	10.0	–	5.0	40.0
MDJ	44.47	60.5	+	10.0	20.0	–	10.0	25.0	–	3.0	20.0
TSUM	74.85	231.8	+	15.0	30.0	–	4.0	14.0	–	10.0	50.0
KBS	48.69	347.2	+	10.0	20.0	+	1.0	10.0	–	10.0	40.0
PAB	57.80	297.9	+	10.0	20.0	U	0.05	5.0	–	8.0	40.0
YAK	44.06	35.4	+	10.0	20.0	–	5.0	15.0	–	10.0	40.0
DPC	41.11	307.5	+	10.0	20.0	U	0.0	4.0	–	6.0	35.0
SUR	82.98	220.9	+	10.0	20.0	–	5.0	18.0	–	5.0	30.0
FFC	89.02	355.9	+	10.0	20.0	–	1.0	8.0	–	5.0	30.0

13 May 1997, IASP91 parameters						
Stn.	α	γ	β	i	R_{pP}	R_{sP}
XAN	42.4	137.1	158.2	27.2	–0.68	–0.31
KMBO	35.8	143.2	161.1	23.4	–0.75	–0.28
SSE	38.5	140.4	159.8	25.0	–0.72	–0.29
MDJ	37.5	141.6	160.3	24.4	–0.74	–0.29
KBS	35.8	143.2	161.0	23.4	–0.75	–0.28
PAB	32.3	146.8	162.7	21.3	–0.79	–0.26
NWAO	23.7	155.7	167.1	15.8	–0.88	–0.20
YAK	37.6	141.4	160.2	24.4	–0.73	–0.29
LVZ	40.2	138.8	159.0	25.9	–0.70	–0.30
DPC	38.7	140.1	159.7	25.1	–0.72	–0.29
ESK	34.5	144.7	161.7	22.6	–0.77	–0.27
SUR	23.2	156.3	167.4	15.5	–0.89	–0.20
FFC	21.9	158.6	168.6	14.3	–0.91	–0.18
SHEL	20.9	158.6	168.6	14.0	–0.91	–0.18
CMLA	26.7	152.7	165.6	17.7	–0.85	–0.22
BJT	41.0	138	158.7	26.4	–0.69	–0.30
KEV	38.8	140	159.6	25.2	–0.72	–0.29
YSS	34.3	144.9	161.8	22.5	–0.77	–0.27
SFJ	28.7	150.6	164.6	19.0	–0.83	–0.24
KONO	37.2	141.9	160.4	24.2	–0.74	–0.29
TSUM	26.1	153.2	165.9	17.4	–0.86	–0.22
BILL	32.0	147.2	162.9	21.0	–0.80	–0.26
COLA	26.2	153.1	165.8	17.4	–0.86	–0.22
BOSA	25.1	154.3	166.4	16.7	–0.87	–0.21
OBN	42.6	136.7	158.2	27.3	–0.68	–0.31
CHTO	42.6	136.8	158.2	27.3	–0.68	–0.31
KIEV	41.8	137.4	158.4	26.9	–0.69	–0.31
GRFO	37.5	141.6	160.3	24.4	–0.74	–0.29
KMI	42.7	136.5	158.1	27.4	–0.68	–0.31
MA2	33.7	145.4	162.1	22.1	–0.78	–0.27
BGCA	32.6	146.5	162.6	21.4	–0.79	–0.26

28 November 1997, 22:53:41.5 UT, Broadband records											
Station			P			pP			sP		
Code	Δ	Az.	Pol.	Min.	Max.	Pol.	Min.	Max.	Pol.	Min.	Max.
PMSA	51.08	177.4	+	20.0	40.0	+	8.0	20.0	−	10.0	30.0
SJG	31.76	4.8	−	3.0	6.0	−	2.0	8.0	+	2.0	12.0
TUC	60.92	319.6	−	7.0	13.0	−	6.0	13.0	+	2.0	20.0
HRV	56.02	357.5	−	15.0	25.0	−	10.0	20.0	+	10.0	30.0
ANMO	60.18	324.6	−	9.0	15.0	−	7.0	15.0	+	2.0	30.0
CCM	55.66	338.6	−	14.0	26.0	−	5.0	10.0	+	3.0	30.0
HKT	50.66	329.3	−	17.0	35.0	−	15.0	35.0	+	8.0	45.0
SSPA	54.75	351.5	−	20.0	30.0	−	10.0	20.0	+	14.0	26.0
PTCN	58.49	248.9	+	15.0	40.0	+	2.0	20.0	U	0.0	30.0
CMB	70.62	319.0	−	8.0	12.0	−	2.0	6.0	+	4.0	12.0
KONO	95.97	30.0	−	6.0	12.0	−	9.0	17.0	+	8.0	25.0
GRFO	94.01	39.9	−	5.0	12.0	−	7.0	15.0	+	8.0	18.0
BOSA	87.01	118.6	−	13.0	19.0	U	10.0	25.0	+	4.0	15.0
PAB	79.95	45.1	−	19.0	27.0	−	19.0	27.0	+	10.0	30.0
BFO	91.79	40.6	−	9.0	15.0	−	10.0	18.0	+	8.0	20.0
RPN	40.08	244.1	+	10.0	30.0	U	0.0	5.0	U	0.0	10.0
PFO	65.41	317.3	−	10.0	30.0	−	3.0	15.0	+	2.0	20.0
SHEL	60.78	100.7	−	10.0	30.0	U	0.0	10.0	U	0.0	20.0
SBA	83.44	190.1	+	5.0	10.0	+	3.0	15.0	U	0.0	10.0
ESK	87.94	31.4	−	3.0	12.0	−	8.0	20.0	+	5.0	30.0
FFC	73.77	340.7	−	10.0	20.0	−	4.0	18.0	+	1.0	15.0
SUR	82.44	121.4	−	1.0	100.0	+	1.0	100.0	U	0.0	100.0
RAR	86.02	249.3	+	1.0	∞	U	0.0	∞			
PLCA	26.93	183.0	+	1.0	100.0	−	1.0	100.0			
ALE	96.15	0.8	−	1.0	100.0	−	1.0	100.0			

28 November 1997, 22:53:41.5 UT, Long–period records											
Station			P			pP			sP		
Code	Δ	Az.	Pol.	Min.	Max.	Pol.	Min.	Max.	Pol.	Min.	Max.
PMSA	51.08	177.4	+	30.0	60.0	+	10.0	80.0	–	20.0	80.0
SJG	31.76	4.8	–	40.0	80.0	–	40.0	80.0	+	40.0	170.0
TUC	60.92	319.6	–	14.0	20.0	–	7.0	14.0	+	5.0	35.0
HRV	56.02	357.5	–	25.0	45.0	–	18.0	36.0	+	25.0	55.0
ANMO	60.18	324.6	–	17.0	29.0	–	7.0	17.0	+	7.0	40.0
CCM	55.66	338.6	–	18.0	32.0	–	14.0	24.0	+	15.0	35.0
HKT	50.66	329.3	–	20.0	40.0	–	12.0	24.0	+	13.0	40.0
SSPA	54.75	351.5	–	24.0	52.0	–	18.0	34.0	+	25.0	50.0
PTCN	58.49	248.9	+	15.0	40.0	+	10.0	35.0	–	10.0	60.0
CMB	70.62	319.0	–	13.0	25.0	–	8.0	16.0	+	8.0	35.0
KONO	95.97	30.0	–	9.0	17.0	–	8.0	18.0	+	13.0	35.0
GRFO	94.01	39.9	–	8.0	16.0	–	10.0	18.0	+	10.0	30.0
BOSA	87.01	118.6	–	16.0	30.0	U	1.0	11.0	+	10.0	50.0
PAB	79.95	45.1	–	24.0	36.0	–	15.0	40.0	+	30.0	100.0
BFO	91.79	40.6	–	12.0	23.0	–	10.0	20.0	+	10.0	40.0
RPN	40.08	244.1	+	20.0	40.0	U	0.0	20.0	–	5.0	70.0
PFO	65.41	317.3	–	10.0	20.0	–	5.0	15.0	+	5.0	35.0
SHEL	60.78	100.7	–	10.0	20.0	–	4.0	12.0	+	6.0	30.0
SBA	83.44	190.1	+	18.0	32.0	+	19.0	40.0	–	20.0	55.0
ESK	87.94	31.4	–	15.0	25.0	–	12.0	28.0	+	10.0	50.0
FFC	73.77	340.7	–	28.0	52.0	–	15.0	30.0	+	17.0	50.0
SUR	82.44	121.4	–	1.0	100.0	+	1.0	100.0	U	0.0	100.0
RAR	86.02	249.3	+	1.0	∞	U	0.0	∞			
PLCA	26.93	183.0	+	1.0	100.0	–	1.0	100.0			
ALE	96.15	0.8	–	1.0	100.0	–	1.0	100.0			

28 November 1997, IASP91 parameters						
Stn.	α	γ	β	i	R_{pP}	R_{sP}
PMSA	45.5	129.1	155.6	22.2	–0.75	–0.28
SJG	56.8	116.3	151.5	26.3	–0.67	–0.31
TUC	40.3	135.5	158.0	20.0	–0.80	–0.25
HRV	42.7	132.5	156.8	21.0	–0.78	–0.27
ANMO	40.7	135	157.8	20.2	–0.79	–0.26
CCM	42.9	132.3	156.7	21.1	–0.77	–0.27
HKT	45.7	128.8	155.5	22.3	–0.75	–0.28
SSPA	43.4	131.7	156.5	21.3	–0.77	–0.27
PTCN	41.5	133.9	157.4	20.5	–0.79	–0.26
CMB	35.4	141.2	160.4	17.8	–0.84	–0.23
KONO	26.0	153.1	165.8	13.4	–0.91	–0.18
GRFO	26.4	152.9	165.6	13.6	–0.91	–0.18
BOSA	27.4	150.1	164.5	14.1	–0.90	–0.19
PAB	30.8	146.3	162.7	15.7	–0.87	–0.21
BFO	26.8	152.7	165.5	13.8	–0.91	–0.18
RPN	51.6	121.2	152.9	24.5	–0.70	–0.30
PFO	37.9	138.2	159.1	19.0	–0.82	–0.25
SHEL	40.4	135.4	158.0	20.0	–0.80	–0.25
SBA	29.2	148.2	163.6	14.9	–0.88	–0.20
ESK	27.2	150.6	164.8	14.0	–0.90	–0.19
FFC	33.9	143	161.2	17.1	–0.85	–0.23
SUR	29.6	147.7	163.3	15.2	–0.88	–0.20

10 January 1994, UT, Broadband records											
Station			P			pP			sP		
Code	Δ	Az.	Pol.	Min.	Max.	Pol.	Min.	Max.	Pol.	Min.	Max.
SJG	31.49	6.0	–	5.0	10.0	U	2.0	15.0	+	10.0	40.0
PMSA	51.44	177.0	+	10.0	20.0	+	3.0	15.0	–	4.0	30.0
CCM	55.13	339.1	–	10.0	20.0	–	2.0	9.0	+	4.0	30.0
HRV	55.67	358.1	–	10.0	20.0	–	3.0	10.0	+	3.0	25.0
ANMO	59.54	325.0	–	10.0	20.0	–	1.0	5.0	+	5.0	20.0
TUC	60.26	319.9	–	10.0	20.0	–	2.0	9.0	+	8.0	35.0
TBT	65.04	49.4	–	10.0	20.0	–	3.0	10.0	+	15.0	40.0
SVD	65.46	317.6	–	10.0	20.0	–	1.0	5.0	+	5.0	20.0
CMB	69.96	319.3	–	20.0	40.0	–	2.0	8.0	+	10.0	40.0
FFC	73.25	341.0	–	10.0	20.0	–	2.0	8.0	+	5.0	25.0
SPA	76.68	180.0	+	10.0	20.0	+	8.0	40.0	U	1.0	10.0
PAB	80.17	45.4	–	10.0	20.0	–	1.0	7.0	+	15.0	60.0
VNDA	84.69	189.8	+	10.0	20.0	+	20.0	60.0	–	5.0	25.0
BOSA	87.72	118.7	U	10.0	20.0	O1	10.0	60.0	U	7.0	60.0
ESK	87.99	31.6	–	10.0	20.0	–	2.0	10.0	+	7.0	40.0
LBTB	88.89	115.3	U	10.0	20.0	+	8.0	50.0	–	4.0	35.0
ALE	95.83	0.9	–	10.0	20.0	–	2.0	8.0	+	7.0	25.0
KONO	96.0	30.1	–	10.0	20.0	–	2.0	9.0	+	6.0	50.0
NEE	64.31	319.7	U	30.0	70.0	U	1.0	18.0	U	0.5	25.0
PFO	64.74	317.5	–	10.0	20.0	–	1.0	7.0	+	3.0	18.0
ISA	67.31	318.2	–	5.0	10.0	–	0.1	3.0	+	0.5	8.0

10 January 1994, UT, Long–period records											
Station			P			pP			sP		
Code	Δ	Az.	Pol.	Min.	Max.	Pol.	Min.	Max.	Pol.	Min.	Max.
SJG	31.49	6.0	–	5.0	10.0	U	2.0	15.0	+	10.0	40.0
PMSA	51.44	177.0	+	10.0	20.0	+	3.0	15.0	–	4.0	30.0
CCM	55.13	339.1	–	10.0	20.0	–	2.0	9.0	+	4.0	30.0
HRV	55.67	358.1	–	10.0	20.0	–	3.0	10.0	+	3.0	25.0
ANMO	59.54	325.0	–	10.0	20.0	–	1.0	5.0	+	5.0	20.0
TUC	60.26	319.9	–	10.0	20.0	–	2.0	9.0	+	8.0	35.0
TBT	65.04	49.4	–	10.0	20.0	–	3.0	10.0	+	15.0	40.0
SVD	65.46	317.6	–	10.0	20.0	–	1.0	5.0	+	5.0	20.0
CMB	69.96	319.3	–	20.0	40.0	–	2.0	8.0	+	10.0	40.0
FFC	73.25	341.0	–	10.0	20.0	–	2.0	8.0	+	5.0	25.0
SPA	76.68	180.0	+	10.0	20.0	+	8.0	40.0	U	1.0	10.0
PAB	80.17	45.4	–	10.0	20.0	–	1.0	7.0	+	15.0	60.0
VNDA	84.69	189.8	+	10.0	20.0	+	20.0	60.0	–	5.0	25.0
BOSA	87.72	118.7	U	10.0	20.0	O1	10.0	60.0	U	7.0	60.0
ESK	87.99	31.6	–	10.0	20.0	–	2.0	10.0	+	7.0	40.0
LBTB	88.89	115.3	U	10.0	20.0	+	8.0	50.0	–	4.0	35.0
ALE	95.83	0.9	–	10.0	20.0	–	2.0	8.0	+	7.0	25.0
KONO	96.0	30.1	–	10.0	20.0	–	2.0	9.0	+	6.0	50.0
NEE	64.31	319.7	U	30.0	70.0	U	1.0	18.0	U	0.5	25.0
PFO	64.74	317.5	–	10.0	20.0	–	1.0	7.0	+	3.0	18.0
ISA	67.31	318.2	–	5.0	10.0	–	0.1	3.0	+	0.5	8.0

10 January 1994, IASP91 parameters						
Stn.	α	γ	β	i	R_{pP}	R_{sP}
SJG	57.7	114.6	151.0	26.3	–0.67	–0.31
PMSA	45.8	128.4	155.3	22.0	–0.74	–0.29
CCM	43.6	131.1	156.2	21.2	–0.77	–0.27
HRV	43.3	131.5	156.4	21.1	–0.77	–0.27
ANMO	41.4	133.9	157.4	20.3	–0.79	–0.26
TUC	41.1	134.3	157.6	20.1	–0.79	–0.26
TBT	38.5	137.4	158.7	19.0	–0.81	–0.25
SVD	38.3	137.6	159.8	18.9	–0.82	–0.25
CMB	36.1	140.2	160.0	18.0	–0.83	–0.23
FFC	34.5	142.2	160.8	17.2	–0.85	–0.23
SPA	32.8	144.1	161.7	16.5	–0.86	–0.22
PAB	31.0	146	162.5	15.7	–0.87	–0.21
VNDA	28.8	148.5	163.7	14.6	–0.89	–0.20
BOSA	27.5	150.1	164.5	14.0	–0.90	–0.19
ESK	27.5	150.2	164.6	14.0	–0.90	–0.19
LBTB	27.5	150.7	164.8	14.0	–0.90	–0.19
ALE	26.3	152.8	165.6	13.4	–0.91	–0.18
KONO	26.3	152.8	165.6	13.4	–0.91	–0.18
NEE	38.9	137.1	158.5	19.2	–0.81	–0.25
PFO	38.7	137.2	158.7	19.1	–0.81	–0.25
ISA	37.3	138.6	159.3	18.5	–0.82	–0.24

9 June 1994, UT, Broadband records											
Station			P			pP			sP		
Code	Δ	Az.	Pol.	Min.	Max.	Pol.	Min.	Max.	Pol.	Min.	Max.
SJG	31.77	2.5	–	5.0	10.0	U	0.0	10.0	+	1.0	100.0
RPN	41.12	244.5	+	20.0	40.0	+	1.0	15.0	–	0.1	20.0
PMSA	50.94	178.1	+	20.0	40.0	+	1.0	18.0	–	0.1	30.0
HRV	56.18	356.4	–	10.0	20.0	–	1.0	11.0	+	2.0	50.0
CCM	56.19	337.6	–	10.0	20.0	–	0.1	15.0	+	2.0	60.0
TUC	61.77	318.8	–	10.0	20.0	–	1.0	15.0	+	2.0	45.0
CMB	71.47	318.4	–	20.0	40.0	–	2.0	15.0	+	2.0	30.0
SPA	76.26	180.0	+	10.0	20.0	+	3.0	20.0	U	0.0	20.0
COR	77.02	322.7	–	10.0	20.0	–	2.0	9.0	U	0.0	15.0
PAB	79.17	44.6	–	10.0	20.0	–	0.5	12.0	+	1.0	70.0
SUR	81.38	121.2	+	10.0	20.0	+	15.0	50.0	U	0.0	40.0
BOSA	85.92	118.3	+	15.0	50.0	+	15.0	100.0	U	0.0	40.0
LBTB	87.06	114.9	+	10.0	20.0	+	12.0	40.0	–	1.0	30.0
RAR	87.11	249.0	+	10.0	20.0	+	15.0	60.0	–	1.0	25.0
ESK	87.40	31.1	–	10.0	20.0	–	10.0	20.0	+	1.0	30.0
KIP	95.36	290.6	–	20.0	40.0	–	2.0	12.0	+	2.0	60.0
KONO	95.45	29.8	–	10.0	20.0	–	7.0	17.0	+	1.0	45.0
PFO	66.29	316.6	–	10.0	20.0	–	1.0	7.0	+	1.0	40.0
ISA	68.85	317.3	–	20.0	40.0	–	0.1	14.0	+	5.0	70.0

9 June 1994, IASP91 parameters						
Stn.	α	γ	β	i	R_{pP}	R_{sP}
SJG	58.6	112.6	150.6	26.1	−0.67	−0.31
RPN	52.6	118.7	152.2	24.2	−0.70	−0.29
PMSA	46.8	126.7	154.7	22.1	−0.75	−0.28
HRV	43.7	130.6	156.0	20.9	−0.77	−0.27
CCM	43.7	130.6	156.0	20.9	−0.77	−0.27
TUC	40.9	134.3	157.6	19.7	−0.80	−0.25
CMB	35.8	140.2	160.0	17.6	−0.84	−0.23
SPA	33.4	143.3	161.2	16.5	−0.86	−0.22
COR	33.0	143.5	161.4	16.3	−0.86	−0.22
PAB	32.0	144.7	162.0	15.8	−0.87	−0.21
SUR	30.9	145.9	162.5	15.3	−0.88	−0.21
BOSA	28.6	148.5	163.7	14.3	−0.89	−0.19
LBTB	28.0	149.1	164.0	14.0	−0.90	−0.19
RAR	28.0	149.2	164.1	14.0	−0.90	−0.19
ESK	28.0	149.3	164.1	14.0	−0.90	−0.19
KIP	26.8	152.3	165.3	13.5	−0.91	−0.18
KONO	26.8	152.3	165.3	13.4	−0.91	−0.18
PFO	38.4	137.1	158.6	18.7	−0.82	−0.24
ISA	37.1	138.6	159.3	18.1	−0.83	−0.24

31 March 1994, 22:40:53.9 UT, Broadband records											
Station			P			pP			sP		
Code	Δ	Az.	Pol.	Min.	Max.	Pol.	Min.	Max.	Pol.	Min.	Max.
PMSA	80.36	156.9	+	0.01	∞	U	0.0	∞	U	0.0	∞
WRAB	43.07	264.0	−	20.0	35.0	U	0.0	25.0	+	25.0	80.0
CTAO	32.03	267.2	−	20.0	30.0	−	25.0	50.0	+	30.0	100.0
PMG	34.44	286.2	−	25.0	45.0	−	20.0	60.0	+	10.0	80.0
COR	83.82	36.6	+	2.0	6.0	+	4.0	20.0	−	0.1	8.0
NWAO	56.46	244.4	−	15.0	30.0	−	6.0	30.0	+	10.0	50.0
CMB	81.54	43.2	+	3.0	9.0	+	6.0	25.0	−	4.0	30.0
GSC	82.33	47.1	+	8.0	16.0	+	8.0	19.0	−	4.0	20.0
PFO	81.63	48.7	+	6.0	12.0	+	4.0	18.0	−	4.0	20.0
COL	90.09	12.9	−	20.0	40.0	+	18.0	45.0	U	1.0	80.0
YSS	76.80	334.5	−	19.0	30.0	−	2.0	15.0	+	1.0	20.0
TUC	85.02	52.3	+	6.0	14.0	+	8.0	23.0	−	5.0	25.0
MAJO	70.71	324.9	−	22.0	40.0	−	6.0	18.0	+	12.0	50.0
CHTO	89.53	290.4	−	10.0	20.0	−	2.0	12.0	+	10.0	40.0
VTV	81.56	47.5	+	2.0	10.0	+	2.0	20.0	−	2.0	30.0
PAS	80.75	47.5	+	6.0	13.0	+	6.0	30.0	−	5.0	35.0
USC	80.60	47.5	+	6.0	14.0	+	7.0	30.0	−	5.0	35.0
TATO	74.00	305.9	−	20.0	40.0	−	5.0	20.0	+	3.0	30.0
SVD	81.46	48.0	+	6.0	14.0	+	8.0	25.0	−	4.0	25.0
BJI	86.09	316.1	−	17.0	30.0	−	4.0	20.0	+	8.0	60.0
SBC	79.87	46.5	+	4.0	12.0	+	12.0	30.0	−	7.0	30.0
XAN	88.04	307.9	−	13.0	26.0	−	5.0	20.0	+	8.0	50.0
LZH	92.68	307.9	−	12.0	22.0	−	7.0	20.0	+	6.0	60.0
SSE	77.70	310.9	−	5.0	40.0	−	5.0	20.0	+	10.0	80.0
QIZ	80.30	295.1	−	10.0	40.0	U	0.0	5.0	U	0.0	6.0
MDJ	81.06	325.8	U	10.0	40.0	U	0.0	5.0	U	0.0	8.0
ENH	85.83	304.9	−	10.0	40.0	U	0.0	5.0	U	0.0	7.0
KMI	88.88	297.6	U	10.0	40.0	U	0.0	5.0	U	0.0	7.0
HIA	89.22	325.1	−	10.0	100.0	U	0.1	8.0	U	0.1	9.0
GUMO	49.83	312.1	−	30.0	60.0	U	0.0	40.0	+	4.0	30.0

continued on next page

continued from previous page

Station			P			pP			sP		
Code	Δ	Az.	Pol.	Min.	Max.	Pol.	Min.	Max.	Pol.	Min.	Max.
ISA	81.41	46.1	+	5.0	12.0	+	7.0	20.0	–	2.0	16.0
BAR	80.97	49.4	+	6.0	15.0	+	8.0	20.0	–	1.0	30.0
ANMO	89.44	51.8	+	3.0	10.0	+	6.0	16.0	–	2.0	20.0

31 March 1994, 22:40:53.9 UT, Long–period records

Station			P			pP			sP		
Code	Δ	Az.	Pol.	Min.	Max.	Pol.	Min.	Max.	Pol.	Min.	Max.
PMSA	80.36	156.9	+	0.01	∞	U	0.0	∞	U	0.0	∞
WRAB	43.07	264.0	–	18.0	32.0	–	10.0	23.0	+	25.0	80.0
CTAO	32.03	267.2	–	20.0	38.0	–	16.0	28.0	+	30.0	100.0
PMG	34.44	286.2	–	21.0	42.0	–	18.0	36.0	+	20.0	70.0
GUMO	49.83	312.1	–	20.0	35.0	–	6.0	50.0	+	15.0	50.0
ISA	81.41	46.1	+	6.0	12.0	+	7.0	15.0	–	5.0	25.0
BAR	80.97	49.4	+	5.0	11.0	+	8.0	16.0	–	8.0	40.0
ANMO	89.44	51.8	+	4.0	10.0	+	6.0	12.0	–	5.0	30.0
COR	83.82	36.6	+	3.0	7.0	+	5.0	11.0	–	1.0	15.0
NWAO	56.46	244.4	–	15.0	30.0	–	10.0	23.0	+	20.0	55.0
CMB	81.54	43.2	+	6.0	12.0	+	7.0	15.0	–	7.0	25.0
GSC	82.33	47.1	+	5.0	11.0	+	8.0	15.0	–	5.0	30.0
PFO	81.63	48.7	+	6.0	12.0	+	9.0	18.0	–	6.0	30.0
COL	90.09	12.9	–	16.0	34.0	+	17.0	36.0	U	8.0	80.0
YSS	76.80	334.5	–	14.0	28.0	–	6.0	12.0	+	10.0	50.0
TUC	85.02	52.3	+	7.0	14.0	+	8.0	16.0	–	5.0	25.0
MAJO	70.71	324.9	–	18.0	35.0	–	8.0	15.0	U	15.0	55.0
CHTO	89.53	290.4	–	11.0	19.0	–	6.0	17.0	+	9.0	35.0
VTV	81.56	47.5	+	10.0	20.0	+	8.0	25.0	–	6.0	35.0
PAS	80.75	47.5	+	6.0	10.0	+	7.0	16.0	–	7.0	30.0
USC	80.60	47.5	+	6.0	12.0	+	7.0	15.0	–	7.0	32.0
TATO	74.00	305.9	–	15.0	30.0	–	10.0	20.0	+	10.0	50.0
SVD	81.46	48.0	+	7.0	15.0	+	8.0	16.0	–	8.0	25.0

continued on next page

continued from previous page

Station			P			pP			sP		
Code	Δ	Az.	Pol.	Min.	Max.	Pol.	Min.	Max.	Pol.	Min.	Max.
BJI	86.09	316.1	–	16.0	28.0	–	10.0	20.0	+	15.0	50.0
SBC	79.87	46.5	+	6.0	12.0	+	8.0	18.0	–	7.0	25.0
XAN	88.04	307.9	–	12.0	23.0	–	7.0	15.0	+	10.0	45.0
LZH	92.68	307.9	–	8.0	24.0	–	6.0	20.0	+	8.0	50.0
QIZ	80.30	295.1	–	8.0	24.0	U	2.0	10.0	U	4.0	40.0
MDJ	81.06	325.8	U	8.0	24.0	U	1.0	10.0	U	3.0	40.0
ENH	85.83	304.9	U	8.0	24.0	U	1.0	10.0	U	2.0	50.0
KMI	88.88	297.6	U	8.0	24.0	U	1.0	10.0	U	2.0	50.0
HIA	89.22	325.1	U	8.0	24.0	U	2.0	20.0	U	2.0	45.0
SSE	77.70	310.9	–	10.0	30.0	–	2.0	10.0	+	8.0	60.0

31 March 1994, IASP91 parameters						
Stn.	α	γ	β	i	R_{pP}	R_{sP}
ISA	30.2	147	163.0	15.4	-0.88	-0.21
BAR	30.4	146.8	162.9	15.5	-0.88	-0.21
ANMO	27.2	151.4	165.1	14.0	-0.90	-0.18
COR	29.0	148.3	163.7	14.8	-0.88	-0.20
NWAO	42.5	132.6	157.8	20.9	-0.78	-0.26
CMB	30.1	147.1	163.1	15.4	-0.88	-0.21
GSC	29.8	147.5	163.3	15.2	-0.88	-0.20
PFO	30.1	147.2	163.1	15.4	-0.88	-0.21
COL	27.1	151.7	165.3	13.9	-0.91	-0.18
YSS	32.4	144.5	161.9	16.5	-0.86	-0.22
TUC	28.4	149	164.0	14.5	-0.89	-0.20
MAJO	35.4	141.1	160.4	17.8	-0.84	-0.23
CHTO	27.2	151.4	165.1	14.6	-0.90	-0.18
VTV	30.1	147.1	163.1	15.4	-0.89	-0.21
PAS	30.5	146.7	162.9	15.6	-0.87	-0.21
USC	30.6	146.6	162.8	15.6	-0.87	-0.21
TATO	33.8	143.1	161.2	17.1	-0.85	-0.22

continued on next page

continued from previous page

Stn.	α	γ	β	i	R_{pP}	R_{sP}
SVD	30.2	147.1	163.1	15.4	-0.88	-0.21
BJI	27.9	149.6	164.2	14.3	-0.89	-0.19
SBC	30.9	146.2	162.7	15.8	-0.87	-0.21
XAN	27.3	150.6	164.7	14.0	-0.90	-0.19
LZH	26.7	152.7	165.5	13.7	-0.91	-0.18
SSE	32.0	145	162.1	16.2	-0.86	-0.22
QIZ	30.7	146.4	162.8	15.7	-0.87	-0.21
MDJ	30.4	146.8	163.0	15.5	-0.88	-0.21
ENH	28.0	149.4	164.2	14.4	-0.89	-0.19
KMI	27.2	151.1	165.0	14.0	-0.90	-0.19
HIA	27.2	151.3	165.1	14.0	-0.90	-0.18
PMSA	30.7	146.5	162.8	15.6	-0.87	-0.21
WRAB	50.1	123	153.5	23.9	-0.72	-0.29
CTAO	56.8	116.2	151.4	26.2	-0.67	-0.31
PMG	55.3	118	151.7	25.7	-0.68	-0.31
GUMO	46.3	128.1	155.2	22.4	-0.75	-0.28

4 September 1997, 04:23:38.5 UT, Broadband records											
Station			P			pP			sP		
Code	Δ	Az.	Pol.	Min.	Max.	Pol.	Min.	Max.	Pol.	Min.	Max.
NWAO	52.79	247.5	–	5.0	10.0	U	0.0	5.0	U	5.0	30.0
KIP	52.85	28.0	–	8.0	16.0	+	10.0	25.0	+	5.0	50.0
SPA	63.70	180.0	+	2.0	5.0	+	2.0	6.0	U	0.0	7.0
VNDA	51.72	184.5	+	15.0	30.0	+	4.0	40.0	U	3.0	45.0
PMSA	77.18	157.1	+	20.0	40.0	+	30.0	60.0	U	0.0	100.0
DAV	61.00	295.5	–	6.0	12.0	U	0.0	5.0	U	0.0	30.0
SSE	79.04	312.8	–	60.0	100.0	–	10.0	50.0	+	40.0	300.0
COR	88.54	37.5	–	3.0	11.0	+	20.0	50.0	U	0.0	15.0
TATO	74.95	308.2	–	5.0	10.0	–	1.0	4.0	+	3.0	40.0
BJT	87.79	317.2	–	5.0	15.0	–	1.0	4.0	+	5.0	40.0
ADK	78.12	3.2	–	3.0	6.0	U	0.0	4.0	+	1.0	10.0
KMI	89.09	298.6	–	30.0	70.0	–	7.0	25.0	+	20.0	150.0
HIA	91.62	326.0	–	25.0	50.0	–	6.0	18.0	+	20.0	100.0
CMB	86.12	44.0	–	3.0	8.0	+	30.0	100.0	U	0.0	25.0
PET	80.96	348.1	–	4.0	8.0	U	0.0	4.0	+	3.0	15.0
TUC	89.30	53.2	U	0.0	5.0	+	30.0	60.0	–	5.0	30.0
XAN	89.10	309.0	–	40.0	60.0	–	15.0	35.0	+	30.0	100.0
BILL	94.64	355.6	–	20.0	40.0	–	4.0	20.0	+	20.0	60.0
MA2	88.66	346.4	–	25.0	50.0	–	10.0	30.0	+	25.0	80.0
COLA	94.75	13.8	–	10.0	20.0	U	1.0	15.0	+	6.0	40.0
MDJ	83.53	327.3	–	4.0	8.0	–	1.0	3.0	+	3.0	15.0
ANMO	93.75	52.8	U	0.0	2.0	+	15.0	50.0	–	4.0	40.0
CHTO	89.13	291.4	–	40.0	70.0	–	15.0	45.0	+	30.0	140.0
PLCA	87.60	134.8	+	15.0	30.0	+	30.0	100.0	–	20.0	150.0
QIZ	80.32	296.8	–	6.0	12.0	–	1.0	4.0	+	5.0	20.0
LZH	93.72	308.6	–	30.0	60.0	–	5.0	20.0	+	20.0	90.0
TAU	30.07	229.0	–	10.0	20.0	U	0.0	7.0	+	20.0	160.0
WRAB	40.74	269.7	–	10.0	20.0	–	3.0	8.0	+	8.0	60.0
GUMO	51.37	316.7	–	10.0	20.0	–	0.01	5.0	+	7.0	70.0
COCO	77.09	262.7	–	10.0	20.0	–	0.1	6.0	+	1.0	25.0

continued on next page

continued from previous page

Station			P			pP			sP		
Code	Δ	Az.	Pol.	Min.	Max.	Pol.	Min.	Max.	Pol.	Min.	Max.
RPN	63.73	108.7	+	10.0	20.0	U	0.0	100.0	–	3.0	50.0
PFO	86.05	49.4	U	0.0	5.0	+	10.0	30.0	–	5.0	20.0
ERM	75.46	333.7	–	10.0	20.0	–	0.1	7.0	+	10.0	60.0
PTCN	46.26	100.2	+	6.0	12.0	U	0.0	∞			

4 September 1997, 04:23:38.5 UT, Long–period records

Station			P			pP			sP		
Code	Δ	Az.	Pol.	Min.	Max.	Pol.	Min.	Max.	Pol.	Min.	Max.
NWAO	52.79	247.5	–	10.0	20.0	–	2.0	7.0	+	10.0	50.0
KIP	52.85	28.0	–	5.0	10.0	+	4.0	15.0	+	10.0	50.0
SPA	63.70	180.0	+	10.0	20.0	+	9.0	35.0	U	10.0	80.0
VNDA	51.72	184.5	+	10.0	20.0	+	7.0	15.0	U	2.0	50.0
PMSA	77.18	157.1	+	10.0	20.0	+	12.0	25.0	U	4.0	40.0
DAV	61.00	295.5	–	10.0	20.0	–	8.0	20.0	+	12.0	40.0
SSE	79.04	312.8	–	10.0	20.0	–	2.0	8.0	+	7.0	30.0
COR	88.54	37.5	–	2.0	5.0	+	8.0	25.0	U	0.0	5.0
TATO	74.95	308.2	–	10.0	20.0	–	3.0	7.0	+	9.0	25.0
BJT	87.79	317.2	–	10.0	20.0	–	4.0	10.0	+	10.0	30.0
ADK	78.12	3.2	–	10.0	20.0	–	1.0	5.0	+	9.0	30.0
KMI	89.09	298.6	–	15.0	30.0	–	6.0	15.0	+	12.0	45.0
HIA	91.62	326.0	–	10.0	20.0	–	3.0	9.0	+	9.0	30.0
CMB	86.12	44.0	–	1.0	3.0	+	10.0	40.0	U	3.0	7.0
PET	80.96	348.1	–	10.0	20.0	–	2.0	8.0	+	10.0	40.0
TUC	89.30	53.2	+	2.0	5.0	+	10.0	35.0	–	4.0	20.0
XAN	89.10	309.0	–	10.0	20.0	–	4.0	10.0	+	10.0	30.0
BILL	94.64	355.6	–	10.0	20.0	–	2.0	6.0	+	10.0	35.0
MA2	88.66	346.4	–	10.0	20.0	–	2.0	6.0	+	10.0	30.0
COLA	94.75	13.8	–	10.0	20.0	U	1.0	14.0	+	7.0	25.0
MDJ	83.53	327.3	–	10.0	20.0	–	3.0	12.0	+	10.0	40.0
ANMO	93.75	52.8	+	1.0	3.0	+	10.0	30.0	–	5.0	12.0

continued on next page

continued from previous page

Station			P			pP			sP		
Code	Δ	Az.	Pol.	Min.	Max.	Pol.	Min.	Max.	Pol.	Min.	Max.
CHTO	89.13	291.4	−	10.0	20.0	−	4.0	10.0	+	10.0	30.0
PLCA	87.60	134.8	+	5.0	10.0	+	9.0	25.0	−	10.0	50.0
QIZ	80.32	296.8	−	10.0	20.0	−	6.0	15.0	+	10.0	35.0
LZH	93.72	308.6	−	10.0	25.0	−	4.0	15.0	+	9.0	30.0
TAU	30.07	229.0	−	10.0	30.0	U	0.0	12.0	+	30.0	120.0
WRAB	40.74	269.7	−	10.0	20.0	−	5.0	12.0	+	9.0	40.0
GUMO	51.37	316.7	−	10.0	20.0	−	5.0	18.0	+	15.0	40.0
COCO	77.09	262.7	−	10.0	20.0	−	3.0	9.0	+	8.0	25.0
RPN	63.73	108.7	+	20.0	40.0	+	15.0	40.0	−	7.0	25.0
PFO	86.05	49.4	U	0.0	3.0	+	8.0	20.0	−	3.0	6.0
ERM	75.46	333.7	−	10.0	20.0	−	2.0	7.0	+	10.0	35.0
PTCN	46.26	100.2	+	6.0	12.0	U	0.0	∞			

4 Spetember 1997, IASP91 parameters						
Stn.	α	γ	β	i	R_{pP}	R_{sP}
NWAO	44.9	129.5	155.7	21.7	-0.76	-0.27
KIP	44.9	129.5	155.8	21.7	-0.76	-0.27
SPA	39.2	136.7	158.4	19.3	-0.81	-0.25
VNDA	45.6	128.7	155.4	22.0	-0.76	-0.27
PMSA	32.5	144.4	161.8	16.3	-0.86	-0.22
DAV	40.6	134.9	157.8	20.0	-0.80	-0.25
SSE	31.6	145.4	162.3	15.9	-0.87	-0.21
COR	27.5	150.5	164.7	14.0	-0.90	-0.19
TATO	33.6	143.2	161.3	16.9	-0.85	-0.22
BJT	27.5	150.2	164.5	14.0	-0.90	-0.19
ADK	32.0	144.9	162.0	16.1	-0.86	-0.22
KMI	27.4	150.9	164.9	14.0	-0.90	-0.19
HIA	27.1	152.3	165.4	13.8	-0.91	-0.18
CMB	28.1	149.3	164.1	14.3	-0.90	-0.19
PET	30.6	146.4	162.8	15.5	-0.88	-0.21

continued on next page

continued from previous page						
Stn.	α	γ	β	i	R_{pP}	R_{sP}
TUC	27.4	151	164.9	14.0	-0.90	-0.18
XAN	27.4	150.9	164.9	14.0	-0.90	-0.19
BILL	26.5	152.7	165.5	13.5	-0.91	-0.18
MA2	27.5	150.6	164.8	14.0	-0.90	-0.19
COLA	26.5	152.7	165.5	13.5	-0.91	-0.18
MDJ	29.4	147.9	163.4	14.9	-0.88	-0.20
ANMO	26.7	152.6	165.5	13.6	-0.91	-0.18
CHTO	27.4	150.9	164.9	14.0	-0.90	-0.18
PLCA	27.5	150.1	164.5	14.0	-0.90	-0.19
QIZ	30.9	146.1	162.6	15.6	-0.87	-0.21
LZH	26.7	152.6	165.5	13.6	-0.91	-0.18
TAU	58.5	114.1	149.7	26.6	-0.67	-0.31
WRAB	51.9	120.5	152.7	24.3	-0.69	-0.31
GUMO	45.8	128.4	155.3	22.1	-0.75	-0.28
COCO	32.5	144.3	161.8	16.4	-0.86	-0.22
RPN	39.2	136.7	158.4	19.3	-0.81	-0.25
PFO	28.1	149.2	164.1	14.3	-0.89	-0.19
ERM	33.3	143.5	161.4	16.7	-0.86	-0.22
PTCN	48.5	124.7		23.1	-0.73	-0.28

29 March 1998, 19:48:16.5 UT, Broadband records											
Station			P			pP			sP		
Code	Δ	Az.	Pol.	Min.	Max.	Pol.	Min.	Max.	Pol.	Min.	Max.
PMG	33.88	279.3	+	8.0	14.0	+	1.0	50.0	–	15.0	50.0
CTAO	32.99	260.0	–	8.0	14.0	+	10.0	30.0	–	14.0	50.0
WRAB	44.17	259.2	–	6.0	10.0	+	0.5	10.0	–	13.0	50.0
TAU	38.16	221.3	–	15.0	32.0	U	0.1	25.0	U	5.0	45.0
GUMO	47.24	308.6	+	20.0	40.0	U	0.0	12.0	U	0.0	10.0
ANMO	86.29	51.7	+	3.0	6.0	+	2.5	7.0	–	8.0	30.0
BILL	86.03	354.6	+	8.0	14.0	+	0.5	5.0	–	7.0	25.0
TATO	71.76	304.5	+	15.0	25.0	U	0.0	4.0	–	4.0	20.0
CMB	77.94	43.6	+	5.0	10.0	+	4.0	10.0	–	9.0	30.0
SBA	60.75	183.4	–	4.0	10.0	–	5.0	20.0	U	0.0	12.0
COR	79.92	36.8	+	6.0	12.0	+	6.0	12.0	–	6.0	20.0
DAV	59.99	289.3	+	10.0	40.0	U	0.0	15.0	–	7.0	20.0
PET	72.89	346.1	+	14.0	28.0	U	0.0	10.0	–	5.0	30.0
XAN	85.62	307.6	+	14.0	28.0	U	0.0	8.0	–	5.0	16.0
VNDA	60.76	184.7	–	5.0	11.0	–	4.0	10.0	U	2.0	11.0
PMSA	84.35	157.0	–	1.0	4.0	–	10.0	40.0	+	5.0	15.0
ENH	83.63	304.3	+	15.0	30.0	U	0.0	5.0	–	3.0	13.0
NWAO	58.92	241.8	–	7.0	14.0	U	0.0	5.0	–	6.0	25.0
INCN	74.92	317.9	+	15.0	30.0	U	0.0	5.0	–	10.0	50.0
SSE	75.10	309.9	+	10.0	20.0	U	0.0	4.0	–	7.0	25.0
MAJO	67.30	323.6	+	15.0	30.0	+	0.1	5.0	–	8.0	30.0
YSS	72.92	333.7	+	18.0	32.0	U	0.0	6.0	–	6.0	16.0
ADK	69.16	1.5	+	12.0	22.0	+	2.0	8.0	–	10.0	50.0
CHTO	88.38	290.2	+	6.0	10.0	U	1.0	4.0	–	4.0	14.0
PFO	78.32	49.1	+	3.0	8.0	+	4.0	9.0	–	7.0	25.0
MDJ	77.58	325.1	+	15.0	30.0	U	0.0	6.0	–	6.0	16.0
MA2	80.71	344.9	+	10.0	20.0	+	0.5	6.0	–	6.0	16.0
BJT	83.14	315.5	+	16.0	30.0	U	0.0	5.0	–	9.0	28.0
KMI	87.20	297.3	+	6.0	12.0	U	0.0	3.0	–	5.0	15.0
HIA	85.77	324.8	+	10.0	20.0	U	0.0	4.0	–	6.0	22.0

continued on next page

continued from previous page

Station			P			pP			sP		
Code	Δ	Az.	Pol.	Min.	Max.	Pol.	Min.	Max.	Pol.	Min.	Max.
TLY	96.02	322.3	+	4.0	8.0	U	0.0	1.8	–	2.0	8.0
PLCA	91.96	133.8	U	0.0	2.0	–	8.0	16.0	+	2.5	9.0
HKT	92.85	59.6	+	1.5	4.5	+	2.0	8.0	–	6.0	18.0
ULN	92.41	319.3	+	6.0	15.0	U	0.0	3.0	–	3.0	12.0

29 March 1998, 19:48:16.5 UT, Long–period records

Station			P			pP			sP		
Code	Δ	Az.	Pol.	Min.	Max.	Pol.	Min.	Max.	Pol.	Min.	Max.
PMG	33.88	279.3	+	8.0	15.0	+	5.0	12.0	–	18.0	50.0
CTAO	32.99	260.0	–	7.0	14.0	+	4.0	20.0	–	17.0	80.0
WRAB	44.17	259.2	–	4.0	10.0	+	3.0	15.0	–	16.0	50.0
TAU	38.16	221.3	–	14.0	30.0	U	1.0	20.0	U	10.0	40.0
GUMO	47.24	308.6	+	16.0	30.0	U	1.0	15.0	U	1.0	15.0
ANMO	86.29	51.7	+	4.0	8.0	+	1.0	4.0	–	6.0	28.0
BILL	86.03	354.6	+	9.0	18.0	+	2.0	6.0	–	8.0	25.0
TATO	71.76	304.5	+	10.0	20.0	U	0.0	4.0	–	5.0	40.0
CMB	77.94	43.6	+	6.0	12.0	+	4.0	10.0	–	9.0	30.0
SBA	60.75	183.4	–	6.0	12.0	–	6.0	18.0	U	3.0	12.0
COR	79.92	36.8	+	6.0	12.0	+	4.0	9.0	–	8.0	25.0
DAV	59.99	289.3	+	10.0	40.0	U	0.0	15.0	–	4.0	40.0
PET	72.89	346.1	+	14.0	28.0	U	0.0	15.0	–	4.0	40.0
XAN	85.62	307.6	+	7.0	17.0	U	0.0	4.0	–	4.0	40.0
VNDA	60.76	184.7	–	5.0	9.0	–	6.0	15.0	U	2.0	12.0
PMSA	84.35	157.0	–	1.0	4.0	–	10.0	30.0	+	5.0	15.0
ENH	83.63	304.3	+	15.0	30.0	U	0.0	5.0	–	6.0	60.0
NWAO	58.92	241.8	–	6.0	12.0	U	0.0	7.0	–	10.0	35.0
INCN	74.92	317.9	+	16.0	30.0	U	0.0	5.0	–	10.0	40.0
SSE	75.10	309.9	+	10.0	20.0	U	0.0	4.0	–	7.0	30.0
MAJO	67.30	323.6	+	15.0	30.0	U	0.0	4.0	–	7.0	30.0
YSS	72.92	333.7	+	15.0	30.0	U	1.0	8.0	–	9.0	30.0

continued on next page

continued from previous page

Station			P			pP			sP		
Code	Δ	Az.	Pol.	Min.	Max.	Pol.	Min.	Max.	Pol.	Min.	Max.
ADK	69.16	1.5	+	10.0	20.0	+	2.0	7.0	–	8.0	30.0
CHTO	88.38	290.2	+	6.0	12.0	U	0.5	4.0	–	5.0	25.0
PFO	78.32	49.1	+	5.0	10.0	+	3.0	6.0	–	7.0	25.0
MDJ	77.58	325.1	+	15.0	30.0	U	0.0	6.0	–	6.0	28.0
MA2	80.71	344.9	+	10.0	20.0	+	1.0	5.0	–	5.0	18.0
BJT	83.14	315.5	+	16.0	30.0	U	0.0	4.0	–	6.0	30.0
KMI	87.20	297.3	+	6.0	12.0	U	0.0	3.0	–	4.0	15.0
HIA	85.77	324.8	+	10.0	20.0	U	0.0	4.0	–	6.0	25.0
TLY	96.02	322.3	+	4.0	8.0	U	0.0	2.0	–	3.0	15.0
PLCA	91.96	133.8	U	0.0	3.0	–	7.0	100.0	+	4.0	70.0
HKT	92.85	59.6	+	2.0	6.0	+	1.0	7.0	–	5.0	50.0
ULN	92.41	319.3	+	7.0	40.0	U	0.0	4.0	–	5.0	80.0

29 March 1998, IASP91 parameters						
Stn.	α	γ	β	i	R_{pP}	R_{sP}
PMG	53.4	121.9	152.8	26.0	-0.68	-0.31
CTAO	53.9	121.2	152.7	26.2	-0.68	-0.31
WRAB	47.6	127.3	154.9	23.8	-0.72	-0.29
TAU	50.9	123.6	153.5	25.1	-0.70	-0.30
GUMO	45.8	129.4	155.6	23.1	-0.74	-0.28
ANMO	26.9	151	164.9	14.3	-0.89	-0.19
BILL	27.0	150.8	164.9	14.4	-0.89	-0.19
TATO	33.8	143.5	161.5	17.7	-0.84	-0.23
CMB	30.9	146.7	162.9	16.3	-0.87	-0.21
SBA	39.1	137.5	158.9	20.2	-0.80	-0.26
COR	29.9	147.7	163.4	15.8	-0.87	-0.21
DAV	39.5	137.1	158.7	20.3	-0.79	-0.24
PET	33.2	144.2	161.7	17.4	-0.85	-0.23
XAN	27.2	150.6	164.8	14.5	-0.89	-0.19
VNDA	39.1	137.5	158.9	20.2	-0.80	-0.26

continued on next page

continued from previous page						
Stn.	α	γ	β	i	R_{pP}	R_{sP}
PMSA	27.9	150	164.5	14.8	-0.89	-0.20
ENH	28.2	149.6	164.3	15.0	-0.89	-0.20
NWAO	40.0	136.4	158.4	20.6	-0.79	-0.26
INCN	32.3	145.2	162.2	17.0	-0.85	-0.22
SSE	32.2	145.3	162.2	16.9	-0.86	-0.22
MAJO	35.8	141.1	160.4	18.7	-0.82	-0.24
YSS	33.2	144.2	161.8	17.4	-0.85	-0.23
ADK	34.9	142.1	160.8	18.2	-0.83	-0.24
CHTO	26.3	152	165.5	14.0	-0.90	-0.19
PFO	30.7	146.9	163.0	16.2	-0.87	-0.21
MDJ	31.0	146.5	162.8	16.4	-0.86	-0.22
MA2	29.6	148.1	163.6	15.6	-0.88	-0.21
BJT	28.4	149.4	164.2	15.1	-0.88	-0.20
KMI	26.5	151.4	164.1	14.1	-0.90	-0.19
HIA	27.2	150.7	164.8	14.5	-0.89	-0.19
TLY	25.2	154.1	166.3	13.4	-0.91	-0.18
PLCA	25.9	153.7	166.1	13.8	-0.91	-0.18
HKT	25.8	153.8	166.1	13.7	-0.91	-0.18
ULN	25.8	153.7	166.1	13.8	-0.91	-0.18